Olga Barrera
Alan Cocks
Alan Ponter *Editors*

Advances in Direct Methods for Materials and Structures

Springer

Advances in Direct Methods for Materials and Structures

Olga Barrera · Alan Cocks
Alan Ponter
Editors

Advances in Direct Methods for Materials and Structures

Springer

Editors
Olga Barrera
Department of Engineering Science
University of Oxford
Oxford, Oxfordshire
UK

Alan Cocks
Department of Engineering Science
University of Oxford
Oxford, Oxfordshire
UK

Alan Ponter
Department of Engineering
University of Leicester
Leicester, Leicestershire
UK

ISBN 978-3-319-59808-6 ISBN 978-3-319-59810-9 (eBook)
DOI 10.1007/978-3-319-59810-9

Library of Congress Control Number: 2017941059

Printed on acid-free paper

This Springer imprint is published by Springer Nature
The registered company is Springer International Publishing AG
The registered company address is: Gewerbestrasse 11, 6330 Cham, Switzerland

Preface

Direct methods refer to a class of analysis methods that aim to characterise the limit state of a material or structure when subjected to an increasing or cyclic loading history, without the need to generate the entire response to the history of loading. Direct methods were originally developed for limit state and shakedown analysis for an elastic perfectly plastic material model. Developments in recent years have explored cyclic solutions for more general material models and for optimal design and the characterisation of material behaviour in terms of material microstructure. The resulting methods have been successfully applied to a number of industrially important structural problems, including the design and prediction of life expectancy of structures subjected to complex thermo-mechanical loading; and the behaviour of road pavements subjected to repeated loading. Computational methods of increased efficiency continue to be developed.

The papers in this volume provide a state-of-the-art insight into the subject and have arisen from an International Workshop held at the University of Oxford on 6–8 September 2015. More than 30 delegates from eleven countries attended and represent the foremost researchers in this area. The workshop was the fifth such workshop, following previous biannual workshops in Aachen, Lille, Athens and Reggio Calabria. The papers from the previous workshops have also been published by Springer.

The papers are arranged in the same format as the workshop in which groups of papers, are concerned with similar issues. The papers have all been subjected to a rigorous review procedure before acceptance for publication.

The editors would like to thank all the scientists who attended the workshop and have contributed to the high quality of the papers in this volume. Special thanks go to Amanda Bradbury for her exceptional help in organising the Workshop.

We are also grateful to the editorial staff of Springer for their patience and guidance during the production of this volume.

Oxford, UK — Olga Barrera
Oxford, UK — Alan Cocks
Leicester, UK — Alan Ponter

Contents

Limit Load Theorems for the Drucker-Prager Yield Condition with a Non-associated Flow Rule

A.R.S. Ponter

Abstract There exist a number of significant problems where the assumptions of limit and shakedown analysis, i.e. the bounding theorems, are not fully satisfied. Principal amongst such problems are those where the yield surface is convex but the flow rule is non-associated. This includes limit states in geomechanics where yield is pressure dependent but flow remains volume conserving. Coulomb friction between elastic bodies shows related behaviour. The paper explores the extent to which the classical limit theorems may be extended to the Drucker-Prager yield condition with a non-associated flow rule where the plastic strain rate involves no volume change. Bounds that correspond to the classical kinematic and static bounds are derived which defines a range within which consistent limit state solutions will exist, i.e. the limit state is not generally unique.

1 Introduction

The theory of limit analysis, Drucker, Prager and Greenberg [1], forms the foundations of a wide range of design methods in industrial applications. The theory is simple and elegant, derived from a set of specific material assumptions. Small strain theory is assumed, i.e. any displacements prior to the arrival at a limit or shakedown state are such that the equations of equilibrium in the original undeformed state are sufficiently accurate. The material is elastic-perfectly plastic with a convex yield surface and an associated flow rule. Hence the plastic properties are defined by a yield condition, $f(\sigma_{ij}) = 0$, so that for;

$$f(\sigma_{ij}) \leq 0, \quad \dot{\varepsilon}^p_{ij} = 0 \tag{1.1}$$

A.R.S. Ponter (✉)
Department of Engineering, University of Leicester, Leicester LE2 4RH, UK
e-mail: asp@le.ac.uk

O. Barrera et al. (eds.), *Advances in Direct Methods for Materials and Structures*, DOI 10.1007/978-3-319-59810-9_1

$$f(\sigma_{ij}) = 0, \quad \dot{\varepsilon}^p_{ij} = \dot{\eta} \frac{\partial f(\sigma_{ij})}{\partial \sigma_{ij}} \tag{1.2}$$

where $\dot{\eta}$ is a positive scalar multiplier. No plastic strains occur within the yield surface and the plastic strain rate $\dot{\varepsilon}^p_{ij}$ forms an outward normal vector in stress space to the yield surface. States of stress where $f(\sigma_{ij}) \geq 0$ are not allowed.

Consider a volume V subject to surface tractions $\lambda P(x_i)$ acting on part of the surface S of V, namely S_P, and zero displacements $u_i = 0$ over the remainder of S, namely S_u. Limit analysis seeks the value of the load parameter $\lambda = \lambda_L$ corresponding to a state of plastic collapse.

The lower bound theorem for values of $\lambda_{LB} \leq \lambda_L$ involves an arbitrary distribution of stress $\lambda \sigma^P_{ij}(x_i)$ which satisfies the equations of equilibrium and is in equilibrium with $\lambda P(x_i)$ on S_P. For any such distribution there will exist a $\lambda = \lambda_{LB}$ so that;

$$f(\lambda_{LB} \sigma^P_{ij}) \leq 0 \text{ within } V, \text{ and } \lambda_{LB} \leq \lambda_L, \tag{1.3}$$

It is not possible that $\lambda > \lambda_{LB}$ as, in this case the yield condition will be violated somewhere within V. Hence $\lambda_{LB} = \lambda_L$ occurs for some optimal choice of σ^P_{ij}, so that λ_{LB} is an absolute maximum over all possible σ^P_{ij}. Note that this argument makes no reference to the flow rule, it is entirely concerned with finding the largest value of λ for which the yield condition may be satisfied throughout V. Hence the result is equally applicable to a non-associated flow rule. There is, however, a distinction between the two cases. For an associated flow rule this maximum λ is the limit load, whereas for a non-associated flow rule this may not be the case and a limit state occurs at a lower value of λ. This is a restatement of Radenkovic's result [2] and will be discussed in the next Sect. 3.3.

The upper bound theorem is expressed in terms of a distribution of plastic strain rate $\dot{\varepsilon}^p_{ij} = \dot{\varepsilon}^c_{ij}$ that satisfies the compatibility equations and is compatible with a displacement rate field $\dot{u}^c_i$ satisfying $\dot{u}^c_i = 0$ on S_u. An upper bound on λ_L, λ_{UB} is then defined by the work balance equation;

$$\lambda_{UB} \int_{S_P} P_i \dot{u}^c_i dS = \int_V \sigma^c_{ij} \dot{\varepsilon}^c_{ij} dV, \ \lambda_{UB} \geq \lambda_L \tag{1.4}$$

Here σ^c_{ij} is the state of stress on the yield surface that is associated with the plastic strain rate $\dot{\varepsilon}^c_{ij}$, i.e. $\sigma^c_{ij} \dot{\varepsilon}^c_{ij}$ is the rate of plastic energy dissipation per unit volume.

The upper bound is concerned with finding a mechanism so that the rate of work done by the applied load is exactly balanced by the rate of plastic energy dissipation. The limit load corresponds to the mechanism for which the load factor is least.

The proofs of these results [1] rely upon the Maximum Work Principle, given by the inequality,

$$(\sigma_{ij}^{c} - \sigma_{ij}^{*})\dot{\varepsilon}_{ij}^{c} \geq 0 \tag{1.5}$$

where σ_{ij}^{*} satisfies the yield condition $f(\sigma_{ij}^{*}) \leq 0$. The inequality (1.5) is only satisfied for the yield condition so that $f(\sigma_{ij}) = 0$ defines a convex surface in stress space, and the flow rule is associated, i.e. given by (1.2).

As well as the bounds (1.3) and (1.4), the Maximum Work Principle also allows the proof of a related result, first proven by Symonds [3]. Symond's result was concerned with a history of loading $\lambda P(x_i, t)$ between an initial state, where the body possesses some complex initial distribution of stress (resulting, for example, from the fabrication of a structure). Symonds showed that the limit state (and the shakedown state for variable loading) was independent of how the load history arrived at $\lambda_L P(x_i)$ and also the initial state of stress. In the development of Limit State Design this result was particularly important. Elastic design methods had always ignored initial residual stress in the structure as they were essentially unknown, leaving the elastic approach, in an important way, inconsistent with the known properties of metallic structures.

The subsequent development of design methods based on the Limit Theorems, produced a methodology that was consistent with known properties of steel structures, resulting in procedures that were easier to apply than elastic methods and required less material. This last feature undoubtedly contributed to the rapid advance of Limit State Design in the 1940s and 50s when steel was in short supply and there was a pressing need to rebuild after World War 2.

Although it has always been known that association of the flow rule was not consistent with materials that exhibit frictional behaviour, the elegance and simplicity of the theory allowed whole ranges of calculations to be made. Radenkovic [2], demonstrated that the limit load for the non-associated case is always less than for the associated case for the same yield surface. Since that time the solution of particular problems in geomechanics has usually assumed an associated flow rule and often, in the literature, there is no mention of the underlying issue of the non-association of the flow rule. Certainly, the assumption that a unique limit load always existed that is independent of the initial state of stress, seems to persist.

In the following section, the extent to which the classical theorems may be extended to a convex yield surface with a non-associated flow rule is discussed for the Drucker-Prager yield condition [4].

2 Limit States—A General Definition

The conditions for a limit state may be defined without placing restrictions on the flow rule. Consider a body of volume V which experiences elastic strains e_{ij} and plastic strains ε_{ij}^{p}

$$\varepsilon_{ij} = e_{ij} + \varepsilon_{ij}^{p} \quad \text{and} \quad e_{ij} = C_{ijkl}\sigma_{kl} \tag{2.1}$$

where C_{ijkl} denotes the elastic stiffness tensor.

A history of loading to the limit state involves the generation of a distribution of plastic strain $\varepsilon_{ij}^{p}(x_i) = \overline{\varepsilon}_{ij}^{p}(x_i)$ which, generally, will not be compatible. As a result the state of stress at a limit state $\lambda = \lambda_L$ will be given by,

$$\sigma_{ij}^{*} = \lambda_L \widehat{\sigma}_{ij}^{P}(x_i) + \overline{\rho}_{ij}(x_i) \tag{2.2}$$

where $\widehat{\sigma}_{ij}^{P}(x_i)$ denotes the linear elastic solution for $\lambda = 1$ and $\overline{\rho}_{ij}(x_i)$ is the residual stress field derived from the solution of the initial strain problem for $\overline{\varepsilon}_{ij}^{p}(x_i)$.

$$\varepsilon_{ij}^{T} = C_{ijkl}\overline{\rho}_{kl} + \overline{\varepsilon}_{ij}^{p} \tag{2.3}$$

where ε_{ij}^{T} is a compatible strain field consistent with corresponding displacements consistent with the boundary conditions. σ_{ij}^{*} must satisfy two conditions;

(a) Yield:

$$f(\sigma_{ij}^{*}) \le 0 \tag{2.4}$$

(b) Consistency with a failure mechanism: There exists a compatible distribution of plastic strain rate $\dot{\varepsilon}_{ij}^{c}(x_i)$ with corresponding displacement field $\dot{u}_i^{c}(x_i)$, so that at positions x_i where $\dot{\varepsilon}_{ij}^{c}(x_i) \neq 0$,

$$\sigma_{ij}^{*} = \sigma_{ij}^{c}. \tag{2.5}$$

We know, from general theory, that the value of λ_L is uniquely defined for an associated flow rule and convex yield surface. For a non-associated flow rule, we begin with the assumption that λ_L will generally not be unique and consistent solutions may exist for a range of plastic strain distributions $\overline{\varepsilon}_{ij}^{p}(x_i)$. In terms of step by step calculations, the expectation must be that a limit state will depend upon both the initial state of residual stress and the particular history of loading that leads to a

limit state. An important issue is the range of possible λ within which limit states exist. In the following sections this is discussed for the Drucker-Prager yield condition with volume conserving plastic flow.

3 Limit Analysis for a Non-associated Plastic Flow

3.1 Material Model

Consider, again, a body of volume V which experiences elastic strains e_{ij} and plastic strains ε_{ij}^{p};

$$\varepsilon_{ij} = e_{ij} + \varepsilon_{ij}^{p} \quad \text{and} \quad e_{ij} = C_{ijkl}\sigma_{kl} \tag{3.1}$$

where C_{ijkl} denotes the elastic stiffness tensor.

Consider the Prager-Drucker yield condition:

$$f(\sigma_{ij}^{'}, p) = \tilde{\sigma}(\sigma_{ij}^{'}) - c - |p|\ \tan\phi \leq 0,\ p \leq 0 \tag{3.2}$$

where $\tilde{\sigma}(\sigma_{ij}^{'}) = \sqrt{3/2\sigma_{ij}^{'}\sigma_{ij}^{'}}$ is the von Mises effective stress for the deviatoric stress $\sigma_{ij}^{'} = \sigma_{ij} - p\delta_{ij}$, and where $p = 1/3\sigma_{kk}$ is the hydrostatic component of stress, c is the cohesion and ϕ is an angle of friction. Plastic strain rates $\dot{\varepsilon}_{ij}^{p}$ for $f(\sigma_{ij}^{'}, p) = 0$ occur according to the non-associated flow rule;

$$\dot{\varepsilon}_{ij}^{'p} = \dot{\eta}\frac{\partial\tilde{\sigma}(\sigma_{ij}^{'})}{\partial\sigma_{ij}^{'}} \quad \text{and} \quad \dot{\varepsilon}_{kk}^{p} = 0 \tag{3.3}$$

where $\dot{\eta}$ is a positive scalar multiplier.

The rate of plastic work may be written in term of effective quantities;

$$\dot{W}^{p} = \sigma_{ij}^{'}\dot{\varepsilon}_{ij}^{p} = \tilde{\sigma}\tilde{\dot{\varepsilon}}^{p} \tag{3.4}$$

where $\tilde{\dot{\varepsilon}}^{p} = \sqrt{2/3\dot{\varepsilon}_{ij}^{p}\dot{\varepsilon}_{ij}^{p}}$ denoted the von Mises effective plastic strain rates. Note that the equality (3.4) only holds when $\sigma_{ij}^{'}$ is the state of deviatoric stress at yield corresponding to $\dot{\varepsilon}_{ij}^{p}$. However, the Cauchy-Schwartz[1] inequality;

[1]The inequality may be recognised as a generalisation of the cosine rule for the dot product of two vectors.

$$\sigma_{ij}^{'*}\dot{\varepsilon}_{ij}^{p} \le \tilde{\sigma}^{*}\tilde{\dot{\varepsilon}}^{p} \tag{3.5}$$

holds for a state of stress within yield $\sigma_{ij}^{'*}$ and not necessarily corresponding to $\dot{\varepsilon}_{ij}^{p}$. Equality in (3.5) hold if and only if $\sigma_{ij}^{'*}$ corresponds to the stress where $\dot{\varepsilon}_{ij}^{p}$ occurs, (3.4).

In the following sections we consider bounds on the value of tanϕ for which consistent limit states may exist for a constant λ. The choice of tanϕ allows entirely frictional behaviour, c = 0, to be included in a natural way.

3.2 The Static Bound Theorem

Consider a state of stress defined by the chosen load parameter λ and a distribution $\overline{\varepsilon}_{ij}^{p}(x_i)$ with associated residual stress field $\bar{\rho}_{ij}$. The resulting distribution of stress

$$\sigma_{ij}^{*} = \lambda\widehat{\sigma}_{ij} + \overline{\rho}_{ij} \tag{3.7a}$$

$$p^{*} = 1/3\left\{\sigma_{kk}^{*}(x_i,t)\right\} = 1/3\left\{\lambda\widehat{\sigma}_{kk}(x_i,t) + \overline{\rho}_{kk}(x_i)\right\} = \lambda\hat{p} + \bar{p} \ge 0 \tag{3.7b}$$

will lie within yield provided tanϕ is sufficiently large.

Consider

$$\tan\phi_{UB}^{L}(\overline{\varepsilon}_{ij}^{p}(x_i)) = \max\left\{\frac{\tilde{\sigma}^{*} - c}{|p^{*}|}\right\} \tag{3.8}$$

over all x_i in V. If tan$\phi \ge$ tan$\phi_{UB}^{L}(\overline{\varepsilon}_{ij}^{p}(x_i))$ then σ_{ij}^{*}, (3.7a), (3.7b), lies within yield.

This argument may now be extended by seeking, over all $\overline{\varepsilon}_{ij}^{p}(x_i)$, the absolute minimum upper bound tanϕ_{AUB}^{L};

$$\tan\phi_{AUB}^{L} = \min\left\{\tan\phi_{UB}^{L}(\overline{\varepsilon}_{ij}^{p}(x_i)\right\} \text{ over all } \overline{\varepsilon}_{ij}^{p}. \tag{3.9}$$

Hence for tan$\phi <$ tanϕ_{AUB}^{L} there exists no $\overline{\varepsilon}_{ij}^{p}(x_i)$ so that $\sigma_{ij}^{*} = \lambda\widehat{\sigma}_{ij} + \overline{\rho}_{ij}$ lies within yield everywhere. The limit tanϕ_{AUB}^{L} may be recognised as the limit state for the associated flow rule: the friction angle corresponds to the least value of tanϕ for which an equilibrium stress state exists within yield everywhere within V for any $\overline{\varepsilon}_{ij}^{p}(x_i)$.

It is worth including a note of caution concerning the argument in the previous paragraph. If the plastic strain distribution accumulated from plastic strain rates is given by the flow rule (3.3), then $\overline{\varepsilon}_{ij}^{p}(x_i)$ contains no volumetric component, $\overline{\varepsilon}_{kk}^{p}(x_i) = 0$. However, if plastic strain accumulation begins with a strain field with a volumetric component or, alternatively, the flow rule (3.3) applies only at the limit

state but volumetric strains occur beforehand (as occurs in the numerical solution of Krabbenhoft et al. [5]), then the plastic strain defines a potentially wider class of residual stress field $\overline{\rho}_{ij}$.

3.3 The Kinematic Bound Theorem

A kinematic bound is concerned with values of $\tan\phi$ where there is a balance between the work done by the applied load and the plastic energy dissipation, which depends upon both c and λ. For such an argument to be meaningful λ must be greater than λ_L for the associated flow rule for $\tan\phi = 0$.

Consider, again, a distribution of plastic strain $\overline{\varepsilon}^p_{ij}(x_i)$ with corresponding $\overline{\rho}_{ij}$. In addition, consider a compatible distribution of strain rate $\dot{\varepsilon}^c_{ij}(x_i)$ with $\dot{\varepsilon}^c_{kk}(x_i) = 0$ and a corresponding displacement field $\dot{u}^c_i(x_i)$ which satisfies $\dot{u}^c_i(x_i) = 0$ on S_u.

Although the Maximum Work Principal does not hold for (3.2) and (3.3), a restricted form is possible by considering the inequality applied to the cross section of the yield surface defined by p^*, (3.7b), which is defined by $\overline{\varepsilon}^p_{ij}(x_i)$;

$$(\sigma'^{ac}_{ij} - \sigma'^{*}_{ij})\dot{\varepsilon}'^{c}_{ij} \geq 0 \tag{3.10}$$

where σ'^{ac}_{ij} is the stress at yield associated with $\dot{\varepsilon}'^{c}_{ij}$ within the plane $p = p^*$ and σ'^{*}_{ij} is the deviatoric components of σ^*_{ij}, (3.7a).

From (3.2) and (3.7a), (3.7b), (3.10) may be rewritten as

$$\widetilde{\sigma}^{ac}\widetilde{\dot{\varepsilon}}^c - (\lambda\widehat{\sigma}'_{ij} + \overline{\rho}'_{ij})\dot{\varepsilon}'^{c}_{ij} = (c + |\hat{p} + \bar{p}|\tan\phi)\widetilde{\dot{\varepsilon}}^c - (\lambda\widehat{\sigma}_{ij} + \overline{\rho}_{ij})\dot{\varepsilon}'^{c}_{ij} \geq 0 \tag{3.11}$$

Integrating (3.11) over the volume V we obtain,

$$\int_V (c + |\hat{p} + \bar{p}|\tan\phi)\widetilde{\dot{\varepsilon}}^c dV \geq \int_V \lambda\widehat{\sigma}_{ij}\dot{\varepsilon}'^{c}_{ij} dV \tag{3.12}$$

Note that $\int_V \overline{\rho}_{ij}\dot{\varepsilon}'^{c}_{ij} dV = \int_V \overline{\rho}_{ij}\dot{\varepsilon}^c_{ij} dV = 0$ from the principle of virtual work.

Now consider (3.12) arranged so that it makes a statement about the friction angle ϕ consistent with σ^*_{ij} satisfying yield and assuming fixed values of c and λ, and chosen distributions $\overline{\varepsilon}^c_{ij}$ and $\dot{\varepsilon}^c_{ij}$;

$$\tan\phi \geq \frac{\int_V \left\{\lambda\widehat{\sigma}_{ij}\dot{\varepsilon}'^{c}_{ij} - c\widetilde{\dot{\varepsilon}}^c\right\} dtdV}{\int_V |\hat{p} + \bar{p}|\widetilde{\dot{\varepsilon}}^c dV} = \tan\phi^L_{LB}(\dot{\varepsilon}^c_{ij}, \overline{\varepsilon}^p_{ij}) \tag{3.13}$$

Note that the bounds (3.13) depend upon both the mechanism $\dot{\varepsilon}_{ij}^{c}$ and the plastic strain distribution $\overline{\varepsilon}_{ij}^{p}$ from which $\bar{p}$ is derived. For any chosen $\widehat{\varepsilon}_{ij}^{p}$, and hence $\overline{\rho}_{ij}$, there will exist a maximum bound with respect to $\overline{\varepsilon}_{ij}^{c}$; this corresponds to a conventional limit load problem where the yield condition is defined everywhere in V. Hence

$$\tan\phi \geq \tan\phi_{LB}^{L}(\overline{\varepsilon}_{ij}^{p}) \geq \tan\phi_{LB}^{L}(\dot{\varepsilon}_{ij}^{c}, \overline{\varepsilon}_{ij}^{p}) \tag{3.14}$$

where $\tan\phi_{LB}^{L}(\overline{\varepsilon}_{ij}^{p}) = \max\left\{\tan\phi_{LB}^{L}(\dot{\varepsilon}_{ij}^{c}, \overline{\varepsilon}_{ij}^{p})\right\}$ over all kinematically admissible mechanisms $\dot{\varepsilon}_{ij}^{c}$.

It is now possible to take this argument a step further by seeking the absolute maximum of $\tan\phi_{LB}^{L}(\overline{\varepsilon}_{ij}^{p})$ for all possible $\overline{\varepsilon}_{ij}^{p}$, giving the extended inequality;

$$\tan\phi \geq \tan\phi_{ALB}^{L} \geq \tan\phi_{LB}^{L}(\overline{\varepsilon}_{ij}^{p}) \geq \tan\phi_{LB}^{L}(\dot{\varepsilon}_{ij}^{c}, \overline{\varepsilon}_{ij}^{p}) \tag{3.15}$$

where $\tan\phi_{ALB}^{L} = \max\left\{\tan\phi_{LB}^{L}(\overline{\varepsilon}_{ij}^{p})\right\}$ over all admissible $\overline{\varepsilon}_{ij}^{p}$. Hence, for potential limit states, allowing for all possible mechanism $\dot{\varepsilon}_{ij}^{c}$ and plastic strain distributions $\overline{\varepsilon}_{ij}^{pc}$ then $\tan\phi \geq \tan\phi_{ALB}^{L}$. This implies that for $\tan\phi < \tan\phi_{ALB}^{L}$ there exists no consistent limit states.

Hence both kinematic and static bounds exist but, for the non-associated case, they are not defined independently of each other. Each is dependent on the choice of the plastic strain field $\overline{\varepsilon}_{ij}^{p}$ and each possess, independently, extreme values. For any particular choice of $\overline{\varepsilon}_{ij}^{p}$ the bounds, $\tan\phi_{LB}^{L}(\overline{\varepsilon}_{ij}^{p})$ (3.15) and $\tan\phi_{UB}^{L}(\overline{\varepsilon}_{ij}^{p})$ (3.14) may not coincide and only for particular $\overline{\varepsilon}_{ij}^{p}$ will

$$\tan\phi_{UB}^{L}(\overline{\varepsilon}_{ij}^{p}) = \tan\phi_{LB}^{L}(\overline{\varepsilon}_{ij}^{p}) \tag{3.16}$$

Such distributions are termed *consistent* distributions, producing equal upper and lower bounds that correspond to a limit state. It is immediately evident that the absolute extremes $\tan\phi_{ALB}^{L}$ (3.15) and $\tan\phi_{AUB}^{L}$, (3.9), may not necessarily correspond to consistent states, although this, no doubt, may occur in some circumstances. Hence the search for limit states is the search for distributions of $\overline{\varepsilon}_{ij}^{p}$ and mechanisms $\dot{\varepsilon}_{ij}^{c}$ that correspond to consistent equal upper and lower bounds. These consistent limit states may not be unique but are bounded by the absolute limits (3.9) and (3.15). In the following section the relationship between the upper and lower bounds is explored with this in mind.

4 Consistent Limit States

The remaining question concerns the relationship between $\tan\phi^L_{LB}(\dot{\varepsilon}^c_{ij}, \overline{\varepsilon}^p_{ij})$ and $\tan\phi^L_{UB}(\overline{\varepsilon}^p_{ij}(x_i))$ for an arbitrary $\overline{\varepsilon}^p_{ij}$ and $\dot{\varepsilon}^c_{ij}$.

First note, as described earlier, for any $\overline{\varepsilon}^p_{ij}$ that there will exist a maximum lower bound corresponding to $\dot{\varepsilon}^c_{ij} = \dot{\varepsilon}^m_{ij}$ so that;

$$\tan\phi^L_{LB}(\dot{\varepsilon}^c_{ij}, \overline{\varepsilon}^p_{ij}) \leq \tan\phi^L_{LB}(\dot{\varepsilon}^m_{ij}, \overline{\varepsilon}^p_{ij}) = \tan\phi^L_{LB}(\overline{\varepsilon}^p_{ij}) \tag{4.1}$$

for all $\dot{\varepsilon}^{pc}_{ij}(x_i)$.

Consider the kinematic lower bound for $\overline{\varepsilon}^p_{ij}$. From (3.13)

$$\int_V \left\{ \lambda \widehat{\sigma}_{ij} \dot{\varepsilon}^{'m}_{ij} - c\widetilde{\dot{\varepsilon}}^m \right\} dV = \tan\phi^L_{LB}(\dot{\varepsilon}^m_{ij}, \overline{\varepsilon}^p_{ij}) \int_V |\lambda\hat{p} + \bar{p}| \widetilde{\dot{\varepsilon}}^m dV \tag{4.2}$$

Now consider the static upper bound (3.8) which may be written as

$$\widetilde{\sigma}(\lambda\widehat{\sigma}^{'}_{ij} + \overline{\rho}^{'c}_{ij}) - c \leq |\lambda\hat{p} + \bar{p}| \tan\phi^L_{UB}(\overline{\varepsilon}^p_{ij}) \tag{4.3}$$

Noting the Cauchy Schwartz inequality (3.5);

$$(\lambda\widehat{\sigma}^{'}_{ij} + \overline{\rho}^{'c}_{ij})\dot{\varepsilon}^{'m}_{ij} \leq \widetilde{\sigma}(\lambda\widehat{\sigma}^{'}_{ij} + \overline{\rho}^{'c}_{ij})\widetilde{\dot{\varepsilon}}^m \tag{4.4}$$

where equality only occurs if and only if the stress and strain rate correspond at yield. Hence, generally, from (4.3) and (4.4);

$$(\lambda\widehat{\sigma}^{'}_{ij} + \overline{\rho}^{'c}_{ij})\dot{\varepsilon}^{'m}_{ij} - c\widetilde{\dot{\varepsilon}}^m \leq |\lambda\hat{p} + \bar{p}| \tan\phi^L_{UB}(\overline{\varepsilon}^c_{ij})\widetilde{\dot{\varepsilon}}^m \tag{4.5}$$

Integrating (4.5) over the volume V yields

$$\int_V \left\{ \lambda\widehat{\sigma}^{'}_{ij}\dot{\varepsilon}^{'m}_{ij} - c\widetilde{\dot{\varepsilon}}^m \right\} dV \leq \tan\phi^L_{UB}(\overline{\varepsilon}^p_{ij}) \int_V |\lambda\hat{p} + \bar{p}| \widetilde{\dot{\varepsilon}}^m dV \tag{4.6}$$

Comparison of (4.6) with (4.2) yields;

$$\tan\phi^L_{LB}(\overline{\varepsilon}^p_{ij}, \dot{\varepsilon}^c_{ij}) \leq \tan\phi^L_{LB}(\overline{\varepsilon}^p_{ij}) \leq \tan\phi^L_{UB}(\overline{\varepsilon}^p_{ij}) \tag{4.7}$$

Hence, for any choice of $\overline{\varepsilon}^p_{ij}$, the static upper bound $\tan\phi^L_{UB}(\overline{\varepsilon}^p_{ij})$ forms a bound on all kinematic lower bounds $\tan\phi^L_{LB}(\overline{\varepsilon}^p_{ij}, \dot{\varepsilon}^c_{ij})$ for the same $\overline{\varepsilon}^p_{ij}$.

To summarize, for a chosen $\overline{\varepsilon}^p_{ij}$, there exist upper and lower bounds to the ranges of values of $\tan\phi$ for which a distribution of stress exists that lies within yield,

$\tan\phi < \tan\phi^L_{AUB}$ and for which an energy balance exists, $\tan\phi > \tan\phi^L_{LB}(\overline{\varepsilon}^p_{ij})$. Each of these bounds have extreme values over all possible $\overline{\varepsilon}^p_{ij}$,

$$\tan\phi^L_{ALB} = \max\left\{\tan\phi^L_{LB}(\overline{\varepsilon}^p_{ij})\right\} \quad \text{over all} \quad \overline{\varepsilon}^p_{ij} \tag{4.8}$$

$$\tan\phi^L_{AUB} = \min\left\{\tan\phi^L_{UB}(\overline{\varepsilon}^p_{ij}\right\} \quad \text{over all} \quad \overline{\varepsilon}^p_{ij}. \tag{4.9}$$

Hence for $\tan\phi > \tan\phi^L_{ALB}$ and $\tan\phi < \tan\phi^L_{AUB}$ consistent limit states cannot exist. Consistent limit states occur for plastic strain distributions such that $\tan\phi^L_{LB}(\overline{\varepsilon}^p_{ij}) = \tan\phi^L_{UB}(\overline{\varepsilon}^p_{ij})$ within the range $\tan\phi^L_{ALB} < \tan\phi < \tan\phi^L_{AUB}$. For an arbitrarily chosen $\overline{\varepsilon}^p_{ij}$, $\tan\phi^L_{LB}(\overline{\varepsilon}^p_{ij}) \leq \tan\phi^L_{AUB}(\overline{\varepsilon}^p_{ij})$.

5 Conclusions

The extension of the limit theorems to the Drucker-Prager yield condition with a non-associated flow rule demonstrates, in a limited way, that it is possible to make general statements about the properties of limit states in such circumstances. The limit state is defined by the plastic strain accumulated during the load history and may not be unique. This aspect has been discussed at some length for the problem of frictional contact between contacting elastic bodies by Barber, Hills, Klarbring and others [6–8]. In particular, Flecek et al. [8] have shown, for variable loading, the shakedown limits for such problems is non-unique. A theory for this class of problems has been given by Ponter [9], based upon a similar approach to that used in this paper. It is noticeable that, whereas in the study of frictional contact non-uniqueness has been a dominant concern, in geomechanics it is relatively ignored.

This paper does not discuss here applications of the theory to specific problems. The limit theorems are more complex than those for the associated case but, as has been shown by Ponter [9], it is possible to develop programming methods for the identification of consistent limit states, at least for the much simpler case of friction between elastic bodies. It seems likely that such programming methods are possible where a primal-dual structure exists so that compatibility and equilibrium conditions can occur within the same discretized structure.

There are, however, important implications of the theory. In pursuit of limit states for non-associated flow rules, the limit state may well depend upon both the assumed initial state of stress and the precise history of loading. The arrival at a limit state may result in the decline in the load until a minimum alternative limit state is found, i.e. overshooting of the limit state in numerical solutions may occur. This implies that a safe load is provided by a minimum consistent limit state.

The full behaviour of geotechnical material is far more complex than the behaviour contained in the Drucker Prager yield condition. At best it is a simulation

of the flow conditions at a Critical State condition. However, it seems possible that the type of theory described here may be extended to complex constitutive laws that include state variables.

References

1. Drucker DC, Prager W, Greenberg HJ (1952) Extended Limit design theorems for continuous media. Q Appl Math 9:381–389
2. Radenkovic D (1961) Theorie des charges limitees, extension a la mecanique des solls. In: Seminaires de Plasticité. Ecole Polytechnique, Publisher of Science, Technology, p 116
3. Symonds PS (1951) Shakedown in continuous media. J Appl Mech 18:85–89
4. Drucker DC, Prager W (1952) Soil mechanics and plastic analysis for limit loads. Q Appl Math 10:157–165
5. Krabbenhoft KK, Karim MR, Lyamin AV, Sloan SW (2012) Associated computational plasticity schemes for nonassociated frictional materials. Int J Numer Methods Eng 90:1089–1117
6. Bjorkman G, Klarbring A (1987) Shakedown and residual stresses in frictional systems. In: Gladwell GML, Ghonem H, Kalousek J (eds) Proceedings of 2nd international symposium on contact problems and wear of rails/wheel systems II, pp 27–39
7. Klarbring A, Ciavarella M, Barber JR (2007) Shakedown in elastic contact problems with coulomb friction. Int J Solids Struct 44(25–26):8355–8365
8. Flecek RC, Hills DA, Barber JB, Dini D (2015) Determination of the shakedown limit for large, discrete frictional systems. Eur J Mech A/Solids 49:242–250
9. Ponter ARS (2016) Shakedown limit theorems for frictional contact on a linear elastic body. Eur J Mech A/Solids 60:17–25

A Direct Method for Predicting the High-Cycle Fatigue Regime of Shape-Memory Alloys Structures

Michaël Peigney

Abstract Shape Memory Alloys (SMAs) belong to the class of so-called smart materials that offer promising perspectives in various fields such as aeronautics, robotics, biomedicals or civil engineering. For elastic-plastic materials, there is an established correlation between fatigue and energy dissipation. In particular, high-cycle fatigue occurs when the energy dissipation remains bounded in time. Although the physical mechanisms in SMAs differ from plasticity, the hysteresis that is commonly observed in the stress-strain response of those materials shows that some energy dissipation occurs. It can be reasonably assumed that situations where the energy dissipation remains bounded are the most favorable for fatigue durability. In this contribution, we present a direct method for determining if the energy dissipation in a SMA structure (submitted to a prescribed loading history) is bounded or not. That method is direct in the sense that nonlinear incremental analysis is completely bypassed. The proposed method rests on a suitable extension of the well-known Melan theorem. An application related to biomedical stents is presented to illustrate the method.

1 Introduction

The peculiar properties of Shape Memory Alloys (SMAs)—such as the superelastic behavior or the shape memory effect—are the result of a solid/solid phase transformation between different crystallographic structures (known as austenite and martensite). That phase transformation takes place at the microscopic level and is driven both by thermal and mechanical loading. The crystallographic structure of the austenite is more symmetric than the crystallographic structure of the martensite. This leads one to distinguish between several symmetry related *martensitic variants* corresponding to different orientations of the martensitic lattice with respect to the austenitic lattice [7]. Each martensitic variant is characterized by a transformation

M. Peigney (✉)
Laboratoire Navier (UMR 8205), CNRS, Ecole des Ponts ParisTech, IFSTTAR,
Université Paris-Est, 77455 Marne la Vallée, France
e-mail: michael.peigney@polytechnique.org

O. Barrera et al. (eds.), *Advances in Direct Methods for Materials and Structures*, DOI 10.1007/978-3-319-59810-9_2

strain that describes the deformation from the austenitic lattice to the martensitic lattice.

Shape memory alloys can be relevant in a lot of applications, but for the time being the most successful applications are to be found in the biomedical domain, for devices such as endovascular stents. In vivo, such devices are submitted to a cyclic loading due to the cardiac cycle, and therefore may be subjected to fatigue [9, 28, 30]. Metal fatigue is a crucial issue for structures submitted to variable loading. A conventional way to estimate the fatigue behavior of a material is to establish the so-called S-N curves that show the number of cycles to failure N versus the loading amplitude. Three different regimes are typically observed on S-N curves:

- the *low-cycle fatigue* regime, corresponding to $N < 10^4 - 10^5$ cycles. In that regime, N decreases rapidly with the loading amplitude S.
- the *high-cycle fatigue* regime, corresponding to $N > 10^4 - 10^5$ cycles, for which the decrease of N with the loading amplitude S is much slower.
- the *unlimited lifetime* regime, in which the material shows no sign of fatigue. That behaviour is observed for loading amplitudes S smaller than a characteristic value referred to as the endurance limit.

The demarcation between low- and high-cycle fatigue depends on the material considered [17]. Similarly, depending on the material considered, the endurance limit may exist or not. For Nitinol (which is the most common shape memory alloy used in applications), the three regimes listed above have been observed in cyclic traction experiments [28].

For designing Shape Memory Alloys structures subjected to variable loading, it is essential to have tools for assessing the fatigue life. A case in point is the design of biomedical Nitinol stents. Since biomedical stents are required to have high durability, it is essential to make sure that those devices operate in the high-cycle fatigue regime or—even better—in the unlimited lifetime regime. Although they provide some valuable insight in the fatigue behavior, S-N curves are uniaxial in nature and therefore are not sufficient for estimating the fatigue behavior of complex three-dimensional structures subjected to multiaxial loading.

This contribution presents a rational method for predicting the high-cycle fatigue regime of SMA structures. That method is based on the principle that high-cycle fatigue corresponds to situations where phase transformation is limited, i.e. the energy dissipation is bounded. By analogy with plasticity, that situation is referred to as shakedown. The proposed method relies on recent theoretical results that give a sufficient condition for shakedown to occur in SMA structures submitted to variable loading.

This contribution is organized as follows: We start by setting some notations and making some observations on the constitutive laws commonly used for SMAs. From there we comment on the structural evolution problem, with a special emphasis on the large time behavior and recent results regarding the shakedown behavior. This leads us to propose a direct method for predicting the high-cycle fatigue regime. The implementation of that method is detailed for a parametrized loading history. An

application related to biomedical stents is presented to illustrate the method. In particular, the results delivered by the proposed method are compared with experimental results from the literature.

2 Constitutive Laws

In most existing material models for SMAs, the strain $\boldsymbol{\varepsilon}$ is decomposed in an elastic part $\boldsymbol{M} : \boldsymbol{\sigma}$ proportional to the stress $\boldsymbol{\sigma}$ and an inelastic part $\boldsymbol{K} : \boldsymbol{\alpha}$ related to phase transformation, i.e.

$$\boldsymbol{\varepsilon} = \boldsymbol{M} : \boldsymbol{\sigma} + \boldsymbol{K} : \boldsymbol{\alpha}. \tag{1}$$

In Eq. (1), $\boldsymbol{M}$ is the elasticity tensor, $\boldsymbol{K}$ is a fixed tensor, and $\boldsymbol{\alpha}$ is an internal variable that tracks the phase transformation. The Helmholtz energy w corresponding to (1) is of the form

$$w(\boldsymbol{\varepsilon}, \boldsymbol{\alpha}) = \frac{1}{2}(\boldsymbol{\varepsilon} - \boldsymbol{K} : \boldsymbol{\alpha}) : \boldsymbol{M}^{-1} : (\boldsymbol{\varepsilon} - \boldsymbol{K} : \boldsymbol{\alpha}) + f(\boldsymbol{\alpha}) \tag{2}$$

where f is a positive function of $\boldsymbol{\alpha}$ whose expression depends on the model considered (some examples will be given later on). In the following, we denote by $\boldsymbol{A}$ the thermodynamical force associated with $\boldsymbol{\alpha}$, as defined by

$$\boldsymbol{A} = -\frac{\partial w}{\partial \boldsymbol{\alpha}} = \boldsymbol{K}^T : \boldsymbol{\sigma} - f'(\boldsymbol{\alpha}) \tag{3}$$

where $\boldsymbol{K}^T$ is the transpose of $\boldsymbol{K}$.

To account for hysteresis effects, Eq. (1) is complemented with an elasticity domain $\mathscr{C}$ and a flow rule (describing the evolution of $\boldsymbol{\alpha}$) akin to plasticity. The elasticity domain is assumed to be convex and to contain the origin. The normality flow rule is commonly used, i.e.

$$\dot{\boldsymbol{\alpha}} \in \partial I_{\mathscr{C}}(\boldsymbol{A}) \tag{4}$$

where the dot $\dot{}$ denotes left-time differentiation and $\partial I_{\mathscr{C}}(\boldsymbol{A})$ is the normal cone of the elasticity domain $\mathscr{T}$ at point $\boldsymbol{A}$, defined by

$$\partial I_{\mathscr{C}}(\boldsymbol{A}) = \{\boldsymbol{g} | \boldsymbol{g} : \boldsymbol{A} \geq \boldsymbol{g} : \boldsymbol{A}' \text{ for any } \boldsymbol{A}' \in \mathscr{C}\}. \tag{5}$$

For later reference, we note that the normality flow rule (4) respects the principle of maximum dissipation

$$\dot{\boldsymbol{\alpha}} : (\boldsymbol{A} - \boldsymbol{A}') \geq 0 \; \forall \boldsymbol{A}' \in \mathscr{C}. \tag{6}$$

As a first example, consider the model of Souza et al. [33]. In that model, the internal variable $\boldsymbol{\alpha}$ is a deviatoric strain (referred to as the transformation strain) and $\boldsymbol{K}$ is taken as the projector on the deviatoric space, i.e.

$$\boldsymbol{K} = \mathbb{I} - \frac{1}{3}\mathbb{1} \otimes \mathbb{1}$$

where $\mathbb{1}$ and $\mathbb{I}$ are respectively the second- and fourth-order identity tensors. In such a model, the thermodynamical force $\boldsymbol{A}$ specializes as

$$\boldsymbol{A} = \boldsymbol{s} - f'(\boldsymbol{\alpha})$$

where $\boldsymbol{s}$ is the deviatoric stress. The elasticity domain $\mathscr{C}$ considered by Souza et al. is of the Von Mises type, i.e. defined by $\|\boldsymbol{s} - f'(\boldsymbol{\alpha})\| \leq R$ where $\|\cdot\|$ is the Euclidean norm and R is the yield limit for phase transformation. In addition, the internal variable $\boldsymbol{\alpha}$ is submitted to the constraint $||\boldsymbol{\alpha}|| \leq \varepsilon_L$, which expresses the fact that the transformation strain cannot be arbitrarily large and is bounded by some material parameter ε_L that depends on the alloy considered.

A typical superelastic stress-strain delivered by such a model is represented in Fig. 1. Note in particular that ε_L is the strain amplitude of the plateaux exhibited by the stress-strain response. The hysteresis displayed by the stress-strain curve is directly related to the energy dissipated in a strain-driven loading cycle of sufficiently large amplitude $\boldsymbol{\Delta\varepsilon}$ as represented in Fig. 1. If such a cyclic strain is applied to the material, energy dissipation would occur at each cycle. In such a condition, the material would be subjected to *low-cycle fatigue*. In contrast, if a cyclic strain of low amplitude $\boldsymbol{\Delta\varepsilon}$ is imposed (possibly around a non-zero mean value), then there would be no dissipation in the stabilized regime so that *high-cycle fatigue* will prevail (Fig. 2).

The model of Souza et al., as well as its further refinements and extensions [4, 5] are phenomenological. In contrast, other SMA models rely on a micromechanical approach and make use of detailed information on the crystallography of the phase transformation [2, 12, 13, 24, 25]. The simplest case is that of single

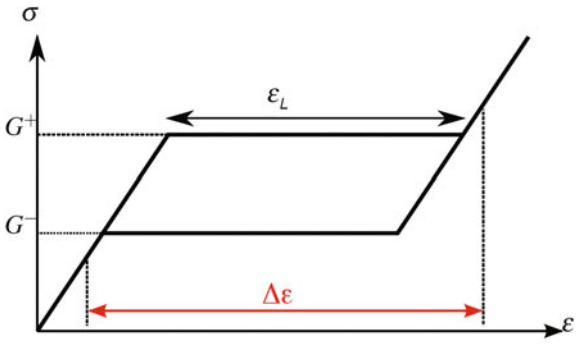

Fig. 1 Superelastic stress-strain response for a loading cycle of large strain amplitude $\boldsymbol{\Delta\varepsilon}$

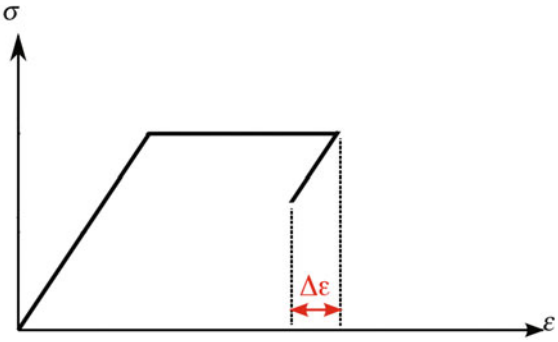

Fig. 2 Superelastic stress-strain response for a loading cycle of small strain amplitude $\Delta\boldsymbol{\varepsilon}$

crystals: the internal variable is typically chosen as $(\theta_1, \cdot, \theta_k)$ where θ_i is the volume fraction of the martensite variant i. The stress-strain relation (1) specializes as

$$\boldsymbol{\varepsilon} = \boldsymbol{M} : \boldsymbol{\sigma} + \sum_{i=1}^{k} \theta_i \boldsymbol{\varepsilon}_i^{tr,0}$$

where $\boldsymbol{\varepsilon}_i^{tr,0}$ is the transformation strain for variant i and k is the number of martensitic variants [7]. Both k and $\boldsymbol{\varepsilon}_i^{tr,0}$ $(i = 1, \ldots, k)$ are to be considered as material parameters. As mentioned in Sect. 1, the transformation strains $\boldsymbol{\varepsilon}_i^{tr,0}$ are symmetry-related i.e. for any (i, j) there exists a rotation R_{ij} such that

$$\boldsymbol{\varepsilon}_i^{tr,0} = \boldsymbol{R}_{ij}^T \cdot \boldsymbol{\varepsilon}_j^{tr,0} \cdot \boldsymbol{R}_{ij}. \tag{7}$$

A common choice is to define the elasticity domain by

$$\max_i |\boldsymbol{\varepsilon}_i^{tr,0} : \boldsymbol{\sigma} - f_{,i}| \leq G$$

where G is a yield limit for phase transformation and $f_{,i}$ is the partial derivative of $f(\theta_1, \cdot, \theta_n)$ with respect to θ_i. Note that the internal variable $(\theta_1, \cdot, \theta_k)$ is bounded because the volume fractions θ_i are positive and their sum is less than 1.

Such a micromechanical approach can be extended to polycrystals, which is the common form of commercially produced SMAs. A polycrystal is an assemblage of N crystalline orientations. Each orientation j is characterized by a rotation $\boldsymbol{R}_j$ with respect to a reference orientation (which can be chosen to coincide with that of the single crystal considered in (7)). In most of micromechanical models of polycrystalline SMAs [13, 19, 20], the internal variable is taken as $\boldsymbol{\alpha} = (\theta_{11}, \cdot, \theta_{kN})$ where θ_{ij} is the volume fraction of martensite variant i in the crystalline orientation j. The internal variable $\boldsymbol{\alpha} = (\theta_{11}, \cdot, \theta_{kN})$ is submitted to the constraint

$$0 \leq \theta_{ij}, \sum_{i=1}^{k} \theta_{ij} = c_j \tag{8}$$

where c_j is the volume fraction of orientation j. The stress-strain relation and the elasticity domain are respectively defined by

$$\boldsymbol{\varepsilon} = \boldsymbol{M} : \boldsymbol{\sigma} + \sum_{i=1}^{k} \sum_{j=1}^{N} \theta_i \boldsymbol{\varepsilon}_{ij}^{tr}$$

and

$$\max_{i,j} |\boldsymbol{\varepsilon}_{ij}^{tr} : \boldsymbol{\sigma} - f_{,ij}| \leq G$$

where $f_{,ij}$ is the partial derivative of f with respect to θ_{ij} and $\boldsymbol{\varepsilon}_{ij}^{tr}$ is the transformation strain of variant i in the crystalline orientation j. The transformation strain $\boldsymbol{\varepsilon}_{ij}^{tr}$ can be written as

$$\boldsymbol{\varepsilon}_{ij}^{tr} = \boldsymbol{R}_j^T \cdot \boldsymbol{\varepsilon}_i^{tr,0} \cdot \boldsymbol{R}_j. \tag{9}$$

In all the models mentioned, observe that the internal variable α used for tracking the phase transformation is always bounded. This requirement can be written as

$$\boldsymbol{\alpha} \in \mathscr{T} \tag{10}$$

where $\mathscr{T}$ is the bounded set of admissible values for $\boldsymbol{\alpha}$. For instance, in the model of Souza et al., the set $\mathscr{T}$ is the set of deviatoric strains with norm less than ε_L. The constraint (10) is a distinctive feature of SMAs (compared to plasticity) and stems from the mass conservation in the phase transformation process. Rigorously speaking, in the presence of such constraints, the normality flow rule (4) needs to be modified as

$$\dot{\boldsymbol{\alpha}} \in \partial I_{\mathscr{C}}(\boldsymbol{A} - \boldsymbol{A}^r);\ \boldsymbol{A}^r \in \partial I_{\mathscr{T}}(\boldsymbol{\alpha}) \tag{11}$$

where $\partial I_{\mathscr{T}}(\boldsymbol{\alpha})$ is the normal cone of $\mathscr{T}$ at point $\boldsymbol{\alpha}$ and is defined in a similar fashion as in Eq. (5). For a convex set $\mathscr{T}$ (which is assumed throughout this chapter), the following inequality—formally similar to (6)—holds [8]:

$$\boldsymbol{A}_r : (\boldsymbol{\alpha} - \boldsymbol{\alpha}') \geq 0\ \forall \boldsymbol{\alpha}' \in \mathscr{T}. \tag{12}$$

Reference is made to [11] for a derivation of (11) from the general principles of thermodynamics. The term $\boldsymbol{A}_r$ in (12) can be interpreted as a 'reaction force' and is non zero only when $\boldsymbol{\alpha}$ saturates the constraint (i.e. when $\boldsymbol{\alpha}$ is on the boundary of $\mathscr{T}$).

3 Structural Evolution Problem

Now consider a structure occupying a domain Ω and submitted to a given loading history. For determining the evolution of the structure, the constitutive laws (1–11) are to be satisfied at each point x and at each time t. In addition, the stress field needs to satisfy the equilibrium equations and the strain field has to derive from a displacement field that respects the boundary conditions, i.e.

$$\boldsymbol{\sigma} \in \mathscr{A}_{\sigma}(t)\ ,\ \boldsymbol{\varepsilon} \in \mathscr{A}_{\varepsilon}(t) \tag{13}$$

where $\mathscr{A}_{\sigma}(t)$ and $\mathscr{A}_{\varepsilon}(t)$ are respectively the sets of statically admissible stress and kinematically admissible strain fields at time t, defined by

$$\begin{aligned} \mathscr{A}_{\sigma}(t) &= \{\sigma | \operatorname{div} \boldsymbol{\sigma} + \boldsymbol{f^d} = 0 \text{ in } \Omega; \boldsymbol{\sigma}.\boldsymbol{n} = \boldsymbol{T^d} \text{ on } \Gamma_T\}, \\ \mathscr{A}_{\varepsilon}(t) &= \{\boldsymbol{\varepsilon} | \boldsymbol{\varepsilon} = (\nabla \boldsymbol{u} + \nabla^T \boldsymbol{u})/2 \text{ in } \Omega;\ \boldsymbol{u} = \boldsymbol{u^d} \text{ on } \Gamma_u\}. \end{aligned} \tag{14}$$

In (14), $\boldsymbol{f^d}$, $\boldsymbol{T^d}$ and $\boldsymbol{u^d}$ are functions of $(\boldsymbol{x}, t)$ and define the loading history. The tractions $\boldsymbol{T^d}$ and the displacements $\boldsymbol{u^d}$ are applied respectively on a part Γ_T and a part $\Gamma_u = \partial\Omega - \Gamma_T$ of the boundary $\partial\Omega$.

Together the Eqs. (1)–(13) define the structural evolution problem. That problem is nonlinear and is usually solved incrementally using space- and time-discretization techniques, resorting for instance to Finite Element Analysis (FEA). Regarding numerical implementation, handling the constraint (10) on the internal variable is an additional difficulty compared to plasticity [3, 4, 31], especially for micromechanical models [12, 22, 23].

Asides from numerical issues, adding a constraint (10) has a profound impact on the properties of the structural evolution problem, especially regarding the large-time behavior. For large loadings, the large-time behavior is indeed strongly dependent on the initial state. For instance, in the case of periodic loading, some initial conditions may lead to shakedown while others may lead to alternate phase transformation (i.e. a periodic but non constant evolution of the phase transformation) [21, 26]. Interestingly, such dependence of the asymptotic regime on the initial state has also been observed in other nonlinear mechanical problems, such as contact with friction [1] and plasticity with temperature-dependent elastic moduli [27].

4 Shakedown Theorem

For fatigue design, we are especially interested in situations where the solutions of the structural evolution problem are such that the energy dissipation remains bounded in time. That situation is referred to as shakedown and corresponds to the most favorable case of high-cycle fatigue. In standard plasticity, the Melan's theorem is a well-known result that gives a sufficient condition for shakedown to occur

[15, 18, 34]. Melan's theorem is path-independent, i.e. the obtained shakedown condition is independent of the initial state. The original theorem cannot be directly applied to SMAs because, contrary to standard plasticity, the internal variable is bounded. The theoretical issue of extending Melan theorem to SMAs has been addressed in [10, 21, 26]. In particular, a path-independent Melan's theorem has been obtained in [21, 26].

Let $(\boldsymbol{\sigma}^E, \boldsymbol{\varepsilon}^E)$ be the fictitious elastic response of the structure, defined by the elasticity problem

$$\boldsymbol{\varepsilon}^E = \boldsymbol{M} : \boldsymbol{\sigma}^E \,,\ \boldsymbol{\sigma}^E \in \mathscr{A}_\sigma(t) \,,\ \boldsymbol{\varepsilon}^E \in \mathscr{A}_\varepsilon(t) \tag{15}$$

The statement of the theorem is the following:

Theorem 1 *If there exists* $m > 1$, $\tau \geq 0$ *and a time-independent field* $\boldsymbol{A}^r_*(\boldsymbol{x})$ *such that*

$$m\boldsymbol{K}^T : \boldsymbol{\sigma}^E(\boldsymbol{x}, t) - \boldsymbol{A}^r_*(\boldsymbol{x}) \in \mathscr{C} \ \forall \boldsymbol{x} \in \Omega, \forall t > \tau \tag{16}$$

then there is shakedown, whatever the initial condition is.

The proof of Theorem 1 is given in the Appendix. Some comments are in order. A first observation is that Theorem 1 is path-independent, just as the standard Melan theorem in perfect plasticity: If the condition in Theorem 1 is satisfied, then shakedown occurs for *all* initial state. The shakedown condition provided by Theorem 1 is thus independent of any residual stress that may exist initially in the structure (as a consequence of material process, for instance). When the loading is beyond the limit provided by Theorem 1, shakedown may still occur for some (but not all) initial conditions (see [21, 26] for some examples). In such case, the asymptotic behavior is strongly dependent on the initial state.

Observe also that the field $\boldsymbol{A}^r_*(\boldsymbol{x})$ in Theorem 1 is free from any constraint. This makes for a simple geometrical interpretation of Theorem 1: Shakedown occurs if, up to a time-independent translation, the local elastic response $t \mapsto \boldsymbol{K}^T : \boldsymbol{\sigma}^E(\boldsymbol{x}, t)$ remains in the elasticity domain $\mathscr{C}$ at each point $\boldsymbol{x}$ (Fig. 3). The situation is reminiscent of linear kinematic hardening plasticity, for which shakedown is ensured under a similar condition [16].

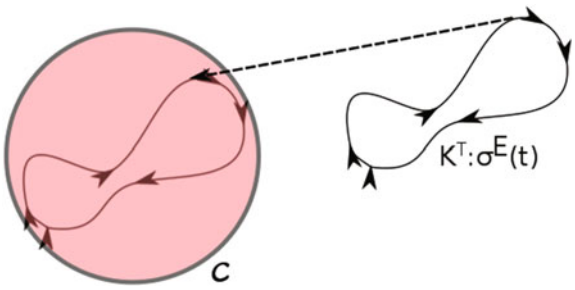

Fig. 3 Geometric interpretation of the local shakedown condition for shape memory alloys

On a final note, we observe that Theorem 1 is largely independent of the details of the SMA model considered. In particular, the function f (that appears in the Helmholtz energy w in Eq. (2)) and the exact expression of the set $\mathscr{T}$ (that defines the constraints on the internal variable in Eq. (10)) do not play a role in Theorem 1.

5 Description of the Method

The above theorem leads to a design method against fatigue that can be broken down into two steps:

1. Calculate the elastic response $\boldsymbol{\sigma}^E(\boldsymbol{x}, t)$ for the considered loading history.
2. Check if the local curve $t \mapsto \boldsymbol{\sigma}^E(\boldsymbol{x}, t)$ can be translated in $\mathscr{C}$ at each point $\boldsymbol{x}$.

Note that Step 1. can be conveniently performed by a (linear elastic) FEA. Step 2. is merely a post-processing of the results obtained in Step 1. Consider for instance a parametrized loading history: The loading consists of body forces $\boldsymbol{f}^{\boldsymbol{d}}(\boldsymbol{x}, t)$, applied tractions $\boldsymbol{T}^{\boldsymbol{d}}(\boldsymbol{x}, t)$ and prescribed displacements $\boldsymbol{u}^d(\boldsymbol{x}, t)$ that vary respectively as

$$\boldsymbol{f}^{\boldsymbol{d}}(\boldsymbol{x}, t) = \lambda(t)\boldsymbol{f}_0(\boldsymbol{x}),\ \boldsymbol{T}^{\boldsymbol{d}}(\boldsymbol{x}, t) = \lambda(t)\boldsymbol{T}_0(\boldsymbol{x}),\ \boldsymbol{u}^d(\boldsymbol{x}, t) = \lambda(t)\boldsymbol{u}_0(\boldsymbol{x})$$

where $\lambda(t)$ is a time-dependent loading parameter. The elastic response $\boldsymbol{\sigma}^E(\boldsymbol{x}, t)$ being defined by a linear problem, we have

$$\boldsymbol{\sigma}^E(\boldsymbol{x}, t) = \lambda(t)\boldsymbol{\sigma}_0^E(\boldsymbol{x})$$

where $\boldsymbol{\sigma}_0^E(\boldsymbol{x})$ is the elastic stress field for the loading $(\boldsymbol{f}_0(\boldsymbol{x}), \boldsymbol{T}_0(\boldsymbol{x}), \boldsymbol{u}_0(\boldsymbol{x}))$. At each point $\boldsymbol{x}$, the curve $t \mapsto \boldsymbol{K}^T : \boldsymbol{\sigma}^E(\boldsymbol{x}, t)$ thus describes the line segment

$$[\lambda_{\boldsymbol{min}}, \lambda_{\boldsymbol{max}}]\boldsymbol{K}^T : \boldsymbol{\sigma}_0^E(\boldsymbol{x})$$

where $\lambda_{\boldsymbol{min}} = \min_t \lambda(t)$ and $\lambda_{\boldsymbol{max}} = \max_t \lambda(t)$.

Details of Step 2. depends on the model used. The simplest case is that of phenomenological models, such as the model of Souza et al. [33] considered previously. In that model, the elasticity domain $\mathscr{C}$ is a ball of radius R in the deviatoric space. Denoting by $\boldsymbol{s}_0^E(\boldsymbol{x})$ the deviatoric part of $\boldsymbol{\sigma}_0^E$, performing Step 2. amounts to checking that

$$(\lambda_{\boldsymbol{max}} - \lambda_{\boldsymbol{min}})\|\boldsymbol{s}_0^E(\boldsymbol{x})\| < 2R$$

at each point x, which is guaranteed if

$$(\lambda_{\boldsymbol{max}} - \lambda_{\boldsymbol{min}}) \max_{\boldsymbol{x}} \|\boldsymbol{s}_0^E(\boldsymbol{x})\| < 2R. \tag{17}$$

If that condition is satisfied, then the structure experiences high-cycle fatigue, whatever the initial state is. In practice, the condition (17) can be used as a criterion

for the design of SMA structures against fatigue: For say a given loading history, the geometry of the structure should be designed in such fashion that $\max_{\boldsymbol{x}} \|\boldsymbol{s}_0^E(\boldsymbol{x})\|$ remains smaller than $2R/(\lambda_{max} - \lambda_{min})$. Note that the exact knowledge of the loading parameter $\lambda(t)$ is not necessary: Only bounds on the extreme values are needed. In particular, $\lambda(t)$ does not need to be periodic in time.

Now consider a micromechanical model of polycrystalline SMAs. Performing Step 2. amounts to check whether there exists $A_{ij}^*(\boldsymbol{x})$ and $m > 1$ such that

$$|m\lambda(t)\boldsymbol{\sigma}_0^E(\boldsymbol{x}) : \boldsymbol{\varepsilon}_{ij}^{tr} - A_{ij}^*(\boldsymbol{x})| \leq G \; \forall (i,j)$$

i.e. that

$$(\lambda_{max} - \lambda_{min})|\boldsymbol{\sigma}_0^E(\boldsymbol{x}) : \boldsymbol{\varepsilon}_{ij}^{tr}| < 2G \; \forall (i,j).$$

This last requirement can be rewritten as

$$(\lambda_{max} - \lambda_{min}) \max_{i,j} |\boldsymbol{\sigma}_0^E(\boldsymbol{x}) : \boldsymbol{\varepsilon}_{ij}^{tr}(\boldsymbol{x})| < 2G. \tag{18}$$

Proceeding further requires to evaluate $\max_{i,j} |\boldsymbol{\sigma}_0^E(\boldsymbol{x}) : \boldsymbol{\varepsilon}_{ij}^{tr}(\boldsymbol{x})|$. This can be done exactly provided that the polycrystalline texture (i.e. the list of N rotations that appear in (9)) is given. As an alternative, a simple bound on $\max_{i,j} |\boldsymbol{\sigma}_0^E(\boldsymbol{x}) : \boldsymbol{\varepsilon}_{ij}^{tr}|$ can be used, as is now explained. For any (i,j) we have indeed

$$\boldsymbol{\sigma}_0^E(\boldsymbol{x}) : \boldsymbol{\varepsilon}_{ij}^{tr} = \frac{1}{3} \operatorname{tr} \boldsymbol{\sigma}_0^E(\boldsymbol{x}) \operatorname{tr} \boldsymbol{\varepsilon}_{ij}^{tr} + \boldsymbol{s}_0^E(\boldsymbol{x}) : \boldsymbol{\varepsilon}_{ij}^{tr,D} \leq \frac{1}{3} \operatorname{tr} \boldsymbol{\sigma}_0^E(\boldsymbol{x}) \operatorname{tr} \boldsymbol{\varepsilon}_{ij}^{tr} + \|\boldsymbol{s}_0^E(\boldsymbol{x})\| \cdot \|\boldsymbol{\varepsilon}_{ij}^{tr,D}\|$$

where the superscript ^{D} denotes the deviatoric part. Two observations are in order. The first one is that, for the most common shape memory alloys, the transformation strains can be considered as trace-free [7]. The second observation is that, as a result of (7)–(9), $\|\boldsymbol{\varepsilon}_{ij}^{tr,D}\|$ takes a constant value (denoted by $\|\boldsymbol{\varepsilon}^{tr}\|$), independently of (i,j). It follows that $\boldsymbol{\sigma}_0^E(\boldsymbol{x}) : \boldsymbol{\varepsilon}_{ij}^{tr} \leq \|\boldsymbol{\varepsilon}^{tr}\| \cdot \|\boldsymbol{s}_0^E(\boldsymbol{x})\|$ for all (i,j), hence

$$\max_{i,j} \boldsymbol{\sigma}_0^E(\boldsymbol{x}) : \boldsymbol{\varepsilon}_{ij}^{tr} \leq \|\boldsymbol{\varepsilon}^{tr}\| \cdot \|\boldsymbol{s}_0^E(\boldsymbol{x})\|. \tag{19}$$

In view of (18) and (19), a sufficient condition for shakedown to occur is thus that

$$(\lambda_{max} - \lambda_{min})\|\boldsymbol{\varepsilon}^{tr}\| \cdot \|\boldsymbol{s}_0^E(\boldsymbol{x})\| < 2G$$

for all $\boldsymbol{x} \in \Omega$. That condition is satisfied if

$$(\lambda_{max} - \lambda_{min}) \max_{x} \|\boldsymbol{s}_0^E(\boldsymbol{x})\| < 2\frac{G}{\|\boldsymbol{\varepsilon}^{tr}\|} \tag{20}$$

Observe that the final condition (20) is formally similar to that obtained in (17) for a phenomenological model.

6 Application to Biomedical Stents

We now describe the application of the proposed method to biomedical stents. Such devices have a tubular geometry and are typically an assemblage of elementary cells. Those cells often have the shape of a 'strut V', as represented in Fig. 4 (left). When the stent is loaded radially (for instance a consequence of blood pressure), each cell primarily experiences some uniaxial traction (along the horizontal direction in Fig. 4). Extensive fatigue tests have been reported in [2]. Those tests were performed on a diamond-shape specimen that consists of 2 'strut Vs' arranged in a symmetric fashion so as to be easily fitted in a fatigue test machine. A simplified model of such specimen is shown in Fig. 4 (right). In the experiments reported in [2], each sample was submitted to a given strain cyclically between a fixed minimum value $\boldsymbol{\varepsilon}_{min}$ and a maximum value $\boldsymbol{\varepsilon}_{max}$. The number of cycles to failure was recorded for each sample. The obtained experimental results showed that a low- to high-cycle fatigue transition occurs at 0.4–0.5% strain amplitude, without any clear influence of the mean strain. In order to illustrate the proposed approach based on shakedown theory, we apply the method detailed previously and compare the predictions with the experimental results in [2].

For the problem at hand, applying the proposed approach merely consists in performing one single elastic calculation, namely calculating the elastic response of the structure in Fig. 4 when it is submitted to a (arbitrary fixed) reference strain $\boldsymbol{\varepsilon}_0$. Such a calculation has been performed in 2D (plane stress) with the FEA software Freefem [14]. We used the values $E = 50\,\text{GPa}$, $\nu = 0.35$ which are representative of Nitinol [33]. Because of the symmetries, only one fourth of the structure needs to be modeled, as represented in Fig. 4. The mesh used in the FEA consists of 121847 triangular elements with linear interpolation. In Fig. 5 is represented the map of $\|\boldsymbol{s}_0^E(\boldsymbol{x})\|$. The maximum value of $\|\boldsymbol{s}_0^E(\boldsymbol{x})\|$ (normalized with respect to $\boldsymbol{\varepsilon}_0$) is approximatively equal to 6860 MPa.

Using the condition (17) with $R = 40$ MPa, we obtain that shakedown occurs provided that

$$|\boldsymbol{\varepsilon}_{max} - \boldsymbol{\varepsilon}_{min}| < 0.58\%. \tag{21}$$

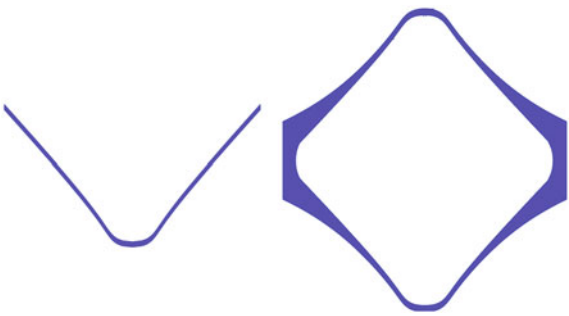

Fig. 4 Strut V (*left*) and diamond-shaped specimen (*right*)

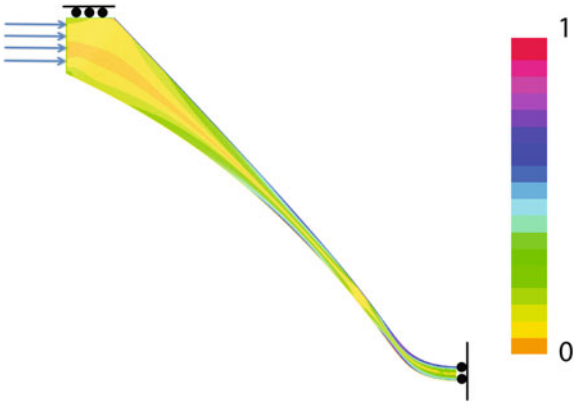

Fig. 5 Map of $\|\boldsymbol{\varepsilon}_0^D(\boldsymbol{x})\|$ on a stent cell (values are normalized with respect to the maximum value $\|\boldsymbol{\varepsilon}_0^D\|_{max}$)

Using lattice parameters from the literature [7], the value $\|\boldsymbol{\varepsilon}^{tr}\|$ for Nitinol is found to be approximatively equal to 0.1048. Applying the conditions (20) with $G = 4.7$ MPa [2], we obtain that shakedown occurs for

$$|\boldsymbol{\varepsilon}_{max} - \boldsymbol{\varepsilon}_{min}| < 0.65\%. \tag{22}$$

Both values in (21) and (22) are above the low- to fatigue transition that is assessed experimentally (0.4–0.5%). However, given the uncertainties in the material parameters and the lack of data on the exact geometry used in the experiments, the agreement with the experimental results can be considered as satisfactory. Also note that the predicted limit is independent of the mean applied strain, which is in line with the experiments.

7 Conclusions

The proposed method is relevant for the fatigue design of SMA structures. It enjoys the following key features:

1. It is based on rational theoretical results.
2. It can be used with a lot of existing SMA models (either phenomenological or micromechanical).
3. It only relies on elastic calculations: Incremental nonlinear analysis is bypassed.
4. Only a partial knowledge of the loading is required (namely the knowledge of the extreme values).
5. It does not require the knowledge of any residual stress that may exist initially (as a consequence of processing for instance).

In spite of all those attractive features, it should be reminded that the presented method does not give all the information regarding the high-cycle fatigue: neither the

exact value of the endurance limit, nor the number of cycles to failure, are provided by the proposed approach (see [6] for recent progress in that direction). However, due to its simplicity, the proposed method could possibly be useful at least in the early stages of design.

Appendix

For the sake of completeness, we give in this Appendix a proof of Theorem 1. Consider a solution $(\boldsymbol{\varepsilon}, \boldsymbol{\alpha}, \boldsymbol{\sigma}, \boldsymbol{A}^r, \boldsymbol{A}^d)$ to the evolution problem (1)–(13). By (11) we have

$$\boldsymbol{A} = \boldsymbol{A}^d + \boldsymbol{A}^r$$

with

$$\dot{\boldsymbol{\alpha}} \in \partial I_{\mathscr{C}}(\boldsymbol{A}^d);\ \boldsymbol{A}^r \in \partial I_{\mathscr{T}}(\boldsymbol{\alpha}). \tag{23}$$

The positive quantity

$$D(t) = \int_{\Omega} \boldsymbol{A}^d . \dot{\boldsymbol{\alpha}} d\boldsymbol{x}$$

can be interpreted as the rate of dissipated energy. Note that $D(t)$ is positive because of the principle of maximum dissipation (6) and the fact that the elasticity domain $\mathscr{C}$ contains the origin. Under the condition (16), we show in the following that the total dissipated energy $\int_0^T D(t)dt$ remains bounded as $T \to \infty$. To that purpose, consider the positive functional $W(t)$ defined as

$$W(t) = \int_{\Omega} w(\boldsymbol{\varepsilon}(t) - \boldsymbol{\varepsilon}^E(t), \boldsymbol{\alpha}(t))\, d\boldsymbol{x}.$$

By time-differentiation we have

$$\dot{W}(t) = \int_{\Omega} [(\boldsymbol{\sigma} - \boldsymbol{\sigma}^E) : (\dot{\boldsymbol{\varepsilon}} - \dot{\boldsymbol{\varepsilon}}^E - \boldsymbol{K} : \dot{\boldsymbol{\alpha}}) + f'(\boldsymbol{\alpha}) : \dot{\boldsymbol{\alpha}}]\, d\boldsymbol{x}.$$

Since $\mathrm{div}(\boldsymbol{\sigma} - \boldsymbol{\sigma}^E) = 0$ in Ω, $(\boldsymbol{\sigma} - \boldsymbol{\sigma}^E).\boldsymbol{n} = 0$ on Γ_T and $\boldsymbol{u} - \boldsymbol{u}^E = 0$ on Γ_u, the principle of virtual power gives $\int_{\Omega} (\boldsymbol{\sigma} - \boldsymbol{\sigma}^E) : (\dot{\boldsymbol{\varepsilon}} - \dot{\boldsymbol{\varepsilon}}^E)\, d\boldsymbol{x} = 0$. Therefore

$$\dot{W}(t) = \int_{\Omega} [-\boldsymbol{K}^T : (\boldsymbol{\sigma} - \boldsymbol{\sigma}^E) + f'(\boldsymbol{\alpha})] : \dot{\boldsymbol{\alpha}}\, d\boldsymbol{x}$$

which using (3) and (23) can be rewritten as

$$\dot{W}(t) = -D(t) + \int_{\Omega} [-\boldsymbol{A}^r + \boldsymbol{K}^T : \boldsymbol{\sigma}^E] : \dot{\boldsymbol{\alpha}}\, d\boldsymbol{x}. \tag{24}$$

Let $(\boldsymbol{A}^r_*, m)$ satisfying (16). Setting $\boldsymbol{A}^d_* = m\boldsymbol{K}^T : \boldsymbol{\sigma}^E(t) - \boldsymbol{A}^r_*$, we find

$$\dot{W}(t) = -D(t) + \int_\Omega [-\boldsymbol{A}^r + \frac{1}{m}(\boldsymbol{A}^d_* + \boldsymbol{A}^r_*)] : \dot{\boldsymbol{\alpha}}\, d\boldsymbol{x}. \tag{25}$$

The property (16) shows that $\boldsymbol{A}^d_* \in \mathscr{C}$ for $t > \tau$. Since $\dot{\boldsymbol{\alpha}} \in \partial I_{\mathscr{C}}(\boldsymbol{A}^d)$, the principle of maximum dissipation (6) gives

$$(\boldsymbol{A}^d - \boldsymbol{A}^d_*) : \dot{\boldsymbol{\alpha}} \geq 0. \tag{26}$$

Moreover, since $\boldsymbol{A}^r \in \partial I_{\mathscr{T}}(\boldsymbol{\alpha})$ and $\boldsymbol{\alpha} \in \mathscr{T}$, Eq. (12) gives $\boldsymbol{A}^r(t) : (\boldsymbol{\alpha}(t) - \boldsymbol{\alpha}(t')) \geq 0$ for any t'. In the limit $t' \longrightarrow t$ with $t' < t$, we obtain

$$\boldsymbol{A}^r : \dot{\boldsymbol{\alpha}} \geq 0. \tag{27}$$

Combining (26)–(27) with (25) gives

$$\dot{W}(t) \leq \frac{1-m}{m} D(t) + \frac{1}{m} \int_\Omega \boldsymbol{A}^r_* : \dot{\boldsymbol{\alpha}}\, d\boldsymbol{x}. \tag{28}$$

Since $\boldsymbol{A}^r_*$ is time-independent, the time-integration of (28) on a time interval $[\tau, T]$ yields

$$(m-1) \int_\tau^T D(t)\, dt \leq mW(\tau) + \int_\Omega \boldsymbol{A}^r_* : (\boldsymbol{\alpha}(T) - \boldsymbol{\alpha}(\tau))\, d\boldsymbol{x} \tag{29}$$

where the property $W(T) \geq 0$ has been used. The set $\mathscr{T}$ being bounded, there exists a positive constant K such that $\|\boldsymbol{\alpha}\| \leq K$ for any $\boldsymbol{\alpha} \in \mathscr{T}$. Therefore

$$\int_\Omega \boldsymbol{A}^r_* : (\boldsymbol{\alpha}(t) - \boldsymbol{\alpha}(\tau))\, d\boldsymbol{x} \leq 2K \int_\Omega \|\boldsymbol{A}^r_*\|\, d\boldsymbol{x}.$$

Combining that inequality with (29) gives

$$(m-1) \int_\tau^T D(t)\, dt \leq mW(\tau) + 2K \int_\Omega \|\boldsymbol{A}^r_*\|\, d\boldsymbol{x}.$$

The right-hand side of that inequality is independent of T. This proves that the dissipated energy $\int_\tau^T D(t)$ remains bounded as $T \longrightarrow +\infty$.

From there we can show (under some technical assumptions) that $\boldsymbol{\alpha}(t)$ tends to a limit as $t \longrightarrow +\infty$. Assume that the elasticity domain $\mathscr{C}$ contains a ball of radius $r > 0$ centered at the origin. In such a condition, we have $r\dot{\boldsymbol{\alpha}}(t)/\|\dot{\boldsymbol{\alpha}}(t)\| \in \mathscr{C}$ for any t. Using the principle of maximum dissipation (6), we find

$$0 \leq \dot{\boldsymbol{\alpha}} : (\boldsymbol{A}^d - r\frac{\dot{\boldsymbol{\alpha}}}{\|\dot{\boldsymbol{\alpha}}\|}).$$

Hence

$$\|\dot{\boldsymbol{\alpha}}\| \leq \frac{1}{r}\boldsymbol{A}^d : \dot{\boldsymbol{\alpha}}$$

which after space integration gives

$$\int_{\Omega} \|\dot{\boldsymbol{\alpha}}\| dx \leq \frac{1}{r} D(t). \tag{30}$$

Let $\mathbb{A}$ be the vectorial space in which $\boldsymbol{\alpha}(\boldsymbol{x})$ takes values and let $L_1(\Omega, \mathbb{A})$ be the space of integrable functions with values in $\mathbb{A}$. The inequality (30) can be rewritten as

$$\|\dot{\boldsymbol{\alpha}}\|_{L_1(\Omega,\mathbb{A})} \leq \frac{1}{r} D(t)$$

where $\|\cdot\|_{L_1(\Omega,\mathbb{A})}$ is the norm in $L_1(\Omega, \mathbb{A})$. Since $\int_0^T D(t)$ is bounded as $T \longrightarrow +\infty$, the integral $\int_0^T \|\dot{\boldsymbol{\alpha}}(t)\|_{L_1(\Omega,\mathbb{A})} dt$ converges as $T \longrightarrow +\infty$. From Riesz-Fischer theorem, the space $L_1(\Omega, \mathbb{A})$ is a Banach space. It follows (see [29] or Theorem 97 in [32]) that the integral $\int_0^T \dot{\boldsymbol{\alpha}}(t) dt$ converges as $T \longrightarrow \infty$. Hence $\boldsymbol{\alpha}(t)$ converges towards a limit as $T \longrightarrow \infty$. □

References

1. Ahn YJ, Bertocchi E, Barber J (2008) Shakedown of coupled two-dimensional discrete frictional systems. J Mech Phys Solids 56:3433–3440
2. Anand L, Gurtin M (2003) Thermal effects in the superelasticity of crystalline shape-memory materials. J Mech Phys Solids 51:1015–1058
3. Artioli E, Bisegna P (2015) An incremental energy minimization state update algorithm for 3d phenomenological internal-variable sma constitutive models based on isotropic flow potentials. Int J Num Meth Eng 105:197–220
4. Auricchio F, Petrini L (2004) A three-dimensional model describing stress-temperature induced solid phase transformations: solution algorithm and boundary value problems. Int J Num Meth Eng 61:807–836
5. Auricchio F, Bonetti E, Scalet G, Ubertini F (2014) Theoretical and numerical modeling of shape memory alloys accounting for multiple phase transformations and martensite reorientation. Int J Plast 59:30–54
6. Auricchio F, Constantinescu A, Menna C, Scalet G (2016) A shakedown analysis of high cycle fatigue of shape memory alloys. Int J Fatigue 87:112–123
7. Bhattacharya K (2003) Microstructure of martensite. Oxford University Press
8. Brézis H (1972) Opérateurs maximaux monotones et semigroupes de contractions dans les espaces de Hilbert. North-Holland, Amsterdam
9. Duda SH, Bosiers M, Lammer J, Scheinert D, Zeller T, Tielbeek A, Anderson J, Wiesinger B, Tepe G, Lansky A (2005) Sirolimus-eluting versus bare nitinol stent for obstructive superficial femoral artery disease: the SIROCCO II trial. J Vasc Interv Radiol 16:331–338
10. Feng X, Sun Q (2007) Shakedown analysis of shape memory alloy structures. Int J Plasticity 23:183–206
11. Frémond M (2002) Non-smooth thermomechanics. Springer

12. Govindjee S, Miehe C (2001) A multi-variant martensitic phase transformation model: formulation and numerical implementation. Comput Meth Appl Mech Eng 191:215–238
13. Hackl K, Heinen R (2008) An upper bound to the free energy of n-variant polycrystalline shape memory alloys. J Mech Phys Solids 56:2832–2843
14. Hecht F (2012) New development in FreeFem++. J Numer Math 20:251–265
15. Koiter WT (1960) General theorems for elastic-plastic solids. In: Progress in solid mechanics
16. Mandel J, Zarka J, Halphen B (1977) Adaptation d'une structure elastoplastique a ecrouissage cinematique. Mech Res Commun 4:309–314
17. Manson SS, Halford GR (2006) Fatigue and durability of structural materials. ASM International
18. Melan E (1936) Theorie statisch unbestimmter systeme AUS ideal-plastischen Baustoff. Sitz Berl Ak Wiss 145:195–218
19. Peigney M (2008) Recoverable strains in composite shape memory alloys. J Mech Phys Solids 56:360–375
20. Peigney M (2009) A non-convex lower bound on the effective free energy of polycrystalline shape memory alloys. J Mech Phys Solids 57:970–986
21. Peigney M (2010) Shakedown theorems and asymptotic behaviour of solids in non-smooth mechanics. Eur J Mech A 29:784–793
22. Peigney M, Seguin JP, Hervé-Luanco E (2011) Numerical simulation of shape memory alloys structures using interior-point methods. Int J Sol Struct 48:2791–2799
23. Peigney M, Seguin JP (2013) An incremental variational approach to coupled thermo-mechanical problems in anelastic solids. Application to shape-memory alloys. Int J Sol Struct 50:4043–4054
24. Peigney M (2013) On the energy-minimizing strains in martensitic microstructures-Part 1: geometrically nonlinear theory. J Mech Phys Solids 61:1489–1510
25. Peigney M (2013) On the energy-minimizing strains in martensitic microstructures-Part 2: geometrically linear theory. J Mech Phys Solids 61:1511–1530
26. Peigney M (2014) On shakedown of shape memory alloys structures. Mech Ann Solid Struct 6:17–28
27. Peigney M (2014) Shakedown of elastic-perfectly plastic materials with temperature-dependent elastic moduli. J Mech Phys Solids 71:112–131
28. Pelton AR, Schroeder V, Mitchell MR, Gong XY, Barney M, Robertson SW (2008) Fatigue and durability of Nitinol stents. J Mech Behav Bio Mat 1:153–164
29. Rudin W (1987) Real and complex analysis. McGraw-Hill, Boston
30. Sabet S, Mlekusch W, Amighi J, Minar E, Schillinger M (2005) Primary patency of long-segment self-expanding nitinol stents in the femoropopliteal arteries. J Endovasc Ther 12:6–12
31. Scalet G, Peigney M (2017) A robust and efficient radial return algorithm based on incremental energy minimization for the 3D Souza-Auricchio model for shape memory alloys. Eur J Mech A 61:364–382
32. Schwartz L (1967) Analyse mathmatique, vol 94. Hermann, Paris
33. Souza A, Mamiya E, Zouain N (1998) Three-dimensional model for solids undergoing stress-induced phase transformations. Eur J Mech A 17:789–806
34. Symonds PS (1951) Shakedown in continuous media. J Appl Mech 18:85–89

Shakedown Within Polycrystals: A Direct Numerical Assessment

D. Magisano, E. Charkaluk, G. de Saxcé and T. Kanit

Abstract It is well known that in high cycle fatigue (HCF), macroscopically, structures undergo elastic shakedown and the stress level commonly determines the lifetime. In this domain, the fatigue phenomena is due to local plasticity at the grain scale. Therefore, some multiscale HCF multiaxial fatigue criteria were proposed, among them the well-known Dang Van criterion. This criterion supposes that in a polycrystal, some misoriented grains can undergo plastic shakedown which conducts to crack initiation. The objective of this work is to validate this assumption by conducting numerical simulations on polycrystalline aggregates. As it is necessary to estimate the stabilized state in each grain of the polycrystal, classical incremental simulations are not the best way as it will be highly time-consuming because of the size of the aggregate. In the recent years, Pommier proposed a method called Direct Cyclic Algorithm to obtain the stabilized response of a structure under cyclic periodic loading, which it is shown to be more efficient compared to an incremental analysis in such situation. However, errors can be obtained in certain case with respect to the incremental solution. In this work, a Crystal Plasticity FEM model, based on dislocation densities, was used. As a first step, an aggregate of 20 grains of AISI 316L stainless steel under strain controlled cyclic loading was studied. Precise comparisons were conducted with incremental analysis and the results show that DCA seems to be an efficient solution in order to estimate the shakedown state of polycrystalline aggregates.

D. Magisano (✉)
Università della Calabria, Rende, Italy
e-mail: domenico.magisano@unical.it

E. Charkaluk
École Polytechnique, Palaiseau, France
e-mail: charkaluk@lms.polytechnique.fr

G. de Saxcé · T. Kanit
Université Lille 1, Villeneuve-d'Ascq, France
e-mail: gery.desaxce@univ-lille1.fr

T. Kanit
e-mail: toufik.kanit@univ-lille1.fr

O. Barrera et al. (eds.), *Advances in Direct Methods for Materials and Structures*, DOI 10.1007/978-3-319-59810-9_3

1 Introduction

The fatigue of metals under cyclic loadings is the consequence of crack initiation and growth until the complete failure of the concerned structure. The design of metal components requires physically based crack initiation criteria compatible with structural computation, performed for example by Finite Element Method. In this aim many theoretical developments were done in the last decades and this conducted to different fatigue criteria. High cycle fatigue (HCF) criteria are generally stress tensor based while low cycle fatigue (LCF) ones are often defined from strain variables [22]. However, if elementary mechanisms have been extensively studied, the complete understanding of transition from cyclic plasticity to strain localization and crack initiation is still an open problem.

A common approach in LCF and HCF and an improvement of such criteria can be researched by taking into account the crystalline microstructure and not only the macroscopic behaviour. In fact, metallic materials are made of an aggregate of grains more or less well-oriented, with respect to the loading axis. Under mechanical loading, this leads to heterogeneous deformation at the microstructure scale [10, 19]. In polycrystals with random crystallographic orientations, inhomogeneous stress and plastic strain fields are established because of orientation, grain shape and size, and geometrical effects. In LCF, bulk plastic deformation takes place, but this is by no means homogeneous. It is expected, therefore, that localized regions of preferential slip develop, leading to similarly localized regions of crack initiation. In HCF, the material undergoes elastic deformation at the macroscopic level, and it is only in small areas that plastic deformation occurs. For the case of a polycrystalline metal subjected to HCF with uniform macroscopic stress, the localized regions deforming plastically are generated again by the inhomogeneity of the stress resulting from crystallographic orientation, grain shape, etc. Even in HCF, as very localized plastic straining develops, hardening can occur, leading to a redistribution of stress and a further localization of plasticity. In other words, this is shakedown occurring, and it is the basis of the Dang Van criterion for crack initiation [3]. Dang Van argues that local plastic flow is essential for crack initiation and that, if shakedown occurs at the grain level, the material would have an infinite fatigue life.

Since many years, experimental tests and numerical simulations on polycrystalline aggregates are made in order to understand and model such mechanisms. Finite element models, incorporating crystal plasticity [8], were developed in order to study the evolution of mechanical quantities in the microstructure, the variables which rule the heterogeneous behaviour, for example the role of grain orientation with respect to the loading axis and misorientation with its neighbours in causing load shedding and stress localizations, and for trying to find a link between macroscopic and microscopic behaviour. Numerical simulations can be conducted on real microstructures, built by using an EBSD technique in order to obtain informations on grain boundaries and orientations, or on fictive microstructures, based on a random distribution of crystallographic orientations and grain sizes [16]. The simulations are then made by using a FE code, after the introduction

of the crystal plasticity models and the definition of boundary conditions and loadings. The classical incremental method (Newton-Raphson) is the standard technique to solve this kind of nonlinear analysis. Due to the size of the aggregates and the nonlinear character of the differential equations, such computations are very time-consuming. Under cyclic loadings these simulations are quite not possible due to the necessary high number of cycles before obtaining the stabilized response of the aggregates. A method called Direct Cycle Analysis (DCA) has been recently implemented in the commercial software ABAQUS [15] and it is today commonly used to obtain the stabilized cycle for LCF design.

The aim of this work is to test the performances and the accuracy of the DCA in the evaluation of the steady state of policrystalline aggregates under cyclic loading. As a first step, an aggregate of 20 grains of AISI 316L stainless steel under strain controlled cyclic loading is studied. A Crystal Plasticity FEM model based on dislocation densities, already implemented in a User-subroutine for ABAQUS/Standard [20], is considered. The fictive microstructure and the finite element mesh are generated by NEPER, a software based on Voronoi tessellation [16]. This work starts with an introduction to the behaviour of metals under cyclic loads. The crystal plasticity model is then described together with how to obtain the geometrical model of a microstructure. The DCA is briefly recalled and it is tested in the case of crystal plasticity. Precise comparisons are conducted with an incremental analysis in order to validate the DCA as an efficient and accurate tool for the evaluation of the shakedown state of polycrystalline aggregates.

2 Steady State and Fatigue Criteria

Among different methods of fatigue design of metal structures, a decoupled approach can be used. It plans to perform a thermomechanical analysis without taking into account the damage and then appropriate fatigue criteria allow to link the mechanical parameters of the stabilized state to the lifetime of the structure. A structure whose material obeys Drucker's postulate, will reach, after some cycles of loading, a steady cycle in which the stresses and the strain rates gradually stabilize and remain unaltered on passing to the next cycle. There are three different categories of steady stress cycles:

- Ratcheting (or incremental collapse), where non-vanishing plastic strain rates $\dot{\varepsilon}^p$ and a non-vanishing plastic strain ratchet $\Delta\varepsilon^p \neq 0$ occurs at various parts of V. This happens for sufficiently high load amplitudes and is a dangerous long-term response as the plastic strains grow bigger from cycle to cycle leading to large displacements so that the structure becomes unserviceable or the ultimate strain of the material is reached.
- Alternating plasticity (or plastic shakedown), in which non-vanishing plastic strain rates $\dot{\varepsilon}^p$ exist but there is no increment of plastic strains, i.e. $\Delta\varepsilon^p = 0$. This also

occurs for high load amplitudes and this type of long-term response leads to low cycle fatigue, which reduces the working life of a structure or of a component.
- Shakedown (or elastic shakedown), where plastic strain rate $\dot{\epsilon}^p$ vanish over the whole body. In this case further plastic straining stops when the steady cycle is reached and the structure subsequently responds, to further cycling, purely elastically. This long-term response occurs for relative low load amplitudes and is a favourable situation provided the plastic deformation that has been produced at the transient phase is sufficiently small. In this case the structure or a structural component can have infinite fatigue life, i.e. there is no failure even after many cycles, or finite life due to high cycle fatigue.

In the case of elastic shakedown the structure, suddenly or after some cycles, has an elastic response. Even if the stress is less than yield stress failure can occurs because of HCF. The HCF design is based on the stress control and the stress is computed by considering the metal as homogeneous, without taking into account stress concentration due to the material heterogeneity. Some metals, if the stress level is low, show an infinite life, i.e. fatigue does not occur even if the number of cycles is very high. When the structure undergoes plastic shakedown, fatigue occurs after a lower number of cycle and the LCF design is usually strain controlled. Both criteria are purely phenomenological, relying directly on the interpretation of experimental results at the macroscopic scale. An example of fatigue criterion that takes into account the difference between the macroscopic and the mesoscopic mechanical fields is the Dang Van criterion for infinite life.

2.1 Dang Van Criterion

One of the fatigue models including grain level phenomena in a macroscopic fatigue criterion is the Dang Van–Papadopulos criterion based on the following assumption:

- In the LCF regime, physical observations at both macroscopic and mesoscopic scale show extensive plastic strains. Moreover homogenisation theory shows that strains and stresses at the two scales tend to be closer to each other with increasing plastic strain. This can be translated into saying that the higher the applied load, the more similar mesoscopic and macroscopic scales will behave.
- In the HCF regime, two fatigue domains corresponding to finite and infinite lifetime can be considered. Physical observations at the macroscopic scale show that structures are macroscopically in an elastic shakedown state. At the mesoscopic scale of the grains, it is now commonly accepted that elastic shakedown occurs only in the case of infinite lifetime. If lifetime is finite, some grains will be oriented such that they can not reach an elastic shakedown state, but will experience a plastic shakedown or ratcheting state leading to failure after a finite number of cycles. The stress concentration due to this mesoscopic failure marks the initiation of a macroscopic crack associated with failure on the macroscopic scale.

Focusing on the case of HCF, one can imagine a case where only one misoriented grain is subject to plastic slip. Then a simple homogenisation scheme of a plastic inclusion in an elastic matrix can be used to derive closed-form relations between mesoscopic and macroscopic fields. Examples of possible homogenisation assumptions are:

- Lin–Taylor strain equality: $\varepsilon = E$, that is the hypothesis of the initial Dang Van–Papadopoulos fatigue criterion;
- Sachs stress equality $\sigma = \Sigma$;

where ε and σ are strain and stress at grain level, E and Σ are strain and stress at macroscopic level.

If, in all the cases, the same elastic behaviour at the mesoscopic and the macroscopic scale is assumed, the relation between mesoscopic and macroscopic fields can be written in the general form:

$$\sigma = \Sigma - C^* \varepsilon^p = \Sigma + \rho^* \tag{1}$$

where ρ^* should be interpreted as mesoscopic residual stress field. The particular case of each homogenisation model is obtained depending on the form of C^*:

- Lin–Taylor's model: $C^* = C$
- Sachs's model $C^* = 0$;

As we will see better in the next chapter the plastic deformation is the consequence of atomic slip in preferential directions on particular atomic planes (slip systems). However under the assumption that the grain orientations statistically cover all directions [14], and so even the slip systems, according to Dan Vang fatigue criterion infinite life occurs if

$$\max_t(\tau^T(t) + a\sigma^H(t)) < b \tag{2}$$

where τ^T is the Tresca norm of mesoscopic shear, $\sigma^H = 1/3\,\mathrm{tr}(\sigma)$ is the hydrostatic mesoscopic stress, a and b are material parameters.

The homogenisation assumptions seen previously cannot represent at the best the reality. Numerical simulations on polycrystalline aggregates can be the way to improve the link between mesoscopic and macroscopic quantities.

3 The Crystal Plasticity Model

3.1 Single Crystal Plasticity

In crystal plasticity theory, plastic deformation is modelled by using the slip system activity concept. It is a physically based plasticity theory that represents the deformation of a metal at the microscale. It is important to note that, in this theory,

the continuum framework is kept even if at such scale the physics is not continuous anymore. Dislocations are assumed to move across the crystal lattice along specific crystallographic planes and directions. When the material is subjected to loading, the local resolved shear stress occurs on a slip plane and along a slip direction and its magnitude controls the movement, the creation and the annihilation of dislocations. Consequently the material is locally loaded on specific directions while the volume remains constant. Moreover the crystal lattice could deform elastically while the resolved shear stress has not reached its critical level. Two laws are necessary to describe the single crystal plasticity:

- the flow rule, that describes, for intragranular variable, the slip initiation for each system;
- the hardening rule, that describes the hardening which occurs on each system after successive loadings.

The crystal plasticity model described in the following is that already implemented as a User-subroutine for ABAQUS/Standard [20].

3.1.1 Flow Rule

The Resolved Shear Stress vector τ^s is the projection of the local stress tensor expressed in the global reference system on every possible slip system s. The Schmid law takes the following general form [17]:

$$\tau^s = \sigma : D^s \tag{3}$$

$$D^s = \frac{1}{2}(b^s \otimes n^s + n^s \otimes b^s) \tag{4}$$

where σ is the local stress tensor, n^s is the slip plane normal, b^s is the the slip direction and D^s is the Schmid matrix, that is the symmetric part of the Schmid tensor $L^s = b^s \otimes n^s$ and we denote here W^s its antisymmetric part. One can easily find that, in the case of a single crystal submitted to a uniaxial loading, the Schmid matrix D^s is reduced to a simple composition of crystallographic orientations $cos\psi cos\lambda$, where λ is the slip direction angle related to the load direction and ψ is the slip plane normal angle. According to the Schmid law, a single crystal leaves the elasticity and shear occurs when the Resolved Shear Stress on a slip system s reaches its threshold value, the Critical Resolved Shear Stress (CRSS), noted τ_c^s. It could basically be written as

$$\begin{cases} \dot{\gamma}^s = 0, \ \tau^s < \tau_c^s \\ \dot{\gamma}^s > 0, \ \tau^s \geq \tau_c^s \end{cases} \tag{5}$$

with $\dot{\gamma}^s$ the slip rate associated to system s. The flow rule introduces a rate dependent formulation. Classically one use a viscoplastic formulation more convenient for numerical simulation [9], that consists in a power law:

$$\dot{\gamma}^s = \dot{\gamma}_0 \left| \frac{\tau^s}{\tau_c^s} \right|^n \operatorname{sign}(\tau^s) \tag{6}$$

where $\dot{\gamma}_0$ is a reference value of the slip rate and n is the strain rate sensibility parameter. The rate dependent approach in fact avoids to deal with discontinuous conditions because all slip systems are allowed to be active but only some systems have non-negligible slips (when $n \gg 1$, $\dot{\gamma}^s \cong 0$ unless $\tau^s \cong \tau_c^s$).

3.1.2 Hardening Rule

When sliding occurs on a specific system, it interacts with different obstacles: additive elements, precipitates, dislocations "forest", etc. The increasing of dislocation density and these interactions lead to a local material resistance which results in critical shear stress increasing. In some cases an annihilation process could occurs leading to a decrease of dislocation density storage rate. One experimentally observes that there is a critical distance between dislocation systems with opposite sign leading to their annihilation. This process could conduct to a saturation process of hardening and also softening process. A physical based hardening rule has to take into account these basic mechanisms of dislocations generation and annihilation. It can take the following general expression proposed by [11]:

$$\tau_c^s = \sum_u H^{su} |\dot{\gamma}^s| \tag{7}$$

where the H^{su} terms are the components of the hardening matrix. This matrix takes into account the slip on the considered system also on the others. Diagonal terms H^{ss}, called self-hardening, account for the hardening on slip system s due to its own slip activity. Remaining terms, called latent-hardening, account for the hardening on slip system s due to the slip activity on the whole set of other systems u. The form of the hardening matrix depends on the considered physical mechanisms.

To account for more physics Eq. 7 should be based on dislocation density. Basically, the total dislocation density could be divided in two parts: statistically stored dislocations ρ_s^s, which trap each others in a random way and/or are required for compatible deformation of various part of the crystal, and geometrically stored dislocations ρ_g^s, which are required when gradient of plastic shear exists. For simplicity's sake in this model it's implicitly assumed that only ρ_s^s influences the work hardening. No geometrically stored dislocations are therefore considered. The form of the slip resistance classically used was introduced in [5]:

$$\tau_c^s = \tau_0 + \mu b \sqrt{\sum_u d^{su} \rho^u} \tag{8}$$

where τ_0 is an initial value of Critical Resolved Shear Stress, μ is the shear modulus, b the magnitude of the Burgers vector, d^{su} the interaction coefficient between

the slip systems s and u and ρ^u represents the local density of the statistically stored dislocations on the slip system u. In the case of FCC structure the hardening interaction matrix is a 12×12 matrix composed by only 4 independent coefficients due to crystal symmetries. The identification of these coefficients is still complicated and is classically done by Discrete Dislocation Dynamics simulations. In practice one uses here a simple form of the matrix depending on only two parameters: d_p for the self-hardening ($s = u$) and d_f for the latent-hardening ($s \neq u$).

The hardening rule needs to be completed by a flow rule for dislocation density on each slip system s, function of slip rate $\dot{\gamma}^s$. The description of dislocation generation was firstly figured out by Frank and Read [6]. It takes generally the following form:

$$\dot{\rho}^s = \frac{1}{b}\left(\frac{\sum_u (a^{su}\rho^u)}{L} - 2y_c\rho^s\right)\left|\dot{\gamma}^s\right| \tag{9}$$

in which the term $\frac{\sum_u (a^{su}\rho^u)}{Lb}$ accounts for dislocation creation and the term $2y_c\rho^s$ accounts for dislocation annihilation.

The material parameter $2y_c$ associated to annihilation is related to the critical annihilation distance, which is here taken constant. The parameter L is the mean free path of the mobile dislocations in system s, also assumed to be constant in this study. Finally a^{su} accounts for the geometrical interaction between dislocation densities. Assuming that collinear, coplanar and orthogonal crystal interactions have the same impact on mean free paths allows to reduce the number of a_i unknown to only four independent coefficients as shown in Table 1. Note that the Eq. 9 implies that there exists a saturation of dislocation production which depends on the deformation path, and more precisely on the dislocation quantity accumulated on the whole set of slip systems. Note also that dislocation production rate $\dot{\rho}^s$ depends on the absolute value

Table 1 Dislocation density interaction matrix of FCC material

	A_2	A_3	A_6	B_2	B_4	B_5	C_1	C_3	C_5	D_1	D_4	D_6
A_2	a_1	a_3	a_3	a_3	a_5	a_5	a_3	a_5	a_6	a_3	a_6	a_5
A_3		a_1	a_3	a_5	a_3	a_6	a_5	a_3	a_5	a_6	a_3	a_5
A_6			a_1	a_5	a_6	a_3	a_6	a_5	a_3	a_5	a_5	a_3
B_2				a_1	a_3	a_3	a_3	a_6	a_5	a_3	a_5	a_6
B_4					a_1	a_3	a_6	a_3	a_5	a_5	a_3	a_5
B_5						a_1	a_5	a_5	a_3	a_6	a_5	a_3
C_1							a_1	a_3	a_3	a_3	a_5	a_5
C_3								a_1	a_3	a_5	a_3	a_6
C_5				Sym					a_1	a_5	a_6	a_3
D_1										a_1	a_3	a_3
D_4											a_1	a_3
D_6												a_1

of slip rate $\dot{\gamma}^s$ and this hardening is therefore isotropic. Nevertheless, as each slip direction has its own dislocation and yield evolution, the yield surface in spatial domain evolves from an initial sphere of radius τ_0 to a more complex form (Fig. 1).

3.2 Microstructure Geometry

Numerical simulation can be computed on two different kind of polycrystalline aggregates:

- real microstructure, built by E.S.B.D. analysis which provides information on grain boundaries and crystallographic orientation
- fictive microstructure, based on a random distribution of crystallographic orientations and grain sizes.

3.2.1 Fictive Microstructures

Several authors have proposed analytical and numerical methods to construct random polycrystalline morphologies. These methods can be rooted in the basic principles of phase transformations (leading in some cases to Voronoi tessellations), physically-driven simulations of annealing or recrystallization, or algorithms that attempt to directly reproduce statistical data coming from experimental characterizations. Among randomly generated morphologies, Voronoi tessellations have the advantages of being defined analytically and having straight triple lines and flat grain

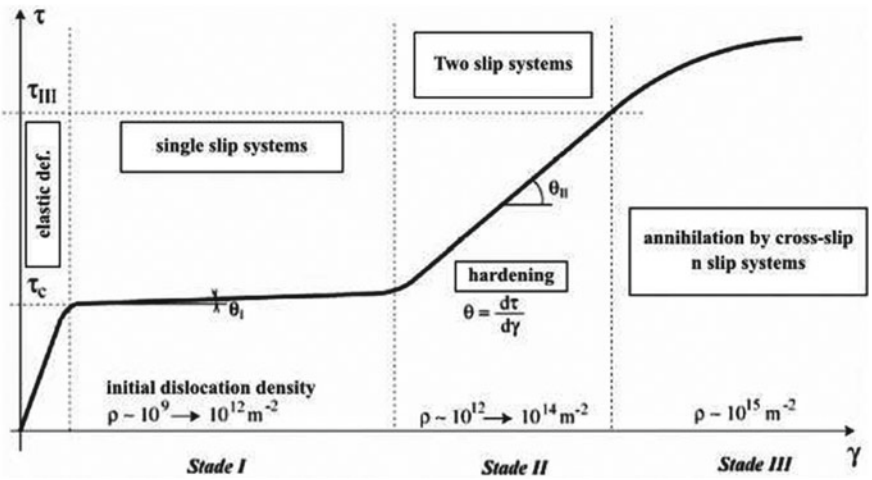

Fig. 1 Hardening evolution with dislocation density

boundaries. Still, Voronoi tessellations show important variabilities in grain size and shape which are representative of real polycrystalline morphologies [16].

Mathematically a Voronoi tessellation of a n-D space is a collection of n-D entities that fills the space with no overlaps and no gaps. These entities are polyhedra and are formally defined as zones of influence of a particular set of points, corresponding to their centres. Being given a spatial domain $D \in R^n$, a set of points $G_i(x_i)$ within D and a norm $d(\bullet, \bullet)$, a Voronoi polyhedron C_i is associated to every point G_i as follows:

$$C_i = \left\{ P(x) \in D | d(P, G_i) \leq d(P, G_j) \quad \forall j \neq i \right\} \tag{10}$$

There are different available software which provide a Voronoi tesselation of 2-D and 3-D domains, like for example NEPER [16], which provides the polycrystal morphology, described by sets of points, lines, surfaces and volumes, and the free meshing of the morphology. It uses an Euclidean distance like norm and the set of points G_i is taken randomly distributed. By construction, a Voronoi polyhedron is convex; hence in 3-D the intersection of two Voronoi polyhedra is a plane, called "tessellation face", the intersection of three Voronoi polyhedra is a straight line, called "tessellation edge", and the intersection of four Voronoi polyhedra is a point, called "tessellation vertex". From a physical point of view, the generation of Voronoi tessellations corresponds to a process of solidification or recrystallization where all grains nucleate at the same time and grow isotropically at the same rate. Voronoi tessellations qualitatively reproduce some important properties of real polycrystalline morphologies, like the distribution of grain size and the number of first neighbours.

4 Review of the DCA

The classical approach in FE codes to obtain the stabilized response of an elastic-plastic structure subjected to cyclic loading is to apply the periodic loading cycles repetitively to the unstressed structure until a stabilized state is obtained. At each instant in time it typically involves using Newton's method to solve the nonlinear equilibrium equations. To avoid the considerable numerical expense associated with such a transient analysis, a DCA has been suggested in [15] and has been recently implemented in the commercial software ABAQUS. It is based on the following assumption:

- quasi-static analysis, i.e. without taking into account dynamic effect
- geometrically linear behavior
- use of Fourier series to describe the stabilized state
- direct research of the stabilized cyclic response of the structure iteratively using the Modified Newton's method with the elastic stiffness matrix

4.1 Description of the Algorithm

In a quasi-static analysis with cyclic periodic loads the nonlinear equilibrium equations can be written as:

$$R(t) = F(t) - I(t) = 0 \tag{11}$$

where $F(t)$ is the discretized form of a cyclic load that has the characteristic $F(t + T) = F(t)$ at all times t during a load cycle with period T, $I(t)$ represents the internal force vector generated by the stress, and $R(t)$ is the residual vector. We are looking for a displacement function that describes the stabilized response of the structure, i.e. a displacement function $u(t)$ that at all times t during a load cycle with period T has the characteristic $u(t) = u(t + T)$. Since the periodicity of the solution, the best choice for this purpose seems to be a truncated Fourier series:

$$u(t) = u_0 + \sum_{k=1}^{N} \left[u_k^s \sin k\omega t + u_k^c \cos k\omega t \right] \tag{12}$$

where n stands for the number of terms in the Fourier series; $\omega = 2\pi/T$ is the angular frequency; and u_0, u_k^s and u_k^c are unknown displacement coefficients.

We also expand the residual vector in a truncated Fourier series in the same form as the displacement solution:

$$R(t) = R_0 + \sum_{k=1}^{N} \left[R_k^s \sin k\omega t + R_k^c \cos k\omega t \right] \tag{13}$$

where each residual vector coefficient R_0, R_k^s and R_k^c in the Fourier series corresponds to a displacement coefficient. At each instant in time in the cycle the residual vector $R(t)$ is obtained by using standard element-by-element calculations and provides the Fourier coefficients:

$$\begin{aligned} R_0 &= \frac{2}{T} \int_0^T R(t) dt \\ R_k^s &= \frac{2}{T} \int_0^T R(t) \sin(k\omega t) dt \\ R_k^c &= \frac{2}{T} \int_0^T R(t) \cos(k\omega t) dt \end{aligned} \tag{14}$$

For the computing of the residual Fourier terms we need to evaluate the residual vector at some time points obtained by a discretization of time period in time increments. ABAQUS uses a trapezoidal rule, which assumes a linear variation of the residual over a time increment, to integrate the residual coefficients. For accurate integration the number of time points must be larger than the number of Fourier coefficients (which is equal to $2n + 1$, where n represents the number of Fourier terms).

The unknown displacement coefficients can now be computed iteratively by using the Modified Newton method. Starting from their approximations obtained after an iteration (i), the coefficient after an iteration ($i + 1$) are:

$$\begin{aligned} u_0^{(i+1)} &= u_0^{(i)} + c_0^{(i+1)} \\ u_k^{s(i+1)} &= u_k^{s(i)} + c_k^{s(i+1)} \\ u_k^{c(i+1)} &= u_k^{c(i)} + c_k^{c(i+1)} \end{aligned} \tag{15}$$

where the corrections to the coefficients of the displacement solution are found by solving the following linear systems:

$$\begin{aligned} K c_0^{(i+1)} &= R_0^{(i)} \\ K c_k^{s(i+1)} &= R_k^{s(i)} \\ K c_k^{c(i+1)} &= R_k^{c(i)} \end{aligned} \tag{16}$$

with K the initial elastic stiffness matrix. The updated displacement coefficients are used in the next iteration to obtain displacements at each instant in time. This process is repeated until convergence is obtained. Each pass through the complete load cycle can therefore be thought of as a single iteration of the solution to the nonlinear problem [1]. Since the use of the Modified Newton iterative scheme, the DCA cannot be utilized in the presence of strong nonlinearities, such as geometric nonlinearities and contact.

During the iterative solution process, the DCA imposes periodic conditions by using the state obtained at the end of the previous iteration as the starting state for the current iteration, i.e. $s_{t=0}^{i+1} = s_{t=T}^{i}$, where s is a solution variable such as plastic strain.

5 Numerical Simulations on a Polycrystal

5.1 Geometric Model and Material

In this section we analyse a polycrystal composed by 20 grains. The specimen is a square cuboid in which two dimensions are ten times the other one. The microstructure, the crystal orientations and the mesh are generated by NEPER. The geometrical model and the boundary conditions are shown in Fig. 2. The model is composed by 2094 tetrahedral elements C3D4 and 636 nodes. The material used in the simulation is the AISI 316L austenitic stainless steel, a material used for many structural applications. It is a polycrystalline aggregates with FCC structure and its crystal plasticity parameters are available in literature and are reported below. The definition of elastic fourth rank stiffness tensor C for a FCC crystal need only 3 parameters, due to the

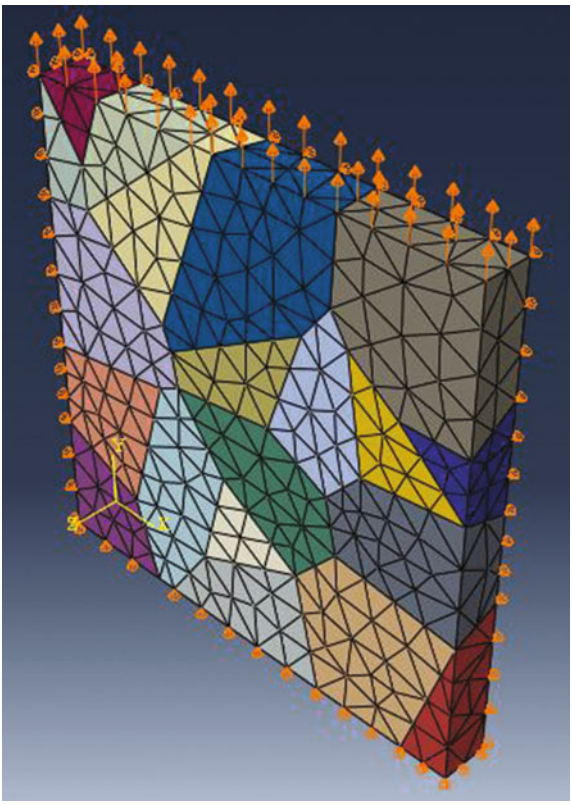

Fig. 2 Geometrical model and boundary condition of the polycrystal

cubic symmetry, which for 316 L are shown in Table 2, where $a = 2C_{44}/(C_{11} - C_{22})$ is the coefficient of anisotropy ($a = 1$ for isotropic material). The flow rule consists in a power low defined by 2 parameters reported in Table 3: the reference value of the slip rate $\dot{\gamma}_0$ and the strain rate sensitivity parameter. Eleven parameters are required to define the hardening behaviour of an FCC crystal and are summarized in Tables 4 and 5.

Table 2 Elastic parameters of CPFEM for 316L [13]

C_{11} (MPa)	C_{12} (MPa)	C_{44} (MPa)	a
248000	142000	71000	1.34

Table 3 Flow parameters of CPFEM for 316L [2, 21]

$\dot{\gamma}_0\,(s^{-1})$	n
3.4×10^{-6}	10

Table 4 Hardening parameters of CPFEM for 316L [4, 7]

tau_0 (MPa)	b (mm)	y_c	L (mm^{-2})	ρ_0	d_p	d_f
35	3.2×10^{-7}	3.2×10^{-6}	33	10^{-3}	0.06	0.004

Table 5 Dislocation density interaction parameters of CPFEM for 316L [12]

a_1	a_3	a_5	a_6
0.12	0.07	0.14	0.12

5.2 Monotonic Tensile Test

A strain controlled monotonic tensile test with a constant strain rate of 0.005 s^{-1} is realized. The simulation is first performed without taking into account the geometric nonlinearities, i.e. the rotation of crystal axis during the deformation.

Figure 3 shows the heterogeneous mechanical average behaviour of the different grains in loading direction. At 2.5% of average strain the heterogeneity on strain is about 1% and about 144 MPa on stress. We can see on the average strain vs stress curve that, at 2.5% of average strain, the stress is 263 MPa and is consistent with experimental and other numerical results [18]. The behaviour obtained is qualitatively acceptable although the number of grains is very low and the microstructure

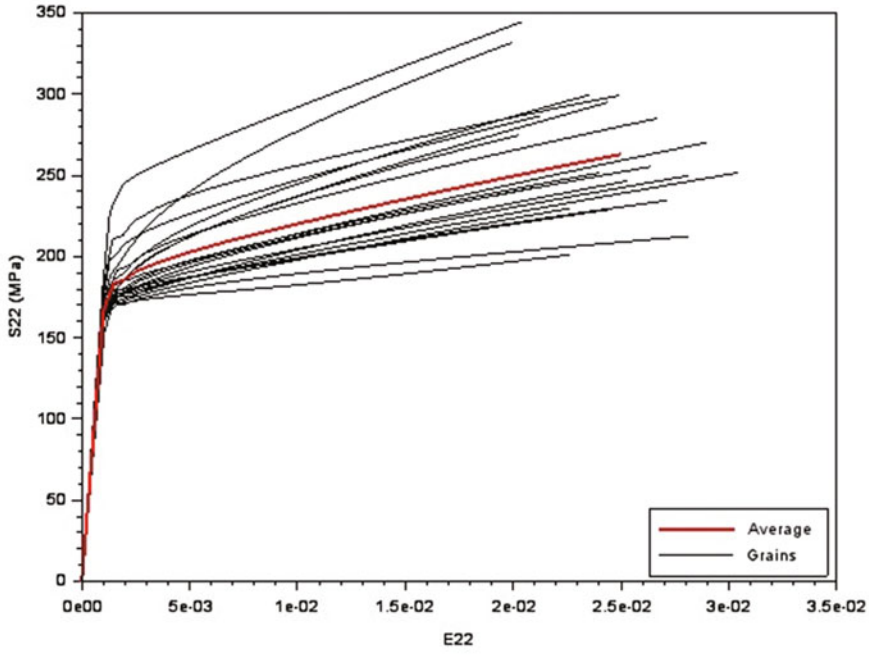

Fig. 3 Monotonic test, stress-strain curve in load direction for each grain

is fictive. The influence of the mesh on the results is not tested. The same test is performed with both models, geometrically linear and nonlinear, up to 5% of average strain in order to quantify the error of neglecting the rotation of crystal axis during the deformation. In Fig. 4 we can see that, even at 5% of average strain, the error on the strain is certainly negligible, while the error on the average strain and on the maximum stress becomes to be of few percent. However in fatigue design the values of strain reached are usually much lower that 5% and so the neglecting of geometric nonlinearities are surely acceptable. After this observation we can safely use the Direct Cyclic Algorithm on polycrystalline aggregates. In fact it cannot be used for geometrically nonlinear analysis since it uses the modified Newton-Raphson method to solve the equilibrium equations.

5.3 *Cyclic Test*

A strain controlled cyclic symmetric tensile-compression test up to 0.25% with a constant strain rate of $0.0025\,s^{-1}$ is now performed on the same aggregate and the results are discussed. Figures 5 and 6 show the average behaviour and the behaviour

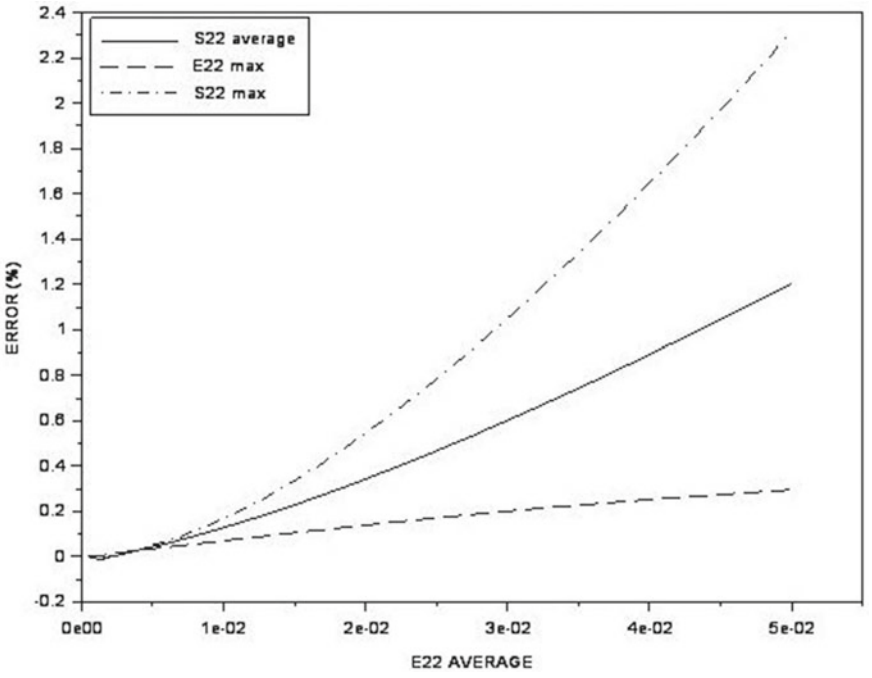

Fig. 4 Error of neglecting geometric nonlinearities on maximum stress, maximun strain and average stress in load direction

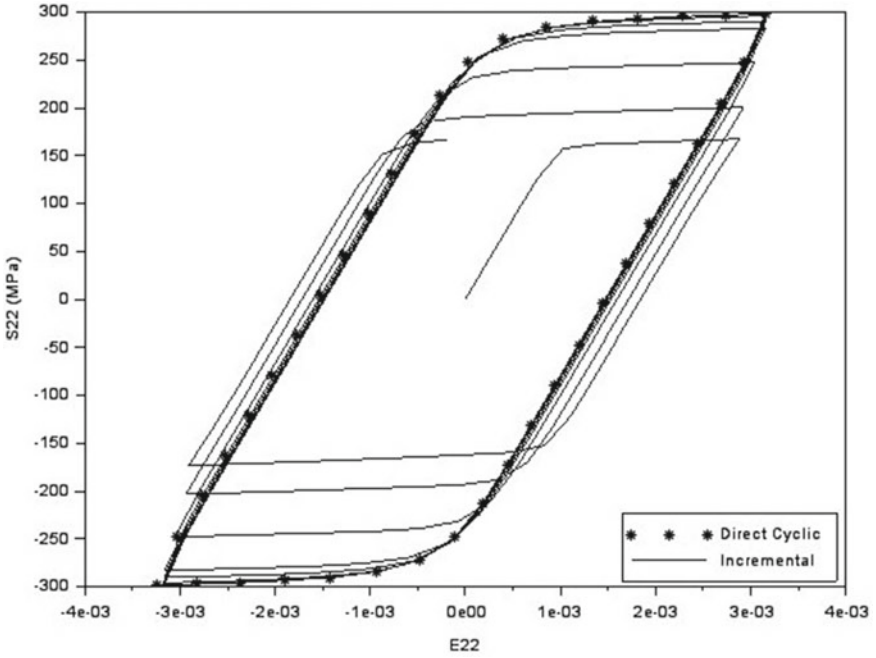

Fig. 5 Stress-strain curve in load direction for the misoriented grain: direct cyclic and incremental (cycle 1, 20, 100, 200, 600 and 1000) solution

of the misoriented grain. We can see that the steady cycle is reached by an incremental analysis about 600 cycles. The DCA requires with 19 terms, the maximum number of Fourier terms, 682 iterations to converge. We can also see that the results obtained by DCA and Incremental analysis are roughly equivalent by looking at the two stress-strain curves.

Figure 7 shows that the strain field obtained with the two method has practically the same form and the same values. Looking at Fig. 8 we can see that even with only 5 Fourier terms and practically the same number of iterations we can obtained a solution very close to the incremental one. In fact, if we exclude the decomposition of the stiffness matrix and the evaluation of the residual vector in each time increment, which are the same in both analysis, we can link the remaining computational time to the number linear systems required to achieve the convergence:

- 19 F.T. $\Rightarrow$ 682 iterations $\times$ (2 $\times$ 19+1) F.C. = 26598 L.S.
- 5 F.T. $\Rightarrow$ 682 iterations $\times$ (2 $\times$ 5+1) F.C. = 7480 L.S.

In this case the number of linear systems with 5 Fourier terms is 3.5 times lower than the number required with 19. The error is quantify in Tables 6 and 7 for the misoriented grain and for the average behaviour for different number of terms. Looking to these results we can make some consideration:

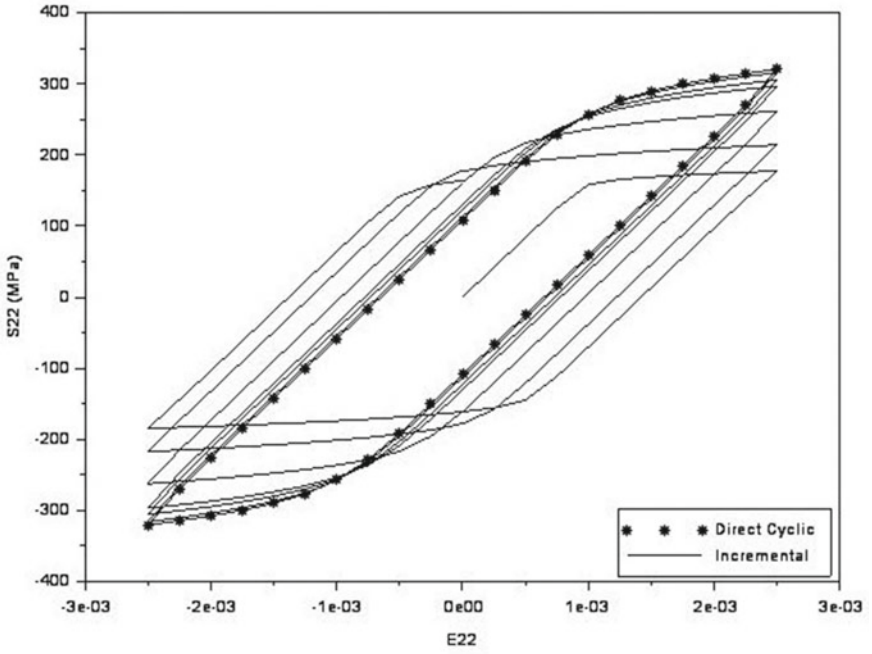

Fig. 6 Stress-strain average curve in load direction: direct cyclic and incremental (cycle 1, 20, 100, 200, 600 and 1000) solution

- the DCA solution seems to converge to the solution with more Fourier terms;
- at convergence, the DCA solution is not coincident with the incremental one and then a lower number of Fourier terms can provide better results.

In Fig. 9 it is shown the behaviour of two different grains with respect to the average behaviour. The load transfer between groups of grains of different orientation occurs due to plastic deformation governed by crystal slip. In this respect the grain 7 and 8 in this polycrystalline aggregates are representative of the extremes of behaviour, grain 7 being the strongest orientation, and grain 8 being the softest and the most compliant. It is interesting to note that grain 7 undergoes practically elastic shakedown, while the response of grain 8 exhibits a significant hysteresis area. This is indicative of inelastic deformation by crystal slip, which leads to energy dissipation. It is interesting to interpret this result within the framework of energy-related criteria of fatigue crack initiation. For example, Dang Van postulates that infinite life may be expected, but only if after a certain initial period grain level shakedown occurs, the cyclic deformation becomes purely elastic, and no energy dissipation takes place. The result shown in Fig. 9 indicates that the situation is different between grains even within the same macroscopic sampling volume. Some grains, e.g. grain 8, satisfy the initiation criterion, while others, e.g. grain 7, must be expected to have infinite fatigue life (Table 8).

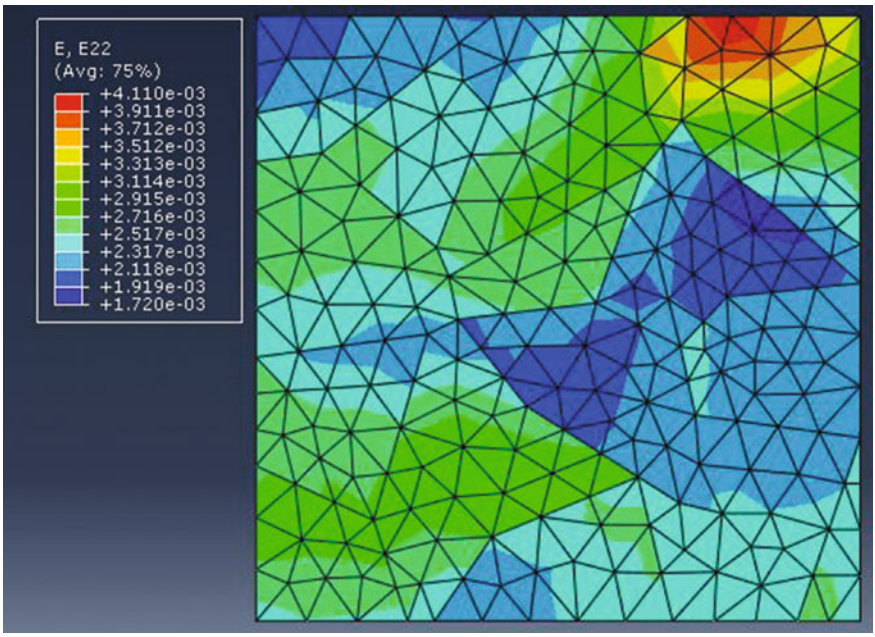

(a) Incremental

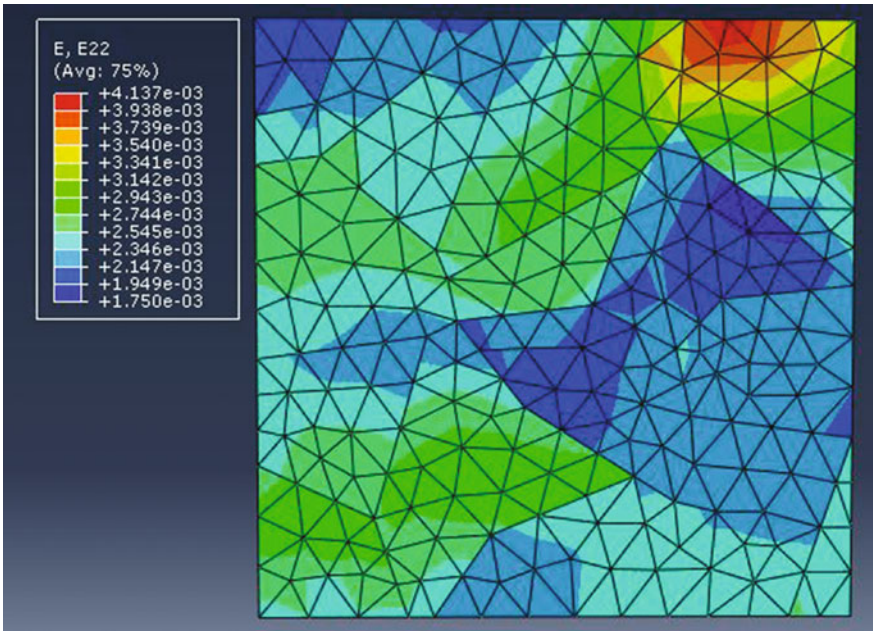

(b) Direct Cyclic

Fig. 7 Strain field in load direction at 0.25% of average axial strain at steady cycle

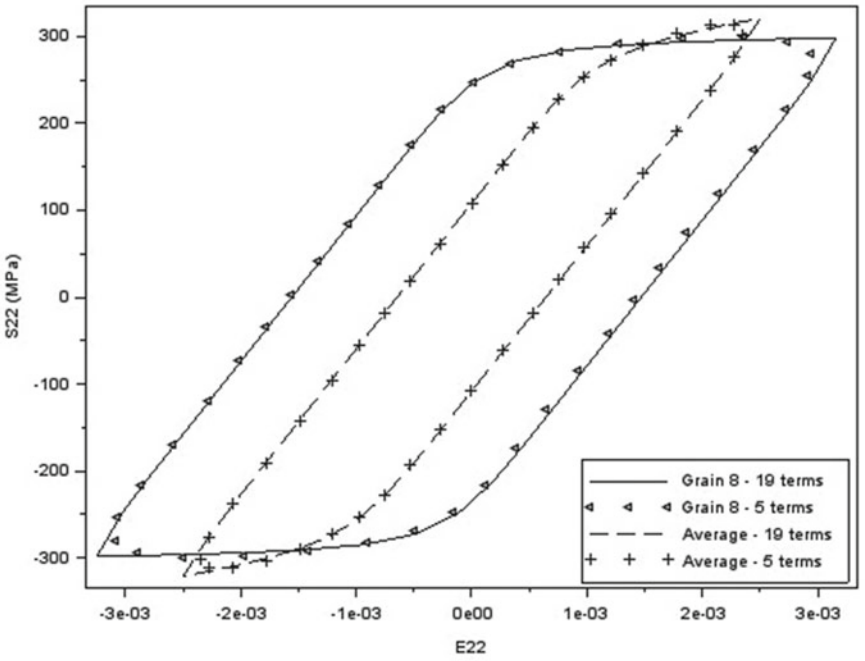

Fig. 8 Comparison of the stress-strain curve in load direction of the misoriented grain and the average behaviour obtained by DCA with 19 and 5 Fourier terms

Table 6 Direct cyclic error for the misoriented grain

Analysis	ΔE	err (%)	ΔS (MPa)	err (%)	Energy (MPa)	err (%)
D.C. 5 F.T.	0.0060	−4.8	599	0.3	1.710	1.5
D.C. 9 F.T.	0.0062	−1.7	602	0.9	1.753	4.0
D.C. 14 F.T.	0.0063	−0.2	605	1.4	1.754	4.1
D.C. 19 F.T.	0.0064	1.3	597	0.0	1.734	2.9
Incremental	0.0063		597		1.685	

Table 7 Direct cyclic error for the average behaviour

Analysis	ΔE	err (%)	ΔS (MPa)	err (%)	Energy (MPa)	err (%)
D.C. 5 F.T.	0.0046	−6.2	625	−2.4	0.743	−2.0
D.C. 9 F.T.	0.0048	−3.2	639	−0.2	0.761	0.4
D.C. 14 F.T.	0.0049	−1.6	640	0.0	0.761	0.4
D.C. 19 F.T.	0.0050	0.0	642	0.2	0.753	−0.6
Incremental	0.0050		640		0.758	

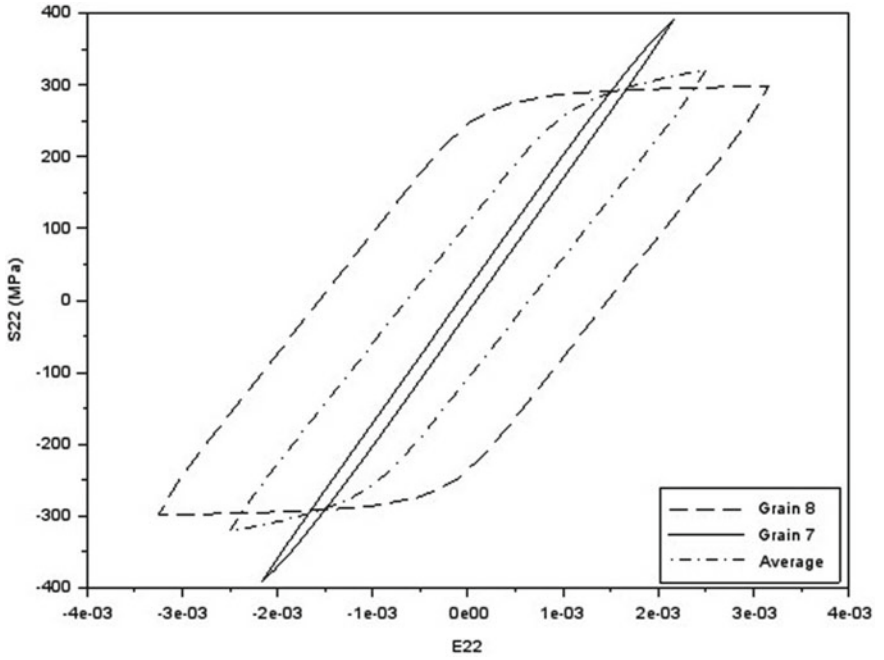

Fig. 9 Comparison of the stress-strain curve in load direction of different grains with respect to the average one

Table 8 Comparison of the behaviour of different grains with respect to the average one

Variable	Average	Grain 7	Grain 8
ΔE	0.0050	0.0043	0.0064
ΔS	642	784	597
Energy	0.75	0.19	1.73

6 Conclusions

Fatigue criteria based on stress and strain control are commonly used to link the steady response to the number of cycles that provides failure. In HCF the structure undergoes elastic shakedown and the life time is commonly determined by the macroscopic stress level. In LCF the structure undergoes alternating plasticity and the lifetime is estimated with the difference of strain of the steady cycles. However, a metal is a polycrystalline aggregate made of many grains with different orientations of the crystals. A heterogeneous response is expected due to the anisotropy of each crystal with regard to the elastic and, much more, the plastic behaviour. An improvement of fatigue criteria could be made by considering the behaviour of metals at the microstructure scale. To understand and to model such heterogeneity Crystal

Plasticity theory was used in the last years to build Crystal Plasticity FEM models. In this work a model based on dislocation density and large deformation was considered. The numerical model was already implemented as a UMAT for ABAQUS standard. We have seen that this model allows to achieve a first approximation of the heterogeneity of an aggregate of 20 grains of AISI 316L stainless steel under strain controlled monotonic and cyclic loading. The aggregate was built with the software NEPER that provides a random distribution of grain size and orientations and at first the analysis was performed incrementally with a full Newton method. This approach is quite expensive in the case of cyclic loading, since the application of many loading cycles may be required before the stabilized response is obtained, about 600 cycles for our aggregate.

Recently, Pommier proposed a method called Direct Cyclic Algorithm to obtain the stabilized response of a structure under cyclic periodically loading, which it is shown to be more efficient of an incremental analysis, much more increasing the size of the problem and the number of cycles required to obtain the steady cycle, but with a small error with respect to the incremental solution. The same cyclic analysis of the aggregate was performed by DCA, with the same time increment of the incremental analysis and the maximum number of Fourier terms allowed, that provides the steady cycle in 682 iterations. The convenience of this kind of analysis in terms of time is clear because the number of linear systems to be solved for a single cycle with the incremental method is surely higher that the number of linear system required for a single iteration of DCA. Moreover the full Newton method needs to assemble and decompose the stiffness matrix many times during a cycle, operation that dominates the entire computational effort, while the DCA uses always the elastic matrix. Each pass through the complete load cycle with DCA can therefore be thought of as few iterations of incremental method. In the simulation performed in this work, the DCA is about four time faster than the Incremental method. The DCA solution is close to the incremental solution but it is not exactly coincident. The error with the maximum number of Fourier terms on the strain difference, stress difference and energy of steady cycle is, however, a few percent for the softest grain and negligible for the average behaviour. The DCA is not able to deal with geometric non-linearities, but the error of neglecting the rotation of crystal axis during the deformation has tested and it was shown to be acceptable. We have also seen that a further reduction of the computational cost can be achieved by using a lower number of Fourier terms with a slightly larger error.

This result can be surely used in a future work where the model will take into account the real morphology, number and orientations of grains, using EBSD analysis of specimens used in experimental investigations. Since the size of this aggregates, the DCA is maybe the only possible way to compute numerical simulations, allowing a real comparison between mechanical fields at grain scale and to study the interaction between the local constitutive law of the single crystal and the macroscopic behaviour of the specimen, for example with respect to crack initiation and fatigue life. These informations could lead to the definition of new fatigue criteria.

Acknowledgements This work is the result of the internship of Domenico Magisano at the Laboratory of Mechanics of Lille, funded by an Erasmus Placement Grant of the Lifelong Learning Programme and by a Master Grant provided by the Lille 1 University.

References

1. ABAQUS 6.10 (2010) Theory and user's manual. Dassault systemes
2. Cailletaud G, Doquet V, Pineau A (1991) Cyclic multiaxial behaviour of an austenitic stainless steel. In: Fatigue under biaxial and multiaxial loading 12
3. Dang Van K, Papadopoulos IV (1999) High-cycle metal fatigue: theory to applications. CISM courses and lectures 392. Springer, Vienna
4. Evard P, El Bartali A, Aubin V, Rey C, Degallaix S, Kondo D (2010) Influence of boundary conditions on bi-phased polycrystal microstucture calculation. Int J Solid Struct 47(16):1979–1986
5. Franciosi P (1984) Etude téorique et expérimentale du comportament elastoplastique des monocrystaux métalliques se déformant par glissement. PhD thesis
6. Frank FC, Read WT (1950) Multiplication processes for slow moving dislocation. Phys Rev 79(4):722–723
7. Guilhem Y (2011) Numerical investigation of local mechanical fields in 316L steel polycrystalline aggregates under fatigue loading. PhD thesis
8. Huang Y (1991) A user-material subroutine incorporating single crystal plasticity in the ABAQUS finite element program. Division of applied sciences, Harvard University, Cambridge, MA, pp 02138
9. Hutchinson JW (1976) Bounds and self-consistent estimates for creep of polycrystalline materials. Proc R Soc Lond A 348
10. Korsunsky AM, James KE, Daymond MR (2004) Intergranular stresses in polycrystalline fatigue: diffraction measurement and self-consistent modelling. Eng Fract Mech 71:805–812
11. Mandel J (1965) Generalization de la theorie de la plasticité de W. T. Koiter. Int J Solids Struct 1(3):273–295
12. Monnet G (2009) A crystalline plasticity law for austenitic stainless steel
13. Mu P (2011) Study of crack initiation in low-cycle fatigue of an austenitic stainless steel. PhD thesis
14. Papadopoulos IV (1994) A new criterion of fatigue strength for out-of phase bending and torsion of hard metals. Int J Fatigue 16(6):377–384
15. Pommier B (2003) Détermination de la réponse asymptotique d'une structure anélastique sous chargement thermomécanique cyclique. PhD thesis
16. Quey R, Dawson PR, Barbe F (2011) Large-scale 3D random polycrystals for the finite element method: generation, meshing and remeshing. Comput Methods Appl Mech Eng 200:1729–1745
17. Schmid E, Boas W (1950) Plasticity of crystals with special reference to metals. F. A, Hughes (London)
18. Seghir R, Charkaluk E, Dufrénoy P, Bodelot L (2010) Thermomechanical coupling in crystalline plasticity under fatigue loading. Proc Eng 2:1155–1164
19. Seghir R, Bodelot L, Charkaluk E, Dufrénoy P (2011) Numerical and experimental estimation of thermochemical fields heterogeneity at grain scale of 316L stainless steel. Comput Mater Sci 53:464–473
20. Seghir R (2012) Experimental and numerical investigation of thermomechanical couplings and energy balance in metallic polycrystals. PhD thesis, Ecole Centrale de Lille
21. Simonovski I, Cizelj L (2009) The influence of grain structure size on microstructurally short crack. J Eng Gas Turbines Power 113(4)
22. Socie DF, et Marquis GB (2000) Multiaxial fatigue. SAE Inc Warrendale

On the Size of the Representative Volume Element Used for the Strength Prediction: A Statistical Survey Applied to the Particulate Reinforce Metal Matrix Composites (PRMMCs)

Geng Chen, Alexander Bezold, Christoph Broeckmann and Dieter Weichert

Abstract Particulate reinforced metal matrix composites (PRMMCs) are typical random heterogeneous materials whose global behavior depends on the microstructural characterisics. Recently a numerical approach was developed (Hachemi et al., Int J Plast 63:124–137, 2014 [1], Chen et al. Direct methods for limit and shakedown analysis of structures, 2015 [2]), by applying it to a typical PRMMC material WC/Co, we presented how the ultimate strength and endurance limit can be predicted from the material microstructures. Due to the randomness in the microstructures of PRMMCs, size of the representative volume element (RVE) has a nontrivial influence over the predicted effective behaviors. In order to understand how size of RVEs contribute to the result and based on that to eliminate its influence, a numerical investigation is performed in the present study. In this study, a large number of representative volume element (RVE) samples representing a representative PRMMC material, WC-20 Wt% Co, were built from artificial microstructures. The samples are obviously different in size, and by deploying the established numerical approach to these samples, ultimate strength and endurance limit were calculated. Afterwards, the derived material strengths were analyzed by multiple inferential statistical models. The statistical study reveals how strength and other effective material properties react to the change of the RVE size. On that basis, the study proposed a feasible and computationally inexpensive solution to minimize the size effect.

G. Chen · A. Bezold · C. Broeckmann (✉)
Institute of Materials Application in Mechanical Engineering, RWTH Aachen University, Augustinerbach 4, 52062 Aachen, Germany
e-mail: c.broeckmann@iwm.rwth-aachen.de

D. Weichert
Institute of General Mechanics, RWTH Aachen University, Templergraben 62, 52062 Aachen, Germany
e-mail: weichert@iam.rwth-aachen.de

O. Barrera et al. (eds.), *Advances in Direct Methods for Materials and Structures*, DOI 10.1007/978-3-319-59810-9_4

1 Introduction

Over the past three decades, particulate reinforced metal matrix composites (PRMMCs) have been transformed from a topic of scientific and intellectual interest to materials of broad technological and commercial significance [3]. In many industrial sectors, a clear trend can be seen that the application of PRMMCs prevail and gradually replace the conventional metallic materials in structural components. This trend in turn fosters the need to strengthen the understanding of the material behavior and based on that further reduce the development period of new PRMMC materials. Components made from PRMMCs often operate under variable loads with unknown time history. In order to evaluate the serviceability of these materials, their fatigue behaviors have to be well understood.

In many existing works, based on experimental observation, the dependence of the fatigue behavior of PRMMCs on the microstructural characteristics, such as size [4, 5] and distribution of the reinforcement phase [6, 7] have been investigated. In addition to these experimental works, numerical methods based on the micromechanical finite element (FE) analysis were also developed and applied to the PRMMC materials. By using these numerical methods, one can predict the macroscopic effective material behavior of interest from the material microstructure, and this significantly reduces the time for developing new PRMMC materials. For PRMMCs, one material behavior of particular interest is their load bearing capacity. However, according to [8], this is probably the most disputed part. Despite the difficulties arising from modeling the representative material morphology and defining the boundary conditions, Füssl and Lachner proposed in [8] to determine the strength from the limit analysis. The similar technique has been presented in many studies, c.f. [9, 10]. In these papers, the global material strength, both ultimate strength and endurance limit, were predicted by applying the direct method to the representative volume element (RVE) and converting the results to their corresponding macro quantities by means of the homogenization. Compared to the analytical approaches, the greatest advantage of such approach is that the influence of the material microstructure can be immediately identified.

In our latest studies, this numerical technique was extended to the random heterogeneous PRMMC materials. One major challenge pertained to these materials is, that the microstructure can not be embodied by one individual RVE model. Due to this reason, we proposed to predict the material strength from many RVE models called statistical equivalent representative volume element (SERVE). Although the method has been successfully implemented to an representative PRMMC material, WC-Co, with different binder contents and the results obtained from SERVEs were carefully interpreted by statistical models, one important issue, the size effect, is still not fully exposed. The size effect can be explained as follows: For nonperiodic materials, the absence of periodicity of material excludes to embody the infinite domain of the material by an individual RVE of finite size; therefore the predicted material behavior depends largely on the adopted RVE size.

In brief, the RVE size has to exceed a critical value to ensure that the simulation results are independent of both the RVE size and the spatial distribution of the reinforcements [11]. Regarding the determination of the RVE size, Hill [12] has provided an insight from an energetic point of view and developed a condition which requires the equality to hold for a sufficiently large RVEs. Because this condition, which is referred as the Hill's condition, made no hypothesis on the link between stresses and strains, therefore it should be compatible with any constitutive law. Beside Hill's condition, there are many pragmatic approaches for determining the RVE size, e.g. windowing method [13] which arbitrarily builds RVEs with fixed window size and compares between predicted results from different windows; boundary condition method [14] which examines the consistency between predictions obtained from statically uniform boundary conditions (SUBC), kinematically uniform boundary conditions (KUBC), and periodic boundary conditions (PBC); size convergence approach [15] which gradually enlarges the RVE size and accepts the size where the prediction is stabilized.

In addition to the pragmatic approaches, the problem of RVE size determination has been intensively studied from a theoretical perspective. For example, Drugan and Willis [16] studied a linear elastic composite and proposed a criterion for determining the minimum RVE size by comparing the ratio of the magnitude of nonlocal terms to the magnitude of local terms. According to this criterion, the minimum RVE size is required to be at maximum twice the reinforcement diameter for any reinforcement concentration level. This criterion has been subsequently approved in few subsequent studies [17, 18]. In multiple studies concerning different types of composite materials, a general observation has been reported that the size required for predicting the effective elastic behavior is relatively small and depends only on the volume fraction [19]. Beyond the scope of linear elasticity, many studies confirmed that the minimum size of an RVE needed to capture the nonlinear behavior are much larger than the ones for determining the linear behavior [20, 21]. In our previous study [22], we observed from few RVE samples built from the real scanning electron microscope (SEM) images of WC-Co, that the disparity between the models becomes more obvious when plastic deformation accumulates. Based on this observation, we concluded that all indicators for checking the fulfillment of the size requirement are necessary but insufficient criteria. Therefore a remedy to the difficulty of determining the RVE size is to use SERVE models.

According to the concept of SERVE, the material behavior of a random composite should be evaluated from a series of statistically equivalent RVE samples [23]. The evaluation should be based on statistical descriptors such as mean-value, variances, and probability density function [24]. When the size of SERVEs increases, each SERVE sample tends to become the RVE and differences among them become negligible [25]. Meanwhile, using typical statistical analysis techniques such as correlation analysis, the dominant factors influencing the material constitutive properties can be identified [26].

To achieve a satisfactory level of reliability, the number of SERVE samples should be guaranteed to exceed a threshold value. This threshold value can be determined from the margin of error, the confidence level and the standard deviation of the data.

Among existing studies, the number of RVEs varies significantly. In most studies only a small number of samples, e.g. 15 [27] or 25 [28], are used to predict the material behavior. Only seldom would an extremely large number of samples be adopted for the analogous purpose [29].

Although by using SERVE models the difficulty for determining the RVE size and eliminating the size effect is greatly reduced, it is still an open question that, how large should each statistically equivalent RVE be—especially, if the aim of the homogenization study is not only to predict the mean value, but also other statistical characteristics of an effective behavior. As has been summarized, the minimal RVE size depends on the type of the behavior to be studied. Due to this reason, the objective of the present study is to expose how to determine the size of RVEs used for determining the material strength. In the present study, the material investigated in our previous works, tungsten carbide-cobalt hard metal with 20 Wt.% of the binder phase, WC-20 Wt.% Co, was again used as an representative PRMMC material. WC-Co is one of the most used materials in industrial applications where hardness and wear resistance are crucial. The initial phase of this composite, WC, is the toughest in comparison to other hard phases used in tool materials. However, due to the lack of sufficient toughness WC alone is not applicable for harsh applications since it cannot resist deformation and wear well. This drawback can be compensated by the counterpart Co phase. As the second phase, Co provides the necessary toughness and other advantageous binder properties. In addition to that, what is also unique of WC-Co is the almost perfect compatibility existed between its two constitutes and, as a consequence, WC-Co is widely used in the machining, mining, forming and similar industries [30].

To understand how size of the RVE models influences the effective ultimate strength and endurance limit predicted for this material, we built 3 sample groups. Each sample group consists of 500 RVE models built from artificial microstructures of the material. RVE models in 3 sample groups have the same configuration but the different RVE size. By deploying the established numerical approach to these samples, ultimate strength and endurance limit were calculated and the results were analyzed through statistical models with a particular focus on the size effect. On the basis of the statistical analyses, in the end of the work, a feasible and computationally inexpensive solution is proposed for minimizing the size effect.

2 Shakedown of RVE Models

The strength of the WC-Co composite was predicted from RVE samples using the static direct method based on the Melan's theorem [31]. Before presenting how this method was applied to heterogeneous materials, first we revisit some fundamental micromechanical principles. Based on these principles results of the numerical simulation of the RVE models were interpreted and converted to the corresponding macroscopic effective quantities. The micromechanical laws adopted in the present study were based on the mean field homogenization theory according to which the

material can be reflected in two well-separated scales: the microscopic scale is small enough for the heterogeneities to be identified. In contrary to that, the macroscopic scale is large enough for the heterogeneities to be expelled. The two scales are well-separated and they are described by two coordinate systems: the global coordinate system $\boldsymbol{x}$ and local coordinate system $\boldsymbol{y}$. The following relationship holds

$$\boldsymbol{y} = \frac{\boldsymbol{x}}{\varepsilon} \,. \tag{1}$$

ε is a small scale parameter which determines the size of the RVE.

For a heterogeneous material, when it is submitted to an external loading, its microscopic stress field $\boldsymbol{\sigma}$ in $\boldsymbol{y}$ and its macroscopic counterpart $\boldsymbol{\Sigma}$ satisfy the relationship

$$\boldsymbol{\Sigma} = \frac{1}{\Omega} \int_{\Omega} \boldsymbol{\sigma}(\boldsymbol{y}) dV = \langle \boldsymbol{\sigma}(\boldsymbol{y}) \rangle \,. \tag{2}$$

Here $\langle \cdot \rangle$ stands for the averaging operator, and Ω indicates the RVE domain. Similarly, the relationship between strain measures satisfies

$$\boldsymbol{E} = \frac{1}{\Omega} \int_{\Omega} \boldsymbol{\varepsilon}(\boldsymbol{y}) dV = \langle \boldsymbol{\varepsilon}(\boldsymbol{y}) \rangle \,. \tag{3}$$

The local strain $\boldsymbol{\varepsilon}$ can be decomposed into two parts: The average value $\boldsymbol{E}$ and a fluctuating part $\boldsymbol{\varepsilon}^*$

$$\boldsymbol{\varepsilon}(\boldsymbol{u}) = \boldsymbol{E} + \boldsymbol{\varepsilon}^* \,. \tag{4}$$

When all constituents of a RVE are elastic, the overall behavior of the RVE is elastic as well. In this circumstance, $\boldsymbol{\Sigma}$ and $\boldsymbol{E}$ are correlated by an effective elastic tensor $\overline{\mathbb{C}}$

$$\boldsymbol{\Sigma} = \overline{\mathbb{C}} : \boldsymbol{E}. \tag{5}$$

In case that the heterogeneous material to be considered behaves isotropically in the macro scale, same to the single phase material, $\overline{\mathbb{C}}$ can be uniquely determined from two elastic constants, such as effective Young's modulus $\bar{E}$ and effective Poisson's ratio $\bar{\nu}$.

When the composite material is composed of elasto-plastic constituents, its macroscopic ultimate strength Σ_U and endurance limit Σ_∞, which correspond to plastic and shakedown limit in the RVE scale, can be studied by incorporating homogenization techniques with direct methods. As formulated by Magoariec et al. [32], when the shakedown state is attained in the micro scale, stress field pertained to the reference elastic body $\mathscr{B}^E$, $\boldsymbol{\sigma}^e$, and the time invariant residual stress field $\bar{\boldsymbol{\rho}}$ are required to satisfy following conditions

$$\boldsymbol{\sigma}^e : \begin{cases} \boldsymbol{\nabla} \cdot \boldsymbol{\sigma}^e = 0 & \text{in } \Omega, \\ \boldsymbol{\sigma}^e = \mathbb{C} : (\boldsymbol{E} + \boldsymbol{\varepsilon}^*) & \text{in } \Omega, \\ \boldsymbol{\sigma}^e \cdot \boldsymbol{n} & \text{anti-periodic on } \partial\Omega, \\ \boldsymbol{u}^* & \text{periodic on } \partial\Omega, \\ \langle \boldsymbol{\varepsilon} \rangle = \boldsymbol{E}. \end{cases} \tag{6}$$

$$\bar{\boldsymbol{\rho}} : \begin{cases} \boldsymbol{\nabla} \cdot \bar{\boldsymbol{\rho}} = 0 \text{ in } \Omega, \\ \bar{\boldsymbol{\rho}} \cdot \boldsymbol{n} \quad \text{anti-periodic on } \partial\Omega. \end{cases} \tag{7}$$

Here, Ω indicates the RVE domain, $\partial\Omega$ the surface, $\boldsymbol{n}$ the outer normal, and $\boldsymbol{u}^*$ the fluctuation part of the displacement corresponds to $\boldsymbol{\varepsilon}^*$.

Although shakedown problem in the RVE scale can be studied by either strain or stress approach [32], in present study we consider exclusively the stress approach. For stress approach the load prescribed on RVE is the macroscopic stress $\boldsymbol{\Sigma}$. Because the material to be studied is non-periodic, a small specification is made on conditions (6) and (7), where, instead of enforcing the node-wise anti-periodicity of the residual stresses and periodicity of the fluctuating displacement, we apply the statically uniform boundary conditions (SUBC) on the purely elastic reference RVE. As a consequence, the shakedown problem yields $\bar{\boldsymbol{\rho}} \cdot \boldsymbol{n} = \boldsymbol{0}$ on $\partial\Omega$ and one can prove that, in the absence of the body force $\langle \bar{\boldsymbol{\rho}} \rangle = \boldsymbol{0}$, so $\bar{\boldsymbol{\rho}}$ does not contribute to the macroscopic stress.

By discretizing the physical fields in (6) and (7) by means of the FE formulations, the application of the static theorem to RVEs composed of elastic perfectly plastic materials leads to following optimization problem

$$\begin{aligned} &\underset{\bar{\boldsymbol{\rho}}, \alpha}{\text{minimize}} \; -\alpha \\ &\text{subject to} \sum_{i=1}^{NG} \boldsymbol{C}_i \, \bar{\boldsymbol{\rho}}_i = \boldsymbol{0} \, , \\ &\qquad F(\alpha \boldsymbol{\sigma}^e_{ik} + \bar{\boldsymbol{\rho}}_i) - \sigma^2_{Y\,i} \leq 0 \\ &\qquad \forall i \in [1, NG] \, ; k \in [1, NV] \, . \end{aligned} \tag{8}$$

Here, α is referred to as the load factor, $\boldsymbol{C}$ the equilibrium matrix, $\bar{\boldsymbol{\rho}}_i$ the stress tensor associated with the i*th* Gaussian point, $\boldsymbol{\sigma}^e_{ik}$ the abbreviation of $\boldsymbol{\sigma}^e_i(\boldsymbol{P}_k)$ which means the $\boldsymbol{\sigma}^e$ at Gaussian point i and load vertex k, σ_Y the yield strength, F the yield function, NG the number of Gaussian points, and NV the number of vertices. Both phases were assumed to obey the von Mises yield condition. Meanwhile, it is worthy to note that, although in few studies, e.g. [33], it is suggested to replace the yield strength by fatigue limit of the material to meet with the safety requirement, the present study still sticks with the convention adopted in most existing works, such as [10, 34], in which initial yield strength of the material is used. This choice is made since there is no available data on the fatigue test of the binder cobalt alloy. Solving (8) yields the load capacity of the RVE, and depending on if $k = 1$ or $k > 1$ the calculated strength

corresponds to either plastic limit or endurance limit. In the present study, the load scenario considered is restricted to non-reversed uniaxial stress, in this case $NV = 2$ and $\boldsymbol{\sigma}_{ik}^{e} = 0$ for all $k = 2$.

For RVE models considered in the present study, (8) turns out to be a large scale optimization problem. In order to solve such a problem within a reasonable time, it requires the problem to be carefully formulated and submitted to powerful optimization algorithm. Several studies, e.g. [35, 36], acknowledged that by replacing the original inequality constraints by Euclidean ball constraints, the sparsity of the Karush-Kuhn-Tucker (KKT) system can be better exploited and thus the problem can be solved more efficiently. This conclusion is approved by our own observations. For this reason, the recommended reformulation is applied to all optimization problems evaluated in the present study. The specific workflow to reformulate (8) can refer to [35].

After reformulation, the static problem can be viewed as a typical SOCP problem with $n_i = 5$, and therefore it can be handled by commercial optimization solvers such as Gurobi [37], CPLEX [38], MOSEK [39], among others. In our previous studies [1, 2], we proposed to solve (8) by the general purpose interior-point method solver IPOPT [40, 41]. Compared to listed commercial SOCP solvers, the advantage of IPOPT is that it can handle a large variety of nonlinear optimization problems. However, the price paid to achieve such a generality is that, when IPOPT is not carefully customized to the problem, its efficiency on solving particular typed problems, such as SOCP, is inferior to the listed commercial solvers. In order to find a solver that, besides rendering an accurate solution, also demonstrates an excellent numerical efficiency, in the present study we compared results from two selected solvers: the general purpose solver IPOPT and the SOCP solver Gurobi; after confirming that the discrepancy between results obtained from two solvers is negligible, the SOCP solver Gurobi is adopted for solving optimization problems originating from PRMMC samples due to its outstanding efficiency (Details see this chapter).

3 Statistical Models for the Interpretation of Numerical Results

Since we propose to predict the global material behavior from SERVE samples, the study of the size effect is also based on rigorous statistical methods. In the present study, we consider an RVE size to be sufficient if it results in effective behaviors that are statistically equivalent to their counterparts predicted from larger RVEs. Here, statistical equivalent is reflected from two aspects: the statistical characteristics of one effective behavior and the correlation between different effective behaviors. These two conditions were checked by statistical models presented in the present section.

In order to check if the statistical characteristics of one effective behavior is size independent, its mean value $\bar{x}$ and the standard deviation s were compared to

quantities derived from RVEs of a greater size. Next to that, hypothesis tests were applied to examine if effective behaviors predicted from the current size and a larger size can be regarded as belonging to the same statistics. To this end, two hypothesis tests, namely the Kolmogorov-Smirnov test (K-S test) and Wilcoxon rank sum test (rank sum test), were employed. K-S test examines if two samples X and Y are from the same continuous distribution. Null and alternative hypotheses of this test are

$$H_0 : \text{Two samples are from the same continuous distribution}$$
$$H_a : \text{Two samples are from the distinctive continuous distribution}$$

The decision of a two samples K-S test is made based on the distance between the empirical distribution functions of two samples, where the empirical distribution function indicates the cumulative distribution function of a sample that jumps up by $1/n$ at each of the n data points. The rank sum test, on the other hand, can be seen as a nonparametric equivalent to t-test which does not require the data to be subjected to the normal distribution. Null and alternative hypotheses of rank sum test are

$$H_0 : \text{Two samples are from continuous distributions with equal medians}$$
$$H_a : \text{Two samples are not from continuous distributions with equal medians}$$

In addition to the hypothesis test, we also study if the relationship between different effective behaviors, e.g. the relationship between the effective Young's modulus $\bar{E}$ and the global endurance limit Σ_∞, changes if the size of RVE increases. To this end, the Pearsons correlation coefficient r from two random variables X and Y defined as follows is evaluated

$$r_{XY} = \frac{\sum_{i=1}^{N}(X_i - \bar{X})(Y_i - \bar{Y})}{\sqrt{\sum_{i=1}^{N}(X_i - \bar{X})^2}\sqrt{\sum_{i=1}^{N}(Y_i - \bar{Y})^2}} . \tag{9}$$

Here $\bar{X}$ and $\bar{Y}$ are mean values of the statistics X and Y, respectively. When more than two random variables are considered, matrix of correlation plots is a convenient way to present the data. In such matrix, the correlation between every two random variables (X_i, Y_j) is plotted as a component of the matrix, and the histogram of an individual variable is plotted in the diagonal. Matrix correlation plot is employed as a main tool for data presentation in the present study.

4 Comparison Between Optimization Solvers

Before investigating the size effect on the strength prediction for PRMMC samples, a comparative study was performed on a benchmark model to check if results from the general purpose nonlinear optimization solver IPOPT and the SOCP solver Gurobi

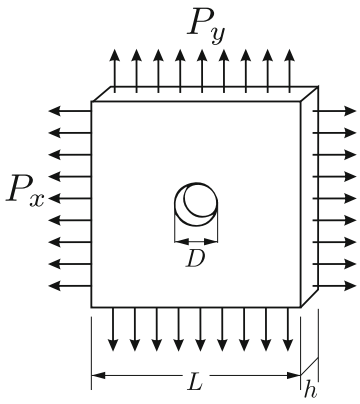

Fig. 1 Geometry of the plate with a hole model

Table 1 Dimensions of the benchmark model

Length L (mm)	Diameter D (mm)	Thickness h (mm)	D/L
100	20	2	0.2

Table 2 Material properties of the benchmark model

	E (GPa)	ν (−)	σ_Y (MPa)
Steel	210	0.3	280

are consistent. The benchmark model chosen for the comparative study is the classic plate with a hole model that has been studied in abundant direct method literature, c.f. [42–44]. The geometry of the model is shown in Fig. 1 with the dimensions given in Table 1. We study the strength of the structure submitted to two distributed pressures P_x and P_y. By considering P_x and P_y as basic loads $\hat{P}_1$ and $\hat{P}_2$, a vertex in the load space spanned by $\hat{P}_1$ and $\hat{P}_2$ can be uniquely defined as $(\cos\theta, \sin\theta)$ by introducing an angle θ. This way, the load factor α under different combinations of two loads can be calculated by varying the magnitude of θ. Due to the symmetry of the geometry and loads, the finite element model contains only $1/4$ of the geometry. The model adopts eight node linear solid elements and material properties outlined in Table 2. In order to be consistent with existing literature, the material is considered in this numerical study as an elastic-perfect plastic material.

To evaluate the limit and shakedown load of the given model, first the geometry and the FE mesh were built in the commercial FE software ABAQUS [45] for calculating the elastic stress $\boldsymbol{\sigma}^e$. In this calculation, the magnitude of both basic loads were fixed to 100 MPa. The model configuration and the von Mises stress of $\boldsymbol{\sigma}^e$ can be seen in Fig. 2.

After $\boldsymbol{\sigma}^e$ was calculated, the information of the finite element model and the elastic stresses were output to Matlab [46]. In Matlab the formulation of the shakedown

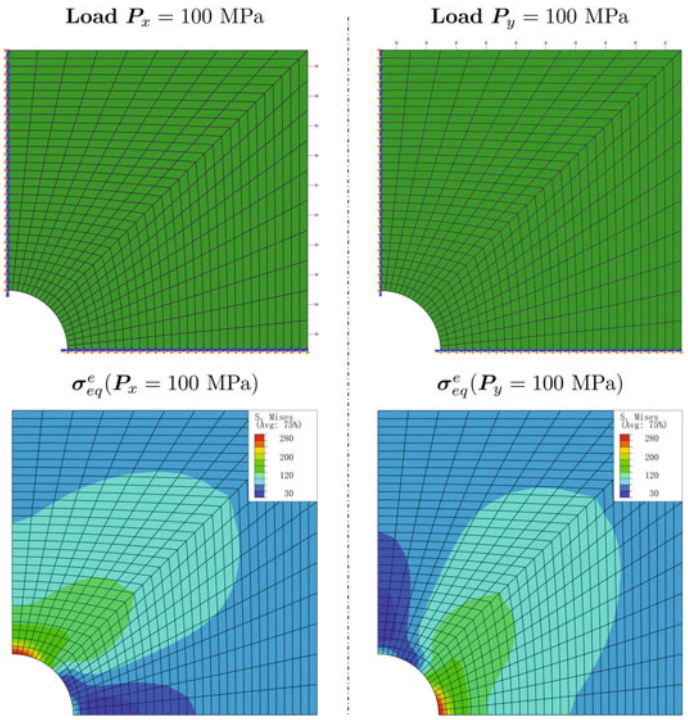

Fig. 2 Elastic stresses of the plate with a hole model

problem (8) is realized through an in-house Matlab finite element code. Using the information passed by the commercial finite element software, the matrices involved in the objective function and constraints were first evaluated on the element level and then assembled into global matrices in sparse forms. The form of the shakedown problem eventually used for the computation was customized to the solver. When IPOPT is used as the solver, Jacobian and Hessian matrices used to assemble the reduced Karush-Kuhn-Tucker (KKT) system were calculated. Based on the Jacobian and Hessian matrices provided, IPOPT finds the optimal solution to a series of barrier problems following the steps outlined in [41]. When commercial solver Gurobi is used, the effort for evaluating Jacobian and Hessian matrices can be reduced, and the difficulties lie in finding an appropriate scaling factor and an optimal set of solver parameters which prevent the solver from slow convergence near the optimum. In the present study, the linear system corresponding to the equality constraints was scaled so that the entries in it are in the same order.

Before the shakedown problem pertained to the benchmark model was calculated by two solvers, we first compared results of IPOPT adopting original formulation (8) and the reformulated one. We noticed that, although original form demands more time to compute, results derived from both forms are identical (discrepancy between results is less than 0.001%). Next we fixed to the reformulated form and compared

Table 3 Comparison of load factor α determined by two optimization solvers (Gurobi and IPOPT)

θ [rad]	α^{1P}(GUR)	α^{1P}(IPO)	||Err.||%	α^{2P}(GUR)	α^{2P}(IPO)	||Err.||%
0	2.259	2.259	0.0	1.847	1.847	0.0
$\pi/18$	2.446	2.446	0.0	2.007	2.006	0.1
$\pi/9$	2.686	2.686	0.0	2.267	2.267	0.0
$\pi/6$	2.976	2.976	0.0	2.684	2.684	0.0
$2\pi/9$	3.356	3.356	0.0	3.484	3.485	0.0
$5\pi/18$	3.356	3.356	0.0	3.484	3.488	0.1
$1\pi/3$	2.976	2.976	0.0	2.684	2.684	0.0
$7\pi/18$	2.685	2.687	0.1	2.272	2.269	0.1
$4\pi/9$	2.446	2.446	0.0	2.007	2.007	0.0
$\pi/2$	2.259	2.259	0.0	1.847	1.847	0.0

results of two solvers. Result of the comparative study can be seen in Table 3. In this table, abbreviation "GUR" indicates the solver Gurobi, and "IPO" the solver IPOPT. Superscript 1P means only one load vertex is considered, and this corresponds to the limit analysis. In contrast to that, the superscript 2P indicates that load P_x and P_y are enforced to vary proportionately. Table 3 shows that, although the discrepancy is slightly increased, the error is still tolerable and with the maximum value around 0.1%. This way, we confirmed that the problem can be handled by both IPOPT and Gurobi. In the present study, most configuration parameters in IPOPT use the default values, and in this circumstance the time it costs for IPOPT to solve this problem is about 10 times compared to the Gurobi. For this reason, Gurobi was used to solve the shakedown problems pertained to RVE models, while IPOPT was used only occasionally to cross-validate the results of IPOPT on selected models.

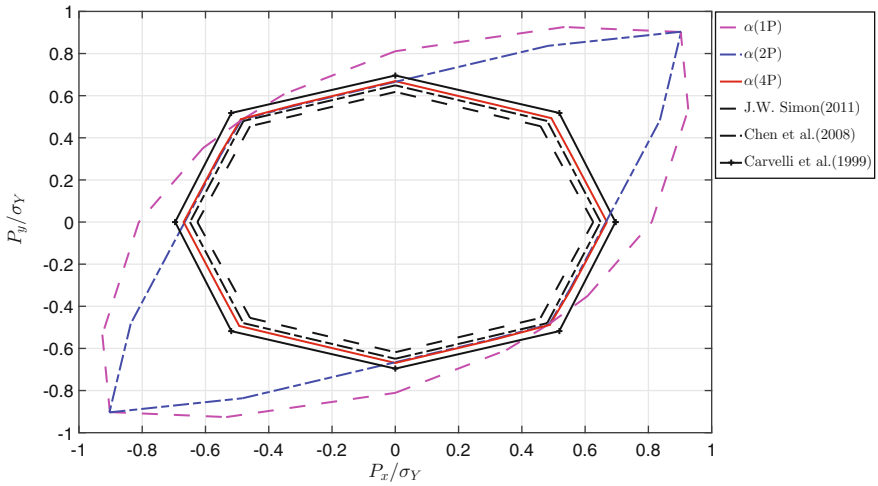

Fig. 3 Feasible load domains of the plate with a hole model

Next, we compared our own results to literature in Fig. 3. Because results from IPOPT and Gurobi are almost identical, the discrepancy between them is neglected; in the following the result is presented indiscriminately as α. Results in Fig. 3 were obtained by shakedown analyses considering one vertex (limit load), two vertices (proportionally varied tow loads) and four vertices (independently varied two loads). Results from our own calculation are found to be in line with results in [42–44]. For this reason, we confirmed the validity of our numerical formulation.

5 Numerical Study of PRMMC Samples

The numerical study of the representative PRMMC material, WC-Co 20 Wt.%, is based on 1,500 RVE models. The models fall into three sample groups, each group consists of 500 samples. The samples were modeled from artificial morphologies generated by a simple random sequential adsorption (RSA) algorithm as shown in Fig. 4. The algorithm is developed in Matlab on the matrix basis. According to this algorithm, the RVE domain is initialized as a zero matrix and the program continuously projects prism shaped geometry into this matrix. After each projection, zero elements in the matrix are set to one if they belong to the prism domain and remain zero otherwise. The value of elements will not be reset if they have already been picked in previous iterations. Parameters controlling the projection, such as prism

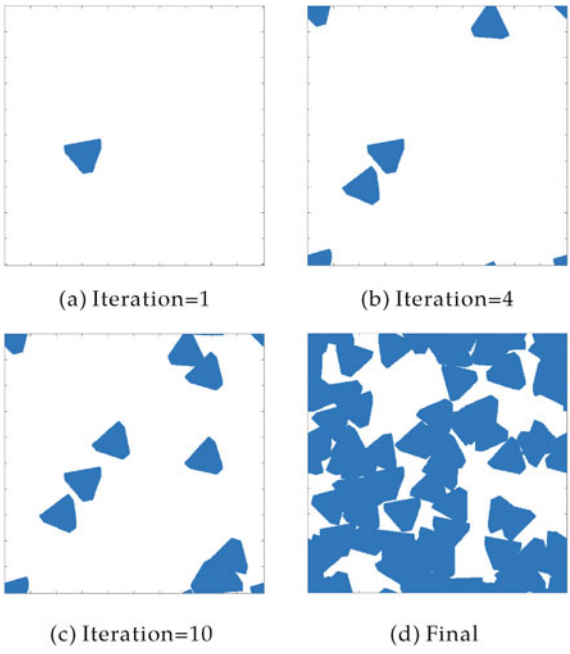

Fig. 4 Inclusion process with fixed grain size

size, rotation angle, and center of the projection, are all random numbers. In order to be consistent with real WC-Co microstructures, the algorithm adopts a configuration that the diameter of WC grains, d_{WC}, obeys a normal distribution with mean value 3 μm and standard deviation 0.8 μm. The position where each particle locates is independent from the others and therefore there is no predefined clustering. Due to the high carbide content of the material, before a new grain is to be projected, it is very likely that the corresponding RVE domain is already partially assigned to other grains. When this happens, the algorithm will neither reject the projection of the new grain nor record the overlapping information such as the grain boundaries. The new grain is simply projected and merged with the old ones to form a unity. Although there are many obvious advantages to introduce grain boundaries to the model, due to the numerical difficulty and tremendous computational cost it requires, the data may become too expensive and thus statistical analysis becomes impossible. For this reason, the simplest idealization is adopted and the overlapping problem between grains is not explicitly accounted for. The projection stops when binder contents reach a certain threshold. Based on the image analyses of 50 SEM images obtained from WC-20 Wt.% Co, we noticed that the volume percent of the binder phase, Co Vol.%, follows a normal distribution featured by the mean value 37.5 and the standard deviation 2.7. This distribution was adopted as the termination criterion for generating artificial RVE samples that represent the material. The finite element models were built in commercial FE solver ABAQUS and meshed by a uniform mesh configuration: the element type is fixed to linear wedge elements (C3D6); elements covering non-critical regions were assigned with a global size of 0.8 μm; while elements near the phase boundaries are of a finer density with an edge size of 0.2 μm. Under this configuration, the number of elements for an RVE sample having a size 40–40–1 μm varies between 15,000 and 20,000. The reason of using a layer of 3D wedge elements instead of 2D elements to represent the composite structure is that the results of direct method predicted from the former element type demonstrate significantly less mesh dependency. More detailed discussion on this issue can be found in [2].

The sample groups used to study the size effect were numbered successively as Group 1, 2 and 3, the parameters used for generating the models in these groups are detailed in Table 4. The RVEs in three groups differ only in their size: Samples in Group 1 have a size of 30–30–1 μm, while in Group 2 a greater size 40–40–1 μm, and in Group 3 the greatest size 80–80–1 μm. In order to provide an intuitive insight about the models, we randomly picked one sample from each group and compared the microstructures in Fig. 5. The binder content in three groups is slightly different—this can be interpreted as a consequence of converting microstructures to finite element mesh. The mesh pattern adopted for all three groups are identical and, in consequence, FE models in different groups have very different number of nodes and elements (Fig. 5). The load type used for calculating the strength were uniformly fixed to SUBC. According to this boundary condition configuration, nodes lying on the RVE surfaces were prescribed with nodal forces corresponding to the global stress, and their degrees of freedoms are not restrained so that they can deform freely. Materials of both phases are considered as elastic perfect plastic materials with para-

Table 4 Description of sample groups

	Num.RVEs	Wt./Vol.% Co	Length (μm)	Type	Particle size (μm)
Group 1	500	20/N(37.2, 2.7)	30	Artificial	$d_{WC} \sim N(3.0, 0.8)$
Group 2	500	20/N(37.3, 2.9)	40	Artificial	$d_{WC} \sim N(3.0, 0.8)$
Group 3	500	20/N(37.5, 2.8)	80	Artificial	$d_{WC} \sim N(3.0, 0.8)$

(*Num.RVEs* number of RVE samples, $x \sim N(\mu, s)$: random variable x obeys a normal distribution characterized by the mean value μ and the standard deviation s)

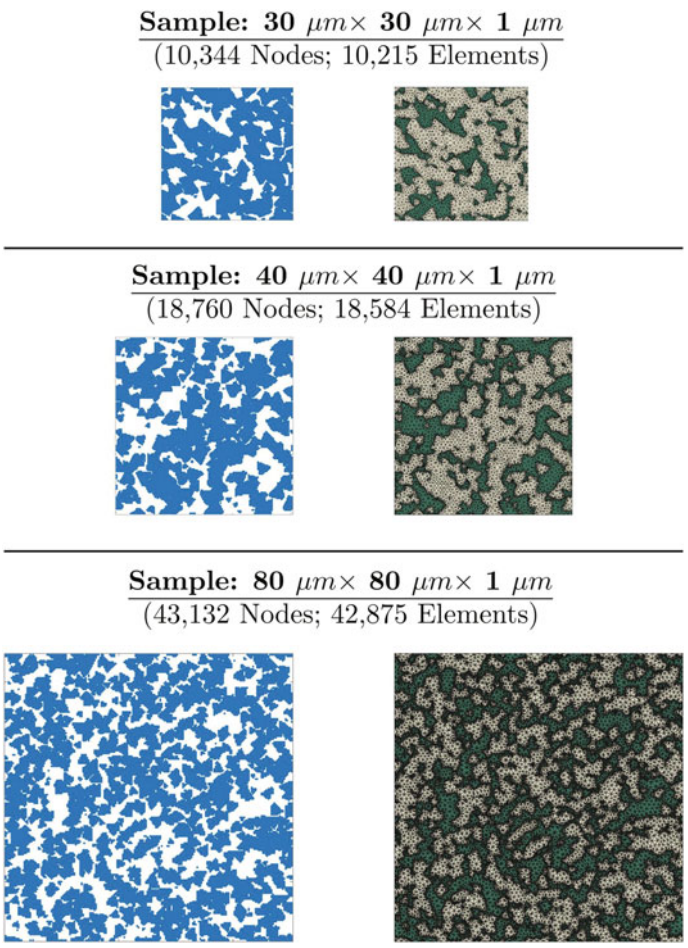

Fig. 5 RVE samples of WC-20 Wt.% Co with $d_{WC} \sim N(3.0, 0.8\,\mu\text{m})$ in different sizes

Table 5 Material properties of both phases

	E (GPa)	ν (−)	σ_Y (MPa)
WC	700	0.24	2000
Co	210	0.30	683

meters given in Table 5. In the present study, we investigate only the strength of the composite material subjected to the uniaxial tensile load: For each RVE, it's ultimate strength Σ_U derived by solving the optimization problem (8) with $NV = 1$ and endurance limit Σ_∞, which corresponds to the case $NV = 2$, were calculated on both x and y directions, and the average was considered as the effective property of the sample. In order to emphasize the strengthening effect of the reinforcement phase, the strength of an RVE was presented after normalized with respect to the yield strength of the binder phase σ_Y^{Co}. The anisotropy ratio of a predicted effective behavior x defined as

$$\zeta_x = \max(x_1/x_2, x_2/x_1) \tag{10}$$

which measures the dissimilarity of a predicted effective behavior in two normal directions was evaluated for selected macroscopic properties and considered as an important indicator for evaluating the sufficiency of the RVE size. One necessary condition for an RVE size to be sufficient is that ζ_x predicted from this size should be close to one.

We evaluated several key effective material parameters and their associated statistical descriptors (Table 6). Unlike most numerical studies of this kind, in Table 6 we did not observe a manifest trend where scatter of data reduces when RVE size increases. This phenomenon implies that, for predicting certain material parameters, e.g. $\bar{E}$, a small RVE size may suffice and renders unbiased prediction. Moreover, in a statistical sense, RVE samples become more isotropic when its size becomes larger. The degree of anisotropy reflected by the magnitude of ζ depends on the effective behavior of interests. Roughly speaking, ζ indicates the level how interactive local-

Table 6 Material parameters predicted from RVE samples having different sizes

	30μm (Group 1)		40μm (Group 2)		80μm (Group 3)	
	$\bar{x}$	s	$\bar{x}$	s	$\bar{x}$	s
WC Vol.% [-]	62.81	2.74	62.74	2.84	62.46	2.82
$\bar{E}$ [MPa]	4.41E+05	1.48E+04	4.40E+05	1.53E+04	4.41E+05	1.48E+04
$\bar{\nu}$ [-]	0.277	0.0039	0.278	0.0034	0.277	0.0030
Σ_U/σ_Y^{Co} [-]	1.851	0.097	1.836	0.101	1.867	0.094
$\Sigma_\infty/\sigma_Y^{Co}$ [-]	1.483	0.0798	1.433	0.0750	1.441	0.0602
$\zeta_{\bar{E}}$	1.012	0.008	1.007	0.006	1.004	0.003
ζ_{Σ_U}	1.066	0.11	1.052	0.074	1.048	0.066
ζ_{Σ_∞}	1.100	0.083	1.098	0.077	1.072	0.058

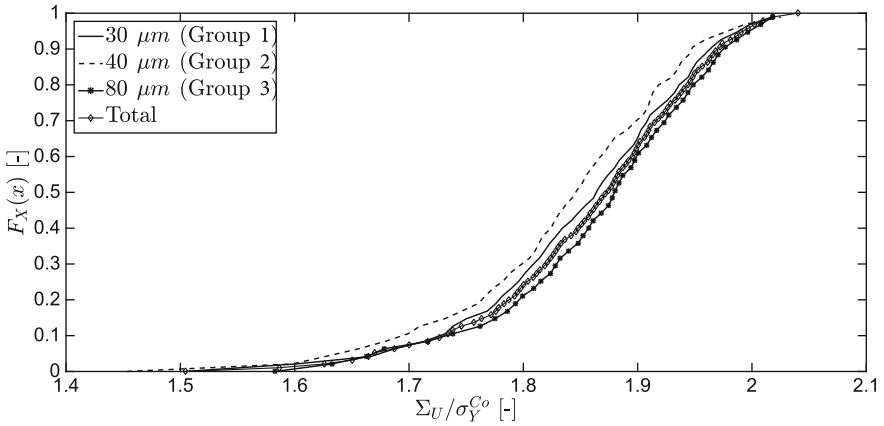

Fig. 6 Cumulative distribution functions of Σ_U for RVEs of different sizes

ized behavior within a RVE body average and set-off. In this vein, comparing three parameters illustrated in Table 6, i.e. $\zeta_{\bar{E}}$, ζ_{Σ_U}, and ζ_{Σ_∞}, it is clear that localized behavior has greatest influence over Σ_∞, and RVEs are required to be exceptionally large to smear out these effects.

Beside presenting results by means of statistical indicators, cumulative distribution function of Σ_U and Σ_∞ are compared in Figs. 6 and 7, respectively. Function diagrams in these figures demonstrate a greater difference among sample groups compared to Table 6. In order to understand quantitatively how similar these results are, we performed hypothesis tests on subsets randomly sampled from the existing data. In this case study, 50 RVEs were randomly picked from each sample group, and every two of them were submitted to K-S test and rank sum test with a significance

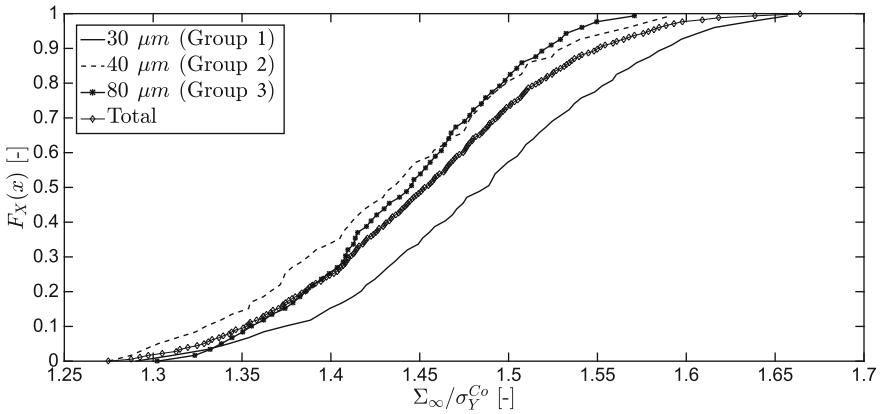

Fig. 7 Cumulative distribution functions of Σ_∞ for RVEs of different sizes

Table 7 Hypothesis tests on randomly sampled RVEs of different sizes

			Group m vs n					
			1 vs 2	2 vs 3	1 vs 3	1 vs All	2 vs All	3 vs All
$\bar{E}$	K-S Test	H_0%	95.00	94.67	97.67	92.67	93.33	95.67
		p^* [-]	0.759	0.678	0.841	0.528	0.931	0.569
	Rank Sum	H_0%	97.67	97.67	95.00	93.67	94.00	94.33
		p^* [-]	0.641	0.950	0.840	0.701	0.783	0.707
Σ_U	K-S Test	H_0%	91.67	72.67	93.33	88.67	67.67	88.67
		p^* [-]	0.840	0.904	0.845	0.948	0.872	0.687
	Rank Sum	H_0%	96.67	94.67	94.67	96.00	89.00	91.00
		p^* [-]	0.678	0.679	0.759	0.772	0.553	0.772
Σ_∞	K-S Test	H_0%	28.00	94.38	27.00	13.33	92.67	15.33
		p^* [-]	0.990	0.678	0.982	0.991	0.942	0.989
	Rank Sum	H_0%	69.00	88.67	91.33	57.00	81.67	90.33
		p^* [-]	0.780	0.769	0.860	0.997	0.705	0.921

level fixed to 0.05. This sampling process was repeated for 300 times and derived results were recorded in Table 7. In this table, H_0% represents the percentage of tests in which null hypothesis H_0 was not rejected. p^* is calculated from the p value as follows

$$p^* = \max(p, 1 - p) \, . \tag{11}$$

p^* value presented in Table 7 is averaged over 300 tests. The purpose for introducing this variable is to avoid averaging p that arises from different sides, such as 0.01 and 0.99. The letter "all" in the table corresponds to samples picked *indiscriminately* from three sizes. One can see from the table that, compared to $\bar{E}$ and Σ_U, Σ_∞ is more sensitive to size because H_0 is rejected for a greater amount of times. Meanwhile, for more than half of 300 tests applied to 40 µm (Group 2) and 80 µm (Group 3) RVEs, H_0 were favored which confirms the similarity of RVEs in these two sizes.

We evaluated the correlation matrix for all aforementioned sample groups. One can notice from Figs. 8, 9 and 10 that, despite different r values, the fashion in which the considered material parameters are correlated is independent from the size. More specifically, homogenized elastic module $\bar{E}$ is strongly correlated to WC Vol.%, but Σ_U and Σ_∞ are only subtly correlated to WC Vol.%. This suggests that morphology has a more crucial impact to Σ_U and Σ_∞ compared to $\bar{E}$. In addition to that, for all three groups, r between Σ_U and Σ_∞ are quite small, which reveals that the linear correlation between them is quite weak.

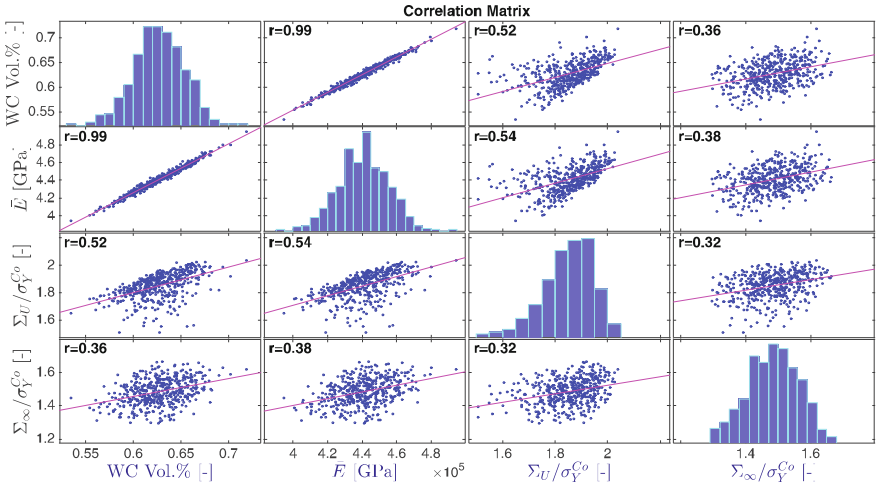

Fig. 8 Correlation matrix evaluated from Group 1 (30–30–1 μm artificial RVEs of WC-20 Wt.% Co, $d_{WC} \sim N(3.0, 0.8)$), r = correlation coefficient

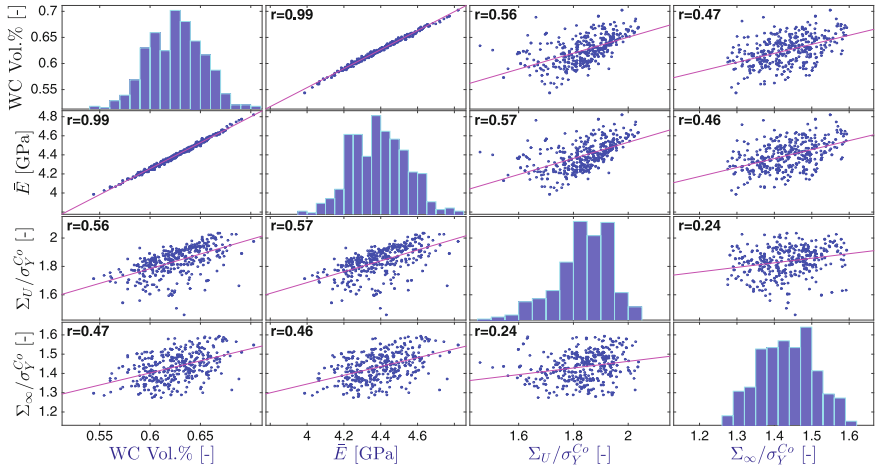

Fig. 9 Correlation matrix evaluated from Group 2 (40–40–1 μm artificial RVEs of WC-20 Wt.% Co, $d_{WC} \sim N(3.0, 0.8)$), r = correlation coefficient

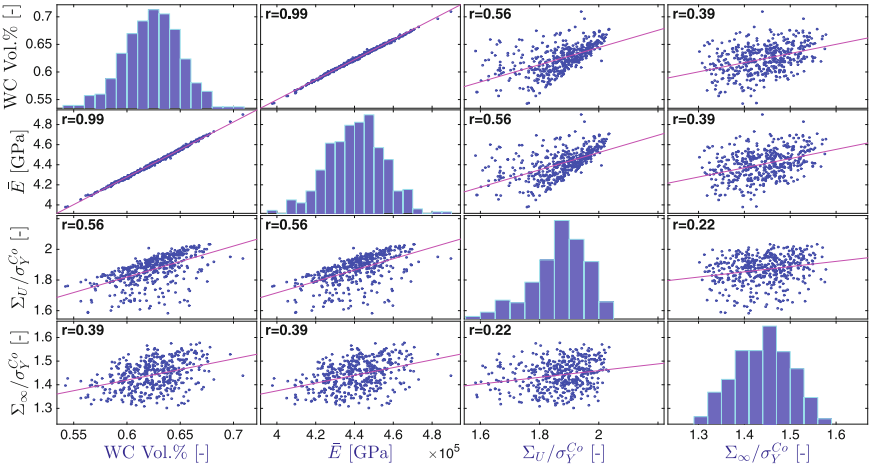

Fig. 10 Correlation matrix evaluated from Group 3 (80–80–1 μm artificial RVEs of WC-20 Wt.% Co, $d_{WC} \sim N(3.0, 0.8)$), r = correlation coefficient

6 Conclusions

In this paper, using an representative material, WC-20 Wt.% Co, it is presented how size of RVE models influences the strength of PRMMC materials predicted from the direct method. On the basis of 500 realizations for each selected RVE size (30, 40 and 80 μm), we performed the shakedown analyses and observed from the result that the global material behavior predicted from different sizes has more commons than dissimilarities in a statistical sense. Also, the correlation between different global material parameters, which is represented by the correlation coefficient r, is independent from the model size. For all concerned material parameters, their mean values are less sensitive to size compared to variances, thus smaller RVEs are sufficient if the task is to predict the mean value of a certain material parameter. The variance of a global material behavior is introduced by both composite structure and the RVE size, where the latter one is undesired and becomes less critical when RVE size exceeds a certain threshold.

On removing the variance caused by RVE size—the so called size effect, a viable solution is proposed in the present paper: One can check the sufficiency of the RVE size through applying hypothesis tests repeatedly on results predicted from one size and a much greater size. If the chance to reject the hypothesis that the data are from the same continuous distribution is small, e.g. less than 10%, then it is justified to conclude that the size effect is expelled and results from two sizes are *statistically equivalent*. According to this criterion, it can be concluded that the size 40–40–1 μm is sufficient for the strength prediction of the current material, because it is statistically equivalent to a much greater size 80–80–1 μm. It is worthy to note that the disadvantage of this method is that it requires a large amount of data as input.

For this reason, the conventional approaches which are based on indicator such as the anisotropy ratio, still have significant practical values and thus should not be abandoned. In addition to that, it is also plausible to overcome the size effect by first taking the size as a random variable for generating RVEs, and then removing its influence by means of advanced statistical learning methods. Although from a theoretical point of view this approach appears to be uncomplicated, in practice it might be challenging to find a capable statistical model to interpret the results.

In our future study, the focus would be put on interpreting the relationship between different effective material behaviors, and the goal is to reveal from a mechanical perspective how do these behaviors are correlate.

References

1. Hachemi A, Chen M, Chen G, Weichert D (2014) Limit state of structures made of heterogeneous materials. Int J Plast 63:124–137
2. Chen G, Ozden UA, Bezold A, Broeckmann C, Weichert D (2015) On the statistical determination of yield strength, ultimate strength, and endurance limit of a particle reinforced metal matrix composite (PRMMC). In: Weichert W, Fuschi P, Pisano AA (eds) Direct methods for limit and shakedown analysis of structures: advanced computational algorithms and material modelling. Springer, pp 105–122
3. Miracle DB (2005) Metal matrix composites-from science to technological significance. Compos Sci Technol 65(15–16):2526–2540. 20th Anniversary Special Issue
4. Chawla N, Jones JW, Andres C, Allison JE (1998) Effect of SiC volume fraction and particle size on the fatigue resistance of a 2080 Al/SiC_p composite. Metall Mater Trans A 29(11):2843–2854
5. Li W, Chen ZH, Chen D, Teng J, Li CH (2011) Understanding the influence of particle size on strain versus fatigue life, and fracture behavior of aluminum alloy composites produced by spray deposition. J Mater Sci 46(5):1153–1160
6. Spowart JE, Miracle DB (2003) The influence of reinforcement morphology on the tensile response of 6061/SiC/25p discontinuously-reinforced aluminum. Mat Sci Eng A-struct 357(1–2):111–123
7. Hartmann O, Herrmann K, Biermann H (2004) Fatigue behaviour of al-matrix composites. Adv Eng Mater 6(7):477–485
8. Füssl J, Lackner R (2009) Homogenization of strength: a numerical limit analysis approach. In: Eberhardsteiner J, Hellmich C, Mang HA, Périaux J (eds) ECCOMAS multidisciplinary jubilee symposium. Computational methods in applied sciences, vol 14. Springer, Netherlands, pp 183–201
9. Weichert D, Hachemi A, Schwabe F (1999) Application of shakedown analysis to the plastic design of composites. Arch Appl Mech 69(9–10):623–633
10. You J-H, Kim BY, Miskiewicz M (2009) Shakedown analysis of fibre-reinforced copper matrix composites by direct and incremental approaches. Mech Mater 41(7):857–867
11. Ostoja-Starzewski M (1998) Random field models of heterogeneous materials. Int J Solids Struct 35(19):2429–2455
12. Hill R (1952) The elastic behaviour of a crystalline aggregate. Proc Phys Soc Sect A 65(5):349–354
13. Sab K (1992) On the homogenization and the simulation of random materials. Eur J Mech A solid 11(5):585–607
14. Kanit T, Forest S, Galliet I, Mounoury V, Jeulin D (2003) Determination of the size of the representative volume element for random composites: statistical and numerical approach. Int J Solids Struct 40(13):3647–3679

15. Galli M, Botsis J, Janczak-Rusch J (2008) An elastoplastic three-dimensional homogenization model for particle reinforced composites. Comput Mater Sci 41(3):312–321
16. Drugan WJ, Willis JR (1996) A micromechanics-based nonlocal constitutive equation and estimates of representative volume element size for elastic composites. J Mech Phys Solids 44(4):497–524
17. Gusev AA (1997) Representative volume element size for elastic composites: a numerical study. J Mech Phys Solids 45(9):1449–1459
18. Segurado J, Llorca J (2002) A numerical approximation to the elastic properties of sphere-reinforced composites. J Mech Phys Solids 50(10):2107–2121
19. Huang J, Krabbenhoft K, Lyamin AV (2013) Statistical homogenization of elastic properties of cement paste based on X-ray microtomography images. Int J Solids Struct 50(5):699–709
20. Pelissou C, Baccou J, Monerie Y, Perales F (2009) Determination of the size of the representative volume element for random quasi-brittle composites. Int J Solids Struct 46(14–15):2842–2855
21. Salahouelhadj A, Haddadi H (2010) Estimation of the size of the RVE for isotropic copper polycrystals by using elastic-plastic finite element homogenisation. Comput Mater Sci 48(3):447–455
22. Chen G, Ozden UA, Bezold A, Broeckmann C (2013) A statistics based numerical investigation on the prediction of elasto-plastic behavior of WC-Co hard metal. Comput Mater Sci 80:96–103
23. Torquato S (2002) Random heterogeneous materials: microstructure and macroscopic properties. Springer
24. Trias D, Costa J, Turon A, Hurtado JE (2006) Determination of the critical size of a statistical representative volume element (SRVE) for carbon reinforced polymers. Acta Mater 54(13):3471–3484
25. Kanit T, N'Guyen F, Forest S, Jeulin D, Reed M, Singleton S (2006) Apparent and effective physical properties of heterogeneous materials: representativity of samples of two materials from food industry. Comput Method Appl M 195(33–36):3960–3982
26. Yin XL, Chen W, To A, McVeigh C, Liu WK (2008) Statistical volume element method for predicting microstructure—constitutive property relations. Comput Method Appl M 197(43–44):3516–3529. Stochastic Modeling of Multiscale and Multiphysics Problems
27. Jr LL (2004) Mishnaevsky. Three-dimensional numerical testing of microstructures of particle reinforced composites. Acta Mater 52(14):4177–4188
28. Vaughan TJ, McCarthy CT (2010) A combined experimental-numerical approach for generating statistically equivalent fibre distributions for high strength laminated composite materials. Compos Sci Technol 70(2):291–297
29. Zohdi TI, Wriggers P, Huet C (2001) A method of substructuring large-scale computational micromechanical problems. Comput Method Appl M 190(43–44):5639–5656
30. Özden UA (2015) Finite element simulation of fatigue crack growth in hardmetal. PhD thesis, RWTH Aachen University
31. Melan E (1938) Zur Plastizität des räumlichen Kontinuums. Ing Arch 9(2):116–126
32. Magoariec H, Bourgeois S, Débordes O (2004) Elastic plastic shakedown of 3D periodic heterogeneous media: a direct numerical approach. Int J Plast 20(8):1655–1675
33. Pham DC (2008) On shakedown theory for elastic-plastic materials and extensions. J Mech Phys Solids 56(5):1905–1915
34. Chen HF, Ponter ARS (2005) On the behaviour of a particulate metal matrix composite subjected to cyclic temperature and constant stress. Comput Mater Sci 34(4):425–441
35. Akoa F, Hachemi A, An M, Said LTH, Tao PD (2007) Application of lower bound direct method to engineering structures. J Global Optim 37(4):609–630
36. Simon J-W (2013) Direct evaluation of the limit states of engineering structures exhibiting limited, nonlinear kinematical hardening. Int J Plast 42:141–167
37. Gurobi Optimization Inc. Gurobi optimizer reference manual (2014)
38. CPLEX , IBM ILOG (2009) V12. 1: user's manual for CPLEX. Int Bus Mach Corp

39. Andersen ED, Andersen KD (2000) The Mosek interior point optimizer for linear programming: an implementation of the homogeneous algorithm. In: Frenk H, Roos K, Terlaky T, Zhang SZ (eds) High performance optimization. Applied optimization, vol 33. Springer, US, pp 197–232
40. Wächter A (2002) An interior point algorithm for large-scale nonlinear optimization with applications in process engineering. PhD thesis, Carnegie Mellon University
41. Wächter A, Biegler LT (2006) On the implementation of an interior-point filter line-search algorithm for large-scale nonlinear programming. Math Program 106(1):25–57
42. Carvelli V, Cen ZZ, Liu Y, Maier G (1999) Shakedown analysis of defective pressure vessels by a kinematic approach. Arch Appl Mech 69(9–10):751–764
43. Chen SS, Liu YH, Cen ZZ (2008) Lower bound shakedown analysis by using the element free galerkin method and non-linear programming. Comput Method Appl M 197(45–48):3911–3921
44. Simon J-W, Weichert D (2011) Numerical lower bound shakedown analysis of engineering structures. Comput Method Appl M 200(41):2828–2839
45. ABAQUS (2013) ABAQUS/CAE user's manual: version 6.13. Simulia, Dassault Systémes
46. MATLAB (2014) version 8.4.0 (R2014b). The MathWorks Inc., Natick, Massachusetts

R-adaptivity in Limit Analysis

José J. Muñoz, James Hambleton and Scott W. Sloan

Abstract Direct methods aim to find the maximum load factor that a domain made of a plastic material can sustain before undergoing full collapse. Its analytical solution may be posed as a constrained maximisation problem, which is computationally solved by resorting to appropriate discretisation of the relevant fields such as the stress or velocity fields. The actual discrete solution is though strongly dependent on such discretisation, which is defined by a set of nodes, elements, and the type of interpolation. We here resort to an adaptive strategy that aims to perturb the positions of the nodes in order to improve the solution of the discrete maximisation problem. When the positions of the nodes are taken into account, the optimisation problem becomes highly non-linear. We approximate this problem as two staggered linear problems, one written in terms of the stress variable (lower bound problem) or velocity variables (upper bound problem), and another with respect to the nodal positions. In this manner, we show that for some simple problems, the computed load factor may be further improved while keeping a constant number of elements.

1 Introduction

Direct methods allow engineers and practitioners to compute the ultimate loads and determine collapse mechanisms of structures made of plastic materials. In the last twenty years, robust and efficient optimisation methods, together with appropriate discretisations of the stress and velocity fields have, respectively, allowed for

J.J. Muñoz (✉)
Universitat Politècnica de Catalunya, 08036 Barcelona, Spain
e-mail: j.munoz@upc.edu

J. Hambleton
Department of Civil and Environmental Engineering, Northwestern University
(Previously at University of Newcastle, Newcastle, Australia), Evanston, USA
e-mail: jphambleton@northwestern.edu

S.W. Sloan
University of Newcastle, Newcastle, Australia
e-mail: Scott.Sloan@newcastle.edu.au

O. Barrera et al. (eds.), *Advances in Direct Methods for Materials and Structures*, DOI 10.1007/978-3-319-59810-9_5

effective computing of upper and lower bounds of the load factors. The accuracy of these bounds is very much dependent on the distribution of the elements in the mesh, which should adapt to the sliplines or, more generally, the collapse mechanism.

This dependence of the accuracy of the discrete solution on the mesh has prompted the use of adaptive meshing strategies. Among them, we highlight element subdivision based on error estimates [10], anisotropic strategies according to the velocity field [8], and fan type meshes [8, 11]. These strategies are applied with sequential subdivisions of the element (embedded remeshing) or by redefining an element size field and direction. In this work we propose an alternative strategy: perturbing the location of the nodes, while keeping the number of elements constant and without altering their connectivity. We in fact include the nodal positions as an additional optimisation variable in the standard upper and lower bound formulations in limit analysis. This is a similar idea to the perturbation analysis in upper bound formulations with rigid blocks introduced in [3], which we here extend to more general finite elements formulations in limit analysis [5–7, 10].

This work is related to similar strategies where the nodal positions of the problem at hand are optimised in order to improve the accuracy of the results. This type of analysis has been so far adopted in elasticity [13], elastodynamics [14], analysis of stochastic materials [2] or in biomechanics [4, 9]. We here carry these ideas over to limit analysis. Instead of moving the nodes as a function of an error estimate, however, we make use of the optimisation problem in order to improve the discrete solution.

In Sect. 2 we revise the discrete solutions of the lower and upper bound problems in limit analysis. In Sect. 3 we present the extension of the previous problems for R-adaptivity. Although we have only implemented R-adaptivity for the lower bound problem, we describe the form of the upper bound solution for completeness. In Sect. 4 we apply the methodology to the vertical cut problem in order to test its efficiency, and Sect. 5 gives some final remarks.

2 Preliminaries

In this work we will restrict our attention to perfectly plastic materials whose yield criterion can be transformed as a second-order cone (SOC). In this case, upper and lower bound solutions may be written as a second-order conic programming (SOCP problem) that has the following general form,

$$\begin{aligned} \textbf{Primal}: \quad \lambda^* = \max_{\lambda,\boldsymbol{\sigma}} \ & \lambda \\ s.t. \ & \mathbf{X}\boldsymbol{\sigma} + \lambda \mathbf{f} = \mathbf{b} \\ & \boldsymbol{\sigma} \in \mathscr{K} \end{aligned} \tag{1}$$

Here, the global vector $\boldsymbol{\sigma}$ denotes stress variables, which have been conveniently transformed in order to write the yield criterion in the form $\boldsymbol{\sigma} \in \mathscr{K}$, with $\mathscr{K}$ a

second-order cone. The variable λ is the load factor, which is maximised in order to compute the ultimate load of the problem at hand.

Matrix $\mathbf{X}$ and vectors $\mathbf{f}$ and $\mathbf{b}$ depend on the discretisation of the domain, that is, on the nodal positions $\mathbf{x}$ and the triangulation $\mathscr{T}$ employed. If these are considered fixed, as it is usually the case, the problem in (1) is convex. The lower and upper formulations of limit analysis require different forms of matrix $\mathbf{X}$ and vectors $\mathbf{f}$ and $\mathbf{b}$, which may be found elsewhere [5–7, 10].

The problem in (1) is the standard form used for the lower bound (LB) limit analysis. The upper bound (UB) problem is generally written in the dual form of this problem, which physically corresponds to minimisation of the power dissipation. It will become convenient to derive next this dual form.

The Lagrangian function of the problem in (1) reads [1]:

$$\mathscr{L}(\boldsymbol{\sigma}, \lambda; \mathbf{v}, \boldsymbol{\omega}) = \lambda + \mathbf{v}^T(\mathbf{b} - \mathbf{X}\boldsymbol{\sigma} - \lambda\mathbf{f}) - \boldsymbol{\omega}^T\boldsymbol{\sigma} \tag{2}$$

The optimal value λ^* may be then obtained as

$$\lambda^* = \max_{\boldsymbol{\sigma},\lambda} \min_{\boldsymbol{\omega}\in\mathscr{K}^*,\mathbf{v}} \mathscr{L}(\boldsymbol{\sigma}, \lambda; \mathbf{v}, \boldsymbol{\omega}) = \min_{\boldsymbol{\omega}\in\mathscr{K}^*,\mathbf{v}} \max_{\boldsymbol{\sigma},\lambda} \mathscr{L}(\boldsymbol{\sigma}, \lambda; \mathbf{v}, \boldsymbol{\omega}) \tag{3}$$

where the second equality holds due to strong duality. The dual set $\mathscr{S}^*$ of a cone $\mathscr{S}$ is defined as [1],

$$\mathscr{S}^* = \{\boldsymbol{\omega} | \boldsymbol{\omega}^T\boldsymbol{\sigma} \geq 0 \; \forall \boldsymbol{\sigma} \in \mathscr{S}\}$$

and for the second-order cone $\mathscr{K}$, it can be proved that $\mathscr{K}^* = \mathscr{K}$. The primal and dual problems are then obtained by keeping the maximisation or the minimisation at the left and right side of the second equality respectively. More explicitly, the primal problem in (1) may be deduced by taking derivatives of the Lagrangian with respect to the dual variables $(\mathbf{v}, \boldsymbol{\omega})$, while the dual form of the optimisation problem is obtained by taking derivatives of the Lagrangian with respect to the primal variables $(\mathbf{x}, \lambda)$, which results in,

$$\begin{aligned} \textbf{Dual}: \quad \lambda^* = \min_{\mathbf{v}} \; & \mathbf{b}^T\mathbf{v} \\ s.t. \; & \mathbf{f}^T\mathbf{v} = 1 \\ & -\mathbf{X}^T\mathbf{v} \in \mathscr{K}^* \end{aligned} \tag{4}$$

In the previous equations, the fields $\boldsymbol{\sigma}$, $\boldsymbol{\omega}$ and $\boldsymbol{v}$ have infinite dimensions. In practice though these fields are interpolated, and depending on the interpolation used, the approximated discrete problem may yield upper, lower or non-strict estimates of the load factor. We do not detail here these interpolations which may be found elsewhere [6, 8, 10]. In our examples, we will use for the lower bound a piecewise linear stress field, which is discontinuous at the element edges, and that yields strict lower bound solutions [10], and a piecewise linear velocity field discontinuous at the element edges, which furnishes a strict upper bound solution [11, 12].

3 R-adaptivity

The previous lower and upper bound problems are usually implemented by appropriately discretising the stress variable $\boldsymbol{\sigma}$ in the primal problem in (1), or by discretising the velocity field $\boldsymbol{v}$ in the dual problem in (4).

We will here present an extension of these problems that includes the nodal positions as additional variables in order to further improve the load factor estimate. Due to the non-linearity of the resulting problem and lack of convexity, the extended problem may not have a unique solution, and the bounds may not be strict. For this reason, the Lagrangian function is linearised at previous solutions.

Since the load factor must be either increased or decreased in the lower or upper bound solution, respectively, the new position variables will be either primal or dual variables in the extended problem. Although we have here implemented the lower bound extension, we present the forms of the lower and upper bound solutions for completeness.

3.1 Lower Bound Problem

We aim to further increase the optimal value of λ by varying the nodal positions $\mathbf{x}$. This corresponds to adding a further maximisation in (3), which now reads,

$$\lambda^{LB} = \max_{\mathbf{x}} \max_{\boldsymbol{\sigma},\lambda} \min_{\boldsymbol{\omega}\in\mathscr{K}^*,\mathbf{v}} \mathscr{L}(\boldsymbol{\sigma},\lambda,\mathbf{x};\mathbf{v},\boldsymbol{\omega})$$

From this expression, the following primal problem is proposed,

$$\begin{aligned} \lambda^{LB} = \max_{\mathbf{x},\lambda,\boldsymbol{\sigma}} \ & \lambda \\ s.t. \ & \mathbf{X}\boldsymbol{\sigma} + \lambda\mathbf{f} = \mathbf{b} \\ & \boldsymbol{\sigma} \in \mathscr{K}\,. \end{aligned} \tag{5}$$

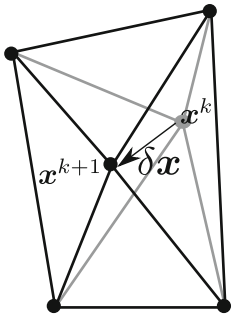

Fig. 1 Scheme of the perturbation on nodal positions. Initial nodal coordinate: $\mathbf{x}^k$. Perturbed nodal coordinate: $\mathbf{x}^{k+1} = \mathbf{x}^k + \delta\mathbf{x}$

It can be observed that the equality constraints above have become non-linear on the variables $\boldsymbol{\sigma}$ and $\mathbf{x}$, so that the optimisation problem is not a SOCP anymore. However, given a (non-optimal) set of primal-dual variables $(\lambda_k, \boldsymbol{\sigma}_k, \mathbf{x}_k; \mathbf{v}_k, \boldsymbol{\omega}_k)$, the Lagrangian may be linearised as follows:

$$\mathscr{L}(\boldsymbol{\sigma}, \lambda, \mathbf{x}; \mathbf{v}, \boldsymbol{\omega}) \approx \lambda + \mathbf{v}^T(\mathbf{b} - \mathbf{X}_k\boldsymbol{\sigma} - \lambda\mathbf{f}_k) - \boldsymbol{\omega}^T\boldsymbol{\sigma} - \mathbf{v}^T\left(\frac{\partial \mathbf{X}_k}{\partial \mathbf{x}}\boldsymbol{\sigma}_k + \frac{\partial \mathbf{f}_k}{\partial \mathbf{x}}\lambda_k\right)\delta\mathbf{x} \quad (6)$$

with $\delta\mathbf{x} = \mathbf{x} - \mathbf{x}_k$, and $\mathbf{X}_k$ denotes matrix $\mathbf{X}$ evaluated at the nodal positions $\mathbf{x}_k$. The approximated Lagrangian gives rise to the following primal problem:

$$\begin{aligned} \textbf{Primal(LB)} - \delta: \quad \lambda^{LB} = \max_{\delta\mathbf{x}, \lambda, \boldsymbol{\sigma}} \ & \lambda \\ s.t.\ & \mathbf{X}_k\boldsymbol{\sigma} + \left(\frac{\partial \mathbf{X}_k}{\partial \mathbf{x}}\boldsymbol{\sigma}_k + \frac{\partial \mathbf{f}_k}{\partial \mathbf{x}}\lambda_k\right)\delta\mathbf{x} + \lambda\mathbf{f} = \mathbf{b} \\ & \boldsymbol{\sigma} \in \mathscr{K}, ||\delta\mathbf{x}|| \leq \boldsymbol{\epsilon} \end{aligned} \quad (7)$$

This problem has only linear and second-order constraints, and is thus a SOCP. We have added the constraint $||\delta\mathbf{x}|| \leq \boldsymbol{\epsilon}$ in order to limit the amount of nodal perturbation $\delta\mathbf{x}$, and therefore avoid elements that are too distorted or posses negative Jacobians. Figure 1 illustrates this perturbation of the nodal positions. The matrices $\frac{\partial \mathbf{X}_k}{\partial \mathbf{x}}\boldsymbol{\sigma}_k$ and $\frac{\partial \mathbf{f}_k}{\partial \mathbf{x}}\lambda_k$ may be approximated by using numerical differentiation as follows:

$$\begin{aligned} \frac{\partial \mathbf{X}_k}{\partial x_i}\boldsymbol{\sigma}_k &\approx \frac{(\mathbf{X}_{k+\delta x_i} - \mathbf{X}_k)\boldsymbol{\sigma}_k}{\delta x_i} \\ \frac{\partial \mathbf{f}_k}{\partial x_i}\lambda_k &\approx \frac{(\mathbf{f}_{k+\delta x_i} - \mathbf{f}_k)\lambda_k}{\delta x_i} \end{aligned}$$

where matrix $\mathbf{X}_{k+\delta x_i}$ and vector $\mathbf{f}_{k+\delta x_i}$ denote $\mathbf{X}$ and $\mathbf{f}$ evaluated with the nodal coordinate x_i^k perturbed by a small quantity δx_i.

We point out that the constraints in (7) are in fact equivalent to imposing the equilibrium constraints on a moving mesh, such that the stresses and the final position of the mesh are unknown. Due to the non-linearity of these constraints, these equilibrium equations are linearised at the previous stress values $\boldsymbol{\sigma}_k$ and previous nodal positions, which gives rise to the approximated equilibrium constraints in (7). As such, this linearisation is an approximation, and thus the obtained solution may be suboptimal with respect to the analytical non-linear problem. We aim though to approach such optimal solutions as we solve successive problems from updated values of $\boldsymbol{\sigma}_k$ and $\mathbf{X}_k$.

3.2 Upper Bound Problem

In contrast to the lower bound problem, we aim now to minimise the optimal value of λ (which is now an upper bound of the analytical optimal λ^*) with respect to the nodal positions $\mathbf{x}$, that is,

$$\lambda^{UB} = \max_{\boldsymbol{\sigma},\lambda} \min_{\mathbf{x}} \min_{\boldsymbol{\omega}\in\mathscr{K}^*,\mathbf{v}} \mathscr{L}(\boldsymbol{\sigma},\lambda;\mathbf{v},\boldsymbol{\omega},\mathbf{x})$$

The nodal positions thus now play the role of the dual variables $\boldsymbol{v}$ and $\boldsymbol{\omega}$. Thus, given a set of primal-dual solution $(\lambda_k,\boldsymbol{\sigma}_k;\mathbf{v}_k,\boldsymbol{\omega}_k,\mathbf{x}_k)$, we approximate the Lagrangian as,

$$\mathscr{L}(\boldsymbol{\sigma},\lambda;\mathbf{v},\boldsymbol{\omega},\mathbf{x}) \approx \lambda + \mathbf{v}^T(\mathbf{b}-\mathbf{X}_k\boldsymbol{\sigma}-\lambda\mathbf{f}_k) - \boldsymbol{\omega}^T\boldsymbol{\sigma} - \mathbf{v}_k^T\left(\frac{\partial\mathbf{X}_k}{\partial\mathbf{x}}\boldsymbol{\sigma}+\frac{\partial\mathbf{f}_k}{\partial\mathbf{x}}\lambda\right)\delta\mathbf{x} \quad (8)$$

From this expression, the following dual problem may be derived,

$$\begin{aligned}\textbf{Dual(UB)-}\delta\ :\ \lambda^{UB} = \min_{\mathbf{v},\delta\mathbf{x}}\ & \mathbf{b}^T\mathbf{v} \\ s.t.\ & \mathbf{f}^T\mathbf{v} + \left(\mathbf{v}_k^T\frac{\partial\mathbf{f}_k}{\partial\mathbf{x}}\right)\delta\mathbf{x} = 1 \\ & -\mathbf{X}_k^T\mathbf{v} - \left(\frac{\partial\mathbf{X}_k^T}{\partial\mathbf{x}}\mathbf{v}_k\right)\delta\mathbf{x} \in \mathscr{K}^* \\ & ||\delta\mathbf{x}|| \le \boldsymbol{\varepsilon}\end{aligned} \quad (9)$$

where again, we have added the last constraint in order to avoid elements with large aspect ratios or a negative Jacobian. This is an extension of the dual problem in (4) for varying nodal positions $\mathbf{x}$. It can be verified that the primal form of (9) reads,

$$\begin{aligned}\textbf{Primal(UB)-}\delta:\ \lambda^{UB} = \max_{\lambda,\boldsymbol{\sigma}}\ & \lambda - \boldsymbol{\omega}_1^T\boldsymbol{\varepsilon} \\ s.t.\ & \mathbf{X}_k\boldsymbol{\sigma} + \lambda\mathbf{f} = \mathbf{b} \\ & -\left(\mathbf{v}_k^T\frac{\partial\mathbf{X}_k}{\partial\mathbf{x}} + \lambda\mathbf{v}_k^T\frac{\partial\mathbf{f}_k}{\partial\mathbf{x}}\right)\boldsymbol{\sigma} = \boldsymbol{\omega}_2 \\ & \boldsymbol{\sigma} \in \mathscr{K} \\ & \{\boldsymbol{\omega}_1, \boldsymbol{\omega}_2\} \in \mathscr{K}_x\end{aligned} \tag{10}$$

where the second set of constraints follows from deriving $\mathscr{L}$ with respect to the dual variable $\delta\mathbf{x}$, and $\mathscr{K}_x$ is a cone equivalent to the constraint $||\delta\mathbf{x}|| \leq \varepsilon$. Variables $\boldsymbol{\omega}_1$ and $\boldsymbol{\omega}_2$ are new primal variables. The relative displacements are obtained from the dual variables (Lagrange multipliers) of the second set of constraints in (10).

3.3 Update of Nodal Positions

The analytical solution of the limit analysis yields a unique value of λ^*, but not necessarily a unique mechanism. For this reason, and due to the finite element discretisation, the optimal nodal positions $\mathbf{x}$ may differ in discrete upper and lower formulations. In our implementation, which focuses on the lower bound solution, we update the nodal positions according to

$$\mathbf{x}_{k+1} = \mathbf{x}_k + \delta\mathbf{x}^{LB} \tag{11}$$

with $\delta\mathbf{x}^{LB}$ the optimal value of the extended lower bound problem. We note though that we could alternatively modify the nodal positions according to the average of the two values of $\delta\mathbf{x}$ obtained in each case, that is according to the following vector:

$$\delta\mathbf{x} = \frac{1}{2}\left(\delta\mathbf{x}^{UB} + \delta\mathbf{x}^{LB}\right)$$

or even from a weighted average according to the gain in each bound,

$$\delta\mathbf{x} = \left(\Delta\lambda^{UB}\delta\mathbf{x}^{UB} + \Delta\lambda^{LB}\delta\mathbf{x}^{LB}\right)/\Delta\lambda$$

where $\Delta\lambda^{UB} = \lambda^{UB} - \lambda^{est}$ and $\Delta\lambda^{LB} = \lambda^{LB} - \lambda^{est}$ correspond to the error of the load factor for each discrete solution with respect to an estimate λ^{est} obtained from the evolution of each bound. In our numerical examples we have not used these averaged updates, and restricted our attention to the simplest case in (11).

As it will be shown, the effectiveness of R-adaptivity depends on the number of elements and distribution. For this reason, we have also tested the combination of R-adaptivity with *h* refinement, where the elements are subdivided according to an error estimator, as described in [10].

4 Results

We test here R-adaptivity in order to compute the safety factor of a vertical cut subjected to an increasing gravitational field $\boldsymbol{f}$. Figure 2 shows the geometry, boundary conditions and initial mesh made of 140 elements. We have also tested an initial coarser mesh made of 28 elements, as shown in Fig. 3a. In this figure, we also show with thicker (black) lines the perturbed mesh after applying R-adaptivity.

The evolution of the upper and lower bounds for the initial meshes with 28 and 140 elements are shown in Fig. 4a, b, respectively. All values plotted in this figure, including those computed from an R-adapted mesh, have been obtained using the original reduced upper and lower bound problem, without approximations arising from R-adaptivity, and are thus strict bounds. When comparing the lower bound results with respect to the evolution when only using h-refinement, the lower bound solution is improved with R-adaptivity: one R-adaptivity iteration is approximately equivalent to one iteration in h-refinement. The latter though is obtained for a higher number of elements, and thus has a higher cost. The upper bound solution though is not necessarily improved. Indeed, it appears that for a low number of elements, the improvement in the lower bound solution worsens the upper bound load factor, as one might expect given the lack of correlation between the optimal meshes for the lower and upper bound problems (see Sect. 3.3).

We note that the maximum nodal displacement in the extended optimisation problem, which is dictated by variable ε, is different for each node. This value is computed from the element sizes around each node. It follows that ε decreases as h-refinement is applied, which consequently reduces the impact of R-refinement.

We have also tested the evolution of the bounds when only using R-adaptivity. Figure 5 shows the initial and final meshes for 12 iterations of R-adaptivity. The

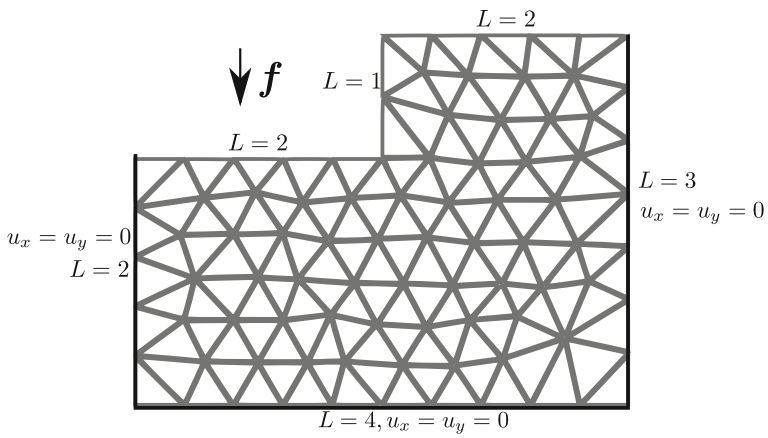

Fig. 2 Vertical cut problem. Dimensions, boundary conditions and initial mesh made of 140 elements

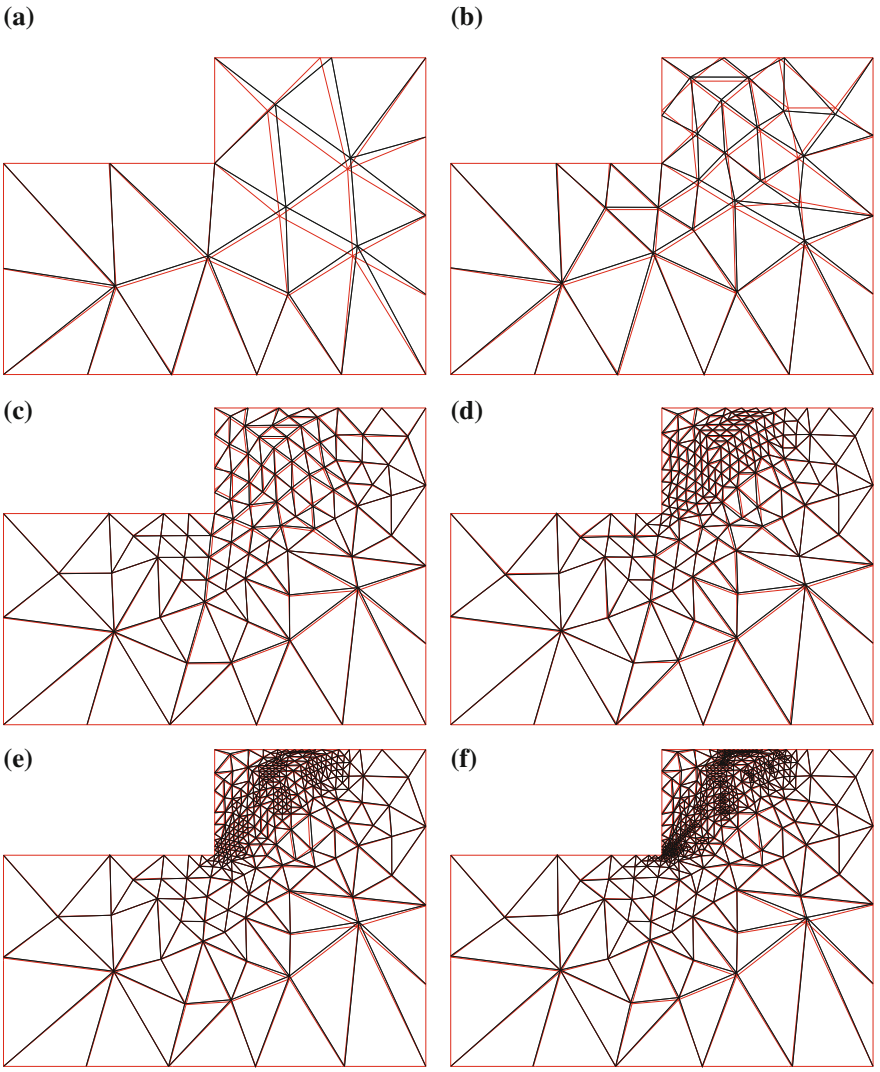

Fig. 3 Comparison of the unperturbed mesh (*thinner* and *lighter lines*) and the R-adapted mesh (*thicker* and *darker lines*) after successive h-refinements, when using an initial mesh of 28 elements. The evolution of the load factor is given in Fig. 4

corresponding evolution of the load factors when using a constant number of elements equal to 28 and 140 are shown in Fig. 6. As before, the load factors shown are those obtained using the reduced optimisation problem (no R extension) for the new meshes, and are thus strict bounds. It can be observed the initial improvement of the lower bounds is greater for lower number of elements, but that the final gain is higher when starting with a larger number of elements, as it should be expected. Indeed, the optimal R-adapted solution in a finer mesh should be more accurate than

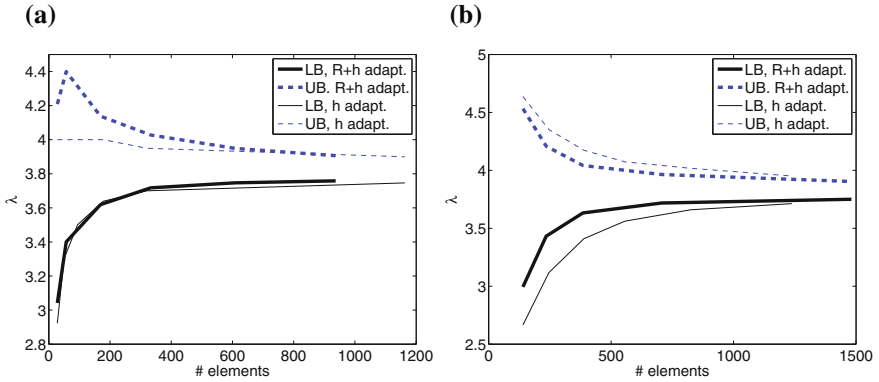

Fig. 4 Evolution of bounds for the vertical cut problem. **a** Mesh with initially 28 elements. **b** Mesh with initially 140 elements

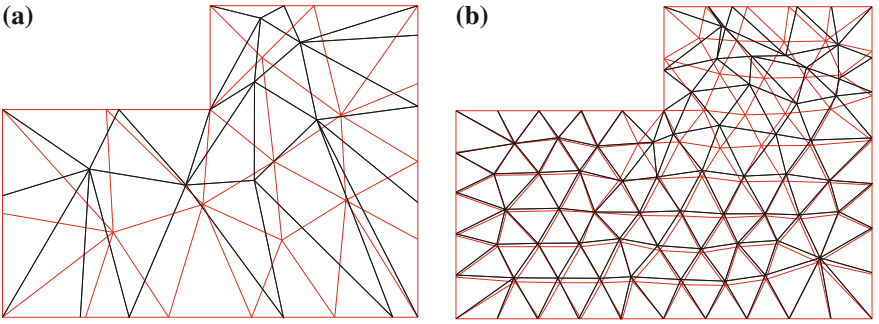

Fig. 5 Initial (*thinner* and *lighter lines*) and final (*thicker* and *darcker lines*) meshes when using R-adaptivity only. **a** Mesh with 28 elements. **b** Mesh with 140 elements. Elements with high aspect ratio can be observed on the *top right side* of the vertical cut

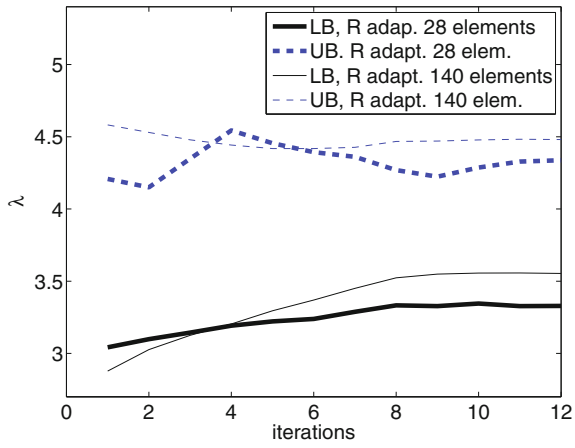

Fig. 6 Evolution of bounds when using only R-adaptivity

the optimal R-adapted solution in a coarse mesh. The limitation on the values of ϵ (which is proportional to the mesh size) limits though the improvement in each iteration in fine meshes, and thus more iterations are required for achieving a R-adapted optimal solution.

Furthermore, after eight or nine iterations, the gain stagnates with small oscillations around an optimal solution. The fact that the extended optimisation problem in R-adaptivity is non-linear with a linearised Lagrangian, one which is only approximate, may be the cause behind these small oscillations. It can be also observed that the upper bound solution does not necessarily improve. As a final remark, we note that some of the elements achieve a high aspect ratio (Fig. 5), and could be removed from the mesh, to obtain further improvements in the computed bounds, as suggested in previous work [3].

5 Conclusions

In this work we have presented a remeshing strategy that extends the limit analysis optimisation problem to include the nodal positions of a given mesh in order to further improve lower and upper bound solutions of the load factor. We have derived the necessary modifications to the optimisation problems to take into account the nodal positions as additional variables, and tested the lower bound formulation.

The strategy may be combined with other error based remeshing techniques such as embedded remeshing [10]. In these techniques, the number of elements increases, and adds new discontinuities in the discretised problem. The strategy described here aims to improve the solution and mesh distribution before further refining the mesh.

Further tests are required in order to apply R-adaptivity on the upper bound solution and wisely combine the two mesh perturbations, and also appropriately combine R-adaptivity with *h*-refinement. Importantly, nodal position perturbation allows us to shift the sliplines that the initial coarse meshes impose when using only embedded remeshing.

We note that the modifications of the optimisation problem are not restricted to the linear interpolations of stresses or velocities employed here. Other discretisations may be equally perturbed, and linearised on the resulting optimal variables. In addition, due to the localisation of the plastic zone, it may be advisable to allow the nodes to move only along a reduced portion of the domain, thus reducing the cost of the complete optimisation problem.

The extension of the optimisation problem with the perturbation of the nodal coordinates has an additional computational cost. This extra cost may be reduced by just adding in the optimisation process the position of those nodes that contribute to the failure mechanism, that is, that are closer to the slipline, but keeping the positions of more distant nodes unaltered. Since many geotechnical problems are driven by localised sliplines, this concentration would have a strong beneficial impact in many applications. In addition, element deletion strategies may be envisaged in order to

remove elements with high aspect ratio, as they were encountered in the final meshes when using R-adaptivity only. These strategies are currently under investigation.

References

1. Boyd S, Vandenberghe L (2004) Convex optimization. Cambridge University, Press
2. Cottereau R, Díez P (2015) Fast r-adaptivity for multiple queries of heterogeneous stochastic material fields. Comput Mech 66:601–612
3. Hambleton J, Sloan S (2013) A perturbation method for optimization of rigid block mechanisms in the kinematic method of limit analysis. Comput Geotech 48:260–271
4. Kim J, Panatinarak T, Shontz SM (2013) A multiobjective mesh optimization framework for mesh quality improvement and mesh untangling. Int J Numer Methods Eng 94(7):20–42
5. Krabbenhøft K, Lyamin AV, Hjiaj M, Sloan SW (2005) A new discontinuous upper bound limit analysis formulation. Int J Numer Methods Eng 63:1069–1088
6. Lyamin AV, Sloan SW (2002a) Lower bound limit analysis using non-linear programming. Int J Numer Methods Eng 55:576–611
7. Lyamin AV, Sloan SW (2002b) Upper bound limit analysis using linear finite elements and non-linear programming. Int J Numer Anal Methods Geomech 26:181–216
8. Lyamin AV, Sloan SW, Krabbenhøft K, Hjiaj M (2005) Lower bound limit analysis with adaptive remeshing. Int J Numer Methods Eng 63:1961–1974
9. Ma L, Klug WS (2008) Viscous regularization and r-adaptive remeshing for finite element analysis of lipid membrane mechanics. J Comput Phys 227(11):5816–5835
10. Muñoz JJ, Bonet J, Huerta A, Peraire J (2009) Upper and lower bounds in limit analysis: adaptive meshing strategies and discontinuous loading. Int J Numer Methods Eng 77:471–501
11. Muñoz JJ, Bonet J, Huerta A, Peraire J (2012) A note on upper bound formulations in limit analysis. Int J Numer Methods Eng 91(8):896–908
12. Sloan SW, Kleeman PW (1995) Upper bound limit analysis using discontinuous velocitiy fields. Comput Methods Appl Mech Eng 127(5):293–314
13. Thoutireddy P, Ortiz M (2004) A variational r-adaption and shape-optimization method for finite-deformation elasticity. Int J Num Methods Eng 61:1–21
14. Zielonka MG, Ortiz M, Marsden JE (2008) Variational r-adaption in elastodynamics. Int J Num Methods Eng 74:1162–1197

Shakedown Analysis Under Stochastic Uncertainty by Chance Constrained Programming

N.T. Tran, T.N. Tran, H.G. Matthies, G.E. Stavroulakis and M. Staat

Abstract In this paper we propose a stochastic programming method to analyse limit and shakedown of structures under uncertainty condition of strength. Based on the duality theory, the shakedown load multiplier formulated by the kinematic theorem is proved actually to be the dual form of the shakedown load multiplier formulated by static theorem. In this investigation a dual chance constrained programming algorithm is developed to calculate simultaneously both the upper and lower bounds of the plastic collapse limit and the shakedown limit. The edge-based smoothed finite element method (ES-FEM) with three-node linear triangular elements is used for structural analysis.

N.T. Tran · M. Staat (✉)
Institute for Bioengineering, Biomechanics Lab, FH Aachen University of Applied Sciences, Jülich Campus, Heinrich-Mußmann-Str. 1, 52428 Jülich, Germany
e-mail: m.staat@fh-aachen.de

N.T. Tran
e-mail: trinhdhkt@gmail.com

T.N. Tran
Chair of Mechanics and Robotics, University of Duisburg-Essen, Lotharstr. 1, 47057 Duisburg, Germany
e-mail: thanh.tran@uni-due.de

H.G. Matthies
Institute of Scientific Computing, Technische Universität Braunschweig, Mühlenpfordtstr. 23, 38106 Braunschweig, Germany
e-mail: wire@tu-bs.de

G.E. Stavroulakis
Institute of Computational Mechanics & Optimization, University Campus, Technical University of Crete, Kounoupidiana, 73100 Chania, Greece
e-mail: gestavr@dpem.tuc.gr

O. Barrera et al. (eds.), *Advances in Direct Methods for Materials and Structures*, DOI 10.1007/978-3-319-59810-9_6

1 Introduction

The plastic collapse limit and the shakedown limit which define the load-carrying capacity of structures are important in assessing the structural integrity. Due to the high expenses of experimental setups and the time consuming elastic-plastic cyclic loading analysis, the determination of these limits by means of numerically direct plasticity methods has been of great interest to many designers. Moreover, a certain evaluation of structural performance can be conducted only if the uncertainty of the actual load-carrying capacity of the structure is taken into consideration since all resistance and loading variables are random in nature. As the result of the need to account in a rational way for such uncertainties, the theory of structural reliability has been introduced and has developed rapidly also for limit and shakedown analysis [e.g. 3–5, 9, 14–19].

Chance constrained programing is an approach of stochastic programming which has originally been developed for decision problems [1, 2, 6, 7]. It seems to be well suited for limit and shakedown analysis under uncertainty and in this application it could be more generally denoted probability constrained programming. Under uncertainty the shakedown problem can be stated with a random objective function or with random constraints, a probability is set with which the constraints have to be satisfied. This has been suggested for limit analysis of beam problems and the Tresca yield function by chance constrained linear programming [3, 4]. Numerical difficulties to calculate the probabilities have prevented a large scale application. Here we assume normally distributed variables for which a simple deterministically equivalent formulation can be found which has a simple solution.

In [5] the stochastic limit load problem has been replaced by a recourse problem. For this a substitute problem is formulated by introducing primary costs for missing carrying capacity and recourse costs (for damage, loss or repair of the structure or for reduced structural capacity). This somewhat indirect approach is thought to be numerically more effective for non-normally distributed variables. However, only examples with normal distributions are shown.

The edge-based smoothed finite element method (ES-FEM) was recently proposed to significantly improve the accuracy and convergence rate of the standard finite element formulation for static, free and forced vibration analyses of solids. It also was applied successfully in shakedown analysis of structures [8, 9].

In this study, we present a new primal-dual numerical algorithm of shakedown problem under uncertainty. We restrict ourselves to the case of random yield limit, the loads applied to the structures are still deterministic. Using the von Mises yield function this leads to nonlinear chance constrained programming problems. Restricting the analysis to normally distributed yield limits, we get deterministic equivalent formulations based on upper bound and lower bound theorems and then prove that both formulations are actually dual to each other. As aforementioned, in the study described here the numerical approach is based on ES-FEM. In ES-FEM, compatible strains are smoothed over the smoothing domains associated with the edges of the finite elements. Using a constant smoothing function, only one

Gaussian point is required for each domain ensuring that the total number of variables in the resulting optimization problem is kept to a minimum compared with the standard finite element formulation. In this study, three-node linear triangular elements are used to analyse plane stress problems.

Some numerical examples were investigated to test the proposed algorithm. The obtained solutions match well with analytical values and show remarkably good performance.

2 Lower Bound Approach to Chance Constrained Programming

Starting from the discretized form of the deterministic formulation [10, 11, 20]:

$$\begin{aligned} &\alpha^- = \max \alpha \\ &\text{s.t.:} \quad \begin{cases} \sum_{i=1}^{NG} w_i \mathbf{B}_i^T \bar{\boldsymbol{\rho}}_i = \mathbf{0} \\ f\left[\alpha \boldsymbol{\sigma}_{ik}^E + \bar{\boldsymbol{\rho}}_i\right] - r_i \le 0, \forall k = \overline{1,m}, \quad \forall i = \overline{1,NG} \end{cases} \end{aligned} \tag{1}$$

in which $\mathbf{B}_i$ denotes the deformation matrix, w_i is the weighting factor of the ith Gauss point and NG is the total number of Gauss points in the problem domain, k is the number of vertices of the load domain, r_i is the strength of the material at Gauss point i. The first constraint of (1) describes the self-equilibrium condition of time independent residual stresses $\bar{\boldsymbol{\rho}}_i, \boldsymbol{\sigma}_{ik}^E$ denotes the vector of elastic reference stress. The second constraint describes the yield condition.

Consider the situation that the strength of the material is not given but must be modelled through random variables $r = r(\omega)$ in a certain probability space. Under uncertainty, the inequalities of (1) are not always satisfied, the probability of the ith yield condition being satisfied is greater than some reliability level ψ_i. Problem (1) becomes a stochastic programming:

$$\begin{aligned} &\alpha^- = \max \alpha \\ &\text{s.t.:} \quad \begin{cases} \sum_{i=1}^{NG} w_i \mathbf{B}_i^T \bar{\boldsymbol{\rho}}_i = \mathbf{0} \\ \text{Prob}\left[f\left(\alpha \boldsymbol{\sigma}_{ik}^E + \bar{\boldsymbol{\rho}}_i\right) - r_i(\omega) \le 0\right] \ge \psi_i \end{cases} \end{aligned} \tag{2}$$

Let us consider the individual chance constraint:

$$\text{Prob}\left[f\left(\alpha \boldsymbol{\sigma}_{ik}^E + \bar{\boldsymbol{\rho}}_i\right) - r_i(\omega) \le 0\right] = \text{Prob}\left[f_i - r_i(\omega) \le 0\right] \ge \psi_i \tag{3}$$

We assume that the strength $r_i(\omega)$ of the material follows a Gaussian distribution $\mathcal{N}(\mu_i, \sigma_i)$ with mean value μ_i and standard deviation σ_i. Let us transform to standard

normal distribution. The yield condition can be written as $\frac{f_i-\mu_i}{\sigma_i} \leq \frac{r_i(\omega)-\mu_i}{\sigma_i}$ and we have:

$$\text{Prob}[f_i \leq r_i(\omega)] = \text{Prob}\left[\frac{f_i-\mu_i}{\sigma_i} \leq \frac{r_i(\omega)-\mu_i}{\sigma_i}\right] \tag{4}$$

Using the property of the cumulative distribution function (c.d.f.) of the standard normal distribution $\Phi(-x) = 1-\Phi(x)$, we can write (4) as follows:

$$\text{Prob}\left[\frac{f_i-\mu_i}{\sigma_i} \leq \frac{r_i(\omega)-\mu_i}{\sigma_i}\right] = 1-\Phi\left[\frac{f_i-\mu_i}{\sigma_i}\right] = \Phi\left[\frac{\mu_i-f_i}{\sigma_i}\right] \tag{5}$$

Now the probabilistic condition (3) is replaced by

$$\Phi\left[\frac{\mu_i-f_i}{\sigma_i}\right] \geq \psi_i \tag{6}$$

Introducing a new variable $\kappa_i = \Phi^{-1}(\psi_i)$ so that $\psi_i = \Phi(\kappa_i)$, inequality (6) becomes:

$$\Phi\left[\frac{\mu_i-f_i}{\sigma_i}\right] \geq \Phi(\kappa_i) \tag{7}$$

Because Φ is monotonic, it holds

$$\kappa_i \leq \frac{\mu_i-f_i}{\sigma_i} \quad \text{or} \quad f_i \leq \mu_i - \kappa_i\sigma_i \tag{8}$$

Finally we get an equivalent deterministic formulation of the static approach:

$$\begin{aligned} &\alpha^- = \max \alpha \\ &\text{s.t.:} \quad \begin{cases} \sum_{i=1}^{NG} w_i \mathbf{B}_i^T \bar{\boldsymbol{\rho}}_i = \mathbf{B}^T \bar{\boldsymbol{\rho}} = \mathbf{0} \\ f\left[\alpha \boldsymbol{\sigma}_{ik}^E + \bar{\boldsymbol{\rho}}_i\right] \leq \mu_i - \kappa_i\sigma_i, \forall k = \overline{1,m}, \forall i = \overline{1,NG} \end{cases} \end{aligned} \tag{9}$$

We also have the discrete ES-FEM equivalent deterministic formulation:

$$\begin{aligned} &\alpha^- = \max \alpha \\ &\text{s.t.:} \quad \begin{cases} \sum_{i=1}^{N_e} \hat{\mathbf{B}}_i^T \bar{\boldsymbol{\rho}}_i = \mathbf{0} \\ f\left[\alpha \boldsymbol{\sigma}_{ik}^E + \bar{\boldsymbol{\rho}}_i\right] \leq \mu_i - \kappa_i\sigma_i, \forall i = \overline{1,N_e}, \forall k = \overline{1,m} \end{cases} \end{aligned} \tag{10}$$

Here $\hat{\mathbf{B}}_i$ is the strain matrix, $\bar{\boldsymbol{\rho}}_i$ is the vector of constant residual stresses on elements sharing edge i. μ_i, σ_i are the mean value and standard deviation of yield stress of material on elements sharing the edge i, respectively, they are constants.

3 Upper Bound Approach to Chance Constrained Programming

Based on Koiter's theorem, the ES-FEM deterministic formulation is created as follows [8, 9, 20]:

$$\alpha^+ = \min \sum_{k=1}^{m} \sum_{i=1}^{N_e} \sqrt{\frac{2}{3}} r_i \sqrt{\dot{\mathbf{e}}_{ik}^T \dot{\mathbf{e}}_{ik} + \varepsilon_0^2}$$
$$\text{s.t.:} \quad \begin{cases} \sum_{k=1}^{m} \dot{\mathbf{e}}_{ik} - \hat{\mathbf{B}}_i \dot{\mathbf{u}} = \mathbf{0} \quad , \forall i = \overline{1, N_e} \\ \mathbf{D}_v \dot{\mathbf{e}}_{ik} = \mathbf{0} \quad , \forall i = \overline{1, N_e}, \quad \forall k = \overline{1, m} \\ \sum_{k=1}^{m} \sum_{i=1}^{N_e} \dot{\mathbf{e}}_{ik}^T \mathbf{t}_{ik} - 1 = 0 \end{cases} \tag{11}$$

in which r_i is the yield stress and ε_0^2 is a small positive number to ensure that the objective function is differentiable everywhere. $\dot{\mathbf{u}}, \dot{\mathbf{e}}_{ik}, \mathbf{t}_{ik}$ and $\hat{\mathbf{B}}_i$ are the displacement rate vector, strain rate vector, fictitious elastic vector and strain matrix, respectively. N_e is the number of edges in ES-FEM mesh. In three-dimensions the square matrix $\mathbf{D}_v$ in the incompressibility condition is

$$\mathbf{D}_v = \begin{bmatrix} 1 & 1 & 1 & 0 & 0 & 0 \\ 1 & 1 & 1 & 0 & 0 & 0 \\ 1 & 1 & 1 & 0 & 0 & 0 \\ 0 & 0 & 0 & 0 & 0 & 0 \\ 0 & 0 & 0 & 0 & 0 & 0 \\ 0 & 0 & 0 & 0 & 0 & 0 \end{bmatrix} \tag{12}$$

If the strength r_i is an uncertain quantity, the objective function of the kinematic problem is a stochastic variable and problem (11) becomes a stochastic programming problem. We can state problem in such a way that one looks for a minimum lower bound η of the objective function under the constraint that the probability ψ of violation of that bound is prescribed [2, 7].

$$\alpha^+ = \min \eta$$
$$\text{s.t.:} \begin{cases} \text{Prob}\left(\sum_{k=1}^{m} \sum_{i=1}^{N_e} \sqrt{\frac{2}{3}} r_i \sqrt{\dot{\mathbf{e}}_{ik}^T \dot{\mathbf{e}}_{ik} + \varepsilon_0^2} \geq \eta \right) = \psi \\ \sum_{k=1}^{m} \dot{\mathbf{e}}_{ik} - \hat{\mathbf{B}}_i \dot{\mathbf{u}} = \mathbf{0} \\ \mathbf{D}_v \dot{\mathbf{e}}_{ik} = \mathbf{0} \\ \sum_{k=1}^{m} \sum_{i=1}^{N_e} \dot{\mathbf{e}}_{ik}^T \mathbf{t}_{ik} - 1 = 0 \end{cases} \tag{13}$$

For the sake of simplicity, we denote the plastic dissipation

$$\theta(\omega) = \sum_{k=1}^{m} \sum_{i=1}^{N_e} \sqrt{\frac{2}{3}} r_i(\omega) \sqrt{\dot{\mathbf{e}}_{ik}^T \dot{\mathbf{e}}_{ik} + \varepsilon_0^2} \tag{14}$$

The first constraint of (13) can be rewritten as:

$$\text{Prob}(\theta \geq \eta) = 1 - \text{Prob}(\theta \leq \eta) = 1 - \text{Prob}\left(\frac{\theta - \mu_\theta}{\sigma_\theta} \leq \frac{\eta - \mu_\theta}{\sigma_\theta} \right) = \psi \tag{15}$$

In (15), $\mu_\theta, \sigma_\theta$ are mean value and standard deviation of $\theta(\omega)$. We can see in the inequality

$$\frac{\theta - \mu_\theta}{\sigma_\theta} \leq \frac{\eta - \mu_\theta}{\sigma_\theta} \tag{16}$$

the left hand side is the normalized random variable with zero mean and unit variance. Hence the probabilistic condition (15) is replaced by

$$\psi = 1 - \Phi\left(\frac{\eta - \mu_\theta}{\sigma_\theta} \right) = \Phi\left(\frac{\mu_\theta - \eta}{\sigma_\theta} \right) \tag{17}$$

Setting $\psi = \Phi(\kappa)$ we have $\Phi^{-1}(\psi) = \kappa = \frac{\mu_\theta - \eta}{\sigma_\theta}$ or $\mu_\theta - \kappa\sigma_\theta = \eta$.

The separate chance constrained program has the deterministic equivalent:

$$\alpha^+ = \min \eta$$
$$\text{s.t.:} \begin{cases} \mu_\theta - \kappa\sigma_\theta = \eta \\ \sum_{k=1}^{m} \dot{\mathbf{e}}_{ik} - \hat{\mathbf{B}}_i \dot{\mathbf{u}} = \mathbf{0} \\ \mathbf{D}_v \dot{\mathbf{e}}_{ik} = \mathbf{0} \\ \sum_{k=1}^{m} \sum_{i=1}^{N_e} \dot{\mathbf{e}}_{ik}^T \mathbf{t}_{ik} - 1 = 0 \end{cases} \tag{18}$$

Finally, we can write clearly the discretized upper bound of shakedown limit load to chance constrained programming:

$$\alpha^+ = \min \sum_{k=1}^{m} \sum_{i=1}^{N_e} \sqrt{\frac{2}{3}}(\mu_i - \kappa\sigma_i)\sqrt{\dot{\mathbf{e}}_{ik}^T \dot{\mathbf{e}}_{ik} + \varepsilon_0^2}$$
$$\text{s.t.:} \quad \begin{cases} \sum_{k=1}^{m} \dot{\mathbf{e}}_{ik} - \hat{\mathbf{B}}_i \dot{\mathbf{u}} = \mathbf{0} \quad \forall i = \overline{1, N_e} \\ \mathbf{D}_v \dot{\mathbf{e}}_{ik} = \mathbf{0} \quad \forall i = \overline{1, N_e}, \quad \forall k = \overline{1, m} \\ \sum_{k=1}^{m} \sum_{i=1}^{N_e} \dot{\mathbf{e}}_{ik}^T \mathbf{t}_{ik} - 1 = 0 \end{cases} \tag{19}$$

4 Duality Approach to Chance Constrained Programming

As it is noted for the deterministic case, limit analysis may be considered as a special case of shakedown analysis. Andersen et al. [12], while considering a problem of minimizing a sum of Euclidean norms, found that in the case of limit analysis there exists a dual form for (11). For the chance constrained shakedown problem, the same property can be presented through the two propositions:

Proposition 1 *If there exists a finite solution* α^+ *for the kinematic shakedown load multiplier* (19) *with* $\varepsilon_0 = 0$ *then* α^+ *has its dual form as*

$$\alpha^- = \max \alpha$$
$$\text{s.t.:} \begin{cases} \sum_{i=1}^{N_e} \hat{\mathbf{B}}_i^T \boldsymbol{\beta}_i = \mathbf{0} \\ \|\boldsymbol{\gamma}_{ik} + \boldsymbol{\beta}_i + \alpha \mathbf{t}_{ik}\| \le \sqrt{\frac{2}{3}}(\mu_i - \kappa_i \sigma_i) \end{cases} \tag{20}$$

where $\|.\|$ *denotes the Euclidean vector norm.*

Proposition 2 *If there exists a finite solution* α^+ *for the kinematic shakedown load multiplier* (19) *with* $\varepsilon_0 = 0$ *and if the incompressibility is automatically satisfied, then the kinematic formulation has its dual form as the static formulation by the Melan theorem*

$$\alpha^+ = \alpha^- = \max \alpha$$
$$\text{s.t.:} \begin{cases} \sum_{i=1}^{N_e} \hat{\mathbf{B}}_i^T \bar{\boldsymbol{\rho}}_i = \mathbf{0} \\ f\left[\alpha \boldsymbol{\sigma}_{ik}^E + \bar{\boldsymbol{\rho}}_i\right] \le \mu_i - \kappa_i \sigma_i \end{cases} \tag{21}$$

Coming from Proposition 1, we can also present the primal-dual form as a set of stationary conditions:

$$\begin{aligned}
&\frac{\sqrt{2/3}(\mu_i - \kappa_i \sigma_i)}{\sqrt{\dot{\mathbf{e}}_{ik}^T \dot{\mathbf{e}}_{ik}}} - (\boldsymbol{\gamma}_{ik} + \boldsymbol{\beta}_i + \alpha \mathbf{t}_{ik}) = \mathbf{0} && \text{(a)}\\
&\mathbf{D}_v \dot{\mathbf{e}}_{ik} = \mathbf{0} && \text{(b)}\\
&\sum_{k=1}^{m} \dot{\mathbf{e}}_{ik} - \hat{\mathbf{B}}_i \dot{\mathbf{u}} = \mathbf{0} && \text{(c)}\\
&\sum_{i=1}^{N_e} \hat{\mathbf{B}}_i^T \boldsymbol{\beta}_i = \mathbf{0} && \text{(d)}\\
&\sum_{i=1}^{N_e} \sum_{k=1}^{m} \dot{\mathbf{e}}_{ik}^T \mathbf{t}_{ik} - 1 = 0 && \text{(e)}
\end{aligned} \tag{22}$$

The second proposition shows that the shakedown load multipliers formulated by static and kinematic theorems are actually the same.

Based on the above discussion on duality, a dual algorithm has been developed, [10, 11, 20]. The objective is to obtain simultaneously both primal and dual values by solving the system of Eq. 22. In order to keep the problem size as small as possible, the penalty method is used to handle the incompressibility and compatibility conditions (22b and 22c). The Lagrange multipliers are used as intermediate variables.

5 Numerical Examples

Two span continuous beam

In the first example, we consider the two span continuous beam with rectangular cross-section. The beam is subjected to two concentrated forces shown in Fig. 1. Each span has the random yield moment characterized by the mean values $\mu_{M_{0,1}} = 2.0\,\text{kNm}$, $\mu_{M_{0,2}} = 3.0\,\text{kNm}$ and the standard deviations $\sigma_{M_{0,i}} = 0.1\,\mu_{M_{0,i}}$. Let us determine the limit load factor if the reliability level is $\psi = \Phi(\kappa) = 0.9999$ for which we get $\kappa = \Phi^{-1}(\psi) = 3.719$. Figure 2 shows the convergence of upper and lower bounds in limit analysis. Figure 3 represents the dependence of the limit load factor on the coefficient of variation for a reliability of 99.99%. The dependence of the limit load factor on the failure probability is shown in Fig. 4.

The limit load problem has an analytical solution. For the kinematic theorem, observe that the plastic moment of the first span is lower than the one of the second span and the applied load P_1 is greater than P_2. The failure mechanism is shown in Fig. 5.

We easily calculate the upper bound limit load factor from the virtual work equation:

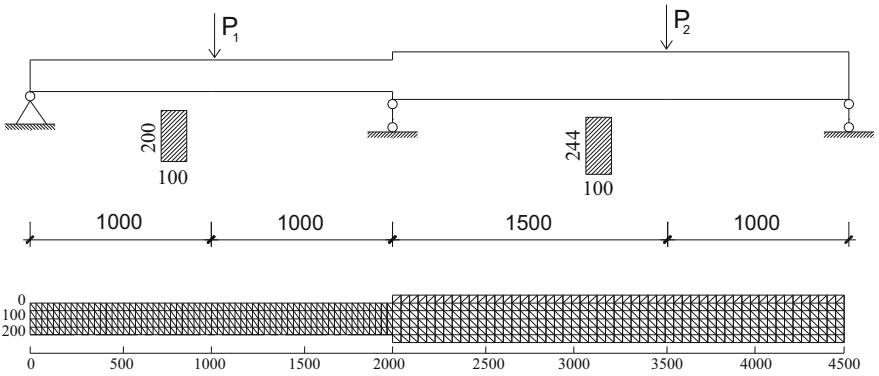

Fig. 1 Two span beam and the mesh using three-node triangular elements

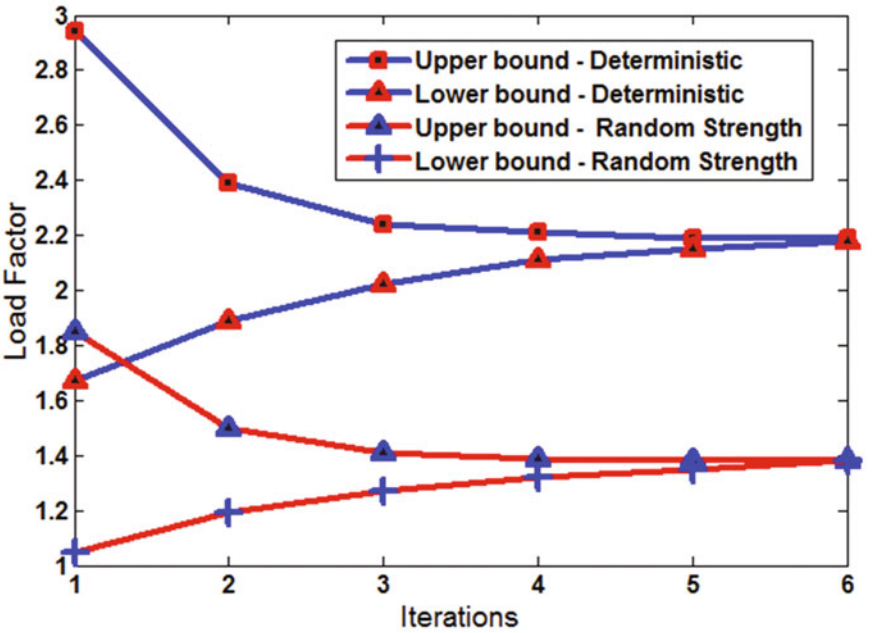

Fig. 2 Convergence of the limit load factor α_{lim}

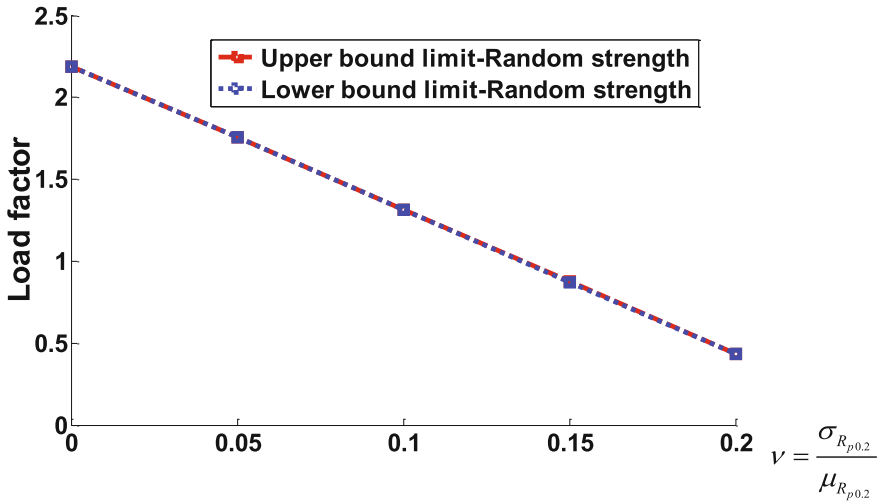

Fig. 3 Dependence of the limit load factor on the coefficient of variation ν

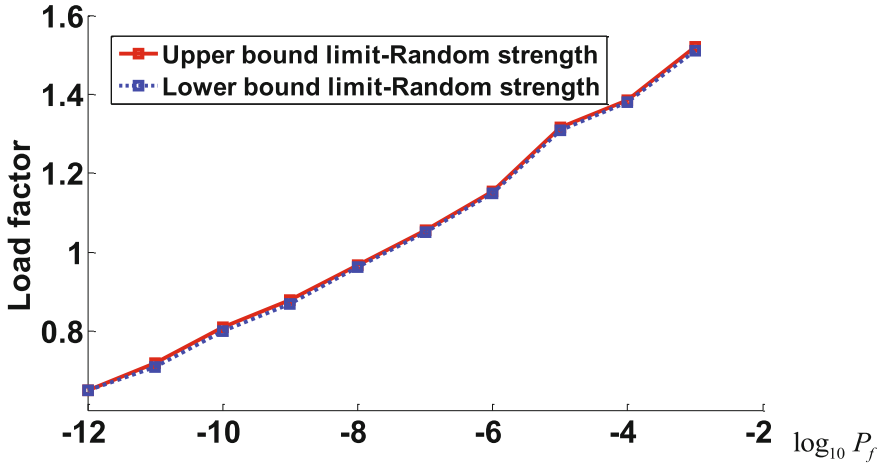

Fig. 4 Dependence of the limit load factor on log failure probability

$$\begin{aligned} &\alpha_{\lim}^{+} P_1 \cdot \delta = M_{0,1} \cdot 2\theta + M_{0,1} \cdot \theta = 3M_{0,1} \cdot \theta = 3M_{0,1} \frac{\delta}{L}, \\ &\Rightarrow \alpha_{\lim}^{+} = \frac{3M_{0,1}}{P_1 \cdot L} = \frac{3 \cdot 2\text{kNm}}{3\text{kN} \cdot 1\text{m}} = 2. \end{aligned} \tag{23}$$

This is the exact limit load because the static theorem has the same result.

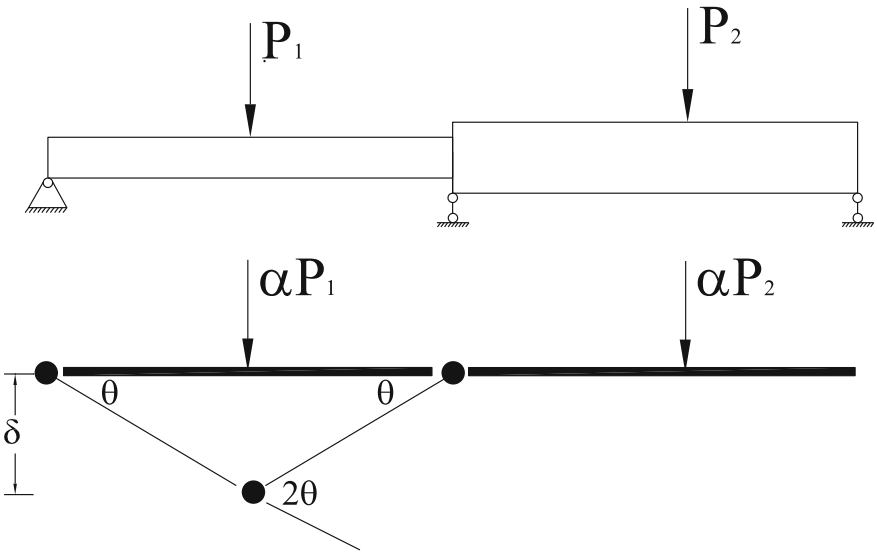

Fig. 5 The failure mechanism of the beam at limit state

For random plastic moment, we can replace $M_{0,1}$ by $\mu_{M_{0,1}} - \kappa\sigma_{M_{0,1}}$ in the deterministic equivalent problem. Let $M_{0,1}$ be normally distributed with mean value $\mu_{M_{0,1}} = 2\,\text{kNm}$ and standard deviation $\sigma_{M_{0,1}} = 0.2\,\text{kNm}$, respectively, and P_1 deterministic. For the chosen reliability level the limit load factor is:

$$\alpha_{\text{lim}}^{+} = \frac{3\left(\mu_{M_{0,1}} - \kappa\sigma_{M_{0,1}}\right)}{P_1 \cdot L} = \frac{3(2 - 3.719 \cdot 0.2)}{3} = 1.256 \tag{24}$$

For comparison, the numerical solution converges to the limit load factors $\alpha_{\text{lim}} = 2.19$ and $\alpha_{\text{lim}} = 1.38$ for deterministic and stochastic strength, respectively. The limit loads in [3] and the analytical limit loads are different from the numerical limit loads because they are based on beam theory (Table 1).

Simple frame

In this example, we investigate a symmetric frame. Its left half depicted in Fig. 6. The beam carries two uniormly distributed loads (p_1, p_2) which can varies in the

Table 1 Limit loads of the two span beam

Lower bound determ.	Upper bound determ.	Lower bound random strength	Upper bound random strength	
2.0	2.0	1.15	1.36	[3]
2.19	2.19	1.38	1.38	Numerically
2.0	2.0	1.256	1.256	Analytically

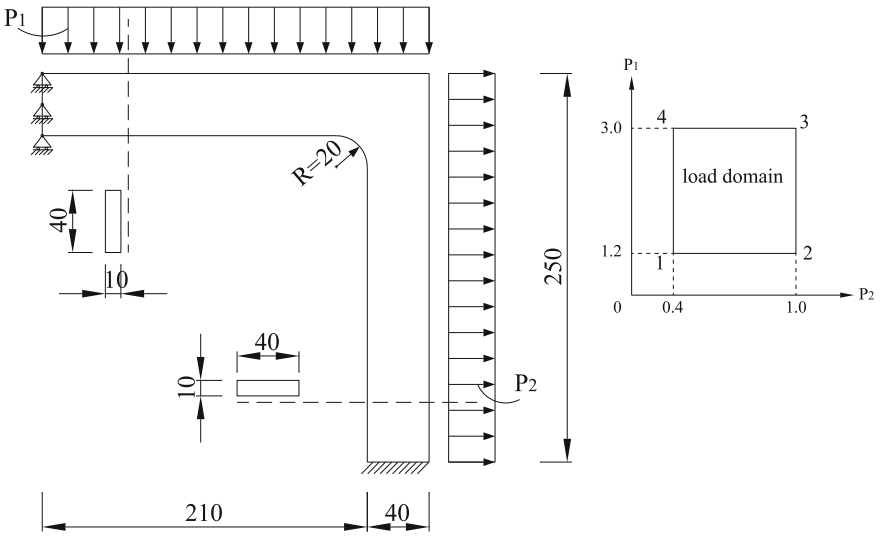

Fig. 6 The geometrical dimensions of frame and load domain

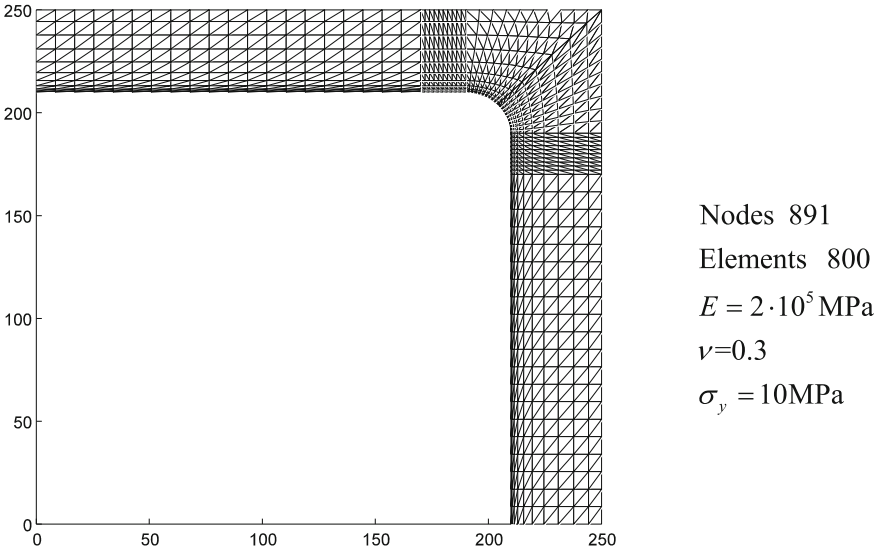

Fig. 7 The FE-mesh of a half of a symmetric frame with 800 T3 elements

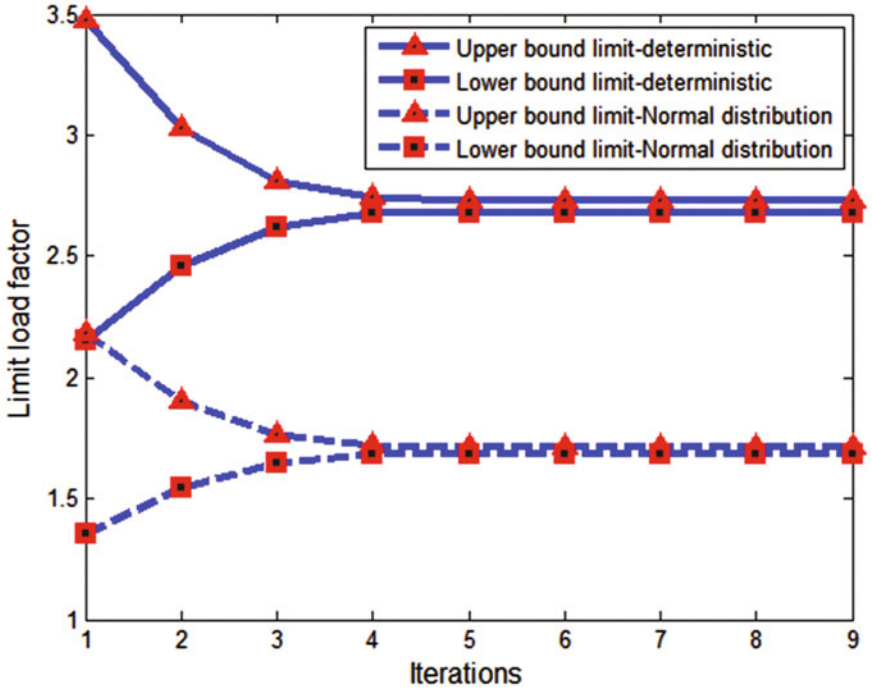

Fig. 8 Convergence of the limit load factor α_{lim}

load domain as shown in Fig. 6. The geometrical data and material are analogously chosen as in [13], i.e. $E = 2 \times 10^5$ MPa, $\nu = 0.3$, and yield stress $\sigma_y = 10$ MPa (for deterministic case). The frame is discretized by 1600 T3 elements as shown in Fig. 7.

Figures 8 and 9 show the convergence of limit and shakedown load factors for both situations: deterministic and random strength. For limit analysis with $p_1 = 3.0$, $p_2 = 1.0$, both bounds converge to the solutions $\alpha_{\text{lim}} = 2.705$ in case of deterministic strength and $\alpha_{\text{lim}} = 1.697$ in case of normally distributed strength. For shakedown analysis, the results give the shakedown load factors $\alpha_{\text{SD}} = 2.521$ and $\alpha_{\text{SD}} = 1.582$ corresponding to deterministic and random strength, respectively. Table 2 shows the present results in comparison with results in [13].

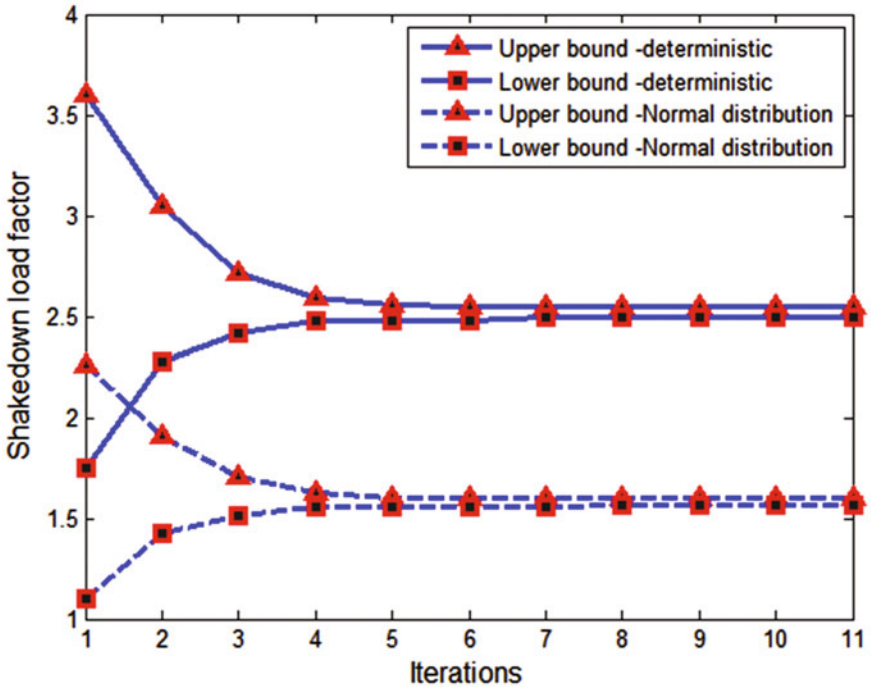

Fig. 9 Convergence of the shakedown load factor α_{SD}

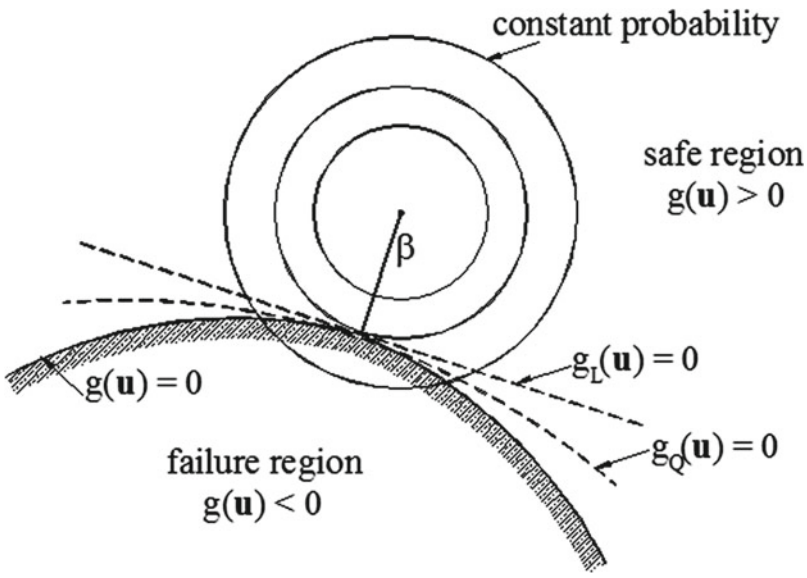

Fig. 10 Domains based on linear and quadratic approximations in **u** space

Table 2 Load factor α for limit and shakedown analysis of a simple frame

	Garcea et al. [13]		Present	
	Deterministic	Random	Deterministic	Random
Limit $(p_1 = 3, p_2 = 1)$	2.645	–	2.705	1.697
Shakedown	2.473	–	2.521	1.582

6 Reliability Analysis with the First Order Reliability Method

So far, we have prescribed a reliability level and calculated the load factor with stochastic programming. In structural reliability the failure probability is calculated for a given load factor. In order to find the relation between both approaches we consider briefly the First Order Reliability Method (FORM), which has been used in [9, 14–19] to calculate failure probabilities in limit and shakedown analysis. For more detail, see the given references.

Let the n-dimensional random vector $\mathbf{X} = (X_1, X_1, \ldots, X_n)$ of basic variables characterize uncertainties in the structure and load parameters. The limit state function $g(\mathbf{x}) = 0$, which is based on the comparison of a structural resistance (threshold) and loading, defines the limit state hypersurface ∂F which separates the failure region $F = \{\mathbf{x} | g(\mathbf{x}) < 0\}$ from safe region.

$$g(\mathbf{X}) \begin{cases} < 0 & \text{for failure,} \\ = 0 & \text{for limit state,} \\ > 0 & \text{for safe structure.} \end{cases} \tag{25}$$

This is shown in Fig. 10 after a transformation of $\mathbf{x}$ in the $\mathbf{u}$ space to be discussed below.

The failure probability P_f is the probability that $g(\mathbf{X})$ is non-positive, i.e.

$$P_f = P(g(\mathbf{X}) \leq 0) = \int_F f_X(\mathbf{x}) dx \tag{26}$$

where $f_X(\mathbf{x})$ is the n-dimensional joint probability density function. Usually, it is not possible to calculate P_f analytically. However, First- and Second-Order Reliability Methods (FORM and SORM) are analytical probability integration methods. FORM and SORM apply to problems, where the set of basic variables are continuous. The numerical effort depends on the number of stochastic variables but not on P_f. Practical experience with FORM and SORM algorithms indicates that their estimates provide very satisfactory reliability measures in limit and shakedown analysis. Especially in the case of small failure probability (large reliability), FORM and SORM are extremely efficient compared with Monte Carlo methods regarding the required of computing time.

The failure probability is computed in three steps. Firstly the physical space $\mathbf{x}$ of uncertain parameters $\mathbf{X}$ is transformed into a new n-dimensional space $\mathbf{u}$ consisting of independent standard Gaussian variables $\mathbf{U}$. By this transformation, the original limit state function $g(\mathbf{x})=0$ is mapped into the new limit state function $g(\mathbf{u})=0$ in the $\mathbf{u}$ space, Fig. 10.

In FORM, $g(\mathbf{U})=0$ with $g(\mathbf{0})>0$ is approximated linearly by its Taylor expansion $g_L(\mathbf{u})=g(\mathbf{u}^*)+(\nabla_u g(\mathbf{u}^*))^T(\mathbf{u}-\mathbf{u}^*)$ at the so-called design point $\mathbf{u}^*\in\partial V$ (so that $g(\mathbf{u}^*)=0$)

$$\begin{aligned} g_L(\mathbf{u}) &= \beta+\boldsymbol{\alpha}^T\mathbf{u}, \\ \boldsymbol{\alpha}=\frac{\nabla_u g(\mathbf{u}^*)}{\|\nabla_u g(\mathbf{u}^*)\|},\ \beta &= -\boldsymbol{\alpha}^T\mathbf{u}^*. \end{aligned} \tag{27}$$

The failure region V is linearly approximated by V_L

$$V_L=\{\mathbf{u}|\beta+\boldsymbol{\alpha}^T\mathbf{u}\le 0\}=\{\mathbf{u}|\boldsymbol{\alpha}^T\mathbf{u}\le -\beta\} \tag{28}$$

The vector $\boldsymbol{\alpha}$ is proportional to the sensitivities $\nabla_u g(\mathbf{u}^*)$. The failure event $\{\mathbf{u}\in\partial V_L\}$ is equivalent to the event $\{\boldsymbol{\alpha}^T\mathbf{u}\le -\beta\}$, such that an approximation of the failure probability P_f is

$$P_f\approx P(\boldsymbol{\alpha}^T\mathbf{U}\le -\beta)=\Phi(-\beta)=\int_{-\infty}^{-\beta} e^{-0.5z^2}dz \tag{29}$$

because the random variable $\boldsymbol{\alpha}^T\mathbf{U}$ is normally distributed.

The failure probability depends only on the so-called called reliability (or safety) index β. For a linear limit state function FORM gives the exact failure probability $P_f=\Phi(-\beta)$. The limit state function is nearly linear for limit and shakedown analyses so that a quadratic second order approximation (SORM) $g_Q(\mathbf{u})$ of $g(\mathbf{u})$ is rarely needed.

Reliability of the two span continuous beam

If it is possible to derive β analytically from the input data, the probability P_f is calculated directly from Φ. With the analytical formulation Eq. (23) of the upper bound (kinematic theorem) the limit state function is

$$g(x,y)=g(P_1,M_{0,1})=3M_{0,1}-\alpha_{\lim}^{+}P_1\cdot L=0 \tag{30}$$

so that $g(x,y)=3M_{0,1}-\alpha_{\lim}^{+}P_1\cdot L<0$ indicates failure by plastic collapse.

Let $M_{0,1}$ be normally distributed with the above mean value $\mu_{M_{0,1}}$ and standard deviation $\sigma_{M_{0,1}}$, respectively, and P_1 deterministic. The normally distributed random

variable Y with mean with $y = \mu_{M_{0,1}} + \sigma_{M_{0,1}} u_M$ transforms the limit state function Eq. (27) into

$$g(y) = 3\mu_{M_{0,1}} + 3\sigma_{M_{0,1}} u_M - \alpha^{+}_{\lim} P_1 \cdot L = 0 \tag{31}$$

With realizations $\mathbf{u} = (u_M)$ of the new random variable $\mathbf{U}$ it may be written in the standard normal space

$$g_L(\mathbf{u}) = \frac{3\sigma_{M_{0,1}}}{\sqrt{3^2\sigma^2_{M_{0,1}}}}\mathbf{u} + \frac{3\mu_{M_{0,1}} - \alpha^{+}_{\lim} P_1 \cdot L}{\sqrt{3^2\sigma^2_{M_{0,1}}}} = \boldsymbol{\alpha}^T\mathbf{u} + \beta \tag{32}$$

such that the reliability index β is

$$\beta = \frac{3\mu_{M_{0,1}} - \alpha^{+}_{\lim} P_1 \cdot L}{3\sigma_{M_{0,1}}} = \frac{3 \cdot 2\,\text{kNm} - 1.256 \cdot 3\,\text{kN} \cdot 1\,\text{m}}{3 \cdot 0.2\,\text{kNm}} = 3.72 \tag{33}$$

and the failure probability is $P_f = \Phi(-\beta) = \Phi(-3.72) = 1 \cdot 10^{-4}$. In this case comparing with the reliability $1 - P_f = \psi = \Phi(\kappa)$ we have

$$\kappa = \beta \tag{34}$$

This is the value $\kappa = 3.719$ which we have used in Sect. 5 for $\psi = 0.9999$.

7 Conclusions

In this paper, we have contributed an approach to show that direct structural reliability design can be achieved by chance constrained programming. In the general case chance constrained programming is a hard problem because probabilities have to be calculated as high dimensional integrals in the optimization algorithm. The investigation shows that for normally distributed stochastic variables deterministic equivalents can be formulated for both linear and nonlinear programming.

For engineering design, structural reliability is a post-design problem while stochastic programming is a pre-design problem. In the simple case of only one uncertain strength variable reliability analysis is "invers" to chance constrained programming and can be used to check the latter. It is also noted that the load factor decreases "quickly" with increasing coefficient of variation of the strength.

Strength is always positive so that strictly it cannot follow a normal distribution. Even so the deterministic equivalent is a great progress because the safety factor can be chosen on the basis of uncertainty quantification and with respect to a chosen reliability level. As next step other uncertain quantities like loads or geometry should be considered. This will guide the next development steps of the theory.

References

1. Rao SS (2009) Engineering optimization. Theory and practice, 4th edn Wiley, Hoboken, NJ. doi:10.1002/9780470549124
2. Kataoka S (1963) Stochastic programming model. Econometrica 31(1–2):181–196
3. Sikorski KA, Borkowski A (1990) Ultimate load analysis by stochastic programming. In: Smith DL (ed) Mathematical programming methods in structural plasticity. CISM courses and lectures no. 299. Springer, Wien, New York, pp 403–424. doi:10.1007/978-3-7091-2618-9_20
4. Tin-Loi F, Qi L, Wei Z, Womersley RS (1996) Stochastic ultimate load analysis: models and solution methods. Numer Funct Anal Opt 17(9–10):1029–1043. doi: 10.1080/01630569608816740
5. Zier S, Marti K (2009) Limit load analysis of plane frames under stochastic uncertainty. In: Weichert D, Ponter A (eds) Limit states of materials and structures: direct methods. Springer Netherlands, pp 113–134. doi:10.1007/978-1-4020-9634-1_6
6. Charnes A, Cooper WW (1959) Chance-constrained programming. Manag Sci 6(1):73–79. doi:10.1287/mnsc.6.1.73
7. Charnes A, Cooper WW (1962) Chance-constrained and normal deviates. J Am Stat Assoc 57 (279):134–148. doi:10.1080/01621459.1962.10482155
8. Tran TN, Liu GR, Nguyen-Xuan H, Nguyen-Thoi T (2010) An edge-based smoothed finite element method for primal-dual shakedown analysis of structures. Int J Numer Methods Eng 82(7):917–938. doi:10.1002/nme.2804
9. Trần TN, Staat M (2013) An edge-based smoothed finite element method for primal-dual shakedown analysis of structures under uncertainties. In: de Saxcé G, Oueslati A, Charkaluk E, Tritsch J-B (eds) Limit states of materials and structures: direct methods 2. Springer, Dordrecht, pp 89–102. doi:10.1007/978-94-007-5425-6_5
10. Vu DK, Yan AM, Nguyen DH (2004) A primal-dual algorithm for shakedown analysis of structures. Comput Methods Appl Mech Eng 193:4663–4674. doi:10.1016/j.cma.2004.03.011
11. Vu DK, Staat M (2007) Shakedown analysis of structures made of materials with temperature-dependent yield stress. Int J Solids Struct 44(13):4524–4540. doi:10.1016/j.ijsolstr.2006.11.038
12. Andersen KD, Christiansen E, Conn AR, Overton ML (2000) An efficient primal-dual interior-point method for minimizing a sum of Euclidean norms. SIAM J Sci Comput 22:243–262. doi:10.1137/S1064827598343954
13. Garcea G, Armentano G, Petrolo S, Casciaro R (2005) Finite element shakedown analysis of two-dimensional structures. Int J Numer Methods Eng **63**:1174–1202. doi:10.1002/nme.1316
14. Staat M, Heitzer M (2003) Probabilistic limit and shakedown problems. In: Staat M, Heitzer M (eds) Numerical methods for limit and shakedown analysis. Deterministic and probabilistic approach, Part VII. NIC Series, vol 15. John von Neumann Institute for Computing, Jülich, pp 217–268. http://hdl.handle.net/2128/2926
15. Tran TN, Kreißig R, Staat M (2009) Probabilistic limit and shakedown analysis of thin plates and shells. Struct Saf 31(1):1–18. doi:10.1016/j.strusafe.2007.10.003
16. Tran TN, Staat M (2015) Uncertain multimode failure and shakedown analysis of shells. In: Fuschi P, Pisano AA, Weichert D (eds) Direct methods for limit and shakedown analysis of structures, Chap. 14. Springer, Cham, Heidelberg, pp 279–298. doi:10.1007/978-3-319-12928-0_14
17. Staat M (2014) Limit and shakedown analysis under uncertainty. Int J Comput Methods 11(2):1343008. doi:10.1142/S0219876213430081
18. Heitzer M, Staat M (2000) Reliability analysis of elasto-plastic structures under variable loads. In: Maier G, Weichert D (eds) Inelastic analysis of structures under variable loads: theory and engineering applications. Kluwer, Academic Press, Dordrecht, pp 269–288. doi:10.1007/978-94-010-9421-4_17

19. Trần TN, Phạm PT, Vũ ĐK, Staat M (2009) Reliability analysis of inelastic shell structures under variable loads. In: Weichert D., Ponter A.R.S. (eds) Limit States of Materials and Structures: Direct Methods. Springer Netherlands, pp 135–156. doi:10.1007/978-1-4020-9634-1_7
20. Vu DK, Staat M, Tran IT (2007) Analysis of pressure equipment by application of the primal-dual theory of shakedown. Commun Numer Methods Eng 23(3):213–225. doi:10.1002/cnm.891

Composite Finite Elements in Structural Analysis

G. Garcea and L. Leonetti

Abstract The paper concerns mixed finite element models and experiments their capability in the analysis plastic collapse of both plane and three-dimensional problems respectively. The models are easy to formulate and implement because are based on simple assumptions for the unknown fields. A composite triangular or tetrahedral mesh is assumed over the domain. Within each element the displacement field is described by a quadratic interpolation, while the stress field is represented by a piece-wise constant description by introducing a subdivision of the element into proper sub-regions. The plastic collapse analysis is formulated as a mathematical programming problem and is accomplished by an Interior Point algorithm which furnishes both the collapse multiplier and the collapse mechanism. A series of numerical experiments shows that the proposed models perform well achieving the favorite context in plastic analysis, taking advantage of the absence of volumetric locking and the possibility of allowing discontinuities in the stress field within the element.

1 Introduction

The improvement in the accuracy and reliability of finite element models for structural analysis has been often pursued by using strategies based on complicated interpolations for the unknown fields or special procedures to filter undesired effects. These approaches usually lead to complex formulations which limit the efficiency of the proposed models. Therefore it is interesting to develop an essential model which is able to work well in a wide context of structural problems.

Some features appear particularly desirable for a finite element procedure. The algorithm should be efficient, that is it should give accurate solutions, in both displacement and stress components, with a moderate computational cost. The numerical process should be robust, that is it should be applicable to a large spectrum of

G. Garcea · L. Leonetti (✉)
Università della Calabria, DIMES, Rende, Italy
e-mail: leonardo.leonetti@unical.it

G. Garcea
e-mail: giovanni.garcea@unical.it

O. Barrera et al. (eds.), *Advances in Direct Methods for Materials and Structures*, DOI 10.1007/978-3-319-59810-9_7

data, without any significative deterioration in the numerical solution. Robustness is required, particularly in analyzing structural problems with constraints on the possible strains, such as plane strain problems and in the case of incompressibility which concerns the elastic behavior of rubber-like materials and the broad field of elastic-plastic analysis of structures when the plastic behavior is controlled by the deviatoric part of the stress tensor.

Standard compatible finite elements are usually unable to ensure the features described above. The accuracy between the displacements and stresses is unbalanced and often they suffer from locking phenomena related to the choice of interpolations which are inadequate to describe internally constrained strains [1, 2].

In the analysis of elastic-plastic problems the finite element model should ensure even greater accuracy in determining the stress field and should be able to give efficient descriptions of discontinuous fields. The presence of discontinuities make many standard models, which furnish results which are poor in localizing the plastic regions and sensitive to the mesh pattern, of little use. The use of compatible elements with a point-wise enforcement of the plastic admissibility conditions in a series of Gauss points is still a popular approach [3]. More recently, several mixed or generalized mixed formulations have been developed. A mixed approach, including internal variables for defining the constitutive laws, has been proposed as a remedy against locking [4]. By formulating the optimality conditions of the elastoplastic problem in a weak form, a class of three field elements has been proposed in [5].

Smoothing techniques have been developed to improve the performances of finite element approximations. In this category we find the Edge-Smoothed and Node-Smoothed finite element model which assume an average strain in a conflicting region associated to each edge, or a node, of a background mesh [6, 7].

This paper proposes a family of mixed finite element models which uses the assumption of an average stress field in the fashion of smoothed elements, while also following the idea underlying the construction of composite elements [8]. The models are very easy to formulate and implement because it is based on simple assumptions for the displacement and stress fields, without any burden deriving from the management of a background mesh. The proposed mixed elements have been designed with the aim of describing well solutions which can include discontinuities in the stress field. As the numerical results show, the model performs well and achieves the favorite framework in plastic analysis where it takes advantage of the absence of volumetric locking and a finer grid for describing the plastic solution within the element. Then the proposed elements are suitable for engineering applications in the plastic range where rather fine meshes are required to describe complex data and constitutive discontinuities.

2 Interpolation of the Displacement and Stress Fields

These finite element models are constructed by assuming independent interpolations to approximate the displacement and the stress fields. Within each element the displacement field is described by a continuous interpolation expressed in terms of

parameters located on its boundary, while the stress field is represented by a discontinuous description obtained by introducing a subdivision of the element. In particular the displacement is based on quadratic triangles and tetrahedrons respectively while the stress interpolation is assumed to be piece-wise constant over the element, allowing discontinuities within it.

With these chooses the element equilibrium operator is obtained by the exact integration of the element contribution to the internal work.

$$\int_V \boldsymbol{\sigma}^T \boldsymbol{\varepsilon} dV = \sum_{i=1}^{sd} \bar{\boldsymbol{\varepsilon}}_i^T \boldsymbol{\sigma}^i V_i = \boldsymbol{\beta}_e^T \boldsymbol{D}_e \boldsymbol{u}_e, \qquad \bar{\boldsymbol{\varepsilon}}_i \equiv \frac{1}{V_i} \int_{V_i} \boldsymbol{\varepsilon} dV \tag{1}$$

where *sd* is the number of sub-domains of the element and the linear strain field $\boldsymbol{\varepsilon}$ is derived through the compatibility equations from the assumed displacements by introducing the small displacement differential operator $\boldsymbol{D}$ that is $\boldsymbol{\varepsilon} = \boldsymbol{D}\boldsymbol{u}$.

The element contribution $\boldsymbol{p}_e$ to the external work is

$$\boldsymbol{p}_e \equiv \int_V \boldsymbol{\Phi}^T \boldsymbol{b} dV + \int_{\partial V_f} \boldsymbol{\Phi}^T \mathbf{t} dA \tag{2}$$

where $\boldsymbol{b}$ and $\mathbf{t}$ are the external bulk loads and assigned tractions on the element boundary ∂V_f and $\boldsymbol{\Phi}^T$ is the interpolation of the displacement field.

2.1 The Mixed 2D Finite Element

With reference to two-dimensional problems, a composite triangular mesh is assumed over the domain lying in the (x, y) plane. Each triangle is divided into three triangular regions (see Fig. 1).

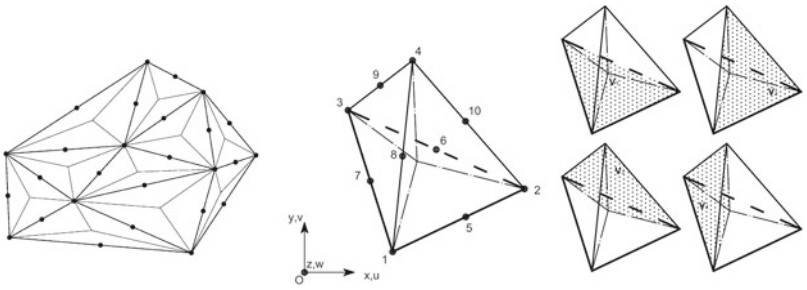

Fig. 1 Displacement nodes and stress regions

A suitable description of the relevant quantities of the discrete model can be obtained by using a triangular area co-ordinate system. The triangular co-ordinates (ξ_1, ξ_2, ξ_3) are related to the Cartesian ones (x, y) by the co-ordinate transformation [9]

$$\begin{bmatrix} \xi_1 \\ \xi_2 \\ \xi_3 \end{bmatrix} = \frac{1}{2A} \begin{bmatrix} a_1 & b_1 & c_1 \\ a_2 & b_2 & c_2 \\ a_3 & b_3 & c_3 \end{bmatrix} \begin{bmatrix} 1 \\ x \\ y \end{bmatrix} \tag{3}$$

where A is the element area and the coefficients of the transformation matrix are defined as

$$a_i = x_j y_k - x_k y_j, \quad b_i = y_j - y_k, \quad c_i = y_k - x_j \tag{4}$$

following the permutation rule

$$i = \overrightarrow{123}, \quad j = \overrightarrow{231}, \quad k = \overrightarrow{312}. \tag{5}$$

The integrals of the products between polynomial terms can be evaluated in closed form through the analytical result

$$\int_A \xi_1^\alpha \xi_2^\beta \xi_3^\gamma dA = \frac{\alpha!\beta!\gamma!}{(\alpha + \beta + \gamma + 2)!} 2A \tag{6}$$

The displacement interpolation uses bidimensional quadratic functions

$$\boldsymbol{\phi} = [2(2\xi_1 - 1)\xi_1,\ 2(2\xi_2 - 1)\xi_2,\ 2(2\xi_3 - 1)\xi_3,\ 4\xi_1\xi_2,\ 4\xi_2\xi_3,\ 4\xi_3\xi_1] \tag{7}$$

The element designed for plane elasticity is denoted with the acronym $MT_{6/3}$, which means Mixed Triangle with 6 displacement nodes and 3 stress regions (Fig. 2).

The displacement is interpolated using the element displacement vector

$$\boldsymbol{u}_e^T = \left[u_1, \ldots, u_6, v_1, ..., v_6\right] \tag{8}$$

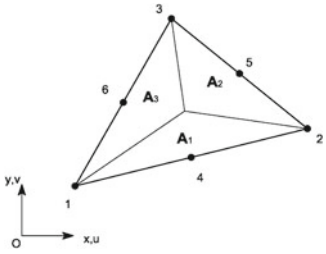

Fig. 2 Displacement nodes and stress regions

which collects the twelve displacement components of the six nodes which are located, as shown in Fig. 3, at the vertices of the triangular element and at the mid points of its edges.

The displacement vector function $\boldsymbol{u}[\xi_1, \xi_2, \xi_3] = \{u, v\}^T$ is related to $\boldsymbol{u}_e$ by the interpolation

$$\boldsymbol{u} = \boldsymbol{\Phi}\boldsymbol{u}_e, \quad \boldsymbol{\Phi} = \begin{bmatrix} \boldsymbol{\phi} & \cdot \\ \cdot & \boldsymbol{\phi} \end{bmatrix} \tag{9}$$

where the matrix $\boldsymbol{\phi}$ collects the quadratic shape functions (7).

The stress components are taken as constant over each triangular region defined by the element edges and the centroid (see Fig. 3).

For the plane stress case, the element vector of the stress parameters

$$\boldsymbol{\beta}_e = \left[\sigma^1_{xx}, \sigma^2_{xx}, \sigma^3_{xx}, \sigma^1_{yy}, \sigma^2_{yy}, \sigma^3_{yy}\sigma^1_{xy}, \sigma^2_{xy}, \sigma^3_{xy}\right]^T \tag{10}$$

is introduced to ordinate the stress components of the vector

$$\boldsymbol{\sigma}^i = [\sigma^i_{xx}, \sigma^i_{yy}, \sigma^i_{xy}]^T$$

associated to each region A_i of the element.

The element equilibrium operator is obtained by the exact integration of the element contribution to the internal work (1) with $sd = 3$ and where the equilibrium/compatibility operator is

$$\boldsymbol{D}^T = \begin{bmatrix} \frac{\partial}{\partial x} & \cdot & \frac{\partial}{\partial y} \\ \cdot & \frac{\partial}{\partial y} & \frac{\partial}{\partial x} \end{bmatrix} \tag{11}$$

The evaluation of the integral contribution is carried out analytically by using the exact formula (6) over each region and using the cyclic rule (5) to consider the vertices of the triangular regions. The equilibrium operator can be expressed in the form

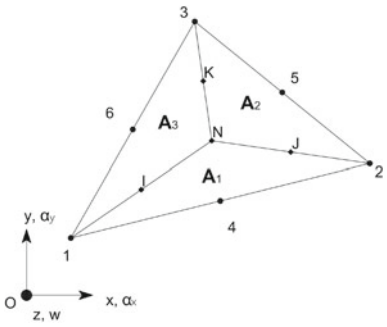

Fig. 3 Displacement nodes $\{1, \ldots, 6\}$, support nodes $\{I, J, K, N\}$ and stress regions $\{A_1, A_2, A_3\}$

$$\boldsymbol{D}_e^T = \frac{1}{54}\begin{bmatrix} \boldsymbol{B} & \boldsymbol{0} & \boldsymbol{C} \\ \boldsymbol{0} & \boldsymbol{C} & \boldsymbol{B} \end{bmatrix} \tag{12}$$

where the matrices $\boldsymbol{B}$ and $\boldsymbol{C}$ are defined in [10].

For the plane strain case, the σ_{zz} components are added to the stress vector and the element compatibility operator is modified by adding null rows in order to ensure that the components ϵ_{zz} are zero.

The case of the Mindlin-Reissner plate developed by using the same element assumption. It is denoted with the acronym $RMT_{6/3}$, which means Reissner Mixed Triangle with 6 displacement nodes and 3 stress regions.

The generalized displacement is interpolated using the element displacement vector

$$\boldsymbol{u}_e^T = \left[w_1, \ldots, w_6, \alpha_{y1}, \ldots, \alpha_{y6}, \alpha_{x1}, \ldots, \alpha_{x6}\right] \tag{13}$$

which collects the eighteen kinematical parameters (transversal displacement and two out-of plane rotations) of the six nodes which are located, as shown in Fig. 3, at the vertices of the triangular element and at the mid points of its edges.

The displacement vector function $\boldsymbol{u}[\xi_1, \xi_2, \xi_3] = \{w, \alpha_y, \alpha_x\}^T$ is related to $\boldsymbol{u}_e$ by the interpolation

$$\boldsymbol{u} = \boldsymbol{\Phi}\boldsymbol{u}_e, \quad \boldsymbol{\Phi} = \begin{bmatrix} \boldsymbol{\phi} & \cdot & \cdot \\ \cdot & \boldsymbol{\phi} & \cdot \\ \cdot & \cdot & \boldsymbol{\phi} \end{bmatrix} \tag{14}$$

The stress interpolation is assumed to be piece-wise constant over the element, allowing discontinuities within it. This choice is useful for the application to the plastic collapse analysis. In particular, the stress components are taken as constant over each triangular region defined by the element edges and the centroid (see Fig. 3).

For a simple formulation of the the Mindlin-Reissner plate, the element vector of the generalized stress parameters

$$\boldsymbol{\beta}_e = \left[M_x^1, M_x^2, M_x^3, M_y^1, M_y^2, M_y^3, M_{xy}^1, M_{xy}^2, M_{xy}^3, S_x^1, S_x^2, S_x^3, S_y^1, S_y^2, S_y^3\right]^T \tag{15}$$

is introduced to ordinate the stress components of the vector

$$\mathbf{t}^i = [M_{xx}^i, M_{yy}^i, M_{xy}^i, S_x^i, S_y^i]^T$$

associated to each region A_i of the element.

The element equilibrium operator is obtained by the exact integration of the element contribution to the internal work by considering, also in this case, $sd = 3$ and using the equilibrium/compatibility operator

$$\boldsymbol{D} = \begin{bmatrix} \boldsymbol{0} & -\boldsymbol{D}_b \\ \boldsymbol{D}_s & \boldsymbol{I} \end{bmatrix}$$

and

$$\boldsymbol{D}_b^T = \begin{bmatrix} \frac{\partial}{\partial x} & \cdot & \frac{\partial}{\partial y} \\ \cdot & \frac{\partial}{\partial y} & \frac{\partial}{\partial x} \end{bmatrix}, \quad \boldsymbol{D}_s^T = \begin{bmatrix} \frac{\partial}{\partial x}, \frac{\partial}{\partial y} \end{bmatrix} \tag{16}$$

With these choices the equilibrium operator is expressed in the form

$$\boldsymbol{D}_e^T = \frac{1}{162} \begin{bmatrix} \boldsymbol{0} & \boldsymbol{0} & \boldsymbol{0} & -\boldsymbol{B} & -\boldsymbol{C} \\ \boldsymbol{B} & \boldsymbol{0} & \boldsymbol{C} & \boldsymbol{S} & \boldsymbol{0} \\ \boldsymbol{0} & \boldsymbol{C} & \boldsymbol{B} & \boldsymbol{0} & \boldsymbol{S} \end{bmatrix} \tag{17}$$

where the matrices $\boldsymbol{B}$, $\boldsymbol{S}$ and $\boldsymbol{C}$ are defined in [11].

To evaluate the integrals some technical detail is necessary. The compatibility equations provide linear and quadratic contributions that have to be integrated in each subregion. To make it simple and effective, linear contributions are expressed in terms of support parameters located at vertices of the subregions. The node at centroid N follows the cycling rule $N = \overrightarrow{312}$ and the values on it are

$$w_N = \frac{w_1 + w_2 + w_3}{3}, \; \alpha_{yN} = \frac{\alpha_{y1} + \alpha_{y2} + \alpha_{y3}}{3}, \; \alpha_{xN} = \frac{\alpha_{x1} + \alpha_{x2} + \alpha_{x3}}{3}$$

The quadratic terms are evaluated by using six support parameters located at the vertices and at mid side of each subregions

$$\begin{aligned} \alpha_{xI} &= \alpha_x(r = 2/3, s = 1/6, t = 1/6) \\ \alpha_{xJ} &= \alpha_x(r = 1/6, t = 1/6, s = 2/3) \\ \alpha_{xK} &= \alpha_x(r = 1/6, t = 2/3, s = 1/6) \end{aligned}$$

(similarly for α_y) where the indices follow the cycling rule $I = \overrightarrow{6 \cdot 4}$, $J = \overrightarrow{54\cdot}$, and $K = \overrightarrow{\cdot 65}$ in performing the integration on each subregions. In the cycling rule the symbol $(\cdot)$ refers to a mid side node of the main triangle. The application in plastic and shakedown analysis requires the definition of the yield admissibility conditions. To this aim, the vector function $\boldsymbol{f}[\boldsymbol{\beta}_e] = [f[\boldsymbol{\sigma}^1], f[\boldsymbol{\sigma}^2], f[\boldsymbol{\sigma}^3]$ is introduced to check the plastic admissibility for the element, decoupled at the stress region level

$$\boldsymbol{f}[\boldsymbol{\beta}_e] \leq \boldsymbol{0} \quad \Rightarrow \quad f[\boldsymbol{\sigma}^i] \leq 0, \;\; i = 1, \ldots, 3 \tag{18}$$

The proposed finite element model is based on simple descriptions of the generalized displacement and stress fields. As it is shown in [10, 11] the resulting discrete operators have a compact form and the computer implementation of the model is very light.

2.2 The Mixed 3D Finite Element

With reference to 3D problems, a composite tetrahedral mesh is assumed over the domain lying in the (x, y, z) space. Within each tetrahedral element the displacement field is described by a continuous interpolation expressed in terms of parameters located on its boundary sides, while the stress field is represented by a discontinuous description obtained by introducing a subdivision of the element into four tetrahedral regions. Each face of the element is a triangle with six nodes [9]. The tetrahedral volume co-ordinate system makes the description of the relevant quantities of the discrete model compact and simple. The tetrahedral co-ordinates $(\xi_1, \xi_2, \xi_3, \xi_4)$ are related to the Cartesian ones (x, y, z) by the transformation [9]

$$\begin{bmatrix} 1 \\ x \\ y \\ z \end{bmatrix} = \begin{bmatrix} 1 & 1 & 1 & 1 \\ x_1 & x_2 & x_3 & x_4 \\ y_1 & y_2 & y_3 & y_4 \\ z_1 & z_2 & z_3 & z_4 \end{bmatrix} \begin{bmatrix} \xi_1 \\ \xi_2 \\ \xi_3 \\ \xi_4 \end{bmatrix} \Rightarrow \begin{bmatrix} \xi_1 \\ \xi_2 \\ \xi_3 \\ \xi_4 \end{bmatrix} = \frac{1}{6V} \begin{bmatrix} a_1 & b_1 & c_1 & d_1 \\ a_2 & b_2 & c_2 & d_2 \\ a_3 & b_3 & c_3 & d_3 \\ a_4 & b_4 & c_4 & d_4 \end{bmatrix} \begin{bmatrix} 1 \\ x \\ y \\ z \end{bmatrix} \tag{19}$$

where V is the element volume and the coefficients a_i, b_i, c_i, d_i are implicitly defined through (19). The integrals of the products between polynomial terms can be evaluated in closed form through the expression

$$\int_V \xi_1^\alpha \xi_2^\beta \xi_3^\gamma \xi_4^\delta dV = \frac{\alpha!\beta!\gamma!\delta!}{(\alpha+\beta+\gamma+\delta+3)!} 6V \tag{20}$$

The interpolations of the Mixed Tetrahedron presented here and denoted, from now on, as $\mathrm{MT}_{10/4}$ are based on 10 displacement nodes and 4 stress regions. The element displacement field $\boldsymbol{u}[\xi_1, \xi_2, \xi_3, \xi_4] = \{u, v, w\}^T$ is an interpolation as

$$\boldsymbol{u}[\xi_1, \xi_2, \xi_3, \xi_4] = \boldsymbol{\Phi}[\xi_1, \xi_2, \xi_3, \xi_4]\boldsymbol{u}_e, \quad \boldsymbol{\Phi} = \begin{bmatrix} \boldsymbol{\phi} & \mathbf{0} & \mathbf{0} \\ \mathbf{0} & \boldsymbol{\phi} & \mathbf{0} \\ \mathbf{0} & \mathbf{0} & \boldsymbol{\phi} \end{bmatrix} \tag{21}$$

where the matrix $\boldsymbol{\phi}$ collects the quadratic shape functions

$$\boldsymbol{\phi} = [\xi_1(2\xi_1 - 1),\ (2\xi_2 - 1)\xi_2,\ (2\xi_3 - 1)\xi_3,\ (2\xi_4 - 1)\xi_4,\\ 4\xi_1\xi_2,\ 4\xi_2\xi_3,\ 4\xi_3\xi_1,\ 4\xi_4\xi_1,\ 4\xi_4\xi_3,\ 4\xi_4\xi_2]$$

while the element displacement vector

$$\boldsymbol{u}_e^T = \left[u_1, \ldots, u_{10}, v_1, \ldots, v_{10}, w_1, \ldots, w_{10}\right] \tag{22}$$

collects the thirty displacement components of the ten nodes located at the vertices of the tetrahedral element and at the mid points of its sides (see Fig. 1).

The stress interpolation is assumed to be piece-wise constant over the element, allowing discontinuities within it. In particular, the stress components are taken as constant over each tetrahedral region defined by the element faces and the centroid (see Fig. 1). The stress components $\boldsymbol{\sigma}^i = [\sigma^i_{xx}, \sigma^i_{yy}, \sigma^i_{zz}, \sigma^i_{yz}, \sigma^i_{xz}, \sigma^i_{xy}]^T$ associated to each region V_i of the element are collected in the element vector of the stress parameters

$$\begin{aligned}\boldsymbol{\beta}_e = \Big[&\sigma^1_{xx}, \dots, \sigma^4_{xx}, \sigma^1_{yy}, \dots, \sigma^4_{yy}, \sigma^1_{zz}, \dots, \sigma^4_{zz},\\ &\sigma^1_{yz}, \dots, \sigma^4_{yz}, \sigma^1_{xz}, \dots, \sigma^4_{xz}, \sigma^1_{xy}, \dots, \sigma^4_{xy}\Big]^T\end{aligned} \tag{23}$$

The evaluation of the integral contribution over each region, by exploiting Eq. (20), is carried out analytically. In this way it is possible to obtain the following closed form expression of the equilibrium operator

$$\boldsymbol{D}_e^T = \frac{1}{96}\begin{bmatrix} \boldsymbol{b} & \boldsymbol{0} & \boldsymbol{0} & \boldsymbol{0} & \boldsymbol{d} & \boldsymbol{c} \\ \boldsymbol{0} & \boldsymbol{c} & \boldsymbol{0} & \boldsymbol{d} & \boldsymbol{0} & \boldsymbol{b} \\ \boldsymbol{0} & \boldsymbol{0} & \boldsymbol{d} & \boldsymbol{c} & \boldsymbol{b} & \boldsymbol{0} \end{bmatrix} \tag{24}$$

where the matrix $\boldsymbol{b}$ and $\boldsymbol{c}$ are defined in [12] Also in this case by introducing the vector function $\boldsymbol{f}[\boldsymbol{\beta}_e] = [f[\boldsymbol{\sigma}^1], f[\boldsymbol{\sigma}^2], f[\boldsymbol{\sigma}^3], f[\boldsymbol{\sigma}^4]]^T$, the plastic admissibility for the element stresses, decoupled at the stress region level, is simply imposed

$$\boldsymbol{f}[\boldsymbol{\beta}_e] \le \boldsymbol{0} \quad \Rightarrow \quad f[\boldsymbol{\sigma}^i] \le 0, \quad i = 1, \dots, 4 \tag{25}$$

2.3 FE Discrete Operators

Making $\boldsymbol{q}$ and $\boldsymbol{\beta}$ the global FE vectors and introducing the incidence element matrices for displacements $\boldsymbol{u}_e = \boldsymbol{T}_{eu}\boldsymbol{q}$ and stresses $\boldsymbol{\beta}_e = \boldsymbol{T}_{e\beta}\boldsymbol{\beta}$ we obtain, from the sum of all the element contributions to the stress-strain work (26), the compatibility/equilibrium operator

$$\sum_e \boldsymbol{\beta}_e^T \boldsymbol{D}_e \boldsymbol{u}_e = \boldsymbol{\beta}^T \boldsymbol{Q}\boldsymbol{q} \quad \text{with} \quad \boldsymbol{Q} \equiv \sum_e \left(\boldsymbol{T}_{\beta e}^T \boldsymbol{D}_e \boldsymbol{T}_{ue}\right) \tag{26}$$

Finally it is possible to obtain the global load vector $\boldsymbol{p}$ as

$$\sum_e \boldsymbol{u}_e^T \boldsymbol{p}_e = \boldsymbol{p}^T \boldsymbol{q} \quad \text{with} \quad \boldsymbol{p} \equiv \sum_e \left(\boldsymbol{T}_{ue}^T \boldsymbol{p}_e\right) \tag{27}$$

With these definitions the collapse multiplier is obtained as a solution of the nonlinear mathematical programming problem

$$\begin{aligned} &\text{maximize} && \lambda \\ &\text{subject to} && \boldsymbol{Q}^T\boldsymbol{\beta} - \lambda\boldsymbol{p} = \boldsymbol{0} \\ & && \boldsymbol{f}[\boldsymbol{\beta}] \leq \boldsymbol{0} \end{aligned} \tag{28}$$

2.4 Further Remarks on the Element Topology

It is worth remarking some aspects regarding the stress interpolation. The piecewise constant approximation of the stress components gives some advantages especially in the present context of analysis. The solution of plastic problems is characterized by discontinuities of the plastic deformation field in the domain [10] while the displacement field (plastic mechanism $\dot{\boldsymbol{u}}$) is continuous everywhere. A finite element designed to this aim needs to catch this behaviour even with few elements. The discontinuous interpolation for the stress field is particularly appreciable in plastic analysis where a fine grid, able to address the localization of the plastic deformation discontinuities, is desirable. Also, Le [13] has shown how a refinement technique aimed to better describe the plastic deformations improves results using a not fine everywhere finite element mesh. In the proposed model, the subgrid is intrinsic in the formulation and good behaviour is expected. Moreover, the mixed nature of the model allows for the introduction of static fields as primary variables of the finite element formulation by enriching the classical Morley element as shown in [14]. Here, the stress field is introduced as primary variables in the weighted problem formulation, by choosing the desired behaviour. The equilibrium equations are then coherently provided, as usual in the finite element technology by using the principle of virtual work. The proposed fields interpolations show both this desirable aspect and, also, fulfils equilibrium equations for zero volume loads in a simple manner, whereas higher order interpolations are typically used in conjunction with equilibrium conditions which reduce the number of independent parameters. In addition, this choice avoids any co-ordinate transformation which could introduce noise related to the mesh distortion.

Moreover, all the elements of this family present a balanced number of displacement and stress parameters. Indeed the number of the stress parameters equals the number of the displacement parameters minus the number of the components of the rigid body motion. This desired feature prevents a redundant description of the stress field which could introduce zero-energy modes with spurious oscillations in the numerical solution. This feature is usually achieved by following particular strategies. A wide class of isostatic mixed formulations can be obtained by adding some incompatible modes $\boldsymbol{u}_\lambda$ which give rise to auxiliary weighted equilibrium equations [15]. This filtering operation furnishes coefficients of the stress description which may depend on the geometry of the element and are usually expressed by very complicated formulas. In these cases often an approximate integration is carried out by using only the constant part of the Jacobian of the isoparametric map [16]. It is worth noting that this filtering effect, enforced through the orthogonality condition

$$\int_A \boldsymbol{\sigma}^T \boldsymbol{D}\boldsymbol{u}_\lambda dA = 0, \tag{29}$$

which tends to exclude the energy contributions associated with the redundant variables from the analysis, can fail for generic geometries.

The proposed mixed finite element has some affinities with models which are known as smoothed finite elements. Edge-based Smoothed (ES-FEM) [7], have been proposed [17] by using the Discrete Shear Gap (DSG) concept [18] to remove shear-locking phenomenon. These models work with background meshes and smoothing overlapping domains on which strains defined by average compatibility operators are assumed. The piece-wise assumption for the strains is near to the assumed stress interpolation of the present element.

The previous descriptions highlight the simplicity of the interpolations adopted for the stress and displacement fields and the compactness of the involved discrete operators.

3 Numerical Results

The good performances of the proposed model are investigated by performing some numerical tests. In particular the capability of the element in reproducing the plastic mechanism of classical 2D problems accurately without any deterioration in the solution when a dimension is small with respect to others in both in-plane bending dominated problems and stress concentration, is checked. The element also shows little sensitivity to the mesh distortion and no locking phenomenon is detected in problems simulating plane strain conditions. Finally a purely 3D test, analyzed in nearly incompressible conditions is performed in order to make an exhaustive picture of the element behaviour. Both the Von Mises and Drucker-Prager failure criterion are adopted in order to show how the stress assumption made is almost indifferent and how simple the numerical solution strategies are with respect to the shape of the yield surface.

3.1 Cook Problem

The following results refer to plastic analysis of the well investigated Cook membrane, reported in Fig. 4. The convergence of the numerical solution has been tested by using three meshes obtained by successive refinements of the coarse mesh (*mesh 1*), having four elements for each side. The analysis was carried out using both regular meshes (r.m.) and same-size irregular meshes (i.m.) constructed without the transfinite setting of the mesh generator GMSH [19].

Table 1 reports a comparison of the computed values of the plastic collapse multiplier and the number of iterations spent on each analysis. The reference result [5] was obtained using a mesh having 1024 elements and 2178 dofs while the finest mesh used in the present analysis has 512 triangular elements and 2112 dofs. The numerical values are also compared with the value furnished in [20] where a very refined mesh was used.

The plots in Fig. 5 show distribution of the plastic multiplier $\dot{\mu}$ obtained by using the Mises criterion, for the coarse and the finest regular mesh. The plastic mechanism furnished by the *mesh 3* is close to the result obtained with a much more refined mesh by [21].

3.2 Plate with a Circular Hole

The square plate with a central circular hole, subjected to a constant traction, is often used as a stress concentration test. The meshes are generated by splitting the right side and the top side into n parts and the remaining sides into $2n$ parts. The grids *mesh* 1, *mesh* 2 and *mesh* 3 refer to $n = 3, 6, 12$, respectively. Figure 6 shows the coarse mesh, in the regular and irregular versions.

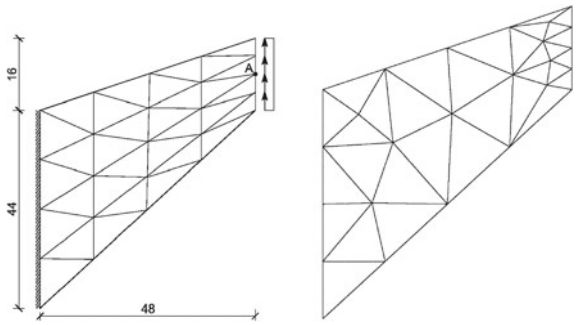

Fig. 4 Cook membrane. Regular and irregular coarse meshes

Table 1 Cook membrane. Plane stress limit analysis

	mesh 1	*mesh 2*	*mesh 3*
	(itrs)λ_c	(itrs)λ_c	(itrs)λ_c
$MT_{6/3}(r.m.)$	(15)0.3930	(30)0.3962	(34)0.3957
$MT_{6/3}(i.m.)$	(17)0.3913	(18)0.3928	(21)0.3945
$E-S$	(13)0.4151	(17)0.4012	(36)0.3970
$N-S$	(13)0.3888	(17)0.3883	(28)0.3935
Reference [5]			0.3956
Reference [20]			0.3955

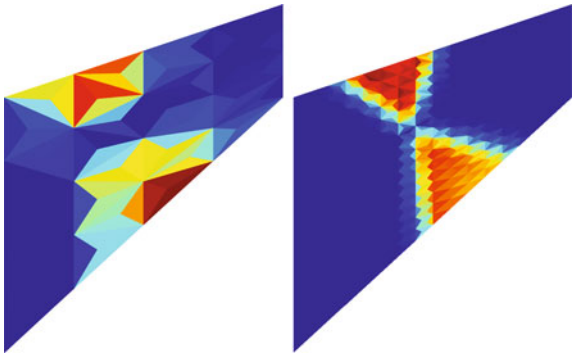

Fig. 5 Cook membrane. Distribution of the plastic multiplier for the coarse and the finest regular mesh

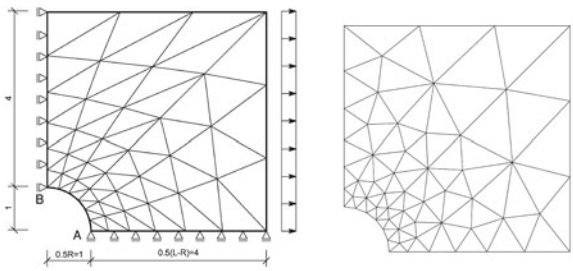

Fig. 6 Square plate with circular hole. Coarse regular and irregular meshes

The numerical values of the collapse multipliers, computed in plane stress condition and by using the Mises criterion, are compared in Table 2 for the three meshes. It is worth noting that the accurate reference results [5] were computed with 4802 dofs, 2304 elements and 9216 admissibility constraints while the finest mesh of the present analysis has 4704 dofs, 1152 elements and uses 3456 constraints. The exact collapse value has been computed with the analytical formula [22]

$$\lambda_c \, t = (1 - \frac{R}{L})\sigma_y \tag{30}$$

Table 2 Square plate with circular hole. Plane stress limit analysis

	mesh 1	*mesh 2*	*mesh 3*
	(itrs)λ_c	(itrs)λ_c	(itrs)λ_c
$MT_{6/3}$(rm)	(24)0.8042	(29)0.8019	(36)0.8007
$MT_{6/3}$(im)	(31)0.8071	(30)0.8022	(36)0.8014
$E-S$	(13)0.8157	(15)0.8067	(25)0.8032
$N-S$	(14)0.8084	(28)0.8027	(30)0.8011
Reference [23]			0.8006
Exact			0.8000

Figure 7 shows the distributions of the plastic multiplier computed by using the coarse and the finest mesh.

3.3 Square Metal Plate

Square metal plates with clamped or simply supports will be tested first. The problems were analyzed using the top right quarter as shown in Fig. 8. The convergence analysis of the numerical solution has been studied using three meshes, having respectively 8, 12 and 16 elements for each side. The analysis was carried out with various ratio of slenderness L/t, different boundary conditions (simply supported (SS) and clamped (C)), and using both uniform and graded meshes constructed as shown in Fig. 8.

Tables 3, 4, 5 and 6 compare the present results with those obtained in [13], showing good agreement between solutions obtained by two methods. The optimiza-

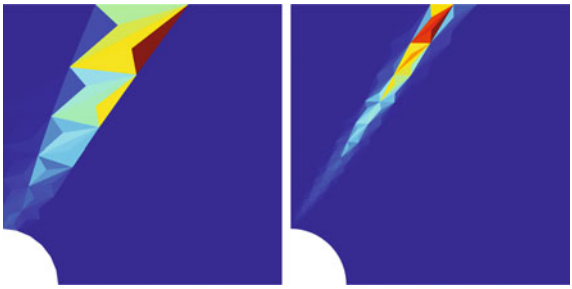

Fig. 7 Square plate with circular hole. Plastic multiplier distributions for *mesh* 1 and *mesh* 3

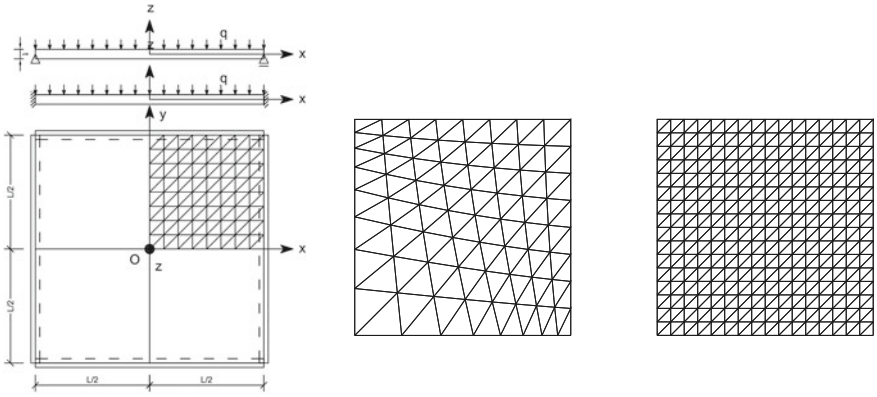

Fig. 8 Square plate: Load and boundary condition (*left*) graded (*middle*) and uniform (*right*) finite element mesh

Table 3 Clamped square plate: computed plastic collapse load using uniform meshes

L/t	*mesh 1* (736, 128)	*mesh 2* (1680, 288)	*mesh 3* (3008, 512)	Uniform mesh [13]
	λ	λ	λ	
1	9.04 (0.88)	8.93 (1.66)	8.88 (3.00)	9.02
4	30.51 (0.77)	30.13 (1.44)	29.93 (2.73)	31.46
10	42.16 (0.74)	41.57 (1.33)	41.24 (2.39)	43.37
40	46.89 (0.67)	45.80 (1.28)	45.27 (2.43)	46.57
50	47.38 (0.69)	46.11 (1.33)	45.50 (2.43)	–
100	48.56 (0.82)	47.02 (1.21)	46.23 (2.31)	46.84

Mesh name (the number of degrees of freedoms, the number of elements)

Table 4 Clamped square plate: computed plastic collapse load using graded meshes

L/t	*mesh 1*	*mesh 2*	*mesh 3*	Adaptive mesh [13]
	λ	λ	λ	λ
1	8.93	8.84	8.81	8.82
4	30.16	29.84	29.70	
10	41.46	40.97	40.76	
40	45.60	44.82	44.53	
50	45.90	45.02	44.69	
100	46.80	45.60	45.12	45.58

Table 5 Simply supported square plate: computed plastic collapse load using uniform meshes

L/t	*mesh 1* (768, 128)	*mesh 2* (1728, 288)	*mesh 3* (3072, 512)	Uniform mesh [13]
	λ	λ	λ	λ
1	9.03 (0.93)	8.93 (1.60)	8.87 (2.73)	9.03
4	23.34 (0.77)	23.37 (1.33)	23.38 (2.24)	23.88
10	24.66 (0.77)	24.69 (1.52)	24.70 (2.51)	24.85
40	24.97 (0.77)	24.98 (1.34)	24.99 (2.28)	25.03
50	24.99 (0.80)	24.99 (1.28)	24.99 (2.28)	–
100	25.03 (0.62)	25.01 (1.15)	25.01 (2.21)	25.05

tion CPU time took to solve the resulting conic optimization problem is indicated in brackets.

Collapse load multipliers against the number of degrees of freedom and nonlinear constraints for thin plate ($L/t = 100$) are also shown in Figs. 9 and 10. The reference values were taken from [13] where 3 Gauss points were used for the the integration along half the thickness (hence, the number of nonlinear constraints is equal to $3 \times N_{ed}$, N_{ed} is the number of edges or smooth regions). These figures show that

Table 6 Simply supported square plate: computed plastic collapse load using graded meshes

L/t	*mesh 1*	*mesh 2*	*mesh 3*
	λ	λ	λ
1	8.92	8.84	8.80
4	23.34	23.36	23.37
10	24.66	24.68	24.69
40	24.98	24.98	24.99
50	25.00	25.00	25.00
100	25.03	25.02	25.02

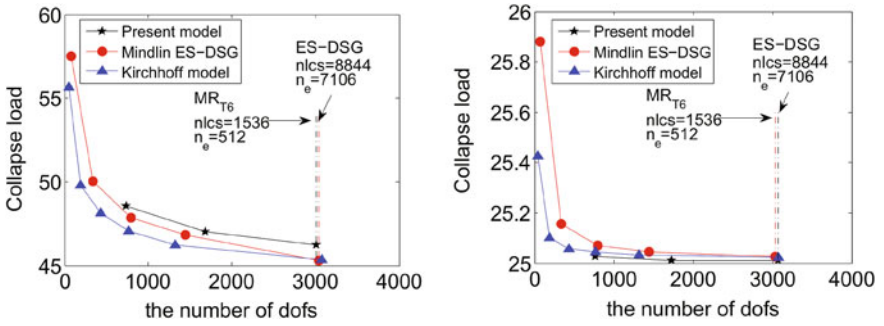

Fig. 9 Square thin plate: collapse load versus the number of degrees of freedom (dofs). Clamped plate (*left*) and simply supported plate (*right*)

when a closely identical number of degrees of freedom was used, the present model results in a very much smaller number of nonlinear constraints than that of ES-DSG based formulation. This means that the present model can reduce effort to solve the resulting optimization, as illustrated by CPU optimization time in Fig. 11. It is also worth noting that kinematical degrees of freedom only involve in equality constraints in the problem (28), being very much different from the ES-DSG based formulation where these kinematical variables also appear in conic constraints. Furthermore, in the thin plate limit ($L/t = 100$) shear deformable plates tend to Kirchhoff's plates behaviour, hence it is meaningful for a comparison between the two solutions. It is evident that the present method can provide lower (safer) collapse multipliers than the reference results given in [14] using Kirchhoff model.

Plastic multiplier distribution for clamped plate and simply supported plate are respectively illustrated in Figs. 12 and 13, where the uniform mesh of the Fig. 8 is used. It can be observed that for a perfect shear plate plastic multiplier is localized in regions close to boundaries, and plastic multiplier distribution for clamped and simply supported plates are virtually identical. Furthermore, these plastic multiplier patterns are clearly identified in the form of yield lines.

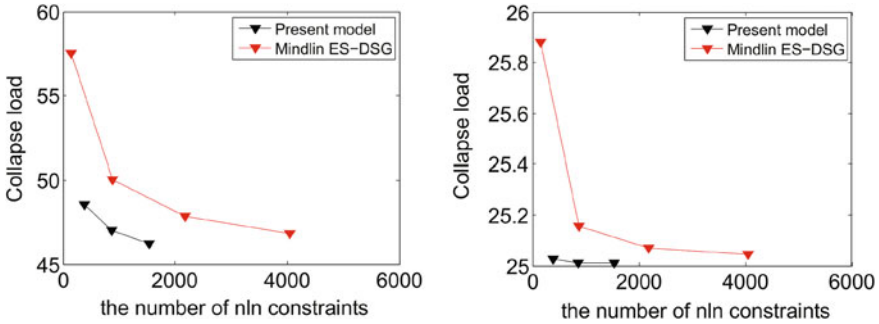

Fig. 10 Square thin plate: collapse load versus the number of nonlinear (nln) constraints. Clamped plate (*left*) and simply supported plate (*right*)

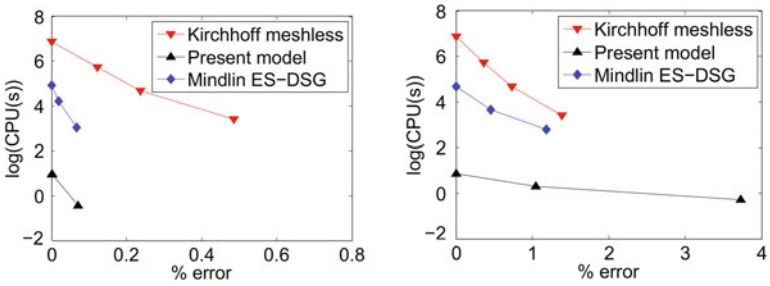

Fig. 11 Square thin plate: collapse load versus optimization CPU time. Clamped plate (*left*) and simply supported plate (*right*). Kirchhoff meshless optimization CPU time was taken from [24]

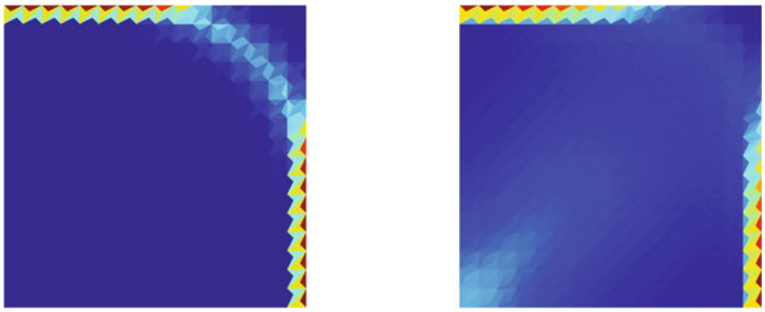

Fig. 12 Square clamped plate: plastic multiplier distribution. Perfect shear $L/t = 1$(*left*) and perfect bending $L/t = 100$ (*right*)

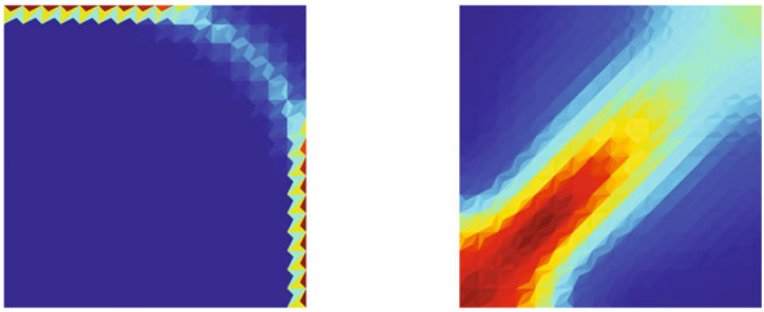

Fig. 13 Simply supported square plate: plastic multiplier distribution. Perfect shear $L/t = 1$(*left*) and perfect bending $L/t = 100$ (*right*)

3.4 An L-Shaped Metal Plate

The next example comprises the benchmark of L-shaped plate subjected to a uniform load as plotted in Fig. 14. The edges of dimension $L/2$ are divided into 4, 6 and 8 elements for both uniform and graded mesh refinement. Boundary conditions and finite element meshes are also shown in Fig. 14. The performance of the model is tested with various slenderness ratios L/t. For thin plate problem, an upper bound of $\lambda^+ = \frac{32}{3\sqrt{3}} = 6.16$ can be obtained using yield line theory with the particular mechanism as a yield line crossing the middle of the plate.

Computed results using the proposed method with uniform mesh are reported in Table 7. It can be seen that the present solutions are in good agreement with those obtained using the ES-DSG method and uniform refinement [13].

Present results for perfect shear and bending plates using graded meshes were compared with ES-DSG solutions using the adaptive mesh strategy presented in [13], see Table 8. Convergence analysis of a thin plate is also shown in Fig. 15. It is evident that the present mixed finite elements can provide more accurate solu-

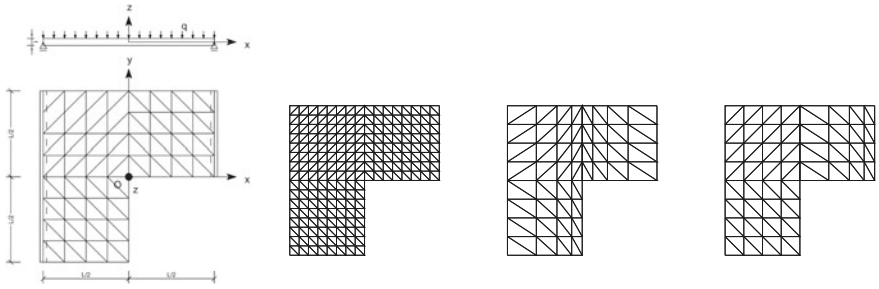

Fig. 14 L-shaped plate: Geometry and loading, uniform, graded bending and graded shear finite element mesh

tions than the adaptive ES-DSG method while the number of elements used in the present procedure is smaller than in ES-DSG.

The plastic multipliers for both perfect shear and bending plates were also plotted in Fig. 16, using the graded shear and graded bending meshes of Fig. 14, respectively.

3.5 3D Vertical Cut

The last test regards the 3D problem as can be seen in Fig. 17 and also analyzed in [25] where it is proposed in order to check the robustness of the finite element formulations with respect to a condition of incompressible elasticity. The problem domain, as can seen in the Figure, is composed of two distinct volumes. The small volume, $5 \times 5 \times 1$, is practically rigid and used to apply the vertical load of 0.01. The second volume, $10 \times 10 \times 10$, is characterized by $E = 1000$, $\nu = 0.499$ and

Table 7 L-shaped plate: plastic collapse load using uniform mesh

	mesh 1 (623, 96)	*mesh 2* (1367, 216)	*mesh 3* (2399, 384)	ES-DSG uniform [13]
	λ	λ	λ	λ
1	3.91	3.84	3.80	3.85
4	5.96	5.92	5.91	6.00
10	6.16	6.09	6.07	6.14
40	6.41	6.26	6.20	6.26
50	6.44	6.29	6.22	–
100	6.50	6.34	6.27	6.34

Table 8 L-shaped plate: plastic collapse load using graded mesh

	mesh 1 (623, 96)	*mesh 2* (1367, 216)	*mesh 3* (2399, 384)	Adaptive ES-DSG [13]
	λ	λ	λ	λ
1	3.81	3.76	3.75	3.73
100	6.32	6.22	6.19	6.18

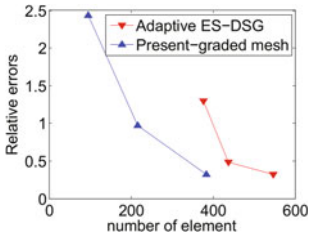

Fig. 15 L-shaped plate: convergence analysis for prefect bending

Fig. 16 L-shaped plate: plastic multipliers distribution, perfect shear (*left*) and prefect bending (*right*)

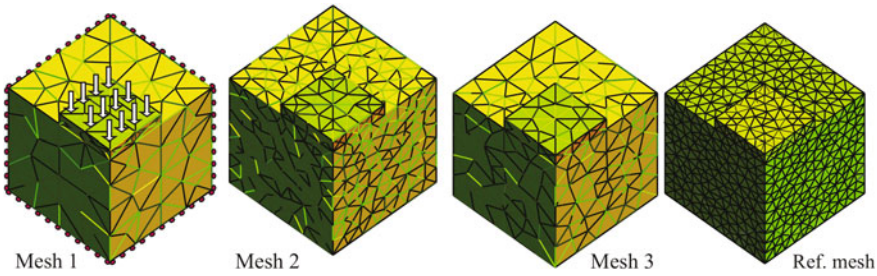

Fig. 17 3D vertical cut. Description of the problem and discretization meshes used in the analysis

$\bar{\sigma}_y = 0.01$. The two vertical faces under the area of application of the load are totally free and the other two vertical faces together with the bottom face are constrained in the normal direction.

Table 9 shows the analysis reports relative to the 3 meshes considered by comparing the elements $CT_{10/4}$, $CT_{10/5}$ and $MT_{10/4}$. As can be observed, the higher accuracy of the $MT_{10/4}$ element is even more evident with an error ranging from 17.2%, for *Mesh 1*, to 0.3% for *Mesh 3*. On the contrary the other elements start with an error equal to 22.7% and finish with an error of 3.4%, see also Fig. 18. The reference collapse multiplier was obtained by using the mesh reported in Fig. 17 which has 4467 $CT_{10/5}$ elements and 22878 dofs.

Figure 19 shows the plot of the equivalent plastic strain field for *Mesh 1* and *Mesh 3* and for each kind of finite element formulation compared here.

In Table 10 the FEM model is employed to test its effectiveness when the Drucker-Prager yield criteria is described as intersections of cones. Different friction angles are used in performing the analysis and the algorithm shows no sensitivity in terms of iterations with respect the constitutive parameters.

The reference results have been obtained by considering a mesh with 4476 elements and 21263 dofs.

Table 9 3D vertical cut. Analysis report

	Mesh 1 (dofs 2946)					*Mesh 2* (dofs 5220)					*Mesh 3* (dofs 10155)				
	λ_c	Loops	CPU_l	Steps	CPU_s	λ_c	Loops	CPU_l	Steps	CPU_s	λ_c	Loops	CPU_l	Steps	CPU_s
$CT_{10/4}$	1.9633	111	0.51	32	1.78	1.7533	114	1.70	34	5.70	1.6552	126	4.60	37	15.65
$CT_{10/5}$	1.9652	102	0.56	29	1.96	1.7535	138	1.70	38	6.19	1.6560	145	4.50	40	16.30
$MT_{10/4}$	1.8771	120	0.60	34	2.10	1.6959	127	1.84	37	6.31	1.6059	140	4.68	40	16.40

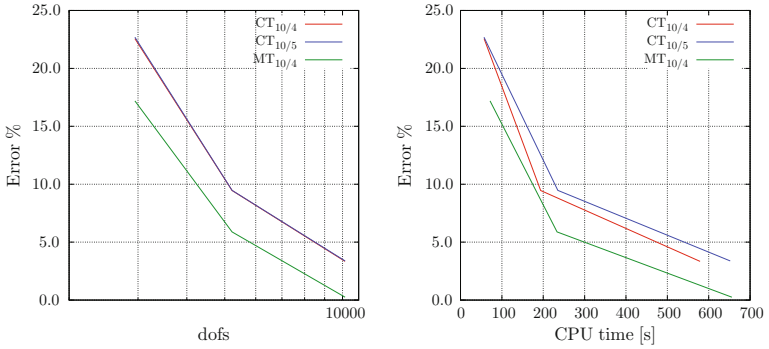

Fig. 18 3D vertical cut. Error in the evaluation of the collapse load multiplier versus the number of degrees of freedom (**a**) and the CPU time (**b**)

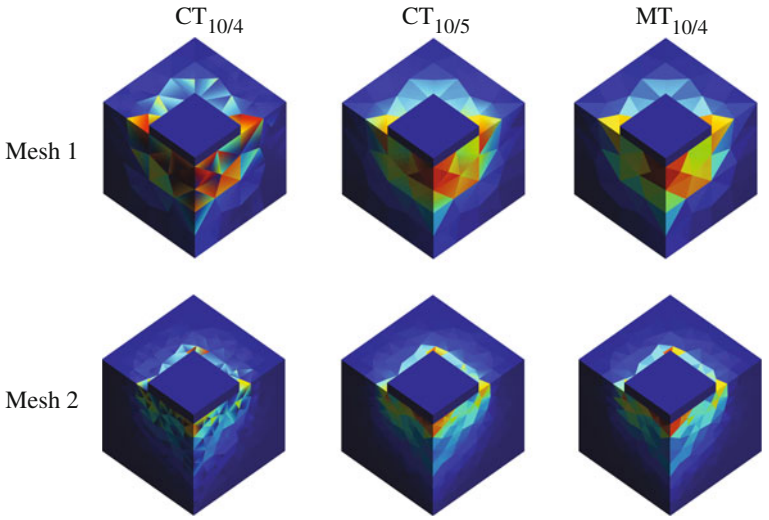

Fig. 19 3D vertical cut. Comparison of the equivalent plastic strain field contour maps relative to the collapse condition

Table 10 3D vertical cut. Limit analysis Drucker-Prager, coesion = 1

	Mesh 1	*Mesh 2*	*Mesh 3*	Reference
	(Loops, CPU)λ_c	(Loops, CPU)λ_c	(Loops, CPU)λ_c	
$MT_{10/4}(\varphi = 20°)$	(18, 1.61) 3.5488	(17, 6.82) 3.2858	(17, 37.94) 3.1968	3.1456
$MT_{10/4}(\varphi = 30°)$	(17, 1.62) 3.7810	(17, 7.14) 3.5447	(17, 39.16) 3.4775	3.4140
$MT_{10/4}(\varphi = 40°)$	(16, 1.62) 3.8435	(17, 7.19) 3.6613	(16, 39.08) 3.5934	3.5439

4 Concluding Remarks

We have proposed a family of mixed composite finite elements based on triangular and tetrahedral meshes for the analysis of plane problems, Reissner-Mindlin plates and 3D problems. The main features of the models are the simplicity and easy implementation within existing computational tools. The efficiency of the models derives from the balanced choice of the interpolations used to describe the displacements and stress fields which prevents spurious energy modes. In particular, the piece-wise constant description of the stress field allows the discontinuities inherent in the plastic solution.

The numerical experimentation of the models, which was carried out on a wide set of problems and data, shows the performance of the models. It is worth noting that the models prove able to furnish very accurate results by employing moderately fine meshes and this is of great interest in technical applications.

The experiments also demonstrate the robustness of the proposed finite elements. The elements are locking-free. The numerical results are stable for both regular and irregular meshes and do not degenerate when marked distortions are present.

In the analysis of plastic collapse states the accurate results achieved in the evaluation of the collapse multiplier and in the description of the collapse mechanism demonstrate that the elements are able to approximate well the discontinuous fields generated by the plastic behavior.

References

1. Bathe K (1996) Finte element procedures. Prentice Hall
2. Nagtegaal J, Parks D, Rice J (1974) On numerically accurate finite element solutions in the fully plastic range. Comput Methods Appl Mech Eng 4
3. de Souza Neto E, Perić D, DRJ O (2008) Computational methods for plasticity. Wiley
4. Capsoni A, Corradi L (1997) A mixed finite element model for plane strain-plastic analysis part i. formulation and assessment of the overall behaviour. Comput Methods Appl Mech Eng 141:67–79
5. Bilotta A, Leonetti L, Garcea G (2011) Three field finite elements for the elastoplastic analysis of 2d continua. Finite Elem Anal Des 47:1119–1130
6. Liu G, Nguyen-Thoi T, Nguyen-Xuan H, Lam K (2009) A node-based smoothed finite element method (ns-fem) for upper bound solutions to solid mechanics problems. Comput Struct 87:14–26
7. Liu G, Nguyen-Thoi T, Lam K (2009) A edge-based smoothed finite element method (ES-FEM) for static, free and forced vibration analyses of solids. J Sound Vib 320:1100–1130
8. Guo Y, Ortiz M, Belytschko T, Repetto E (2000) Triangular composite finite elements. Int J Numer Methods Eng 47:287–316
9. Zienkiewicz O, Taylor R (1989) The finte element method. McGraw-Hill
10. Leonetti L, Aristodemo M (2015) A composite mixed finite element model for plane structural problems. Elem Anal Des 94:33–46
11. Leonetti L, Le CV (2016) Plastic collapse analysis of mindlin-reissner plates using a composite mixed finite element. Int J Numer Methods Eng 105(12)
12. Bilotta A, Garcea G, Leonetti L (2016) A composite mixed finite element model for the elasto-plastic analysis of 3d structural problems. Finite Elem Anal Des 113:45–53

13. Le C (2013) A stabilized discrete shear gap finite element for adaptive limit analysis of mindlin-reissner plates. Int J Numer Methods Eng 96:231–246
14. Le C, Nguyen-Xuan H, Nguyen-Dang H (2010) Upper and lower bound limit analysis of plates using fem and second order cone programming. Comput Struct 88:65–73
15. Taylor R, Beresfort P, Wilson EA (1976) Non-conforming element for stress analysis. Int J Nume Methods Eng 10:1211–1219
16. Bilotta A, Casciaro R (2002) Assumed stress formulation of high order quadrilateral elements with an improved in-plane bending behaviour. Comput Methods Appl Mech Eng 191:1523–1540
17. Nguyen-Xuana H, Liu G, Thai-Hoangd C, Nguyen-Thoi T (2010) An edge-based smoothed finite element method (ES-FEM) with stabilized discrete shear gap technique for analysis of reissner-mindlin plates. Comput Methods Appl Mech Eng 199:471–489
18. Bletzinger K, Bischoff M, Ramm E (2000) A unified approach for shear-locking free triangular and rectangular shell finite elements. Comput Struct 75:321–334
19. Geuzaine C, Remacle J (2009) Gmsh: a three-dimensional finite element mesh generator with built-in pre- and post-processing facilities
20. Ciria H, Peraire J, Bonet J (2008) Mesh adaptive computation of upper and lower bounds in limit analysis. Int J Numer Methods Eng 75(8):899–944. doi:10.1002/nme.2275
21. Le C, Nguyen-Xuan H, Askes H, Bordas S, Rabczuk T, Nguyen-Vinh H (2010) A cell based smoothed finite element method for kinematic limit analysis. Int J Numer Methods Eng 83(10):1651–1674
22. Tran T, Liu G, Nguyen-Xuan H, Nguyen-Thoi T (2010) An edge-based smoothed finite element method for primal-dual shakedown analysis of structures. Int J Numer Methods Eng 82(7):917–938
23. Bilotta A, Leonetti L, Garcea G (2012) An algorithm for incremental elastoplastic analysis using equality constrained sequential quadratic programming. Comput Struct 102–103:97–107
24. Le C, Gilbert M, Askes H (2010) Limit analysis of plates and slabs using a meshless equilibrium formulation. Int J Numer Methods Eng 83:1739–1758
25. Cervera M, Chiumenti M, Valverde Q, de Saracibar AC (2003) Mixed linear/linear simplicial elements for incompressible elasticity and plasticity. Comput Methods Appl Mech Eng 192:5249–5263

Recent Progress on Lower-Bound Shakedown Analysis of Road Pavements

J. Wang, S. Liu and H.S. Yu

Abstract Shakedown theory has been recognised as a more rational basis for structural design of flexible road pavements. A lower-bound shakedown approach, which aims to find the maximum design load of a pavement structure, was developed by the University of Nottingham, that forms part of efforts among other researchers' in applying shakedown theory in pavement designs. The lower-bound shakedown solutions were consistent with existing shakedown solutions assuming that the materials are isotropic and homogeneous following an associated plastic flow rule. Recently, this lower-bound approach was further developed to consider more realistic cases. Both two-dimensional and three-dimensional shakedown analyses were carried out taking into account cross-anisotropic or heterogeneous materials, the properties of which were programmed into a finite element software ABAQUS. For pavement materials obeying a non-associated flow rule, the corresponding two-dimensional lower-bound shakedown limits were also estimated by extending the lower-bound shakedown approach. A numerical step-by-step approach was also applied to address the non-associated problems and obtained similar results. Through these studies, influences of the original assumptions on the shakedown-based pavement designs can be assessed.

J. Wang (✉) · S. Liu
Ningbo Nottingham New Materials Institute, The University of Nottingham Ningbo China, Ningbo 315100, China
e-mail: juan.wang@nottingham.edu.cn

S. Liu · H.S. Yu
Nottingham Centre for Geomechanics, The University of Nottingham, Nottingham NG7 2RD, UK

H.S. Yu
Faculty of Engineering, University of Leeds, Leeds LS2 9JT, UK

O. Barrera et al. (eds.), *Advances in Direct Methods for Materials and Structures*, DOI 10.1007/978-3-319-59810-9_8

1 Introduction

Current analytical design methods for flexible pavements are usually conducted by relating pavement life with elastic stress/strain at critical locations considering several principle failure modes. One major limitation of the analytical design approach is that strength properties of pavement materials are not well considered, especially for the rutting failure which is attributed to material plasticity. A new design approach based on the shakedown concept is more rational for the design of flexible pavements as it can consider the plastic properties of pavement materials.

On the one hand, shakedown phenomena of flexible road pavements have been observed by a number of researchers through wheel tracking tests and field data [6, 7, 13, 20, 33, 44, 45, 47]. Compared with conventional cyclic triaxial tests (e.g. [14, 26–28, 46, 56–59] in which the effect of principle stress rotation in pavements were not considered, the wheel tracking tests can account for the real situation of moving wheel loads. Brown et al. [6] validated the shakedown concept in four types of soils and granular materials by using a small wheel tracking apparatus and a slab test facility at the University of Nottingham (UoN). The experiments were extended to two-layered and three-layered granular systems by Brown et al. [7]. Liu [33] further validate the shakedown concept for bituminous pavement structures by conducting a series of wheel tracking tests on a layered bituminous pavement structure at the UoN.

On the other hand, shakedown analyses of pavements concerning the determination of shakedown limits have been carried out by a number of authors using the classical lower-bound/upper-bound shakedown theorems of Melan [34] and Koiter [22] or numerical elastic-plastic analyses [31, 52–54]. In 1984, Sharp and Booker first stated that the shakedown analysis can be used as a useful tool in pavement design. They reduced the pavement shakedown problem as a problem dependent on the depth only, and proposed a method of conics. Raad et al. [40] proposed a numerical shakedown approach using a finite element formulation coupled with an optimisation technique. The influences of thickness and material properties of the granular layer and the asphalt concrete layer on the shakedown behaviour were examined in detail in their following papers [2, 41, 42]. Radovsky and Murashina [43] presented an analytical approach for the shakedown problem of a two-dimensional (2D) plane strain pavement model. Experimental studies were also conducted to determine the general distribution of horizontal residual stresses in soils. Yu and Hossain [60] developed a linear programming technique to perform shakedown analysis of pavements using a stress-based finite element (FE) with a discontinuous residual stress field. It is then extended to layered pavements in Shiau and Yu [48] and three dimensional (3D) problems in Shiau [49]. Yu [61] proposed an analytical solution for shakedown of a cohesive-frictional half-space under a moving Hertz load using Melan's static shakedown theorem. This solution provides the same 2D shakedown limits as those in Collins and Cliffe [8] which were obtained based on the upper-bound shakedown theorem while assuming a failure mechanism of subsurface slip. In the case of cohesive material, the obtained

shakedown limits are also close to the three-dimensional (3D) upper bound shakedown solutions of Ponter et al. [37]. Yu and Wang [62] further developed a rigorous lower-bound solution to the 3D pavement shakedown problem by searching for a critical self-equilibrated residual stress field using an optimisation procedure. In addition, Krabbenhaft et al. [23] and Zhao et al. [65] suggested a scanning line method to find the lower-bound shakedown limits of plane strain half-space under moving surface loads. The influences of different load distributions on the shakedown limits were examined. Nguyen and his co-authors [35, 36] proposed an interior-point method based on the lower-bound shakedown theorem to solve 2D and 3D shakedown problems with Mohr-Coulomb or Tresca materials. They also mentioned that the interior-point can be easily extended to more complicated materials including the viscosity of asphalt, non-associated plasticity and the presence of pore-water. In terms of the application of the kinematic shakedown theorem in the shakedown analysis, Collins et al. [9, 10] further extended Collins and Cliffe [8] method to obtain upper bound shakedown limits of pavements in both 2D and 3D. The method is then improved by introducing the rut failure mechanism [3, 11, 12], providing more realistic shakedown limits. A nonlinear numerical approach was developed by Li and Yu [29] to implement shakedown analysis in pavement applications by means of the kinematic shakedown theorem. It was further extended to a few cases considering a non-associated plastic flow rule [30]. Moreover, the linear matching method, originally proposed for limit and shakedown analyses of metal structures under static or cyclic load [15, 16, 38, 39], has been applied to the pavement shakedown problem using the Drucker-Prager yield criterion [4]. According to Boulbibane and Ponter [5], the basic idea of this method is that the stress and strain fields for the non-linear material behaviours may be simulated by the solution of linear problems where the linear moduli vary with time and space.

This paper aims to summarise the recent progress on the lower-bound shakedown analysis of road pavements. Of particular interest here is the UoN lower-bound shakedown method for pavements using a critical self-equilibrated residual stress field, as well as the extension of the method to account for pavements with non-standard materials, given the standard materials are homogenous isotropic materials following an associated plastic flow rule.

2 UoN Shakedown Analyses for Pavements with Standard Materials

A 3D lower-bound shakedown approach, which aims to find the maximum admissible load of pavement structures against rutting, has been developed in the UoN [52, 53, 61, 62]. The pavement materials are assumed to be isotropic homogenous materials following Mohr-Coulomb model. And the vertical planes along the wheel moving direction are considered as critical planes. Within these

planes, only the horizontal residual stresses can exist as a result of boundary conditions and equilibrium conditions. Those residual stresses together with the elastic stresses induced by a load p have to fulfil the Mohr-Coulomb yield criterion according to Melan's static shakedown theorem. This leads to the lower-bound shakedown condition for the pavements:

$$f = (\sigma_{xx}^{r} + \mathrm{M})^2 + \mathrm{N} \le 0, \tag{1}$$

where σ_{xx}^{r} is self-equilibrated,

$$\mathrm{M} = \lambda\sigma_{xx}^{e} - \lambda\sigma_{zz}^{e} + 2\ \tan\ \phi_n(\mathrm{c}_n - \lambda\sigma_{zz}^{e}\tan\ \phi_n),$$
$$\mathrm{N} = 4(1 + \tan^2\ \phi_n)[(\lambda\sigma_{xz}^{e})^2 - (\mathrm{c}_n - \lambda\sigma_{zz}^{e}\tan\ \phi_n)^2].$$

In Eq. 1, λ is a dimensionless load factor; ϕ is material friction angle, c is material cohesion; σ^{e} is load-induced elastic stress; $f(\sigma_{ij}) = 0$ is the yield condition for the material; σ^{r} is residual stress; the subscript n (n = 1, 2, 3 …) means the nth layer of the pavement structures; the subscripts x, y and z correspond to traffic moving direction, pavement transverse direction and vertical direction respectively. Tension positive notation is applied throughout the paper.

According to the self-equilibrium condition, a critical residual stress field is conceived by calculating $\min(-\mathrm{M_i} + \sqrt{-\mathrm{N_i}})$ (referred to as 'minimum larger root') or $\max(-\mathrm{M_i} - \sqrt{-\mathrm{N_i}})$ (referred to as 'maximum smaller root') at each depth z = j (i is the node number). The present shakedown problem can be written as a mathematical formulation:

$$\max\ \lambda,$$
$$\text{s.t.}\begin{cases} f(\sigma_{xx}^{r}(\lambda\sigma^{e}), \lambda\sigma^{e}) \le 0, \\ \sigma_{xx}^{r}(\lambda\sigma^{e}) = \min\limits_{z=j}(-\mathrm{M_i} + \sqrt{-\mathrm{N_i}})\ \text{or}\ .\sigma_{xx}^{r}(\lambda\sigma^{e}) = \max\limits_{z=j}(-\mathrm{M_i} - \sqrt{-\mathrm{N_i}}). \end{cases} \tag{2}$$

For each layer of a pavement structure, one maximum admissible λ could be found, marked as λ_{sd}^{n}, and therefore $\lambda_{sd}^{n}p$ is the shakedown limit of the nth layer. The minimum value among all $\lambda_{sd}^{n}p$ is then recorded as the shakedown limit of the pavement structure which is usually normalised by the material cohesion.

This approach can also be applied to the 2D pavement problems. Comparisons between the present solutions with existing results are shown in Fig. 1 for the special case of a homogenous half-space. A frictional coefficient μ is used representing a proportional relationship between surface traction q and normal pressure p (i.e. $\mu = q/p$). As shown in Fig. 1a, the present 2D shakedown solutions agree with the static shakedown solutions of Shiau [49] and Krabbenhaft et al. [23] in which the Hertz load distributions were adopted. Moreover, the present results lie between Sharp and Booker [47] lower-bounds and Li and Yu [29] upper-bounds in which the trapezoidal load distributions were applied. Note that Li and Yu [29] only presented the shakedown limits for the frictional coefficient from 0 to 0.5. In terms

of the 3D solutions (Fig. 1b), the present shakedown limits agree with the upper-bound shakedown limits of Ponter et al. [37] for cases $\mu = 0$ and $\mu \geq 0.3$. The difference between the present and Ponter's solution is largest when $\mu = 0.2$. The upper-bound shakedown limits of Collins and Boulbibane [12] and the numerical lower-bound shakedown limits of Shiau [49] are also presented in this figure using the uniform load distributions. As can be seen, Collins and Boulbibane's upper-bounds are much higher than other solutions. This is because a plane strain condition was assumed for the cross-section perpendicular to the travel direction and therefore the deformations are not fully three-dimensional. The numerical results of Shiau [49] indicate that the shakedown limits for the uniform load distributions are generally lower than those for the Hertz load distributions.

Apparently, the distribution of contact stress also has an effect on the shakedown limit. The influence of dual wheels is thus examined. In this case, the half-space is subjected to 2 Hz pressures with an axle distance (d) ranging from 3*a* to 8*a*, where *a* is half of the contact width. When *d*/*a* are 3, 4 and 8, the corresponding lower-bound shakedown limits are 8.64c, 8.76c and 8.89c respectively, compared with 8.90c for the case of a single wheel.

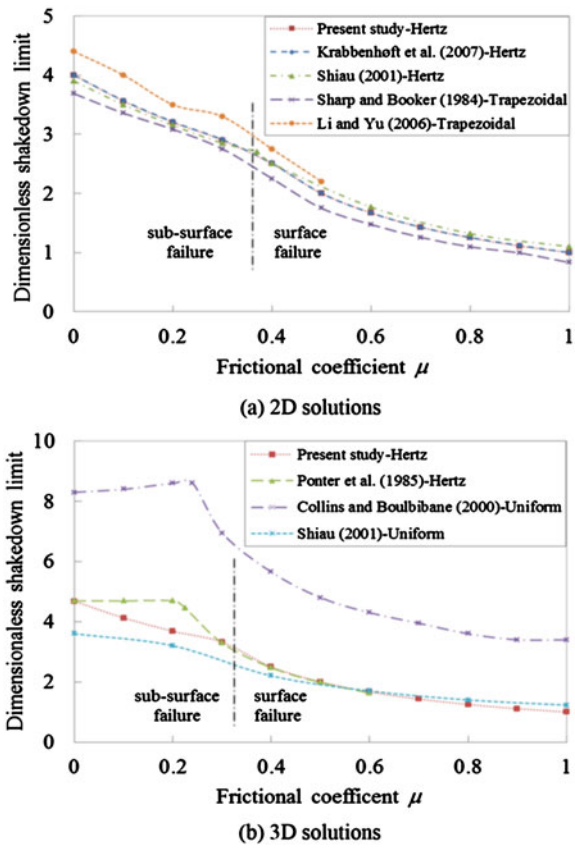

Fig. 1 Comparisons between present shakedown solutions and other shakedown solutions

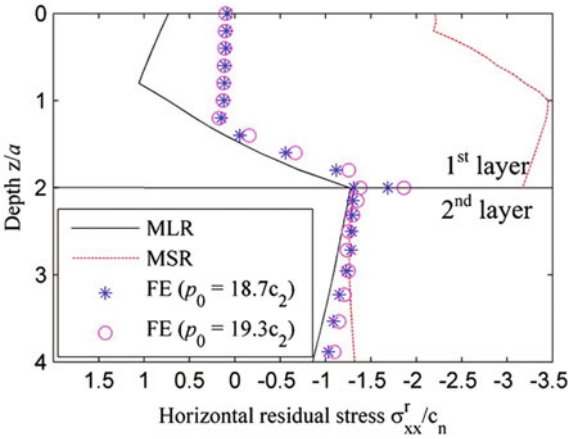

Fig. 2 Comparisons between critical residual stress fields (MLR and MSR) and FE calculated residual stress fields for a two-layered pavement

A numerical step-by-step approach was also developed by the UoN. 2D or 3D pavement models subjected to repeated moving traffic loads were established using a finite element software ABAQUS. After a number of load passes, residual stresses are fully developed within the pavement. A static load is then applied on the pavement surface to check if there is any further plastic strain. The shakedown limit can be determined by trying several loads with different magnitudes. The numerical shakedown results were compared with the lower-bound shakedown solutions and show good agreements [31–33, 52–54]. The maximum difference is within 5% for both single-layered and two-layered problems.

An advantage of the lower-bound shakedown approach is that the details of elastic-plastic stress fields are not required. However, the development of the residual stresses, as the main reason of the shakedown phenomenon, cannot be assessed. By using the numerical step-by-step approach, the development of the residual stresses was obtained. It was found that only when the load applied is no larger than the theoretical shakedown limit, the fully developed residual stresses can be bracketed by the critical residual stress fields calculated by Eq. 2, such as Fig. 2 where the shakedown limit is $18.7c_2$.

3 UoN Shakedown Analyses for Pavements with Non-standard Materials

3.1 Effect of Material Cross-Anisotropy

Soils and pavement materials deposited in the vertical direction tend to have the same properties in any horizontal direction but different properties in the vertical

direction. This is known as cross-anisotropy. Boulbibane et al. [2] first considered the cross-anisotropic effect in 2D pavements structures in which the soil cohesion changed with direction, i.e. strength anisotropy. Results showed that a higher cohesion ratio c_h/c_v (c_h and c_v are the cohesion in the horizontal and vertical directions respectively) resulted in a higher shakedown limit. Wang and Yu [55] considered 3D cross-anisotropic pavement materials and soils and investigated the influences of elastic and plastic anisotropy on the pavement shakedown limit in detail.

In the 3D problem, the behaviour of an elastic cross-anisotropic material can be fully described by five parameters, E_h, E_v/E_h, G_{vh}/G_h, υ_h and υ_{vh}, in which E_h is the Young's modulus in horizontal (H) direction; E_v is the Young's modulus in vertical (V) direction; G_h is the shear modulus in horizontal plane; G_{vh} is the shear modulus in VH plane; υ_h is Poisson's ratio (effect of horizontal strain on complementary horizontal strain); υ_{vh} is Poisson's ratio (effect of vertical strain on horizontal strain); υ_{hv} is Poisson's ratio (effect of horizontal strain on vertical strain). It has been found that typical values of E_v/E_h may range from 0.25 to 1.11 for clays and from 1.06 to 2 for sands [55]. Experimental data of Wang el al. [51] also show that the anisotropy of asphalt concrete under field compaction might also be approximated as cross-anisotropy with $E_v/E_h \approx 3.33$. Graham and Houlsby [19] further proposed that the elastic anisotropy of natural clays can be described by three parameters: E^* and υ^* and an anisotropic factor α by giving the following relationships: $E_v = E^*$, $E_h = \alpha^2 E^*$, $\upsilon_{hh} = \upsilon^*$, $\upsilon_{vh} = \upsilon^*/\alpha$, $G_{vh} = \alpha E^*/(2 + 2\upsilon^*)$, $G_{hh} = \alpha^2 E^*/(2 + 2\upsilon^*)$.

In the work of Wang and Yu [55], a generalised Mohr-Coulomb yield criterion is used to account for the strength anisotropy:

$$\begin{aligned} f = {} & (\sigma_{zz} - \sigma_{xx} - 2\sigma_{xz}\tan\phi)^2 + (c_v - c_h + 2\sigma_{xz} - \sigma_{xx}\tan\phi + \sigma_{zz}\tan\phi)^2 \\ & - (c_v + c_h - \sigma_{xx}\tan\phi - \sigma_{zz}\tan\phi)^2 \le 0. \end{aligned} \tag{3}$$

The lower-bound shakedown condition then can be written as:

$$f = (\sigma^r_{xx} + M)^2 + N + P \le 0, \tag{4}$$

where σ^r_{xx} is self-equilibrated,

$$\begin{aligned} M &= \lambda\sigma^e_{xx} - \lambda\sigma^e_{zz} + 2(c_h - \lambda\sigma^e_{zz}\tan\phi)\tan\phi, \\ N &= 4(\tan^2\phi + 1)[(\lambda\sigma^e_{xz})^2 - (c_h - \lambda\sigma^e_{zz}\tan\phi)^2], \\ P &= 4(c_v - c_h)[\lambda\sigma^e_{xz} - (c_h - \lambda\sigma^e_{zz}\tan\phi)]. \end{aligned}$$

Similarly, the above shakedown problem can be solved by searching for the maximum value of λ in the following formulation:

$$\max \lambda,$$
$$\text{s.t.} \begin{cases} f(\sigma^{r}_{xx}(\lambda\sigma^{e}), \lambda\sigma^{e}) \le 0, \\ \sigma^{r}_{xx}(\lambda\sigma^{e}) = \min\limits_{z=j}(-M_i + \sqrt{-N_i - P_i}) \text{ or } \sigma^{r}_{xx}(\lambda\sigma^{e}) = \max\limits_{z=j}(-M_i - \sqrt{-N_i + P_i}). \end{cases} \tag{5}$$

Parametric studies show that the shakedown limit of a homogenous cross-anisotropic half-space under moving loads is dominated by the Young's modulus ratio E_v/E_h for the cases of subsurface failure but by the shear modulus ratio G_{vh}/G_h for the cases of surface failure. The anisotropic shakedown limit varies with frictional coefficient μ and the peak value may not occur at $\mu = 0$ (i.e. normal load only). For layered pavement systems, detailed solutions can be found in Wang and Yu [55] and Yu et al. [63].

3.2 *Effect of Material Heterogeneity*

It is also commonly known that the property of a soil varies with the depth. A 2D rolling contact problem was first solved by Kapoor and Williams [21] considering that the hardness and the yield strength of a metal depend on the depth. Zhao et al. [64] examined the shakedown limit of a 2D Mohr-Coulomb half-space under moving loads in which material stiffness increases with the depth. The result demonstrated a greater shakedown limit compared to that of a homogenous case. Also, the increase is most prominent for the case of limited surface traction.

In the present study, the effect of material heterogeneity on the 3D shakedown limit is studied for a two-layered pavement. It assumes that the stiffness modulus at the surface of each layer is E_{0n} (n is layer number) and this modulus increases linearly with the depth z at a ratio of ρ_n/E_{0n} as shown in Fig. 3. This ratio is termed as a 'heterogeneous factor'. Typical results are presented for a two-layered pavement system with $E_{01}/E_{02} = 1.39$, $c_1/c_2 = 20$, $\nu_1 = 0.4$, $\nu_2 = 0.3$ and $\phi_1 = \phi_2 = 30°$. Figure 4 demonstrates that the rise of the heterogeneous factor of one layer reduces the shakedown limit of that layer but increases that of the other layer. Finally the shakedown limit of the pavement structure may will first increase then decrease with rising heterogeneous factor.

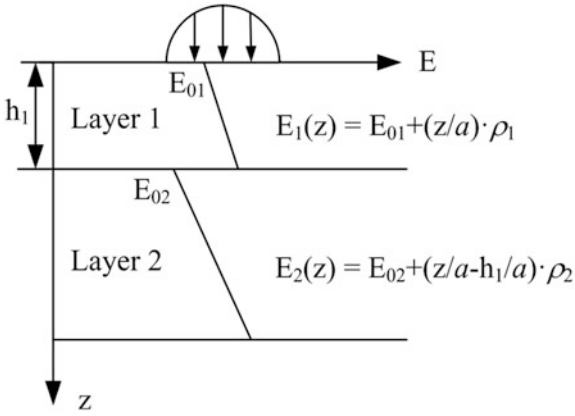

Fig. 3 Definition of heterogeneity problems

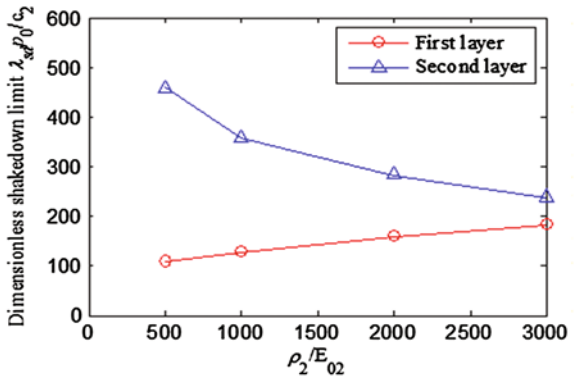

Fig. 4 Influence of material heterogeneity for a 3D two-layered pavement

3.3 *Effect of Plastic Flow Rule*

Soil and pavement materials also exhibit non-associated plastic behaviours [24, 25]. Until now, very limited shakedown results have been reported on this topic for soils and pavements. Boulbibane and Weichert [1] proposed a theoretical framework for the shakedown analysis of soils with a non-associated plastic flow. It was reported by Nguyen [35] that this framework can be applied to the shakedown analysis of footing problems. Using the linear matching method, Boulbibane and Ponter [5] were able to give 3D upper bound shakedown solutions for non-dilatant Drucker-Prager materials; however, the influence of the dilation angle was not evaluated. Numerical studies of Li [30] extended the 2D upper-bound shakedown solutions of Li and Yu [29] to the problems with materials following a non-associated plastic flow and suggested that the pavement upper-bound shakedown limit is reduced due to the use of the non-associated flow rule. The numerical step-by-step approach of Liu et al. [32] provide more shakedown limits for cases with a non-associated flow rule (i.e. $0 \leq \psi < \phi$, ψ is the dilation angle).

A direct method is also developed in the UoN to account for the influence of a non-associated plastic flow ($0 \leq \psi < \phi$). Following the works of Davis [17], Drescher and Detounay [18] and Sloan [50], this method assumes a fictitious material with a reduced strength. The following modified friction angle ϕ^* and cohesion c^* were used:

$$\tan\phi^* = \eta \tan\phi, \tag{6}$$

$$c^* = \eta c, \tag{7}$$

$$\eta = \frac{\cos\psi \cos\phi}{1 - \sin\psi \sin\phi}. \tag{8}$$

By replacing ϕ and c in Eq. 2 with ϕ^* and c^*, shakedown limits of pavements with Mohr-Coulomb materials following a non-associated plastic flow rule (defined by ϕ, ψ, c) can be obtained by solving the following mathematical formulation:

$$\max \lambda,$$
$$\text{s.t.} \begin{cases} f(\sigma^r_{xx}(\lambda\sigma^e), \lambda\sigma^e) \leq 0, \\ \sigma^r_{xx}(\lambda\sigma^e) = \min\limits_{z=j}(-M^*_i + \sqrt{-N^*_i}) \text{ or } \sigma^r_{xx}(\lambda\sigma^e) = \max\limits_{z=j}(-M^*_i - \sqrt{-N^*_i}). \end{cases} \tag{9}$$

where σ^r_{xx} is self-equilibrated,

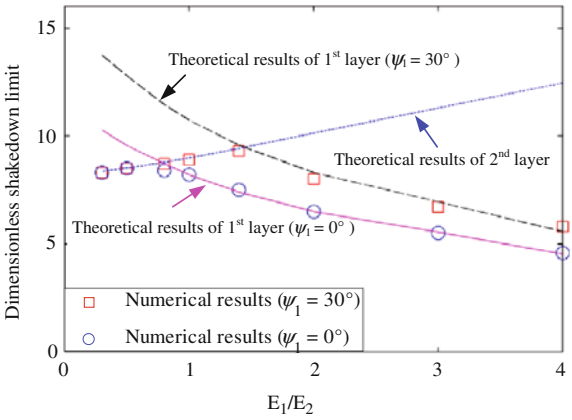

Fig. 5 Comparison of theoretical and numerical shakedown limits with varying stiffness ratio when $\phi_1 = 30°$, $\phi_2 = \psi_2 = 0°$, $c_1/c_2 = 1$, $h_1 = 2a$

$$M^* = \lambda\sigma^e_{xx} - \lambda\sigma^e_{zz} + 2\eta^2 \tan\ \phi(c - \lambda\sigma^e_{zz} \tan\ \phi),$$
$$N^* = 4(1 + \eta^2 \tan^2\ \phi)[(\lambda\sigma^e_{xz})^2 - \eta^2(c - \lambda\sigma^e_{zz} \tan\ \phi)^2].$$

Comparisons between the theoretical shakedown limits and the numerical results for a two-layered pavement system demonstrate good agreements (Fig. 5). The material of the first layer has a friction angle of $\phi = 30°$ and a dilation angle of $\psi = 30°$ or $0°$, while the second layer is a Tresca material (i.e. $\phi = \psi = 0°$). It should be noted: [1] shakedown limit of the pavement structure is the minimum one among the shakedown limits of all layers, and therefore the turning point indicates the change of failure location from one layer to another; [3] the variation of the first layer dilation angle only changes the shakedown limits of the first layer. When the dilation angle of the first layer is decreased from 30° to 0°, the shakedown limit of that layer is slightly reduced. Since the theoretical shakedown limits of the second layer do not change, the turning points of the non-associated cases deviate from those of the associated cases. Therefore, the shakedown limits for non-associated cases are smaller than those for associated cases when E_1/E_2 is relatively large ($E_1/E_2 \geq 0.8$), but remain the same when E_1/E_2 is small enough.

4 Concluding Remarks and Future Work

In summary, shakedown analyses for the pavement problem have been reviewed thoroughly. More specifically, the recent lower-bound studies on pavement shakedown at the UoN have been presented for both standard and non-standard materials. This forms part of the efforts in the UoN in the process of developing a shakedown-based design method for flexible road pavements. It has been found that the assumption of standard materials may lead to a different shakedown limit from the real one. Therefore, a reasonable prediction of the pavement shakedown limit

would require more accurate models for pavement materials and soils, as well as corresponding parameters such as anisotropic factors and dilation angle.

Large scale wheel tracking tests which can simulate the real moving loads are suggested for the validation of the pavement shakedown solutions. However, very limited experimental work was conducted in this aspect and more research efforts are required. Additionally, the influences of air temperature and loading frequency on the shakedown limits of bituminous pavements need to be further studied. It is also worth comparing the shakedown-based design method with the existing design methods.

References

1. Boulbibane M, Weichert D (1997) Application of shakedown theory to soils with non-associated flow rules. Mech Res Commun 24(5):513–519
2. Boulbibane M, Collins IF, Weichert D, Raad L (2000) Shakedown analysis of anisotropic asphalt concrete pavements with clay subgrade. Can Geotech J 37:882–889
3. Boulbibane M, Collins IF, Ponter ARS, Weichert D (2005) Shakedown of unbound pavements. Road Mater Pavement Des 6(1):81–96
4. Boulbibane M, Ponter ARS (2005) Linear matching method for limit load problems using the Drucker-Prager yield condition. Géotechnique 55:731–739
5. Boulbibane M, Ponter ARS (2006) The linear matching method for the shakedown analysis of geotechnical problems. Int J Numer Anal Methods Geomech 30:157–179
6. Brown SF, Juspi S, Yu HS (2008) Experimental observations and theoretical predictions of shakedown in soils under wheel loading. In: Advances in transportation geotechnics. Nottingham
7. Brown SF, Yu HS, Juspi S, Wang J (2012) Validation experiments for lower bound shakedown theory applied to layered pavement systems. Géotechnique 62:923–932
8. Collins IF, Cliffe PF (1987) Shakedown in frictional materials under moving surface loads. Int J Numer Anal Methods Geomech 11(4):409–420
9. Collins IF, Wang AP, Saunders LR (1993) Shakedown in layered pavements under moving surface loads. Int J Numer Anal Methods Geomech 17(3):165–174
10. Collins IF, Wang AP, Saunders LR (1993) Shakedown theory and the design of unbound pavements. Road Transp Res 2(4):28–39
11. Collins IF, Boulbibane M (1998) The application of shakedown theory to pavement design. Met Mater 4(4):832–837
12. Collins IF, Boulbibane M (2000) Geomechanical analysis of unbound pavements based on shakedown theory. J Geotech Geoenviron 126(1):50–59
13. Chazallon C, Allou F, Hornych P, Mouhoubi S (2009) Finite elements modelling of the long-term behaviour of a full-scale flexible pavement with the shakedown theory. Int J Numer Anal Methods Geomech 33(1):45
14. Chazallon C, Koval G, Mouhoubi S (2012) A two-mechanism elastoplastic model for shakedown of unbound granular materials and DEM simulations. Int J Numer Anal Methods Geomech 36(17):1847–1868
15. Chen HF, Ponter ARS (2001) Shakedown and limit analyses for 3-D structures using the linear matching method. Int J Pres Ves Pip 78:443–451
16. Chen HF, Ponter ARS (2005) The linear matching method for shakedown and limit analysis applied to rolling and sliding point contact problems. Road Mater Pavement 6:9–30
17. Davis EH (1968) Theories of plasticity and the failure of soil masses. In: Soil mechanics: chapter 6. Butterworths, London

18. Drescher A, Detournay E (1993) Limit load in translational failure mechanisms for associative and non-associative materials. Géotechnique 43:443–456
19. Graham J, Houlsby GT (1983) Anisotropic elasticity of a natural clay. Géotechnique 33: 165–180
20. Juspi S (2007) Experimental validation of the shakedown concept for pavement analysis and design. PhD thesis, The University of Nottingham, UK
21. Kapoor A, Williams JA (1996) Shakedown limits in rolling-sliding point contacts on an anisotropic half-space. Wear 191(1–2):256–260
22. Koiter WT (1960) General theorems for elastic-plastic solids. In: Sneddon IN, Hill R (eds) Progress in solid mechanics. North Holland, Amsterdam, pp 165–221
23. Krabbenhøft K, Lyamin AV, Sloan SW (2007) Shakedown of a cohesive-frictional half-space subjected to rolling and sliding contact. Int J Solids Struct 44(11–12):3998–4008
24. Lade PV, Nelson RB, Ito YM (1987) Nonassociated flow and stability of granular materials. J Eng Mech 113(9):1302–1318
25. Lade PV, Pradel D (1990) Instability and plastic flow of soils. I: experimental observations. J Eng Mech 116(11):2532–2550
26. Larew HG, Leonards GA (1962) A Strength criterion for repeated loads. In: Highway research board proceedings. Washington, pp 529–556
27. Lashine AKF (1971) Some aspects of the behaviour of Keuper Marl under repeated loading. PhD thesis, The University of Nottingham, UK
28. Lekarp F, Dawson A (1998) Modelling permanent deformation behaviour of unbound granular materials. Constr Build Mater 12(1):9–18
29. Li HX, Yu HS (2006) A nonlinear programming approach to kinematic shakedown analysis of frictional materials. Int J Solids Struct 43:6594–6614
30. Li HX (2010) Kinematic shakedown analysis under a general yield condition with non-associated plastic flow. Int J Mech Sci 52(1):1–12
31. Liu S, Wang J, Yu HS, Wanatowski D (2014) Shakedown of layered pavements under repeated moving loads. In: Geo-Shanghai 2014. Shanghai, pp 179–188
32. Liu S, Wang J, Yu HS, Wanatowski D (2016) Shakedown solutions for pavements with materials following associated and non-associated plastic flow rules. Comput Geotech 78:218–266
33. Liu S (2016) Application of shakedown theory in the structural design of bituminous pavements. PhD thesis, The University of Nottingham, UK
34. Melan E (1938) Der spannungsgudstand eines Henky-Mises Schen Kontinuums Bei Verlandicher Belastung. Sitzungberichte der Ak Wissenschaften Wie 47(73)
35. Nguyen AD (2007) Lower-bound shakedown analysis of pavements by using the interior point method. PhD thesis, The RWTH Aachen University
36. Nguyen AD, Hachemi A, Weichert D (2008) Application of the interior-point method to shakedown analysis of pavements. Int J Numer Methods Eng 75:414–439
37. Ponter ARS, Hearle AD, Johnson KL (1985) Application of the kinematical shakedown theorem to rolling and sliding point contacts. J Mech Phys Solids 33:339–362
38. Ponter ARS, Engelhardt M (2000) Shakedown limits for a general yield condition: implementation and application for a Von Mises yield condition. Eur J Mech A-Solid 19(3):423–445
39. Ponter ARS, Chen HF, Ciavarella M, Specchia G (2006) Shakedown analyses for rolling and sliding contact problems. Int J Solids Struct 43(14–15):4201–4219
40. Raad L, Weichert D, Najm W (1988) Stability of multilayer systems under repeated loads. Transp Res Rec 1207:181–186
41. Raad L, Weichert D, Haidar A (1989) Analysis of full-depth asphalt concrete pavements using shakedown theory. Transp Res Rec 1227:53–65
42. Raad L, Weichert D, Haidar A (1989) Shakedown and fatigue of pavements with granular bases. Transp Res Rec 1227:159–172
43. Radovsky BS, Murashina NV (1996) Shakedown of subgrade soil under repeated loading. Transp Res Rec-TRB 1547(1):82–88

44. Ravindra PS, Small JC (2008) Shakedown analysis of road pavement performance. In: Advances in transportation geotechnics. Nottingham, pp 25–27
45. Ravindra PS (2008) Shakedown analysis of road pavements—an experimental point of view. PhD thesis, University of Sydney
46. Sangrey DA, Henkel DJ, Esrig MI (1969) The effective stress response of a saturated clay soil to repeated loading. Can Geo tech J 6(3):241–252
47. Sharp RW, Booker JR (1984) Shakedown of pavements under moving surface loads. J Trans Eng 110:1–14
48. Shiau SH, Yu HS (2000) Load and displacement prediction for shakedown analysis of layered pavements. Transp Res Rec 1730:117–124
49. Shiau SH (2001) Numerical methods for shakedown analysis of pavements under moving surface loads. PhD thesis, The University of Newcastle, Australia
50. Sloan S (2013) Geotech Stab Anal Géotech 63(7):531–571
51. Wang L, Hoyos LR, Wang J, Voyiadjis G, Abadie C (2005) Anisotropic properties of asphalt concrete: characterization and implications for pavement design and analysis. J Mater Civ Eng 17:535–543
52. Wang J (2011) Shakedown analysis and design of flexible road pavements under moving surface loads. PhD thesis, The University of Nottingham, UK
53. Wang J, Yu HS (2013) Shakedown analysis for design of flexible pavements under moving loads. Road Mater Pavement Des 14:703–722
54. Wang J, Yu HS (2013) Shakedown and residual stresses in cohesive-frictional half-space under moving surface loads. Geomech Geoeng Int J 8:1–14
55. Wang J, Yu HS (2014) Three-dimensional shakedown solutions for anisotropic cohesive-frictional materials under moving surface loads. Int J Numer Anal Methods Geomech 38: 331–348
56. Werkmeister S (2003) Permanent deformation behaviour of unbound granular materials in pavement constructions. PhD thesis, Technical University of Dresden, Germany
57. Werkmeister S, Dawson AR, Wellner F (2004) Pavement design model for unbound granular materials. J Transp Eng 130(5):665–674
58. Werkmeister S, Dawson AR, Wellner F (2005) Permanent deformation behaviour of granular materials. Road Mater Pavement 6(1):31–51
59. Werkmeister S, Dawson AR, Wellner F (2001) Permanent deformation behavior of granular materials and the shakedown concept. In: 80th annual meeting transportation research board, pp 75–81 Washington
60. Yu HS, Hossain MZ (1998) Lower bound shakedown analysis of layered pavements using discontinuous stress fields. Comput Methods Appl Mech Eng 167:209–222
61. Yu HS (2005) Three-dimensional analytical solutions for shakedown of cohesive-frictional materials under moving surface loads. Proc R Soc A Math Phys Eng Sci 461:1951–1964
62. Yu HS, Wang J (2012) Three-dimensional shakedown solutions for cohesive-frictional materials under moving surface loads. Int J Solids Struct 49:3797–3807
63. Yu HS, Wang J, Liu S (2015) Three-dimensional shakedown solutions for cross-anisotropic cohesive-frictional materials under moving loads. In: Direct methods for limit and shakedown analysis of structures, pp 299–313
64. Zhao J, Lyamin A, Sloan S (2008) Shakedown of cohesive-frictional non-homogeneous soils under moving surface loads. In: The 12th international conference of international association for computer methods and advances in geomechanics. India
65. Zhao J, Sloan SW, Lyamin AV, Krabbenhøft K (2008) Bounds for shakedown of cohesivefrictional materials under moving surface loads. Int J Solids Struct 45:3290–3312

Numerical Yield Design Analysis of High-Rise Reinforced Concrete Walls in Fire Conditions

J. Bleyer, D.T. Pham and P. de Buhan

Abstract The present contribution aims at developing a numerical procedure for predicting the failure of high rise reinforced concrete walls subjected to fire loading conditions. The stability of such structures depends, on the one hand, on thermal strains inducing a curved deformed configuration and, on the other hand, on a local degradation of the constitutive material strength properties due to the increase of temperature across the wall thickness. A three step procedure is proposed, in which the yield design (limit analysis) method is applied on two separate levels. First, an up-scaling procedure on the wall unit cell is considered as a way for assessing the generalized strength properties of the curved wall, modelled as a shell, by taking into account reduced strength capacities of the constitutive materials. Secondly, the overall stability of the wall in its fire-induced deformed configuration is assessed using lower and upper bound based on shell finite elements and the previously determined temperature-dependent strength criterion. Second-order cone programming problems are then formulated and solved using state-of-the-art solvers. Different illustrative applications are presented to investigate the sensitivity of the wall stability to geometrical parameters. Finally, the influence of imperfect connections between panels is also considered using a simple joint behaviour.

Keywords Yield design · Limit analysis · Reinforced concrete · Fire conditions · Shells · Finite elements

J. Bleyer (✉) · P. de Buhan
Laboratoire Navier, Université Paris-Est, Ecole des Ponts ParisTech-IFSTTAR-CNRS (UMR 8205), 6-8 avenue Blaise Pascal, Cité Descartes 77455, Champs-sur-Marne, France
e-mail: jeremy.bleyer@enpc.fr

D.T. Pham
Université Paris-Est, Centre Scientifique et Technique du Bâtiment (CSTB), 84 avenue Jean Jaurès, 77447 Marne-la-Vallée Cedex 2, France

O. Barrera et al. (eds.), *Advances in Direct Methods for Materials and Structures*, DOI 10.1007/978-3-319-59810-9_9

1 Introduction

Direct methods such as yield design [1] (or limit analysis in a perfectly plastic framework [2]) are now becoming increasingly popular for computing the bearing capacity of a wide variety of structures (soils [3], masonry [4], reinforced concrete [2, 5], etc.) thanks to the development of efficient interior point algorithms for solving the corresponding optimization problems [6].

Assessing the bearing capacity of reinforced concrete structure in fire conditions has also received increasing attention in the last decade [7–9]. The yield design approach has, for instance, recently been proposed to derive temperature-dependent interaction diagrams of reinforced concrete sections subject to a fire-induced temperature gradient [10].

The stability of high-rise reinforced concrete walls in fire condition has been investigated in [11] using yield design computations at the structure scale. The present paper is a continuation of this work and attempts at providing more insights into the failure of such structures, in particular regarding the influence of the structure geometrical configuration and the influence of imperfect connections between panels. It is a translated version of Chap. 9 of the thesis [12], written in French.

1.1 High-Rise Reinforced Concrete Panels

Prefabricated reinforced concrete panels are increasingly used in modern high-rise industrial buildings. Such panels can be assembled either side by side in vertical strips (Fig. 1-left) or stacked one over another in horizontal strips (Fig. 1-right). They usually rest on concrete ground beams and can be associated to side purlins in the case of a vertical configuration or to columns in the horizontal case. The height obtained in a vertical configuration is limited by the maximal length of a panel, which typically ranges from 8 to 12 m. On the opposite, the horizontal configuration enables to reach total heights up to 20 m.

Such panels must usually be designed to act as fire-walls, limiting the propagation of a potential fire to other zones of the building while keeping, for a given amount of time, a sufficient mechanical strength before the complete structure collapse. Assessing the fire safety of such structures is, thus, of paramount importance and requires a more sophisticated approach than traditional design codes which are currently adapted only to panels of smaller dimensions.

1.2 Behaviour of High-Rise Panels in Fire Conditions

When designing traditional reinforced concrete structures in fire conditions, a reduction of stiffness and strength properties of concrete and steel as a function of temperature has to be taken into account. Including this degradation of strength properties

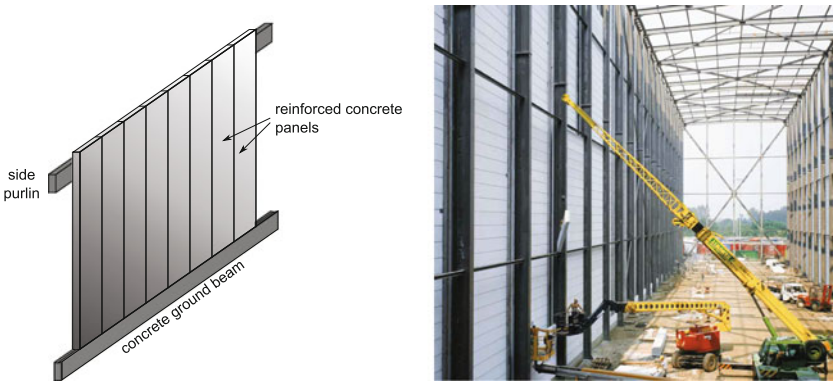

Fig. 1 High-rise reinforced concrete panels: sketch of a vertical configuration (*left*), high-rise industrial hall with HEBEL panels in horizontal configuration (*right*, *source* http://www.xellahebel.fr)

for a reinforced concrete beam/plate section leads to temperature-dependent interaction diagrams in terms of membrane forces and bending moments (Fig. 2-left). Nevertheless, this aspect is not sufficient to fully describe the collapse of high-rise structures.

Indeed, slender structures such as high-rise panels experience important out-of-plane displacements due to thermal deformation. Contrary to the case of smaller panels, these thermally-induced displacements can no longer be neglected and the self-weight eccentricity generates bending moments in addition to the initial compressive membrane forces (Fig. 2-right). This *second-order effect* due to geometrical non-linearities is classically known as "$P-\Delta$-effect". Thus, it is the combined action of a *degradation of material strength capacities* and the effect of *geometrical*

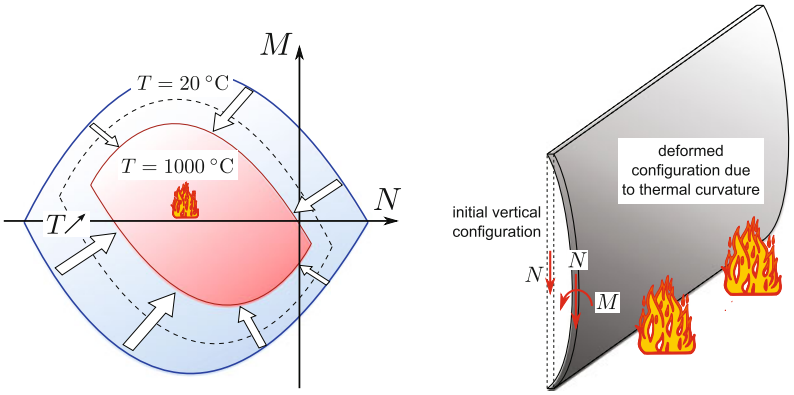

Fig. 2 Effect of fire conditions on the mechanical behaviour of high-rise panels: degradation of strength capacities (*left*) et geometrical changes (*right*)

changes induced by an important temperature increase which leads to the potential collapse of the structure. Its stability analysis is, therefore, relatively complex as the geometrical configuration at which collapse will occur is not initially given but has to be computed beforehand.

1.3 A Simplified Three-Step Procedure

In order to avoid the difficulties of a full thermo-elasto-plastic computation including geometrical non-linearities and strength properties reduction of steel and concrete, a simplified procedure is proposed and relies on three distinctive steps (Fig. 3):

- **Step n°1: Determination of the deformed configuration**.
  Starting from a thermal gradient induced by an increase of temperature on one face of the wall, this steps amounts to compute the equilibrium configuration due to thermal deformation and self-weight.
- **Step n°2: Determination of temperature-dependent strength criteria**.
  Starting from the same thermal gradient and in a completely independent manner, this step consists in evaluating a generalized temperature-dependent strength criterion of the reinforced concrete panel in the form of membrane-bending interaction diagrams of any wall cross-section.
- **Step n°3: Yield design analysis of the wall in its deformed configuration**.
  This last step consists in performing both static and kinematic approaches of yield design on the deformed configuration computed in step n°1 while taking into account the reduced strength-criterion obtained from step n°2. The outcome of this step will yield a bracketing estimate of the stability factor related to the considered configuration.

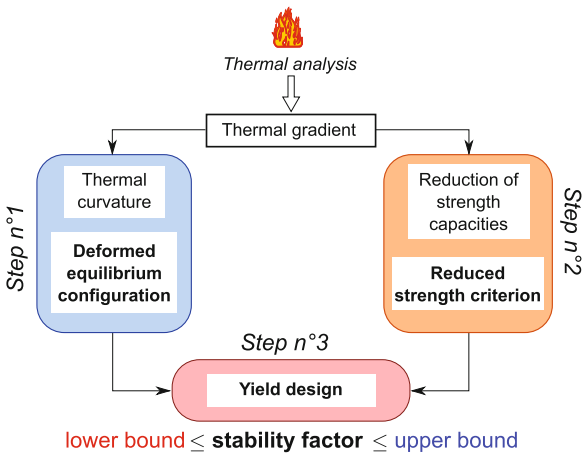

Fig. 3 A three-step procedure for assessing the fire safety of high-rise panels

2 Determination of the Deformed Configuration

2.1 Initial Geometry

In its initial configuration, i.e. before any thermal loading, the panel is modelled as a vertical plate of height H and width L in the (OXZ)-plane. Boundary conditions represented in Fig. 4 correspond to simple supports on all edges (free rotation), while vertical displacements are fixed on the bottom side.

The panel is subjected to its own weight, represented by a uniform vertical density p, and to a thermal loading progressively increasing the $Y \leq 0$ face temperature from $T = 20\,°\text{C}$ to $T = 1050\,°\text{C}$, this corresponds to a ISO 834 fire [13] during 120 min.

2.2 Thermo-Elastic Computations

The deformed equilibrium configuration (step n°1) is computed using the finite element software MARC [14] according to the following points:

- the computation is realized in the context of *finite transformations*: thermo-elastic strains as well as rotations remain small but the change of geometry produced by horizontal out-of-plane displacements is taken into account to determine, in an iterative manner, the final equilibrium computation.
- the influence of temperature on concrete and steel elastic moduli is also taken into account using experimentally determined reduction coefficients [15].

For more details on these aspects, we refer to [10, 16].

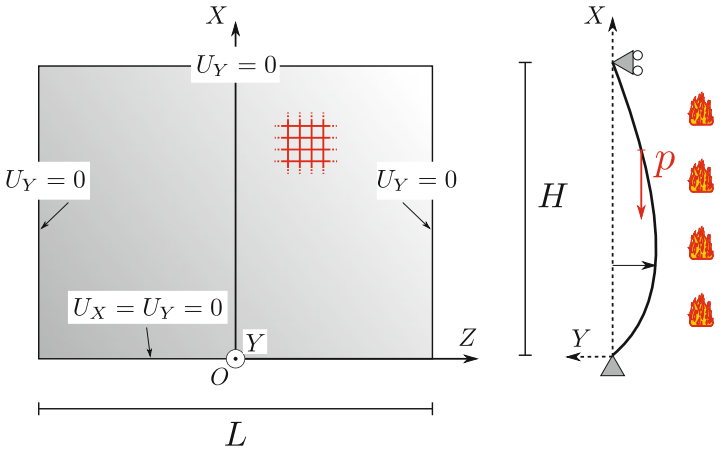

Fig. 4 Initial configuration and boundary conditions

3 Determination of Temperature-Dependent Strength Criteria

3.1 Reduction of Strength Capacities

The influence of temperature on strength properties of concrete and steel is taken into account through the adoption of (non-dimensional) *reduction coefficients*, denoted respectively by k_c and k_y, the variation of which as a function of temperature is given by the Eurocode 2 norm [15] and represented in Fig. 5-left. The compressive strength of concrete and the yield strength of steel at a given point of the panel characterised by a temperature T will then be given by:

$$f_c(T) = k_c(T) \cdot f_{c,amb} \quad \text{for concrete} \tag{1}$$

$$f_y(T) = k_y(T) \cdot f_{y,amb} \quad \text{for steel} \tag{2}$$

where $f_{c,amb}$ and $f_{y,amb}$ represent respective strengths at ambient temperature. One can remark that the concrete compressive strength decreases gradually from ambient temperature, whereas the steel yield strength remains equal to its ambient value up to nearly 400 °C. Past this value, its strength decreases abruptly.

The thermal analysis for a given fire temperature enables to compute the distribution of temperature $T(z)$ across the panel thickness (Fig. 5-right). Using the previously mentioned reduction coefficients, this thermal gradient translates directly in terms of a gradient of concrete and steel strength properties across the panel thickness. For a given fire temperature, it remains now to compute the generalized strength criterion (interaction diagrams) of a plate with non-uniform strength properties.

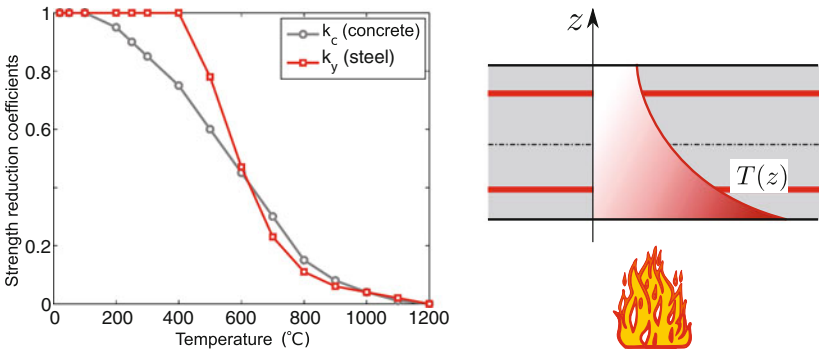

Fig. 5 Degradation of strength capacities: reduction coefficients for concrete and steel as a function of temperature (*left*) and thermal gradient through the panel thickness (*right*)

3.2 Generalized Strength Properties

Generalizing the determination of temperature-dependent interaction diagrams for a beam [17], an up-scaling procedure is adopted to compute the generalized strength criterion of a heterogeneous plate for which an auxiliary problem is formulated on a unit cell consisting of concrete and steel rebars (Fig. 6). This unit cell is represented by a parallelepiped of height h, the panel thickness, and of side e corresponding to the spacing between steel rebars. These reinforcements are placed along four layers oriented along orthogonal directions $\underline{e}_x$ and $\underline{e}_y$ and situated at a distance d from the top and bottom surfaces of the panel (now working in the local frame $Oxyz$).

The generalized strength criterion is obtained as the solution of a yield design problem with membrane forces and bending moments acting as macroscopic loading parameters, the resolution of which can be realized resorting to a 3D discretization [18].

Since we aim at modelling the deformed panel as a curved shell, we choose to take advantage of the construction of generalized strength criteria for shells developed in [19]. Indeed, if steel rebars were absent, we would have been in presence of a shell with strength properties homogeneous in its own local plane but heterogeneous across its thickness. Knowing the concrete plane stress strength criterion at all point across the thickness, it is possible to obtain a semi-analytical expression of the shell strength criterion, which is particularly suited for a numerical implementation [19].

The presence of steel bars is taken into account by adopting a uniaxial traction/compression modelization, embedded in the concrete matrix with a perfect bonding. Let us recall that this choice is equivalent to a lower bound approach to the true generalized strength criterion, which coincides with the latter in the limit of small volume fraction of steel and a large contrast of strength properties between steel and concrete [20].

In the following, a Mohr-Coulomb strength criterion with tension cut-off will be adopted for concrete:

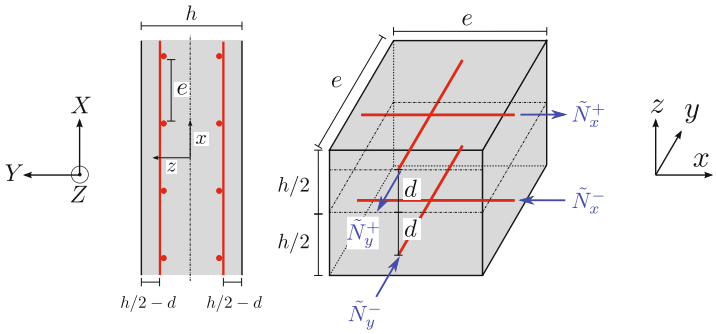

Fig. 6 Auxiliary problem used to determine the reinforced concrete panel strength criterion

$$\underline{\underline{\sigma}} \in \mathscr{G}(z) \Leftrightarrow \begin{cases} \sigma_{xx}\sigma_{yy} \geq \sigma_{xy}^2 \\ (f_c(z) + \sigma_{xx})(f_c(z) + \sigma_{yy}) \geq \sigma_{xy}^2 \\ -f_c(z) \leq \sigma_{xx}, \sigma_{yy} \leq 0 \end{cases} \tag{3}$$

where z is the coordinate across the thickness and $f_c(z)$ the local concrete compressive strength obtained from (1) for a given temperature $T(z)$ at this point.

As regards steel, each bar is supposed to obey a criterion of the form:

$$|\tilde{N}_{x,y}^{\pm}| \leq S f_y(z) \tag{4}$$

where $\tilde{N}_{x,y}^{\pm}$ represent axial forces inside each bar, $S = \pi\phi^2/4$ its cross-section area and $f_y(z)$ its yield strength obtained from (2).

With the previous notations, the generalized strength criterion G in terms of membrane force tensor $\underline{\underline{N}}$ and bending moment tensor $\underline{\underline{M}}$ reads:

$$(\underline{\underline{N}}, \underline{\underline{M}}) \in G \Leftrightarrow \left| \begin{array}{l} \exists\, \underline{\underline{\sigma}}(z) = \sigma_{ij}(z)\underline{e}_i \otimes \underline{e}_j, N_i^{\pm} \text{ and } i,j = x,y \\ N_{ij} = \displaystyle\int_{-h/2}^{h/2} \sigma_{ij}(z)dz + \frac{\tilde{N}_i^+ + \tilde{N}_i^-}{e}\underline{e}_i \otimes \underline{e}_i \\ M_{ij} = \displaystyle\int_{-h/2}^{h/2} (-z)\sigma_{ij}(z)d\xi - \frac{h/2 - d}{e}(\tilde{N}_i^+ - \tilde{N}_i^-)\underline{e}_i \otimes \underline{e}_i \\ \text{s.t. } \underline{\underline{\sigma}}(z) \in \mathscr{G}(z) \text{ and } |\tilde{N}_i^{\pm}| \leq S f_y(z) \quad \forall z \in [-h/2; h/2] \end{array} \right. \tag{5}$$

which implicitly depends on the thermal gradient through the distributions of $f_c(z)$ and $f_y(z)$ across the panel thickness.

4 Yield Design Analysis of the Wall in Its Deformed Configuration

The last step of the simplified procedure consists in implementing numerically both lower and upper bound yield design approaches on the previously determined curved configuration associated to the reduced strength criterion (5).

As mentioned earlier, the panel in its deformed configuration will be viewed as a shell modelled by an assembly of planar facets in membrane-bending interaction as described in [19]. In particular, numerical strategies for approximating the generalized strength criterion G either from the inside or from the outside are employed (respectively for the lower bound static approach and the upper bound kinematic approach) to ensure the strict bounding status of the computed critical load factor [11, 19]. Such strategies are, moreover, particularly suited for formulating the corresponding discrete optimization problems as second-order cone programs.

These optimization problems are then solved using the MOSEK [21] software package which implements efficient interior point algorithms.

The SOCP formulation of the global shell yield design problem, both for the upper and lower bound approaches, follows the procedure described in [11, 19].

The stability analysis of the structure is then assessed by computing a bracketing of the *stability factor*, which is here defined as the multiplicative non-dimensional factor of the loading (here the self-weight) for which the structure will collapse according to the yield design framework.

5 Numerical Investigation of the Structure Stability

In the remainder of this paper, the following parameters have been retained :

$$h = 15 \text{ cm},\ p = 3.68 \text{ kN/m}^2,\ E_{c,amb} = 19.2 \text{ GPa},\ f_{c,amb} = 32 \text{ MPa} \tag{6}$$

where $E_{c,amb}$ corresponds to the concrete Young modulus at ambient temperature. Steel rebars consist of 2 beds of HA6 steels (6 mm diameter), spaced by 10 cm, located 3 cm away from the bottom and top surfaces of the panel and oriented along the $\underline{e}_X$ and $\underline{e}_Z$ directions, i.e. :

$$e = 10 \text{ cm},\ d = 4.5 \text{ cm},\ \phi = 6 \text{ mm},\ f_{y,amb} = 500 \text{ MPa} \tag{7}$$

5.1 Influence of Panel Width and Temperature Increase

For this first series of computations, three different geometrical configurations have been considered (Fig. 7), corresponding to a slender panel in the vertical direction ($L = 3$ m, $H = 12$ m), a square panel ($L = H = 12$ m) and a slender panel in the horizontal direction ($L = 30$ m, $H = 12$ m).

5.1.1 Raising Temperature

The stability of the structure, as described in (Fig. 3), has been analysed every 10 min for an ISO 834 fire during 120 min. Figure 8-left represents the evolution of the temperature profile through the panel thickness every 20 min, starting from an initial state at ambient temperature of 20 °C.

It can be observed that the concrete strength loss is moderate in the upper half thickness of the panel, whereas the lower half loses in average 10% of its strength after only 20 min and roughly 50% after 120 min. Finally, the bottom steel rebars start to loose their strength only after 60 min and is reduced by 40% after 120 min. For the top rebars, their strength is not decreased since the temperature stays below 400 °C

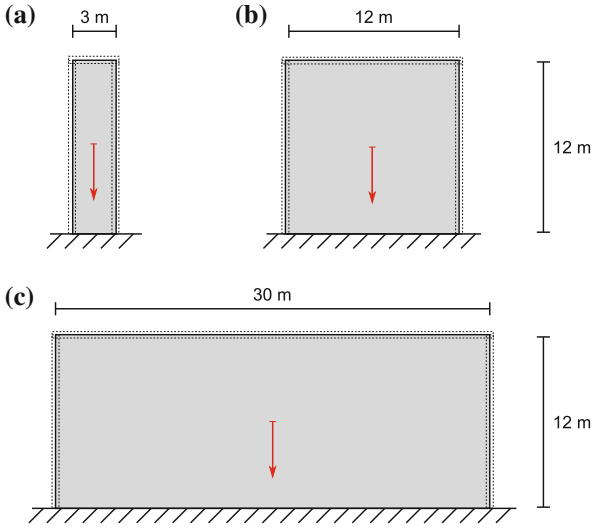

Fig. 7 Three geometrical configurations for panels with the same height ($H = 12$ m) and different widths ($L = 3,\ 12,\ 30$ m)

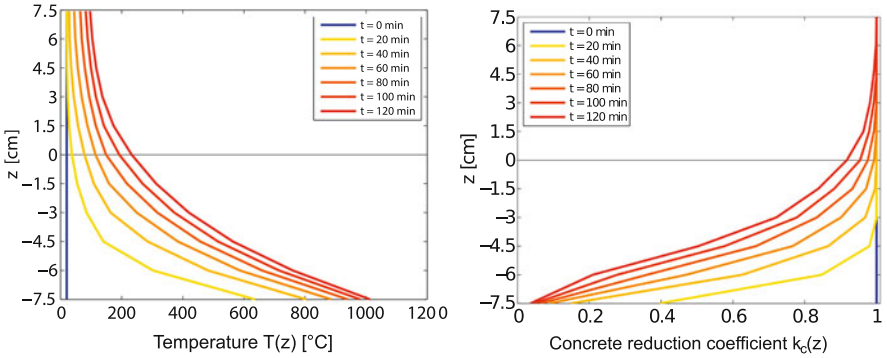

Fig. 8 Evolution of temperature profile $T(z)$ (*left*) and corresponding concrete reduction factor $k_c(z)$ (*right*) through the panel thickness at different times

at this point. All these remarks enable to interpret the evolution of the interaction diagrams during fire exposure (Fig. 9). In particular, the heterogeneous distribution of strength properties across the panel thickness explains the non-symmetric shape of the diagrams in fire conditions, while its global size diminishes due to the reduction of strength properties.

5.1.2 Amplitude of Geometrical Changes

In Fig. 10, the maximum amplitude of the out-of-plane displacement of the thermally-induced deformed equilibrium configuration has been represented during the fire

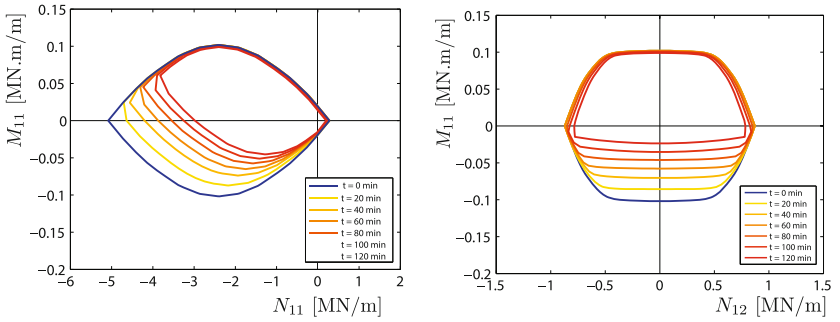

Fig. 9 Evolution of interaction diagrams at different times: *left* (N_{11}, M_{11})-plane, other $N_{ij} = M_{ij} = 0$; *right* (N_{12}, M_{11})-plane for $N_{11} = -2.4$ MN/m, other $N_{ij} = M_{ij} = 0$

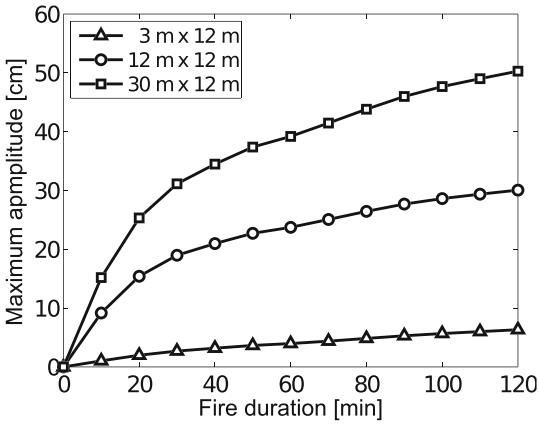

Fig. 10 Out-of-plane displacement maximum amplitude (in the Y direction) of the equilibrium configuration

evolution and for the three panel dimensions. As expected, the width of the panel strongly influences the value of the maximum displacement. The eccentricity remains, however, moderate since the ratio between maximum out-of-plane displacement and the panel height is equal to 4% for $L = 30$ m and 2.5% for $L = 12$ m, justifying a posteriori the small rotation hypothesis.

5.1.3 Stability Analysis

The resolution of the yield design problem on the deformed configuration has been realized by meshing half of the panel, using between 500 and 1000 shell elements. A value of $n = 10$ (resp. $n = 11$) has been used for the approximation of the generalized strength criterion for the static (resp. kinematic) approach (see [19]).

Table 1 collects the numerical estimates of the stability factor in terms of lower and upper bounds for the different geometries after 120 min of fire exposure. Again, the panel width has a strong influence on the stability factor, which is decreased by a factor 4 when the width goes from 12 to 30 m.

Table 1 Bracketing of the stability factor after 120 min ($H = 12$ m)

Geometry (m)	Static (lower bound)	Kinematic (upper bound)	Relative gap (%)
$L = 3$	67.5	78.5	15
$L = 12$	32.4	35.3	8.7
$L = 30$	7.9	8.5	7.6

It is interesting to compare these values to the stability factor which would be obtained without taking into account any geometrical changes (vertical configuration) and without any degradation of strength capacities. In this case, the stability of the panel is limited by its compressive strength $N_{c,amb}$, reached at its bottom. The associated collapse mechanism corresponds to a downwards rigid block translation (purely axial velocity discontinuity at $X = 0$ in the $X \leq 0$ direction). The exact value of the stability factor is thus given by:

$$S.F._{\text{compression}} = \frac{N_{c,amb}}{pH} \quad \text{with } N_{c,amb} = hf_{c,amb} + \frac{2S}{e} f_{y,amb} \tag{8}$$

Using the previous numerical values, we obtain here $S.F._{\text{compression}} = 115.14$. One can observe that this value does not depend on the panel width and that it is much larger than the values obtained when taking into account the combined effect of geometrical changes and strength capacities reduction.

Let us also remark that an analytical collapse mechanism involving 5 hinge lines considered by Pham in [10] using a plate model yielded an upper bound estimate of the stability factor of 36.7 for the square panel $L = H = 12$ m, that is a value slightly higher than the one obtained here with the numerical upper bound approach.

As regards the 3 m wide panel, the optimal collapse mechanism is similar to the vertical rigid block translation previously mentioned, the collapse is thus essentially related to the compressive strength. It is possible to generalize the upper-bound estimate (8) by taking into account the degradation of the compressive strength with temperature as follows:

$$S.F._{\text{compression},T} = \frac{N_c(T)}{pH} \tag{9}$$

$$\text{with } N_c(T) = \left(\int_{-h/2}^{h/2} k_c(z) dz \right) f_{c,amb} + \frac{S}{e} \left(k_y(d) + k_y(-d) \right) f_{y,amb}$$

In this case, an upper bound of $S.F._{\text{compression},T} = 88.1$ after 120 min of fire exposure is obtained, i.e. a value close to the numerical upper bound estimate for $L = 3$ m.

On the other hand, the collapse mechanisms for $L = 12$ m (Fig. 11-left) and $L = 30$ m (Fig. 11-right) are more complex and seem to involve a bending collapse of the central part of the panel at a height of roughly $\frac{1}{4}$ to $\frac{1}{3}$ of the total height, the

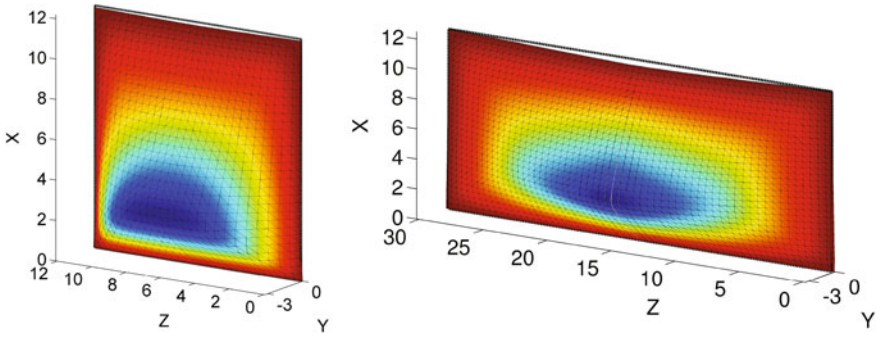

Fig. 11 Collapse mechanism for the 12 m × 12 m (*left*) and 30 m × 12 m (*right*) panels after 120 min (isocontours = relative amplitude of the out-of-plane virtual velocity field U_Y)

upper part being subjected to a rotation about Z as well as a downwards vertical movement.

Finally, the evolution of the stability factor for all configurations during fire exposure has also been reported in Fig. 12. As a comparison, the upper bound estimate (9) corresponding to a pure compression collapse mechanism with reduced strength capacities has been represented as the black dashed line. As mentioned earlier, the stability factor for the 3 m wide panel is relatively close to this value.

Whereas all stability factors initially correspond to the ambient compressive strength, the wider the panel, the stronger the drop of the stability factor after a few

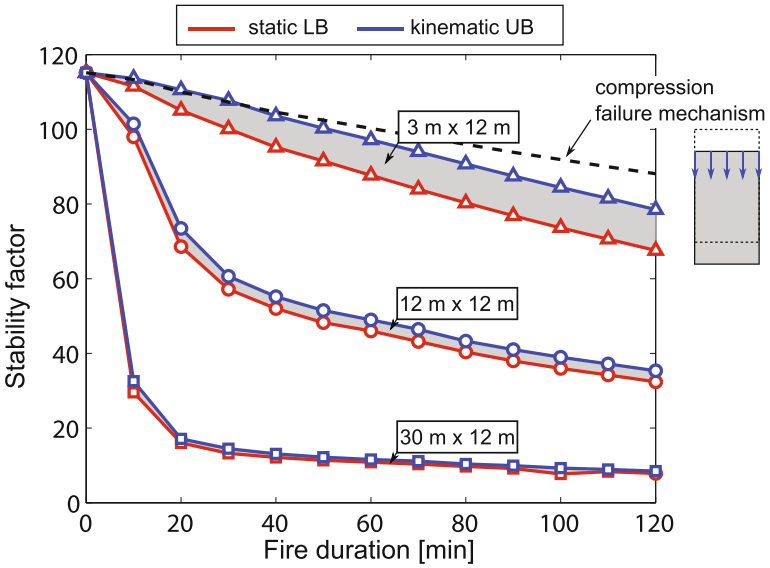

Fig. 12 Stability factor estimates evolution during fire exposure for all geometries

minutes. On the other hand, after 40–60 min of fire, the relative decrease of the stability factor occurs at roughly the same speed for all panel width, roughly 5% every 10 min.

Let us also remark that the relative contribution of steel rebars to the stability factor also strongly changes with time. It is about 6% at $t = 0$ min and reaches 40% for $L = 12$ m and almost 85% for $L = 30$ m after 120 min. Steel rebars thus play an important role in limiting the strength loss of the panel during fire exposure.

5.2 *Influence of Panel Height*

In this second series of computations, the width of the panel is now fixed to $L = 12$ m and we investigate four different values of the total height: $H = 4.8, 9.6, 14.4$ and19.2m. This choice corresponds to the vertical stacking of 2, 4, 6 and 8 individual panels of dimensions 2.4 m × 12 m in horizontal configuration (Fig. 13).

As before, the height H has an important influence on the deformed configuration amplitude. The profile of this configuration in the middle plane ($Z = 6$ m) after 120 min has been represented in Fig. 14-left.

The corresponding evolution of the stability factor at 120 min has been reported in Fig. 14-right. Although an important decrease with an increase of the total height can be observed, its value remains around 20 for the considered numerical value. In practice, it is possible to stack such panels up to a total height of 20 m for modern

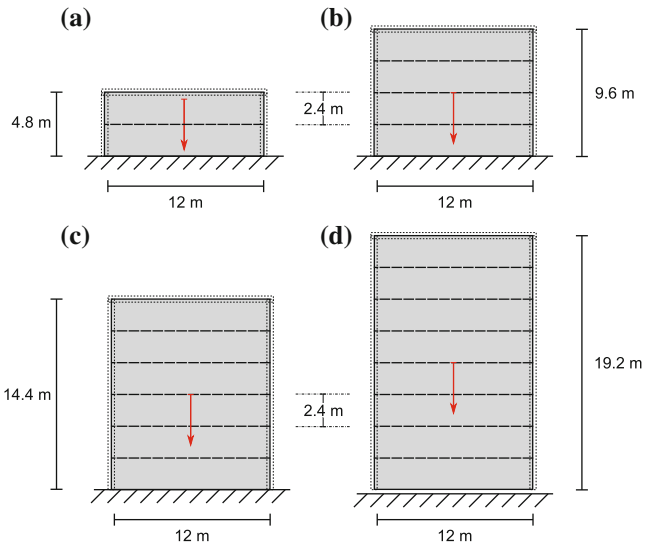

Fig. 13 For geometrical configurations of panels with the same width ($L = 12$ m) stacked horizontally (total height $H = 4.8,\ 9.6,\ 14.4,\ 19.2$ m)

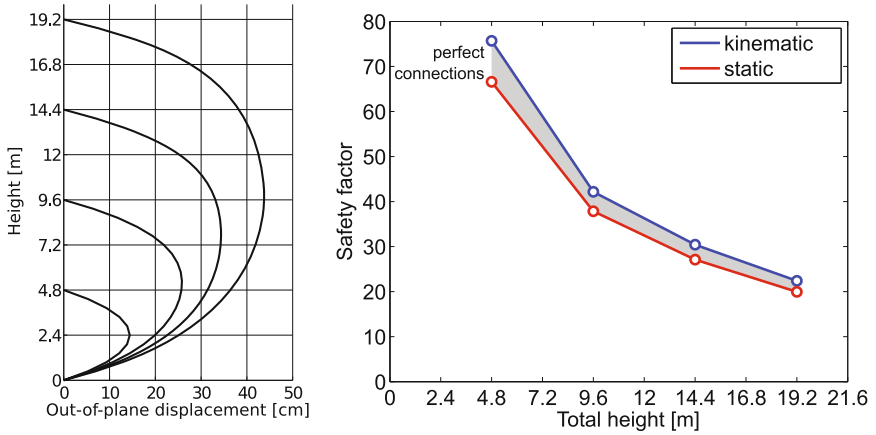

Fig. 14 Influence of total height on the panel stability: profile of the deformed configuration in the middle plane $Z = 6$ m (*left*) and evolution of the stability factor estimates (*right*)

high-rise industrial buildings. For this particular case, the stability of this kind of structure in deformed configuration is thus ensured.

5.3 Taking into Account Imperfect Connections

In the preceding sections, the wall has been modelled as a continuous shell with the same generalized criterion at each point of the structure. However, the connection between two individual panels may not be perfect, the side of the panels being in general assembled using male-female notches (Fig. 15-left). In order to take into account the imperfect aspect of the connection, it has been chosen to model it as a joint oriented in the horizontal direction $\underline{t}$, with a vertical normal vector $\underline{n}$ in the panels plane, which offers a zero strength in bending around the joint (hinge) as well as in tangential shear (perfect sliding). The strength criterion of such a joint can thus be written as:

$$(\mathsf{N},\mathsf{M}) \in \mathsf{G} \Longleftrightarrow \left| \begin{array}{l} \exists (\underline{\underline{N}}, \underline{\underline{M}}) \text{ s.t.} \\ \underline{n} \cdot \underline{\underline{N}} \cdot \underline{n} = \mathsf{N} \\ \underline{t} \cdot \underline{\underline{N}} \cdot \underline{n} = 0 \\ \underline{n} \cdot \underline{\underline{M}} \cdot \underline{n} = 0 \\ \underline{t} \cdot \underline{\underline{M}} \cdot \underline{n} = \mathsf{M} \\ (\underline{\underline{N}}, \underline{\underline{M}}) \in G \end{array} \right. \tag{10}$$

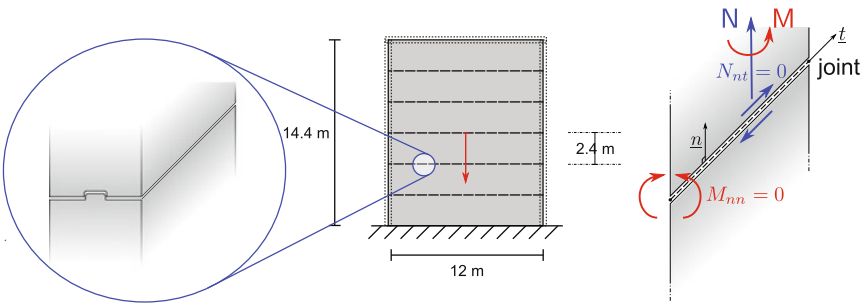

Fig. 15 Taking into account imperfect connections between panels: sketch of a possible connection (*left*) and mechanical model of the connection (*right*)

The static and kinematic approaches are then modified so as to take into account such a criterion at the connections located every 2.4 m in the vertical direction X, as represented in Fig. 13. The finite element mesh is built in such a way that the edge of some elements are located along these connections, the expression of the strength criterion and the support function being modified only for these particular edges. More specifically, as regards the kinematic approach, the support function of the joint is given by:

$$\begin{aligned} \Pi(\underline{n}; [\![u_n]\!], [\![\beta_t]\!]) &= \sup_{(\mathsf{N},\mathsf{M})\in\mathsf{G}} \left\{ \mathsf{N}[\![u_n]\!] + \mathsf{M}[\![\beta_t]\!] \right\} \\ &= \inf_{\hat{v},\hat{\beta}} \ \pi(\underline{n}; [\![u_n]\!]\underline{n} + \hat{v}\underline{t}, \hat{\beta}\underline{n} + [\![\beta_t]\!]\underline{t}) \end{aligned} \tag{11}$$

where $\pi(\underline{n}; [\![\underline{u}]\!], [\![\underline{\beta}]\!])$ is the generalized support function of the panel for velocity discontinuities.

Figure 16 represents the stability factor estimates obtained when considering imperfect connections. An important reduction of roughly 60% can be observed for the different configurations. Let us however highlight that, for the sake of simplicity, the computations have been realized on the same deformed configurations as for the perfect connections case. Now the presence of imperfect connections has certainly a significant influence on the deformed configuration amplitude, which may further reduce the stability factor.

Finally, the shape of the different collapse mechanisms with or without joints is compared in (Figs. 17, 18, 19 and 20). An important difference can be observed when considering joints or not. In particular, sliding and rotation velocity discontinuities can be observed at the joints.

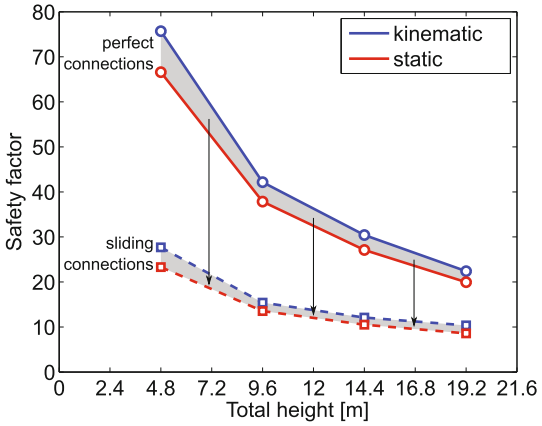

Fig. 16 Stability factor for the panel assembly by taking into account sliding connections between panels

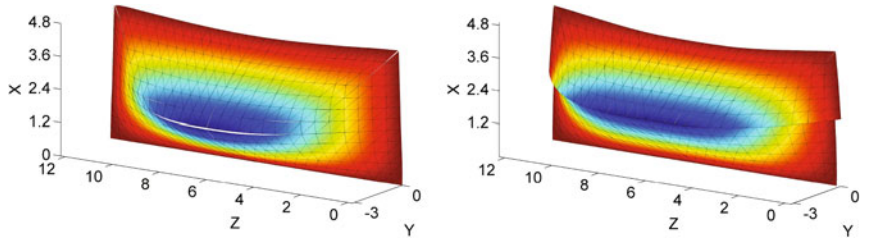

Fig. 17 Collapse mechanisms for 2 panels ($H = 4.8$ m): *left* without joints ($66.6 \leq S.F. \leq 75.7$); *right* with joints ($23.3 \leq S.F. \leq 27.7$)

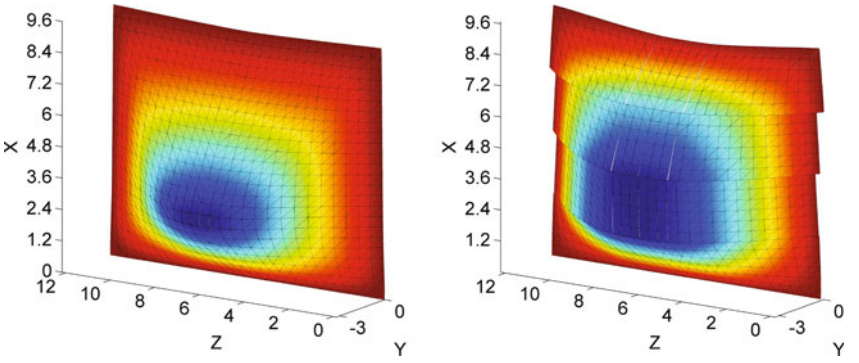

Fig. 18 Collapse mechanisms for 4 panels ($H = 9.6$ m): *left* without joints ($37.8 \leq S.F. \leq 42.2$); *right* with joints ($13.5 \leq S.F. \leq 15.4$)

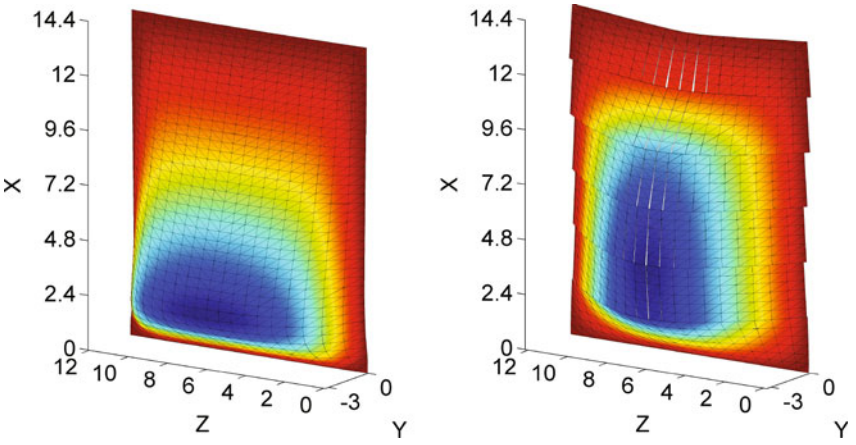

Fig. 19 Collapse mechanisms for 6 panels ($H = 14.4$ m): *left* without joints ($27.1 \leq S.F. \leq 30.4$); *right* with joints ($10.5 \leq S.F. \leq 12.1$)

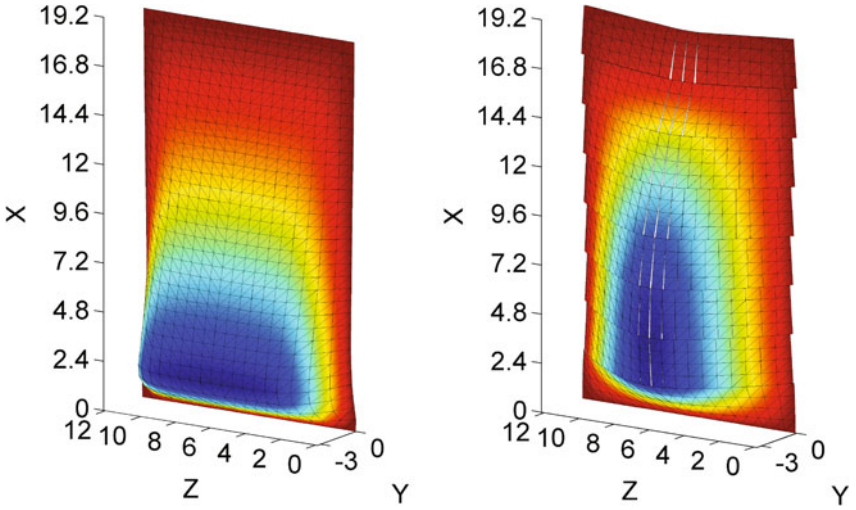

Fig. 20 Collapse mechanisms for 8 panels ($H = 19.2$ m): *left* without joints ($19.9 \leq S.F. \leq 22.4$); *right* with joints ($8.6 \leq S.F. \leq 10.4$)

6 Conclusions

The yield design approach, along with efficient numerical tools such as interior point algorithms for conic programming, enabled to give interesting answers to the stability assessment of a complex engineering problem, involving geometrical changes as well as a reduction of strength capacities in fire conditions. Shell finite elements coupled with a specific strategy to formulate generalized strength criteria from a

heterogeneous distribution of strength properties have been used to obtain satisfying bracketing of the stability factor (10–20% relative gap) with reasonable computing times (around one minute on a standard desktop computer).

This analysis showed a great sensitivity of the stability factor with respect to the panel geometry, mainly due to its influence on geometrical changes. It has also been possible to illustrate the ability of the yield design approach to take into account imperfect connections.

Further work will be devoted to a better understanding of the link between the geometrical changes and the structure collapse. In particular, it will be interesting to investigate how yield strength properties can be accounted for in the computation of the deformed configuration without resorting to complex incremental approaches.

References

1. Salençon J (2013) Yield design. London ISTE Ltd., Wiley, Hoboken
2. Chen WF (2007) Plasticity in reinforced concrete. J. Ross Publishing
3. Lyamin AV, Sloan SW (2002) Int J Numer Anal Methods Geomech 26(2):181
4. Milani G, Lourenço P, Tralli A (2006) J Struct Eng 132(10):1650
5. Nielsen MP, Hoang LC (2016) Limit analysis and concrete plasticity. CRC Press
6. Andersen KD, Christiansen E, Conn AR, Overton ML (2000) SIAM J Sci Comput 22(1):243
7. Franssen JM, Dotreppe JC (2003) Fire Technol 39(1):89
8. El-Fitiany S, Youssef M (2009) Fire Saf J 44(5):691
9. Caldas RB, Sousa JBM, Fakury RH (2010) Eng Struct 32(9):2832
10. Pham DT (2014) Analyse par le calcul à la rupture de la stabilité au feu des panneaux en béton armé de grandes dimensions. Université Paris-Est, Thèse
11. Bleyer J, Pham DT, De Buhan P (2015) Proc ICE-Eng Comput Mech 168(4):178
12. Bleyer J (2015) Méthodes numériques pour le calcul à la rupture des structures de génie civil. Université Paris-Est, Thèse
13. EN 1991-1-2 (2002) Eurocode 1: action on structures—Part 1–2: General actions—actions on structures exposed to fire
14. MSC Software Corporation (2007) MARC finite element software. Los Angeles, CA
15. EN 1992-1-2 (2004) Eurocode 2: design of concrete structures—Part 1–2: General rules—structural fire design
16. Pham DT, de Buhan P, Florence C, Heck JV, Nguyen HH (2015) Eng Struct 87:153
17. Pham DT, de Buhan P, Florence C, Heck JV, Nguyen HH (2015) Eng Struct 90:38
18. Bleyer J, Pham DT, de Buhan P, Florence C (2015) Direct methods for limit and shakedown analysis of structures. Springer, pp 143–158
19. Bleyer J, de Buhan P (2016) Eur J Mech—A/Solids 59:178
20. de Buhan P, Taliercio A (1991) Eur J Mech—A/Solids 10(2):129
21. Mosek (2014) The Mosek optimization software. http://www.mosek.com/. Assessed Dec 2014

Efficient Shakedown Solutions in Complex Loading Domains

K.D. Panagiotou and K.V. Spiliopoulos

Abstract To estimate the life of a structure, or a component, which are subjected to a cyclic loading history, the structural engineer must be able to provide safety margins. This is only possible by performing a shakedown analysis which belongs to the class of direct methods. Most of the existing numerical procedures addressing a shakedown analysis are based on the two theorems of plasticity and are formulated within the framework of mathematical programming. A different approach has recently appeared in the literature. It is rather more physical than mathematical as it exploits the physics of the asymptotic steady state cycle. It has been called RSDM-S and has its roots in a previously published procedure (RSDM) which assumes the decomposition of the residual stresses into Fourier series whose coefficients are found by iterations. RSDM-S is a descending sequence of loading factors which stops when only the constant term of the series remains. The method may be implemented in any existing FE code. It is used herein to establish shakedown boundaries for two-dimensional general loadings consisting of mechanical or thermomechanical loads.

1 Introduction

The high level of variable loading, that most civil and mechanical engineering structures or structural components are subjected to, force them to develop irreversible strains that may lead them to asymptotic limit states related to global excessive deformations (ratcheting) or local ones (low cycle fatigue). For civil engineering structures, like bridges, pavements, buildings, and offshore structures, such typical loadings are heavy traffic, earthquakes or waves. On the other hand, the

K.D. Panagiotou · K.V. Spiliopoulos (✉)
Department of Civil Engineering, Institute of Structural Analysis & Antiseismic Research, National Technical University of Athens Zografou Campus, Zografos 157-80, Athens, Greece
e-mail: kvspilio@central.ntua.gr

K.D. Panagiotou
e-mail: kdpanag@gmail.com

O. Barrera et al. (eds.), *Advances in Direct Methods for Materials and Structures*, DOI 10.1007/978-3-319-59810-9_10

coexistence of thermal and mechanical loadings on mechanical engineering structures, like, for example, nuclear reactors aircraft propulsion engines, lead them also to stress regimes well beyond their elastic limit. Below a certain level of the applied loading, a favorable asymptotic state exists that, after some initial plastic straining the structure behaves elastically. This safe state is known as shakedown which has an effect to extend the life cycle of a structure.

When the exact loading history is known, one may estimate the long term behavior of a structure and determine whether shakedown has occurred, using cumbersome time stepping calculations. A much better alternative, that requires much less computing time, is offered by the direct methods. Moreover, it very often happens that the complete time history of loading is not known, but only its variation intervals. In these cases, direct methods are the only way to establish safety margins.

Based on the fact that for structures made of stable materials [1] an asymptotic state always exists [2], direct methods try to estimate this state right from the start of the calculations. Most direct methods for shakedown analysis are based on the lower bound [3] or the upper bound [4] theorems and they are formulated within the framework of mathematical programming.

The present work refers to a recently appeared in the literature numerical approach, which may be used for the evaluation of the shakedown load of elastoplastic structures under cyclic loading. The approach has been called RSDM-S and has its roots to the Residual Stress Decomposition Method (RSDM) [5, 6] which may estimate any asymptotic state under a given cyclic loading history. According to RSDM the residual stresses are decomposed into Fourier series whose terms are evaluated iteratively by satisfying equilibrium and compatibility at several time points inside the cycle. When looking for shakedown limits the exact history is not known but only the variation intervals of the loads and thus any curve varying between these intervals may convert the problem to an equivalent prescribed loading one. Then the RSDM-S generates a sequence of descending loading cyclic solutions through the use of the RSDM. The limit of this sequence is the shakedown load when the only remaining term in the Fourier series of the residual stresses is the constant term [7–9]. The procedure was originally proposed in [7] and may be implemented in any standard finite element program. In this work the efficiency of the approach to predict shakedown boundaries for complex loading domains is demonstrated by its application to two-dimensional structures under mechanical or thermomechanical loads.

2 Description of the RSDM-S

Let us suppose that a structure made of elastic-perfectly plastic von Mises type of material is subjected to a mechanical and a thermal load that vary independent to each other. These loads may have a cyclic variation between a specified maximum and a minimum value, just like the cyclic program shown in (Fig. 1a)

$(0 \rightarrow P^* \rightarrow (P^*, \theta^*) \rightarrow \theta^* \rightarrow 0)$. Without loss of generality we assume that the minimum values of the two loads are zero with the starred quantities corresponding to the maximum values of the loads. Two-dimensional loading domains are considered herein. In the case the structure is subjected to only mechanical loadings the corresponding cyclic program is $(0 \rightarrow P_1^* \rightarrow (P_1^*, P_2^*) \rightarrow P_2^* \rightarrow 0)$.

In the time domain this cyclic loading may be expressed as:

$$\mathbf{P}(\tau) = \left\{ \begin{array}{c} P(\tau) \\ \theta(\tau) \end{array} \right\} = \left\{ \begin{array}{c} P^* \alpha_1(\tau) \\ \theta^* \alpha_2(\tau) \end{array} \right\} \text{ or } \mathbf{P}(\tau) = \left\{ \begin{array}{c} P_1(\tau) \\ P_2(\tau) \end{array} \right\} = \left\{ \begin{array}{c} P_1^* \alpha_1(\tau) \\ P_2^* \alpha_2(\tau) \end{array} \right\} \tag{1}$$

where τ denotes a cycle time point $(0 \leq \tau \leq 1)$ and $\alpha_1(\tau), \alpha_2(\tau)$ are time functions.

Indicative variations of the two loads may be seen in Fig. 1b. For loads, varying proportionally, different time functions should be used [10].

Due to the convexity of the yield surface it has been stated [11] that if a given structure shakes down over the path of Fig. 1a that defines the domain Ω, then it shakes down over any load path contained within Ω.

Equation (1) converts the problem of a prescribed loading domain to an equivalent prescribed cyclic loading in the time domain. The loading domain may be varied isotropically by multiplying the variation of the loads with a factor γ.

The stresses in the structure at a cycle point τ are decomposed into an elastic part $\boldsymbol{\sigma}^{el}(\tau)$, in equilibrium with the applied external cyclic loading and a residual stress part $\boldsymbol{\rho}(\tau)$. In the search for shakedown the elastic stresses are themselves multiplied by this factor γ. Thus the total stress vector can now be written:

$$\boldsymbol{\sigma}(\tau) = \gamma \boldsymbol{\sigma}^{el}(\tau) + \boldsymbol{\rho}(\tau) \tag{2}$$

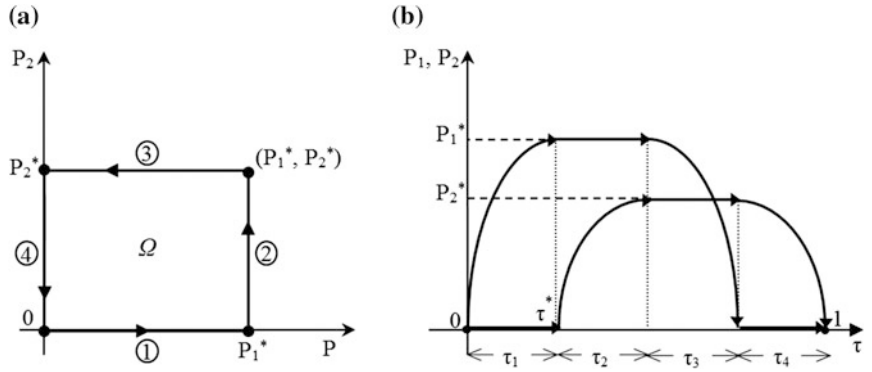

Fig. 1 Independent cyclic loading variation over one time period **a** in load space, **b** in time domain

where $\boldsymbol{\sigma}^{el}(\tau)$ are calculated from the vector of nodal displacements $\mathbf{r}^{el}(\tau)$:

$$\boldsymbol{\sigma}^{el}(\tau) = \mathbf{D} \cdot (\mathbf{B} \cdot \mathbf{r}^{el}(\tau) - \mathbf{e}^{\theta}(\tau)) \tag{3}$$

where $\mathbf{D}$ and $\mathbf{B}$ are the material and compatibility matrices of a continuum which has been discretized with the aid of the finite element (FE) method. $\mathbf{e}^{\theta}(\tau)$ are the thermal strains and may be determined using the coefficient of the thermal expansion.

On the other hand $\mathbf{r}^{el}(\tau)$ is determined by solving the equation:

$$\mathbf{K} \cdot \mathbf{r}^{el}(\tau) = \int_V \mathbf{B}^T \cdot \mathbf{D} \cdot \mathbf{e}^{\theta}(\tau) dV + \mathbf{R}_{\mathrm{P}}(\tau) \tag{4}$$

where $\mathbf{K} = \int_V \mathbf{D}^T \cdot \mathbf{B} \cdot \mathbf{D} dV$ is the stiffness matrix of the structure, and $\mathbf{R}_{\mathrm{P}}(\tau)$ the nodal forces due to the mechanical load.

Also, in relation to (1), $\mathbf{e}^{\theta}(\tau) = \alpha_2(\tau) \cdot \mathbf{e}^{\theta^*}$ and $\mathbf{R}_{\mathrm{P}}(\tau) = \alpha_1(\tau) \cdot \mathbf{R}_{P^*}$.

In the case where a mechanical load is applied in the place of the thermal load the equations are changed appropriately [7, 9].

Having established the elastic part the residual stress part may be estimated based on the expected cyclic nature of the residual stresses at the asymptotic cycle. Thus one may decompose them into Fourier series:

$$\boldsymbol{\rho}(\tau) = \frac{1}{2}\mathbf{a}_0 + \sum_{k=1}^{\infty} \{\cos(2k\pi\tau) \cdot \mathbf{a}_k + \sin(2k\pi\tau) \cdot \mathbf{b}_k\} \tag{5}$$

The RSDM method may be used to find iteratively the coefficients $\mathbf{a}_0, \mathbf{a}_k$ and $\mathbf{b}_k$ [5].

According to Melan's theorem [3] the conditions for shakedown consist of the two following statements [12]:

(a) The structure will shake down under a cyclic loading if there exists a time-independent distribution of residual stresses $\bar{\rho}$ such that, under any combination of loads inside prescribed limits, its superposition with the 'elastic' stresses $\boldsymbol{\sigma}^{el}$, i.e. $\boldsymbol{\sigma}^{el} + \bar{\rho}$, results in a total safe stress state at any point of the structure.

(b) Shakedown never takes place unless a time-independent distribution of residual stresses can be found such that, under all the possible load combinations, the sum of the residual and 'elastic' stresses constitutes an allowable stress state.

For a structure subjected to a prescribed cyclic loading program, these statements define the limit cycle which is a transition cycle between one with plastic straining and one without plastic straining. It may be proved [12] that the residual stress distribution of this cycle is unique, being independent of the preceding deformation history.

The numerical procedure RSDM-S is a transition process to this cycle [7, 8]. It starts from a high load factor, which is sequentially lowered by shrinking the loading domain in a continuous way up to the point that the conditions of the limit cycle are reached.

Decomposition of the residual stresses in Fourier series provides a natural way to implement this transition. Thus the procedure stops the first time the only remaining term of the Fourier series is the constant term $\mathbf{a}_0$. When this is achieved, we have the parameters of the limit cycle for the applied loading (1) together with the shakedown factor γ_{sh} of the loading domain [7].

To briefly describe the numerical implementation one could underline that first there is an initialization phase, where the starting loading factor is definitely higher than the shakedown factor as it is calculated so that the whole structure has become plastic [7].

Then we enter an iterative phase of two iteration loops, one inside the other. Let us denote with μ a typical iteration of the outer loop of the descending load factor. The outer loop includes the following steps:

(1) Enter the inner loop, which consists of the steps of the RSDM [5, 6]. For the current load factor $\gamma^{(\mu)}$, the iterations of RSDM start using, as a first estimate, the Fourier coefficients and the residual stresses of the cyclic solution, of the previous loading factor $\gamma^{(\mu-1)}$.

(2) On exit from the inner loop, a cyclic stress state has been reached and the cyclic solution values
$\mathbf{a}_0^{(\mu)}, \mathbf{a}_k^{(\mu)}, \mathbf{b}_k^{(\mu)} \Rightarrow \boldsymbol{\rho}^{(\mu)}(\tau)$, for the current load factor, have been obtained.

(3) Calculation of the sum of the norms of the vectors of the updated coefficients of the trigonometric part of the Fourier series

$$\varphi\left(\gamma^{(\mu)}\right) = \sum_{k=1}^{\infty} \mathbf{a}_k^{(\mu)} + \sum_{k=1}^{\infty} \mathbf{b}_k^{(\mu)} \tag{6}$$

(4) Obtain an update of the loading factor through the function φ

$$\gamma^{(\mu+1)} \cdot P^* = \gamma^{(\mu)} \cdot P^* - \omega \cdot \varphi\left(\gamma^{(\mu)}\right) \tag{7}$$

where the mechanical load is expressed as pressure load.

(5) Check the convergence of the load factor between two successive iterations within some tolerance.

If they equal each other the procedure stops, as only constant terms remain in the Fourier series.

Due to the positive sign of φ in Eq. (7), a descending sequence of cyclic solutions is produced which ends up with the parameters of the limit cycle for elastic shakedown. To avoid cases of overshooting below shakedown a convergence parameter ω is used. Analytical convergence considerations and a detailed description of the procedure are represented in [7].

3 Application Examples

The versatility of the proposed numerical method, to establish shakedown boundaries, is demonstrated in four examples, a thick cylinder, a holed plate, a frame and a continuous beam. The examples address loading domains of different complexity. Quadrilateral finite elements were used to model all the structures.

3.1 Bree Problem

The first example is a Bree problem where either a plate or a tube wall thickness is subjected to axial stress $P(\tau)$ and a fluctuation of temperature difference $\Delta\theta(\tau)$, assumed to be linearly distributed along the width of the plate (Fig. 2). The plate is assumed homogeneous, isotropic, elastic-perfectly plastic with the material data of Table 1. The plate is constrained from in-plane bending, thus making the problem essentially one dimensional. The finite element mesh consists of one hundred and twenty, eight-noded, iso-parametric elements with 3 × 3 Gauss integration points (Fig. 2). Plane stress conditions are assumed.

Two different load cases of thermo-mechanical loading were considered. In the first one, a constant in time axial load and a variable temperature difference $\Delta\theta(\tau)$ (Fig. 3a), whereas for the second one, a proportional variation between the axial load and the temperature difference (Fig. 3b) is assumed.

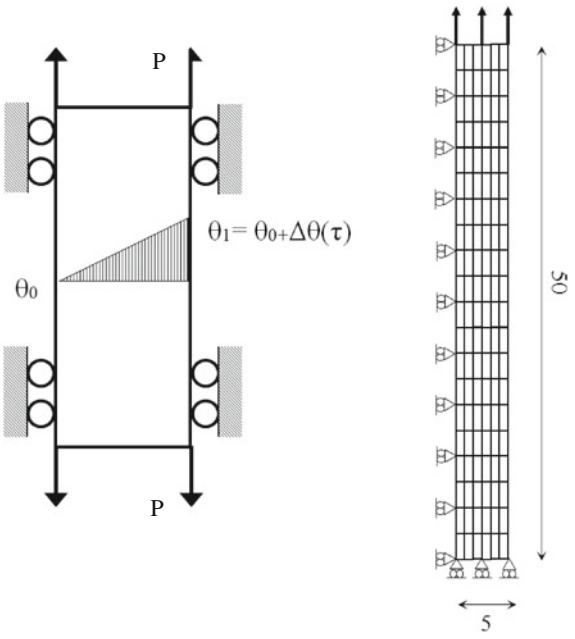

Fig. 2 Geometry, loading and finite element mesh for the Bree problem

Table 1 Material properties of the plate

Young's modulus	Poisson's ratio	Yield stress	Coeff. of thermal expansion
E = 208 GPa	$\nu = 0.3$	$\sigma_Y = 360$ MPa	5×10^{-5} °C

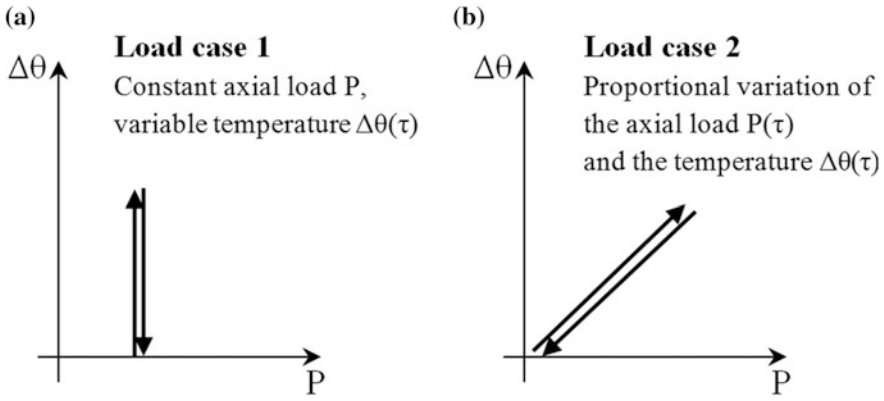

Fig. 3 Different cyclic loading cases

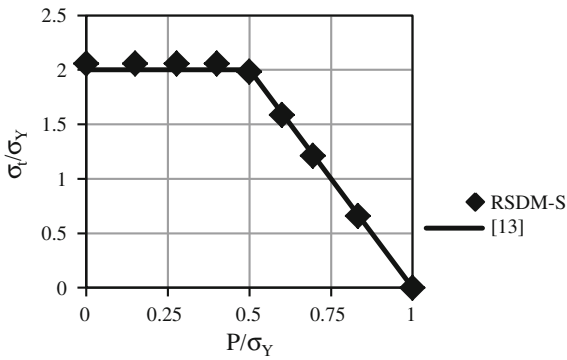

Fig. 4 Shakedown domain produced by the RSDM-S and its comparison with the analytical solution of Bree [13] (load case 1)

3.1.1 Constant Axial Load P, Variable Temperature $\Delta\theta(\tau)$

A prescribed loading in the time domain for the varying temperature may be established using a polynomial time function. One may thus write for both loads:

$$P(\tau) = \left\{ \begin{array}{c} P^* \alpha_1(\tau) \\ \Delta\theta^* \alpha_2(\tau) \end{array} \right\} \text{ where the time functions } \alpha_1(\tau), \alpha_2(\tau) \text{ are:}$$

$$\alpha_1(\tau) = const$$
$$\alpha_2(\tau) = 3.3334\tau^4 - 6.6667\tau^3 + 0.1667\tau^2 + 3.1667\tau$$

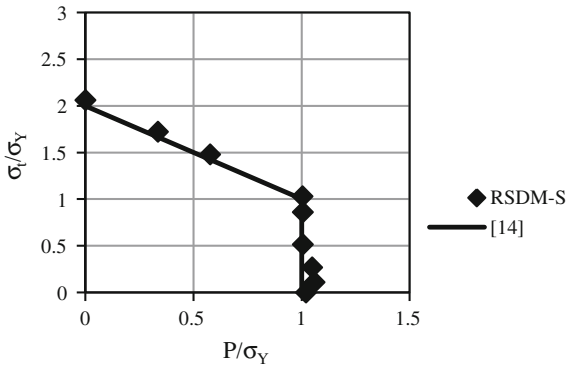

Fig. 5 Shakedown domain produced by the RSDM-S and its comparison with Bradford's solution [14] (load case 2)

In Fig. 4 one may see the constructed shakedown domain by the RSDM-S and its comparison with the analytical solution of Bree [13]. The two domains are almost identical.

3.1.2 Proportional Variation of Axial Load $P(\tau)$ and Temperature $\Delta\theta(\tau)$

The proportional variation of the cyclic loading in the load domain may be described by the path $(0 \rightarrow (P^*, \Delta\theta^*) \rightarrow 0)$ (Fig. 3b).

Let us now consider a prescribed loading in the time domain using the equation:

$$P(\tau) = \left\{ \begin{array}{c} P^* \alpha(\tau) \\ \Delta\theta^* \alpha(\tau) \end{array} \right\} \text{ where } \alpha(\tau) = 3.3334\tau^4 - 6.6667\tau^3 + 0.1667\tau^2 + 3.1667\tau$$

Bree's findings have been analytically extended by Bradford [14] for a case of proportional loading. The results of the RSDM-S as well as its good agreement with Bradford's results [14] may be seen in Fig. 5.

3.2 Square Plate with a Central Hole

The second example of application is a holed square plate under a combination of mechanical and thermal loads (Fig. 6). The plate is assumed homogeneous, isotropic, elastic-perfectly plastic with the material data of Table 1. The boundary conditions as well as its finite element mesh discretization are shown in Fig. 6. The ratio between the diameter D of the hole and the length L of the plate is equal to 0.2. Also the ratio of the thickness d of the plate to its length is equal to 0.05. Due to the symmetry of the structure and the loading, only one quarter of the plate is analyzed. The finite element mesh discretization of the plate consists of ninety-eight, eight-noded, iso-parametric elements with 3 × 3 Gauss integration points (Fig. 6).

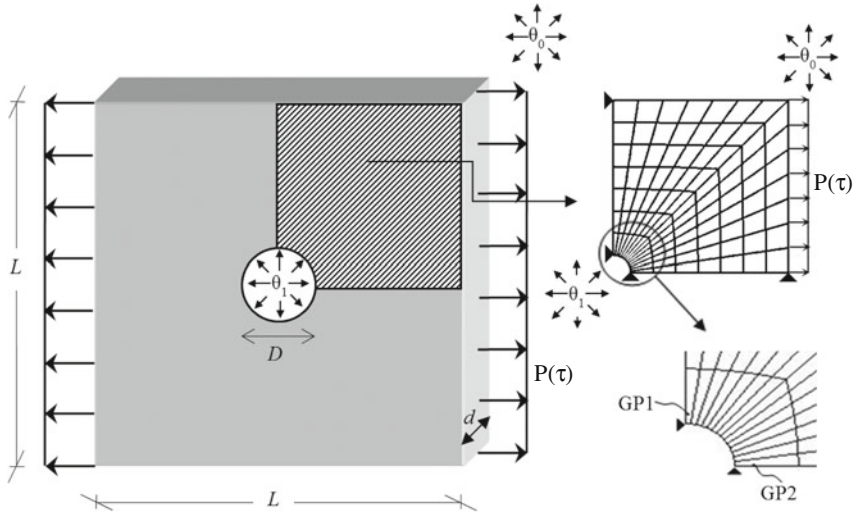

Fig. 6 The geometry, loading and the finite element mesh of a quarter of the plate

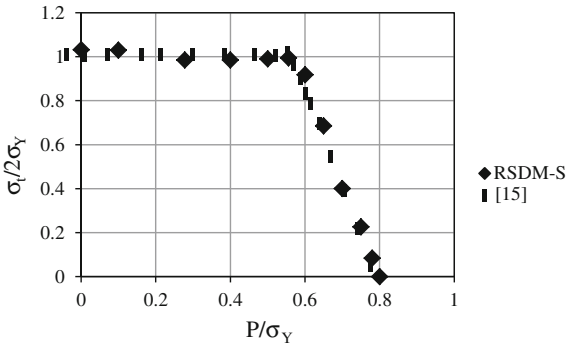

Fig. 7 The elastic shakedown domain for the holed plate (load case 1)

The plate is subjected to a temperature difference $\Delta\theta(\tau)$ between the edge of the hole and the edge of the plate, and a uniaxial tension $P(\tau)$ along the one side of the plate (Fig. 6). The variation of the temperature with radius r has the same logarithmic form as in [8, 15]:

$$\theta(r,\tau) = \theta_0 + \frac{\Delta\theta(\tau) * \ln\left(\frac{5D/2}{r}\right)}{\ln 5}$$

The above relation defines a temperature distribution inside the plate giving a value of $\theta_1(\tau) = \theta_0 + \Delta\theta(\tau)$ around the edge of the hole $(r = D/2)$ and $\theta_1 = \theta_0$ at the outer edges of the plate $(r = 5D/2)$. The temperature θ_0 is assumed to be equal to zero. It should be noted that in the results σ_t denotes the maximum effective thermal elastic stress due to the fluctuating temperature.

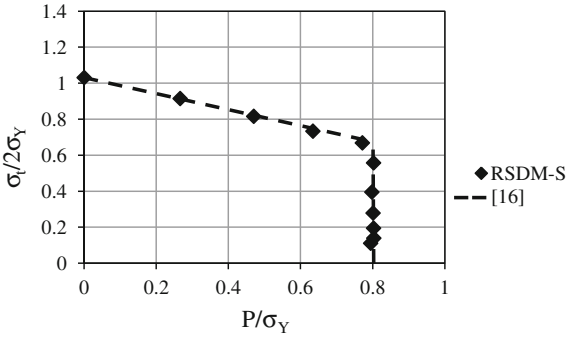

Fig. 8 The elastic shakedown domain for the holed plate (load case 2)

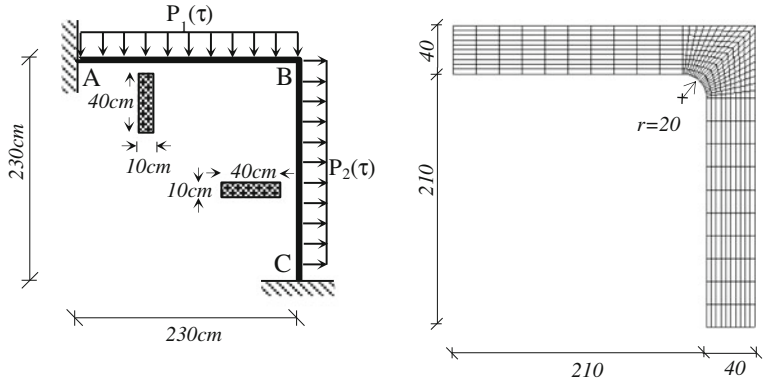

Fig. 9 Geometry, loading and finite element mesh of the frame

The shakedown domains were calculated by the RSDM-S assuming two different load cases (Fig. 3). The polynomial time functions that were used to describe the two load paths are the same ones used in the Bree example.

In Fig. 7 one may see the comparison between the results of the RSDM-S with the ones obtained in [15] for the case of constant mechanical load. On the other hand, assuming simultaneous variation of both the thermal and mechanical load, the results of the RSDM-S and its comparison with [16] are plotted in Fig. 8. The results match quite well.

3.3 Frame in a General Loading Domain

In the third example, a simple frame, shown in Fig. 9 is considered. This example has been investigated by Tran et al. [18] using an edge-based smoothed finite element method (ES-FEM) and a primal-dual shakedown algorithm, and by Garcea et al. [17] using a strain driven strategy.

Table 2 Material properties of the frame

Young's modulus	Poisson's ratio	Yield stress
E = 200 GPa	$\nu = 0.3$	$\sigma_Y = 100$ MPa

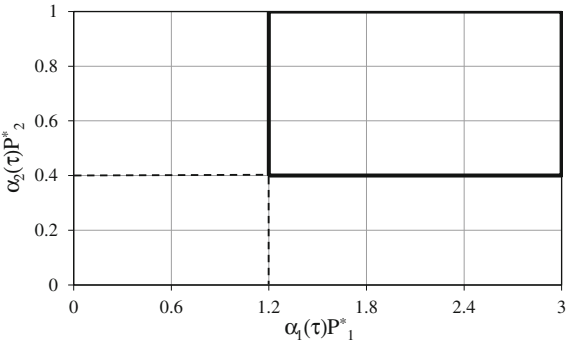

Fig. 10 Loading domain of frame example

Table 3 Comparison of the numerical results

Author	Shakedown factor
Garcea et al. (2005) [17]	3.925
Tran et al. (2010) [18]	4.006
Pham (2011) [19]	4.015
Present	**3.91**

The frame is assumed homogeneous, isotropic, elastic-perfectly plastic, having the material data shown in Table 2. The finite element mesh discretization of the frame, shown also in Fig. 9, consists of 400 eight-noded, iso-parametric elements with 3 × 3 Gauss integration points.

The frame is subjected to two uniform distributed loads $P_1(\tau)$ and $P_2(\tau)$, applied on the external faces of AB and BC respectively. A general rectangular loading domain is considered herein (Fig. 10) with the two loads $P_1(\tau)$ and $P_2(\tau)$ varying independently, between the values $[1.2, 3]$ and $[0.4, 1]$ respectively. A case of a regular loading domain having its origin at zero was studied in [7].

A prescribed loading in time domain that passes through the four vertices of the rectangle may be defined by using the following equations:

$$\text{where } P(\tau) = \left\{ \begin{matrix} P_1^* \alpha_1(\tau) \\ P_2^* \alpha_2(\tau) \end{matrix} \right\} \text{ and the time functions } \alpha_1(\tau),\ \alpha_2(\tau) \text{ are:}$$

$$\begin{aligned}
&\alpha_1(\tau) = -9.6\tau^2 + 4.8\tau + 0.4, \alpha_2(\tau) = 0.4, \quad \tau \in [0, 1/4] \\
&\alpha_1(\tau) = 1, \alpha_2(\tau) = -9.6\tau^2 + 9.6\tau - 1.4, \quad \tau \in (1/4, 1/2] \\
&\alpha_1(\tau) = -9.6\tau^2 + 9.6\tau - 1.4, \alpha_2(\tau) = 1, \quad \tau \in (1/2, 3/4] \\
&\alpha_1(\tau) = 0.4, \alpha_2(\tau) = -9.6\tau^2 + 14.4\tau - 4.4, \quad \tau \in (3/4, 1]
\end{aligned}$$

In this case $P_1^* = 3$, $P_2^* = 1$ and $0.4 \leq \alpha_1(\tau), \alpha_2(\tau) \leq 1$.

For this example the initial convergence parameter ω, in the process of the iterations, had to be halved twice, for the RSDM-S to converge to the final shakedown limit which was found equal to 3.91.

The present results of the RSDM-S, compared to those of different analysis methods in the literature, are shown in Table 3. It may be seen that they match quite well.

3.4 *Symmetric Continuous Beam in a General Loading Domain*

Let us now consider the symmetric continuous beam of Fig. 11. The beam is subjected to two uniform distributed loads $P_1(\tau)$ and $P_2(\tau)$, applied on each span. The beam is assumed homogeneous, isotropic, elastic-perfectly plastic, having the material data shown in Table 4. The finite element mesh discretization of the beam, shown also in Fig. 11, consists of 800 eight-noded, iso-parametric elements with 3×3 Gauss integration points.

A general rectangular loading domain is considered (Fig. 12) with the two loads $P_1(\tau)$ and $P_2(\tau)$ varying independently, between the values $[1.2, 2]$ and $[0, 1]$ respectively. A case of a regular loading domain having its origin at zero was studied in [7].

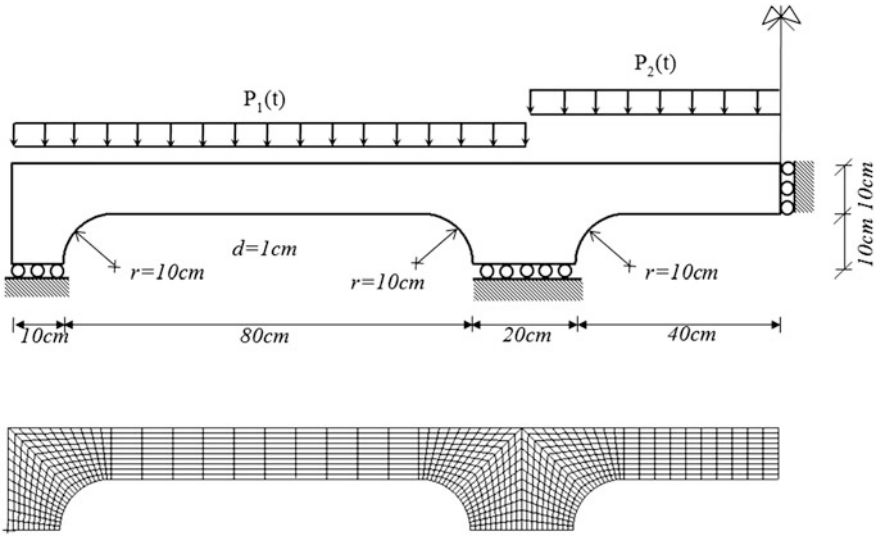

Fig. 11 Geometry, loading and finite element mesh for the continuous beam

Table 4 Material properties of the continuous beam

Young's modulus	Poisson's ratio	Yield stress
E = 180 GPa	$\nu = 0.3$	$\sigma_Y = 100$ MPa

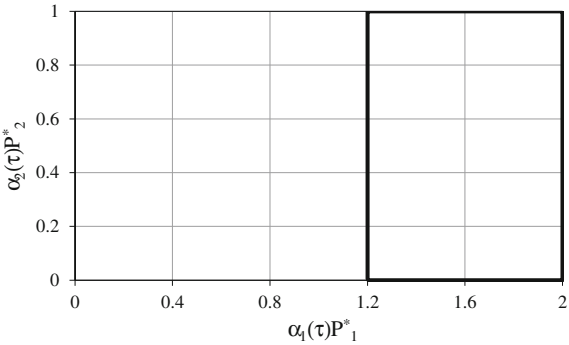

Fig. 12 Loading domain of beam example

Table 5 Comparison of numerical results of the symmetric continuous beam

Author	Shakedown limit
Garcea et al. (2005) [17]	3.244
Tran et al. (2010) [18]	3.377
Pham (2011) [19]	3.264
Present	**3.177**

A prescribed loading in time domain that passes through the four vertices of the rectangular may be defined by using the following time functions $\alpha_1(\tau), \alpha_2(\tau)$:

$$\alpha_1(\tau) = -6.4\tau^2 + 3.2\tau + 0.6, \alpha_2(\tau) = 0, \quad \tau \in [0, 1/4]$$
$$\alpha_1(\tau) = 1, \alpha_2(\tau) = -16\tau^2 + 16\tau - 3, \quad \tau \in (1/4, 1/2]$$
$$\alpha_1(\tau) = -6.4\tau^2 + 6.4\tau - 0.6, \alpha_2(\tau) = 1, \quad \tau \in (1/2, 3/4]$$
$$\alpha_1(\tau) = 0.6, \alpha_2(\tau) = -16\tau^2 + 24\tau - 8, \quad \tau \in (3/4, 1]$$

It is assumed that $P_1^* = 2$, $P_2^* = 1$ and $0.6 \leq \alpha_1(\tau) \leq 1, 0 \leq \alpha_2(\tau) \leq 1$.

For this example, the initial convergence parameter ω, in the process of the iterations, had to be halved three times, for the RSDM-S to converge to the final shakedown limit which is equal to 3.177. The shakedown factor obtained by the RSDM-S, and its comparison with the results of different analysis methods [17–19], is shown in Table 5. It may be seen that there is a good agreement.

Briefing from the present numerical applications, as well as all the ones that have been reported so far, in the literature, one has to note the good and quick convergence characteristics of the RSDM-S approach, as the stiffness matrix must be formed and decomposed only once and only the first three terms of the Fourier series were enough to get accurate results, with the cycle time points being around forty.

4 Concluding Remarks

The direct method, RSDM-S, has been used in the present work to evaluate the shakedown load and provide shakedown boundaries for cyclically loaded elasto-plastic structures under mechanical or thermo-mechanical loading. The loading domain is first converted into a prescribed loading using time functions. In the present work it was shown that the procedure may be easily applied to more general domains, than the already published ones, whose origin is different than zero, by just modifying the time functions. The prescribed loading is then multiplied by a load factor. Starting from a factor high above shakedown, a descending sequence of loading factors is formed which converges to the parameters of the limit cycle, where the residual stresses are constant in time. The approach turns out to be simple, numerically stable and efficient and may be implemented in any existing FE code as opposed to mathematical programming methods where a special optimization algorithm must be supplied.

References

1. Drucker DC (1959) A definition of stable inelastic material. ASME J Appl Mech 26:101–106
2. Frederick CO, Armstrong PJ (1966) Convergent internal stresses and steady cyclic states of stress. J Strain Anal 1:154–169
3. Melan E (1938) Zur plastizität des räumlichen Kontinuums. Ing Arch 9:116–126
4. Koiter W (1960) General theorems for elastic-plastic solids. In: Sneddon IN, Hill R (eds) Progress in solid mechanics. North-Holland, Amsterdam
5. Spiliopoulos KV, Panagiotou KD (2012) A direct method to predict cyclic steady states of elastoplastic structures. Comput Methods Appl Mech Eng 223–224:186–198
6. Spiliopoulos KV, Panagiotou KD (2014) The residual stress decomposition method (RSDM): a novel direct method to predict cyclic elastoplastic states. In: Spiliopoulos KV, Weichert D (eds) Direct methods for limit states in structures and materials. Springer, New York, pp 139–156
7. Spiliopoulos KV, Panagiotou KD (2014) A residual stress decomposition based method for the shakedown analysis of structures. Comput Methods Appl Mech Eng 276:410–430
8. Spiliopoulos KV, Panagiotou KD (2014) A numerical procedure for the shakedown analysis of structures under thermomechanical loading. Arch Appl Mech 85:1499–1511
9. Spiliopoulos KV, Panagiotou KD (2015) RSDM-S: a method for the evaluation of the shakedown load of elastoplastic structures. In: Fuschi P, Pisano AA, Weichert D (eds) Direct methods for limit and shakedown analysis of structures. Springer, New York, pp 159–176
10. Panagiotou KD, Spiliopoulos KV (2016) Assessment of the cyclic behavior of structural components using novel approaches. J Pressure Vessel Technol 138:041201
11. König JA (1987) Shakedown of elastic-plastic structures. Elsevier, Amsterdam
12. Gokhfeld DA, Cherniavsky OF (1980) Limit analysis of structures at thermal cycling. Sijthoff & Noordhoff
13. Bree J (1967) Elastic-plastic behavior of thin tubes subjected to internal pressure and intermittent high-heat fluxes with application to fast-nuclear-reactor fuel elements. J Strain Anal 2:226–238
14. Bradford RAW (2012) The Bree problem with primary load cycling in-phase with the secondary load. Int J Press Vess Pip 99:44–50

15. Chen HF, Ponter ARS (2001) A method for the evaluation of a ratchet limit and the amplitude of plastic strain for bodies subjected to cyclic loading. Eur J Mech—A/Solids 20:555–571
16. Lytwyn M, Chen HF, Ponter ARS (2015) A generalized method for ratchet analysis of structures undergoing arbitrary thermo-mechanical load histories. Int J Numer Meth Eng. 104:104–124
17. Garcea G, Armentano G, Petrolo S, Casciaro R (2005) Finite element shakedown analysis of two-dimensional structures. Int J Numer Methods Eng 63:1174–1202
18. Tran TN, Liu GR, Nguyen XH, Nguyen TT (2010) An edge-based smoothed finite element method for primal-dual shakedown analysis of structures. Int J Numer Eng 82:917–938
19. Pham PT (2011) Upper bound limit and shakedown analysis of elastic–plastic bounded linearly kinematic hardening structure. PhD thesis, RWTH University, Aachen

Some Graphical Interpretations of Melan's Theorem for Shakedown Design

N. Vermaak, M. Boissier, L.Valdevit and R. M. McMeeking

Abstract Bree Interaction Diagrams have long been one of the major visual design guides for employing and evaluating shakedown in engineering applications. These diagrams provide representations of the realms in which elastoplastic behaviors, including shakedown, are found for a material and structure under variable loads. The creation of these diagrams often relies upon some combination of upper or lower bound shakedown theorems and numerical shakedown limit determination techniques. Part of the utility of these diagrams is that, for a given structure and loading conditions, inspecting them is sufficient to determine whether shakedown will occur or not. The diagrams cannot however, give the designer insight into how the conditions for shakedown are met. This chapter presents some graphical interpretations of one of the common methods for shakedown determination: the use of Melan's Lower Bound Theorem. The intent is to provide additional insight for designers regarding how shakedown conditions are satisfied. In this way, additional directions for modifying designs to recover shakedown behavior may also be identified. Revisiting this well-established theorem from a graphical and pedagogical approach, also provides a foundation for interdisciplinary innovation. The particular focus is on simple examples that highlight ways in which Melan's theorem may be applied to shakedown design problems.

N. Vermaak (✉) · M. Boissier
Department of Mechanical Engineering and Mechanics, Lehigh University,
Bethlehem, PA 18015, USA
e-mail: vermaak@lehigh.edu

M. Boissier
e-mail: mathilde.boissier@polytechnique.org

L. Valdevit
Department of Mechanical and Aerospace Engineering, University of California,
Irvine, CA 92697, USA
e-mail: valdevit@uci.edu

R.M. McMeeking
Mechanical Engineering Department, University of California,
Santa Barbara, CA 93106, USA
e-mail: rmcm@engineering.ucsb.edu

O. Barrera et al. (eds.), *Advances in Direct Methods for Materials and Structures*, DOI 10.1007/978-3-319-59810-9_11

1 Introduction

While shakedown concepts, limit theorems, and numerical methods have been developed since the 1920s and 1930s [1–5], their widespread acceptance and application in engineering design communities remains limited [5]. Some of the factors that would promote more widespread use of shakedown concepts and limit theorems include improving awareness through educational materials, more experimental validation efforts, and enhanced communication of shakedown benefits to different design communities. This chapter presents graphical interpretations of shakedown concepts with the intent to provide additional insight and understanding while complementing existing graphical shakedown design tools.

Within the context of plastic design under variable loads, shakedown limit theorems have been used in applications ranging from: vessels for demilitarization of munitions [6], tribology [7], multilayer semiconductor devices [8], pavement design [9, 10], shape memory alloy components [11–13], to nuclear pressure vessels [5]. The theorems delineate the boundaries between reliable and inadmissible behaviors [14–17] (see top of Fig. 1). The theorems often replace traditional yield-limited assessments of structural integrity and can be used in the design process to evaluate a structure's response to unanticipated loads. The operational space is extended by allowing *shakedown* to occur, whereby stresses locally exceed the yield strength of a material in the first few cycles of load and thereafter, fully elastic response is recovered.

More generally, the range of possible structural responses is often illustrated through the use of a Bree Interaction Diagram, which indicates combinations of loads that lead to various material and structural behaviors. Figure 1 illustrates the classic Bree diagram for a thin-walled cylinder (with a radius, R and thickness, t), subjected to a fixed internal pressure and a cyclic radial temperature difference [14]. The ordinate is $\Delta \mathrm{T}/\Delta \mathrm{T}_o$ where $\Delta \mathrm{T}_o$ is the temperature difference required for yield initiation (σ_Y) in the absence of a mechanical load $\left(\Delta T_o = 2(1-\nu)\sigma_Y/E\alpha\right)$; the abscissa is P/P_o with P_o being the pressure that causes yielding in the absence of a temperature gradient $\left(\sigma_Y = P_o R/t\right)$. E, α, ν are the material Young's modulus, coefficient of thermal expansion, and Poisson's ratio, respectively. The elastic domain is defined by $\mathrm{P}/\mathrm{P}_o + \Delta T/\Delta T_o < 1$. At one extreme, wherein $\mathrm{P}/\mathrm{P}_o > 1$, *plastic collapse* occurs on the first load cycle, i.e. the thin wall experiences complete yielding. For intermediate combinations of P and ΔT, one of three behaviors is obtained (Fig. 1) [18]. (i) In the *shakedown* regime, localized plastic deformation that occurs in the early stages of cycling gives rise to residual stresses that stabilize the plastic response. Purely elastic behavior results during any further loading cycles. (ii) *Alternating plasticity* occurs by loading beyond the shakedown limit. Here the plastic strain increment obtained during the first half of each loading cycle is balanced by a plastic strain increment of equal magnitude but opposite sign during the second half of the loading cycle. No net strain accrues during each cycle but the structure ultimately fails by low-cycle fatigue. (iii) *Ratchetting* refers to the condition in which a net increment of plastic strain accumulates during each cycle, eventually causing rupture.

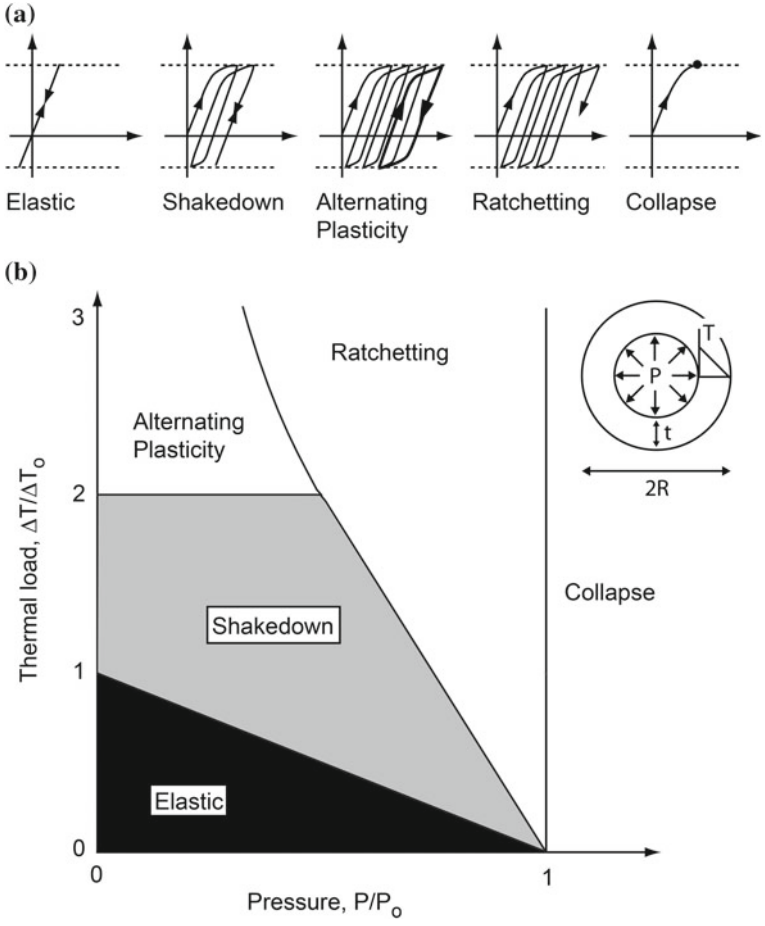

Fig. 1 **a** Prototypical stress-strain behaviors for an elastic-plastic material in the classic Bree problem and **b** the corresponding analytic Bree diagram. A cylindrical vessel is subject to constant internal pressure and a cyclic thermal gradient through the wall thickness

The creation of these diagrams often relies upon some combination of upper or lower bound shakedown theorems and numerical shakedown limit determination techniques. The utility of interaction diagrams such as Fig. 1 is immediately apparent; for an engineering application, designers may easily assess the benefits of allowing shakedown to occur. The interaction diagrams cannot however, give the designer insight into how the conditions for shakedown are met. This chapter presents some graphical interpretations of one of the common methods for shakedown determination: the use of *Melan's Lower Bound Theorem* under small deformation theory assumptions (from Koiter [19]):

> If any time-independent distribution of residual stresses, $\bar{\boldsymbol{\rho}}_{ij}$, can be found such that the sum of these residual stresses and the "elastic" stresses, σ^e_{ij}, is a safe state of stress $\sigma^e_{ij} + \bar{\boldsymbol{\rho}}_{ij} = \sigma^s_{ij}$, *i.e.* a state of stress inside the yield limit, at every point of the body and for all possible load combinations within the prescribed bounds, then the structure will shake down to some time-independent distribution of residual stresses (usually depending on the actual loading program), and the response to subsequent load variations within the prescribed limits will be elastic. On the other hand, shakedown is impossible if no time-independent distribution of residual stresses can be found with the property that the sum of the residual stresses and "elastic" stresses is an allowable state of stress at every point of the body and for all possible load combinations.

In other words, to assure that a structure will shakedown, one has to find a residual stress field, $\boldsymbol{\rho}$, that satisfies the following three conditions: (i) it has to be self-equilibrating, (ii) it has to be time-independent, and (iii) it has to remain within the yield limit when combined with any fictitious "elastic" stress caused by a load combination from the loading domain. This powerful theorem gives a necessary and sufficient condition to determine if a structure will shakedown or not. One of the major advantages of this theorem and this kind of "Direct Method" is that information about the loading path in an arbitrarily complex loading space is not needed. Rigorous bounds and shakedown predictions can be made based on purely elastic solutions or simplified elastoplastic calculations [19–31]. In contrast, the "classical load history approach" follows the incremental or step-by-step evolution of a system and finds the actual residual stress field that would result from the actual loading history that is deterministically known. Direct Methods, which historically developed out of necessity and without access to computational tools, typically take a more mathematical approach to predict shakedown response [5]. It should be noted that "classical incremental or load history approaches" and "direct methods" are not competing methods, but rather complementary as each provides different information and functionality and they often have separate domains of applicability. For example, direct methods avoid cumbersome incremental load-history based calculations and are especially useful when the exact loading history within a domain is unknown. Whereas the load-history based approaches provide the often crucial evolution of local quantities.

Several versions of proofs of Melan's lower bound theorem can be found in the literature [19–21, 32] and many extensions of this theorem have been made to analyze temperature or time-dependent properties, creep, damage, and others [5, 33, 34]. Many ways to implement Melan's theorem to determine shakedown behavior or shakedown limit loads have also been developed; see Weichert and Ponter [5] for a broad historical survey. One way to think about the techniques for lower-bound shakedown determination is by emphasizing "any" in the first part of the limit theorem (*"If **any** time-independent distribution of residual stresses, $\bar{\boldsymbol{\rho}}_{ij}$, can be found..."*). How could one find appropriate residual stress fields? Direct methods exploit the mathematical freedom available by searching for "any" residual stress field that meets the specified shakedown conditions; to do this, direct methods use a variety of procedures from graph theory to optimization [22, 35–43].

In this work, two different direct method implementations of Melan's theorem for shakedown determination are considered. The goal is to illustrate graphically what is mathematically determined when an admissible residual stress field, $\boldsymbol{\rho}$, is sought and the conditions for a structure to shakedown are met. The graphical interpretations also provide a way to understand the role of key parameters and features in the shakedown determination process. Revisiting this well-established theorem from a graphical and pedagogical approach, also provides a foundation for interdisciplinary innovation. In the following, Sect. 2 will present the background and assumptions of the problems analyzed. Sections 3 and 4 present several examples. Discussion of the assumptions and limitations is presented in Sect. 5 and followed by conclusions.

2 Setting of the Problem

Consider an elastic-perfectly-plastic solid, Ω, under small deformation theory assumptions. Its boundary, $\partial\Omega$, characterized by its normal, $\underline{n}$, can be described in parts (Fig. 2): $\partial\Omega_0$ is the part of the boundary on which displacement is imposed, $\partial\Omega_F$ is the part of the boundary on which any traction, F, from the prescribed loading domain, L (Fig. 3), could be applied, and Γ is the part of the boundary that is traction-free. These parts satisfy the conditions:

$$\begin{aligned} &\partial\Omega = \partial\Omega_0 \cup \partial\Omega_F \cup \Gamma, \\ &\partial\Omega_0 \cap \partial\Omega_F = \emptyset, \qquad \partial\Omega_0 \cap \partial\Gamma = \emptyset, \qquad \partial\Omega_F \cap \partial\Gamma = \emptyset. \end{aligned} \tag{1}$$

In the following, a constant scalar yield stress, σ_Y, is considered and a von Mises yield function, f, is adopted. As a result of a load, P, applied to a solid, Ω, on the part $\partial\Omega_F$, two types of stresses will be distinguished: (i) the *actual stresses*, σ^P_{actual}, these are the elastoplastic stresses that would be caused by the load (under the elastic-perfectly-plastic model); (ii) the *fictitious "elastic" stresses*, $\sigma^P_{e,fict}$, these are the stresses that would be caused by the load if the response were purely elastic.

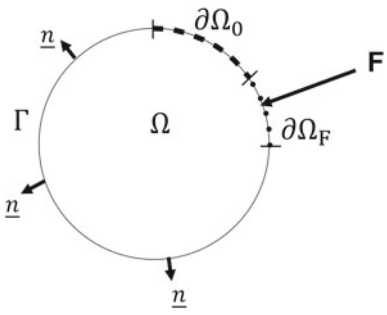

Fig. 2 Schematic of structure and problem parameters

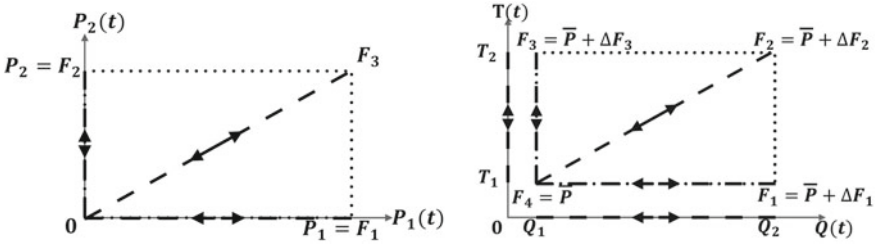

Fig. 3 Loading domains, L

Lastly, the loading domain, L, assumed (Fig. 3) contains every possible loading combination for the loads applied to the solid. By assuming that L is a convex N-dimensional polyhedron [44], it is possible to define the loading corners, F_i, ($i \in [\![1, NC]\!]$ where NC is the number of corners) of the loading domain, and every loading path that connects one corner to another will remain inside the loading domain. Note that all problems considered involve loading by tractions, forces or displacements and no thermal stresses are considered. We therefore keep temperature constant and uniform throughout the examples presented. As a result, two types of loading domains, L, can be considered: only cyclic loads and combined cyclic and constant loads (Fig. 3). For example, at the bottom of Fig. 3, a combined cyclic and constant loading domain is illustrated. It is composed of the loads $Q(t)$ (cycling between Q_1 and Q_2) and $T(t)$ (cycling between T_1 and T_2). It should be noted that for this analysis, the constant load, $\overline{P}$, will be restricted to cause purely elastic response in the structure, so that the actual stress it causes is equivalent to the fictitious "elastic" stress.

For the remainder of this work and using the translations and adaptations of Koiter, Symonds, and König [3, 4, 19, 20, 32], the following formulation of Melan's lower bound shakedown theorem is adopted: *A solid, Ω (Fig. 2), which is subjected to any cyclic traction F, from the loading domain L, (Fig. 3) on a part $\partial\Omega_F$ of its boundary $\partial\Omega$, will shakedown under this loading domain if one can find any residual stress field, $\boldsymbol{\rho}$, which:*

- *Condition 1 (spatial)* is self-equilibrating, meaning that its divergence over the solid, Ω, is zero and the field satisfies the prescribed traction-free conditions on the solid's boundary, $\partial\Omega_F \cup \Gamma$ (with the normal, $\underline{n}$, Fig. 2) [21]:

$$\begin{aligned} div(\boldsymbol{\rho}) = 0 \quad in \quad \Omega, \\ \boldsymbol{\rho} \cdot \underline{n} = 0 \quad on \quad \partial\Omega_F \cup \Gamma. \end{aligned} \tag{2}$$

- *Condition 2 (pointwise)* is time-independent, meaning that its value at each point does not depend on the applied loading corner, F_i ($\forall i \in [\![1, NC]\!]$), in the loading domain L, (note that $\boldsymbol{\rho}_i$ is the field corresponding to loading corner, F_i):

$$\forall i \in [\![1, NC]\!], \qquad \boldsymbol{\rho}_i = \boldsymbol{\rho}. \tag{3}$$

Fig. 4 Loading domain

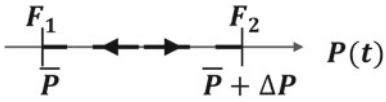

- *Condition 3 (pointwise)* will generate a safe state of stress at each point, $\underline{x}$, in the solid ($\underline{x} \in \Omega$) when it is added to a fictitious "elastic" stress $\sigma_{e,fict}^{F_i}$, associated with any of the loading corners, F_i ($\forall i \in [\![1, NC]\!]$), in the loading domain L. For a yield function, f, and a yield stress, σ_Y, this gives:

$$\forall \underline{x} \in \Omega, \quad \forall i \in [\![1, NC]\!], \qquad f(\boldsymbol{\rho}(\underline{x}) + \sigma_{e,fict}^{F_i}(\underline{x}), \sigma_Y) \leq 0. \tag{4}$$

The conditions have been labeled as pointwise or spatially-dependent (spatial) to highlight differences for use in the following sections. Unlike Conditions 2 and 3 which only have to be satisfied at each point, Condition 1 links all of the points in the solid together through the divergence term and the boundary conditions.

3 Graphical Interpretations of Shakedown Determination with Simplified Elastoplastic Analysis

One approach to finding appropriate residual stress fields for use in Melan's theorem is to use simplified elastoplastic analysis [22–31]. Instead of incrementally following an entire cyclic loading history, a single elastoplastic analysis for one cycle that includes both loading and unloading could be used to calculate a representative residual stress field, $\boldsymbol{\rho}$, developed in a solid, Ω. Then, the residual stress field, $\boldsymbol{\rho}$, is checked so that when it is added to the fictitious "elastic" stresses that would be caused by the same loading process, the sum will remain below the yield level. For more than one cyclic load application (or more than one cyclic load combined with constant loads), the time-independent condition (Eq. 3) is not automatically satisfied. For the following examples, simplified two-corner loading domains (Fig. 4) will be used so that only one path—the one connecting the two corners—has to be analyzed.

In this shakedown determination with a simplified elastoplastic analysis approach, a first step is to compute the residual stress field from loading and unloading the solid, and verify that the self-equilibrating condition is met (Eq. 2). First, the constant load, $\overline{P}$, is applied; this elicits an actual stress which is also the fictitious "elastic" stress (Sect. 2): $\sigma_{actual}^{\overline{P}} = \sigma_{e,fict}^{\overline{P}}$. At this stage, the load applied to the structure is the load corresponding to the first loading corner, $\overline{P} = F_1$. Then, the cyclic load ΔP is applied and the structure is fully loaded (the sum of the constant load, $\overline{P}$ and the extremum value of the cyclic load, ΔP). This corresponds to the second loading corner, F_2. The stress, $\sigma_{actual}^{\overline{P}+\Delta P}$, is now different from the fictitious "elastic" stress, $\sigma_{e,fict}^{\overline{P}+\Delta P}$. This new

fictitious "elastic" stress, $\sigma_{e,fict}^{\overline{P}+\Delta P}$, can be related to the stress caused by the constant load, $\sigma_{e,fict}^{\overline{P}}$ (linearly elastic): $\sigma_{e,fict}^{\overline{P}+\Delta P} = \sigma_{e,fict}^{\overline{P}} + \sigma_{e,fict}^{\Delta P}$.

The residual stress field, $\boldsymbol{\rho}$, is computed by completely unloading the solid: the total fictitious "elastic" stress, $\sigma_{e,fict}^{\overline{P}+\Delta P}$ is subtracted from the total stress, $\sigma_{actual}^{\overline{P}+\Delta P}$:

$$\boldsymbol{\rho} = \sigma_{actual}^{\overline{P}+\Delta P} - \sigma_{e,fict}^{\overline{P}+\Delta P}. \tag{5}$$

The residual stress field, $\boldsymbol{\rho}$, by definition, is automatically self-equilibrating as demonstrated in the following. The stress field, $\sigma_{actual}^{\overline{P}+\Delta P}$, resulting from the applied load $\overline{P} + \Delta P$, satisfies the equilibrium equations (see Fig. 2):

$$\begin{aligned} div\left(\sigma_{actual}^{\overline{P}+\Delta P}\right) &= 0 \quad in\ \Omega \\ \sigma_{actual}^{\overline{P}+\Delta P} \cdot \underline{n} &= \overline{P} + \Delta P \quad on\ \partial\Omega_F \\ \sigma_{actual}^{\overline{P}+\Delta P} \cdot \underline{n} &= 0 \quad on\ \Gamma \end{aligned} \tag{6}$$

The fictitious "elastic" stress field, $\sigma_{e,fict}^{\overline{P}+\Delta P}$, satisfies the same equations, as it is the stress induced by the same loading, $\overline{P} + \Delta P$, but assuming purely elastic behavior:

$$\begin{aligned} div\left(\sigma_{e,fict}^{\overline{P}+\Delta P}\right) &= 0 \quad in\ \Omega \\ \sigma_{e,fict}^{\overline{P}+\Delta P} \cdot \underline{n} &= \overline{P} + \Delta P \quad on\ \partial\Omega_F \\ \sigma_{e,fict}^{\overline{P}+\Delta P} \cdot \underline{n} &= 0 \quad on\ \Gamma \end{aligned} \tag{7}$$

Since the divergence and the scalar product are linear operators, the nullity of the divergence of the residual stress field and the traction-free conditions are ensured by:

$$\begin{aligned} div(\boldsymbol{\rho}) = div\left(\sigma_{actual}^{\overline{P}+\Delta P}\right) - div\left(\sigma_{e,fict}^{\overline{P}+\Delta P}\right) &= 0 \quad in\ \Omega \\ \boldsymbol{\rho} \cdot \underline{n} = \sigma_{actual}^{\overline{P}+\Delta P} \cdot \underline{n} - \sigma_{e,fict}^{\overline{P}+\Delta P} \cdot \underline{n} = \overline{P} + \Delta P &= 0 \quad on\ \partial\Omega_F \\ \boldsymbol{\rho} \cdot \underline{n} = \sigma_{actual}^{\overline{P}+\Delta P} \cdot \underline{n} - \sigma_{e,fict}^{\overline{P}+\Delta P} \cdot \underline{n} &= 0 \quad on\ \Gamma \end{aligned} \tag{8}$$

As the solid, Ω, is elastic-perfectly-plastic, the stress, $\sigma_{actual}^{\overline{P}+\Delta P}$, cannot go beyond the yield limit. One only needs to check that the residual stress field is "safe", meaning that at each point, the residual stress remains below the yield level. In order to illustrate this approach for shakedown determination and gain more insight from a design perspective, a graphical interpretation is presented.

3.1 Example for Combined Cyclic and Constant Loading

Consider a two-component stress state and a von Mises yield function represented as a circle in a S_1, S_2 plane. In this plane, adding and removing stresses can be represented by adding and subtracting vectors; S_1, S_2 are stress components and the plane is not necessarily in principal stress axes. Once the stresses, $\sigma^{F}_{actual}(\underline{x})$, reach the yield limit, they remain at yield on the circle until unloading. For the illustrations presented, only abstract schematic representations are used.

It has been shown above that the residual stress is self-equilibrating. Before considering the following step, a modified stress field, $\tilde{\boldsymbol{\rho}}$, is defined for convenience as the sum of the residual stress field ($\boldsymbol{\rho}$, Eq. 5) with the fictitious "elastic" stress caused by the constant load only, $\sigma^{\overline{P}}_{e,fict}$. This stress is the one remaining in the solid, Ω, after only unloading the cyclic load ΔP:

$$\tilde{\boldsymbol{\rho}} = \boldsymbol{\rho} + \sigma^{\overline{P}}_{e,fict}. \tag{9}$$

The time-independence condition is also automatically satisfied. Once computed, the residual stress ($\boldsymbol{\rho}$, Eq. 5) will not change. Finally, the safe-state condition has only to be checked for the loading corners, at each point, $\underline{x}$, in the solid. For $F_1 = \overline{P}$:

$$\forall\ \underline{x} \in \Omega, \qquad f\left(\boldsymbol{\rho}(\underline{x}) + \sigma^{\overline{P}}_{e,fict}(\underline{x}), \sigma_Y\right) \leq 0 \tag{10}$$

and for $F_2 = \overline{P} + \Delta P$:

$$\forall\ \underline{x} \in \Omega, \qquad f\left(\boldsymbol{\rho}(\underline{x}) + \sigma^{\overline{P}+\Delta P}_{e,fict}(\underline{x}), \sigma_Y\right) = f\left(\sigma^{\overline{P}+\Delta P}_{actual}(\underline{x}), \sigma_Y\right) \leq 0 \tag{11}$$

Equation 11 is automatically satisfied because the solid is elastic-perfectly-plastic. From this point, the safe-state condition must be checked for the modified stress field, $\tilde{\boldsymbol{\rho}}$, (Eq. 9).

For a two-component stress state at a point $\underline{x}$, Fig. 5 illustrates cases where shakedown is and is not possible. If shakedown is not possible at a single point in the structure, shakedown is prevented for the entire structure. In these figures, the *thin solid* lines represent the elastic stresses that result from the applied constant load ($\sigma^{\overline{P}}_{e,fict}\left(\underline{x}\right)$). Following the application of the constant load, an additional cyclic load is then applied and the resulting fictitious "elastic" stresses are shown by the *sparsely-dotted* ($\sigma^{\Delta P}_{e,fict}\left(\underline{x}\right)$). The actual elastoplastic stresses are depicted by *thicker dashed* lines ($\sigma^{F_{a,b}}_{actual}\left(\underline{x}\right)$) and overlap both the *sparsely-dotted* and *thin solid* lines within the elastic domain. The *thick dashed* lines for the actual elastoplastic stresses follow the yield surface (circle) when the yield limit is reached and the load is increased. Upon unloading (elastically), the fictitious "elastic" stress is subtracted from the actual elastoplastic stress ($\sigma^{F_{a,b}}_{actual}\left(\underline{x}\right) - \sigma^{\Delta P}_{e,fict}\left(\underline{x}\right)$). Note that only the cyclic load (and the associated fictitious "elastic" stresses) is removed and the constant load still remains.

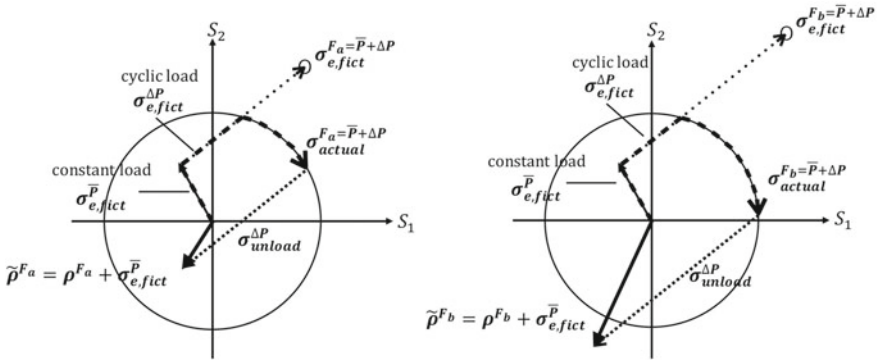

Fig. 5 Schematic illustration of direct method shakedown determination using simplified elasto-plastic analysis. For a two-component stress state at a point ($\underline{x}$), and for a combined cyclic and constant loading case (Fig. 4): shakedown is possible (on the *left*); shakedown is **not** possible (on the *right*)

This process is represented by the *densely-dotted* line ($\sigma^{\Delta P}_{unload}\left(\underline{x}\right)$). The *thick solid* lines show the modified stresses $\tilde{\boldsymbol{\rho}}\left(\underline{x}\right) = \boldsymbol{\rho}\left(\underline{x}\right) + \sigma^{\overline{P}}_{e,fict}\left(\underline{x}\right)$, (Eq. 9). One could argue that although the residual stress found in this way is not necessarily one that allows for shakedown to occur, it could still be possible to find another residual stress that would allow for shakedown. However, the particularity of this approach is that it gives the actual residual stress field that would be caused by the loading and unloading process. If this residual stress field does not allow for shakedown, then the structure will not shakedown. In this versatile approach, a natural ordering of the steps to check the shakedown conditions is suggested by following the physical processes of loading and unloading that the structure experiences. Many other approaches are even more divorced from physical processes and exploit the mathematical freedom in Melan's theorem. Nevertheless, following this process could provide valuable insight for designers regarding how to recover or promote shakedown behavior.

4 Graphical Interpretations of Shakedown Determination with Purely Elastic Analysis

An example of a more mathematical implementation of Melan's theorem uses set theory and can consider the shakedown conditions simultaneously. This kind of approach can also be used to identify new pathways to incorporate shakedown theorems in modern structural topology optimization protocols [45–49]. For the following example, a solid Ω (Fig. 2), and a cyclic loading domain, L, that includes 0 as a loading corner are analyzed (Fig. 3). For ease of understanding, the "pointwise" (time-independence and safe-state) shakedown conditions (Sect. 2) are presented together; the "spatial" (self-equilibrating) condition is applied last.

For each point, $\underline{x}$, in the solid ($\underline{x} \in \Omega$), a feasible stress domain (*for this point*), $f.d.(\underline{x})$, must be found, i.e. all of the stresses $\bar{s}(\underline{x})$ that, for all loading corners F_i ($\forall i \in [\![1, NC]\!]$), satisfy the safe-state condition. The stresses, $\bar{s}(\underline{x})$, are also time-independent because they are load-independent: they do not depend on the loading corner and remain the same for the whole loading domain, L. Note that the new variable, $\bar{s}(\underline{x})$ is defined for convenience to distinguish stresses that only satisfy the pointwise shakedown conditions ($\bar{s}(\underline{x})$) from those that satisfy both the pointwise and spatial shakedown conditions (admissible residual stress fields, $\boldsymbol{\rho}$). Then, for a point in the solid ($\underline{x} \in \Omega$), the feasible stress domain (which will be called a *feasible domain* from now on, $f.d.(\underline{x})$), is composed of the stresses, $\bar{s}(\underline{x})$, satisfying:

$$\forall\, i \in [\![1, NC]\!], \qquad f(\bar{s}(\underline{x}) + \sigma^{F_i}_{e,fict}(\underline{x}), \sigma_Y) \leq 0. \tag{12}$$

For each point, the feasible domain $f.d.(\underline{x})$ can be represented in a stress coordinate system (Fig. 6). Care should be taken to ensure that the same stress coordinate system is used for all of the loading corners. Moreover, the stress coordinate system must also remain the same for the feasible domains at every point in the solid. As a result, the feasible domains, $f.d.(\underline{x})$, are not necessarily determined in principal stress axes as principal stress components depend on the applied loading and they may not be the same for each loading corner and each point in the solid.

With a feasible domain for each point in the solid, combining these domains in space will limit the admissible stress fields. The combination of feasible domains ($f.d.(\underline{x})$) gives a "feasible stress *field* domain" (*for the entire structure*). It is done in a space of dimension (number of stress components) + (number of spatial dimensions): one axis for each stress component and one axis for each spatial direction. In this space, the feasible domain for each point ($\underline{x}$), is drawn at the spatial coordinates of the point in the solid and extends along stress component axes (Fig. 7).

To meet both the pointwise and spatial conditions (Eqs. 2–4, Sect. 2), an admissible stress field, $\boldsymbol{\rho}$, is found in the intersection of the self-equilibrating stress fields and the feasible stress field domain. Thus, the representation of an admissible stress field, $\boldsymbol{\rho}$, in the space of dimension (number of stress components) + (number of spatial dimensions) must remain within the boundaries set by the variation of feasible domains in the solid (i.e. the feasible stress field domain) (see schematic in Fig. 7). For ease of visualization, only the satisfaction of the divergence equation is shown; additional boundary conditions would further limit the admissible fields, $\boldsymbol{\rho}$, within

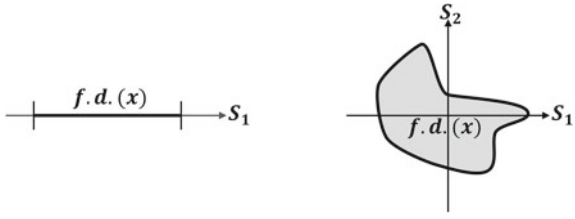

Fig. 6 Schematic of a feasible domain for a point, $f.d.(\underline{x})$, with feasible stress values. *Left* example for a single stress component. *Right* example for a two-component stress

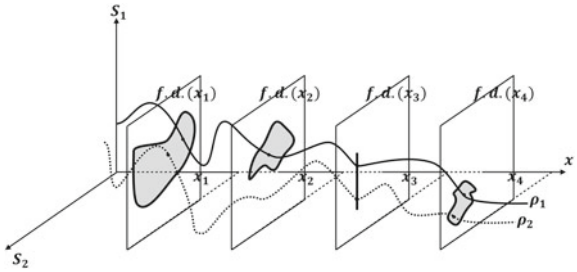

Fig. 7 Schematic illustration of the variation of feasible domains at various points in a structure. Each feasible domain, $f.d.(\underline{x})$, is drawn at the spatial coordinates of the point in the structure and extends along stress component axes (S_1, S_2). The representation of an admissible stress field, $\boldsymbol{\rho}$, in the space of dimension (number of stress components) + (number of spatial dimensions) must remain within the boundaries set by the variation of feasible domains in the solid (i.e. the feasible stress **field** domain). Two possibilities for $\boldsymbol{\rho}$ are given: the example with the *solid line* ($\boldsymbol{\rho}_1$) belongs to the feasible stress field domain whereas the example with the *dotted line* ($\boldsymbol{\rho}_2$) does not

the feasible stress field domain. This "intersection of domains" approach is useful for both understanding and designing to shakedown. Modifications of the material, geometric, and problem parameters will change these two domains: reducing, enlarging, translating them and affecting the size and existence of the intersection zone in which the admissible residual stress fields, $\boldsymbol{\rho}$, reside.

4.1 Example for only Cyclic Loading

To schematically illustrate this kind of implementation of Melan's theorem, a four-corner cyclic loading domain, L (Fig. 3), is used. The simplified example assumes a linear yield function, f, and a one-dimensional structure, Ω, that experiences a single-component stress. To represent this problem in a continuous way, one would have to consider the pointwise shakedown conditions (Eqs. 3 and 4) at each point in the solid. In this example, only three points (x_1, x_2, x_3) are analyzed. The fictitious "elastic" stresses caused by the loading corner (F_1, F_2, F_3, or $F_4 = 0$), for these points in the structure are $\sigma^{F_i}_{e,fict}(x_1)$, $\sigma^{F_i}_{e,fict}(x_2)$, and $\sigma^{F_i}_{e,fict}(x_3)$.

A schematic case where shakedown is possible is illustrated. The feasible domains, $f.d.(\underline{x})$, at each point in the solid ($\underline{x} \in \Omega$) must be computed (Figs. 8, 9 and 10). These computations rely on analytical elasticity solutions or on approximations using finite element analysis. For the examples below, only abstract schematics are presented. The safe-state condition has to be satisfied for all four loading corners (F_1, F_2, F_3, $F_4 = 0$). The feasible domain for the points analyzed in the structure (x_1, x_2, x_3) is determined when the sum of the fictitious "elastic" stresses, $\sigma^{F_1}_{e,fict}\, \sigma^{F_2}_{e,fict}\, \sigma^{F_3}_{e,fict}\, \sigma^{F_4}_{e,fict}$ and $\bar{s}(\underline{x})$ (Eq. 12) remain elastic.

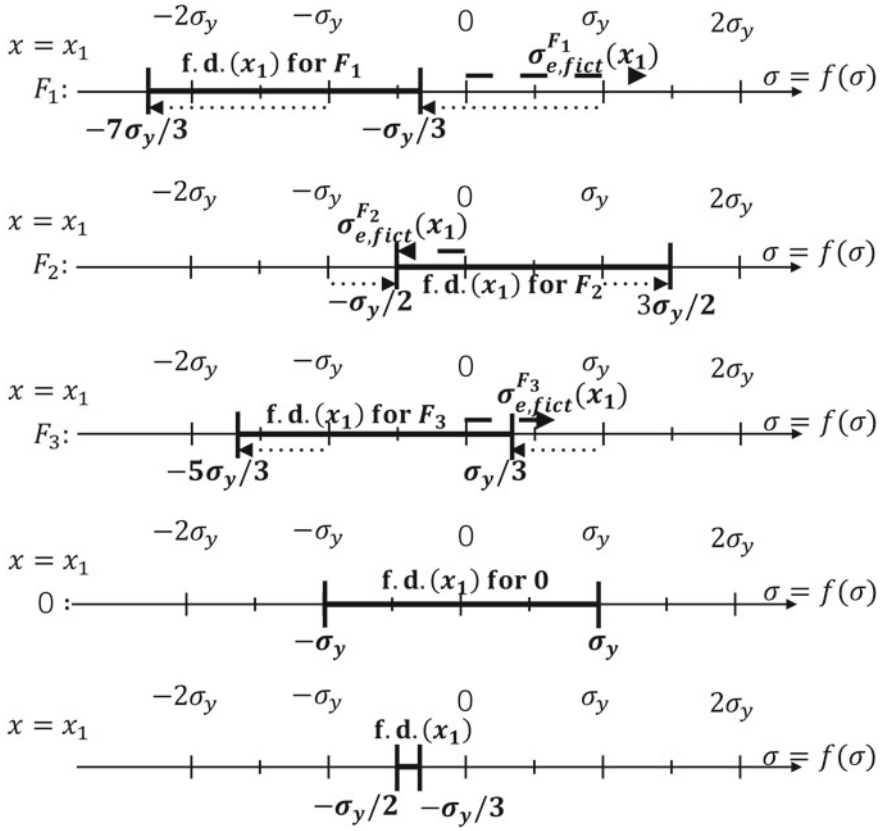

Fig. 8 Feasible domain (f.d.) for point x_1

Within each of the Figs. 8, 9 and 10 (and for each corresponding point x_1, x_2, x_3), there are several linear plots: one indicating the feasible domain for each of the loading corners (F_1, F_2, F_3, $F_4 = 0$) and a final plot that shows the feasible domain for the point (x_1, x_2 or x_3), which is the intersection of all of the feasible domains for each of the loading corners. The fictitious "elastic" stresses are computed for each loading corner and are represented by *dashed vectors* along linear stress continuums. These plots also illustrate the yielding limits (using a von Mises function $f(\sigma) = \sigma$) in tension ($\sigma = \sigma_Y$) and compression ($\sigma = -\sigma_Y$). The feasible domain ($f.d.(\underline{x})$ for F_i) is represented by *thick black lines*. This domain is the translation of the elastic domain ($[-\sigma_Y, \sigma_Y]$) by the fictitious elastic stress ($-\sigma_{e,fict}^{F_i}(\underline{x})$), i.e. in the opposite direction and with the same magnitude. This translation is shown by the *dotted lines* at the boundaries of the elastic domain. Note that for the loading corner $F_4 = 0$, (no external loading), there are no associated fictitious elastic stresses and the translated elastic domain is the original elastic domain.

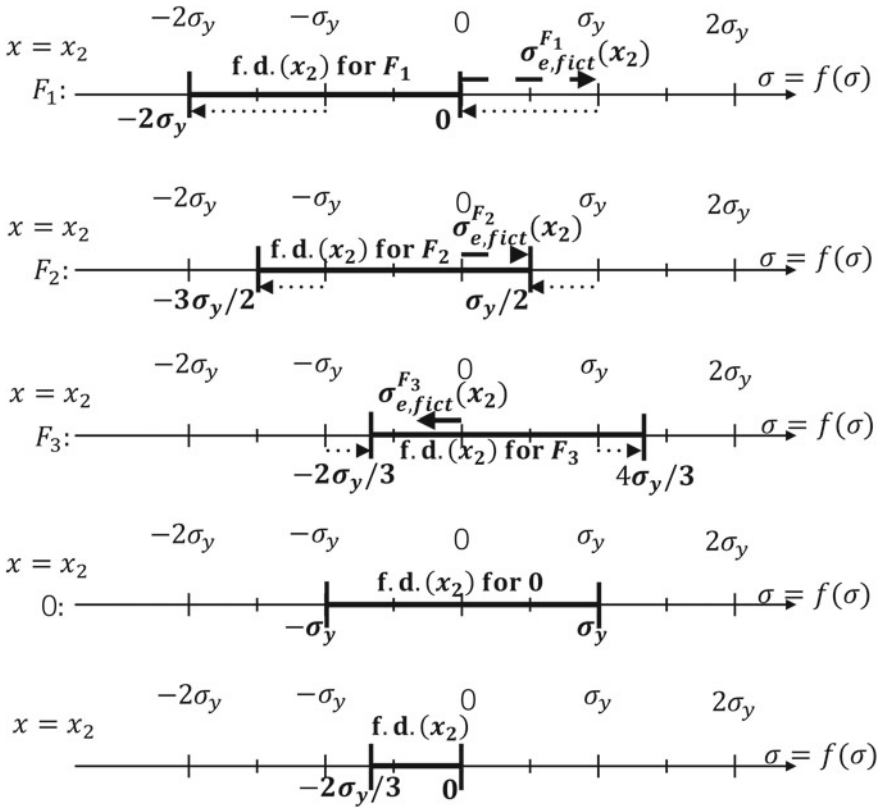

Fig. 9 Feasible domain (f.d.) for point x_2

Combining the final feasible domains in space for each point in the structure ($\underline{x} \in \Omega$)—for example, placing them side by side along a spatial axis, allows one to visualize the limitations on the feasible stress field domain (Fig. 11). For the example presented here, it is assumed that, for points between those considered, the limits of their feasible domains will also fall linearly between the determined limits. For more general problems, finite element approximations and mesh sensitivity studies are needed. With Fig. 11, the self-equilibrating condition can be applied to find the admissible stress field, $\boldsymbol{\rho}$, (i.e. enforcing the nullity of the divergence and the traction-free state on the part of the boundary $\partial\Omega_F \cup \Gamma$):

$$div(\boldsymbol{\rho}) = \frac{\partial \boldsymbol{\rho}(x)}{\partial x} = 0 \quad in\,\Omega, \quad \Rightarrow\ \boldsymbol{\rho} = constant \quad in\,\Omega. \tag{13}$$

For this example, the divergence equation requires one to find a constant function, $\boldsymbol{\rho}$, which, for each point of the solid ($\underline{x} \in \Omega$), would remain in the feasible domain:

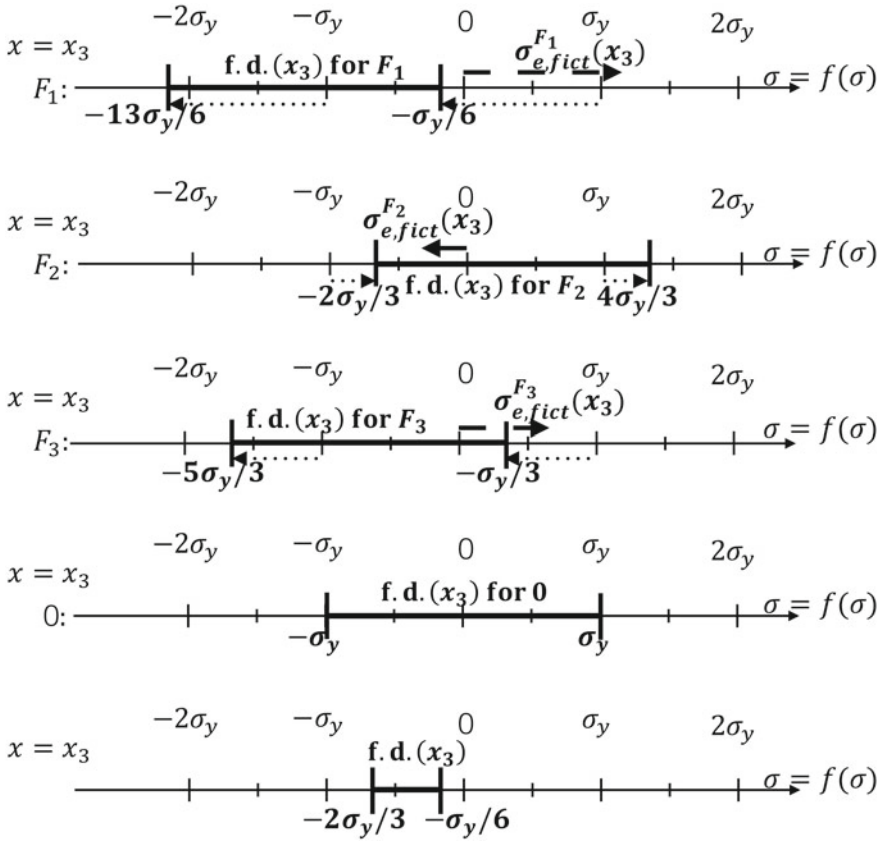

Fig. 10 Feasible domain (f.d.) for point x_3

$$\exists \boldsymbol{\rho} \in \mathbb{R} \quad s.t. \quad \forall \underline{x} \in \Omega, \qquad \boldsymbol{\rho}(\underline{x}) = \boldsymbol{\rho} \in f.d.(\underline{x}), \tag{14}$$

The self-equilibrating shakedown condition (Eq. 2) does not always require a constant residual stress field $\boldsymbol{\rho}$ (Fig. 7).

Figure 11 shows that, for this schematic example, one can find some shakedown solutions (on the left, in the middle). In this way one assures that the whole structure, Ω, will shakedown under the applied loading domain, L. In contrast, one can imagine an alternative scenario for which there is no constant function (i) that will satisfy the self-equilibrating condition and (ii) that is also a member of the feasible stress field domain; thus shakedown is not possible (Fig. 11, on the right).

This example highlights several factors that could prevent shakedown for a structure; these factors present design opportunities to recover shakedown behavior. An empty feasible domain for a single point in the structure will prevent shakedown for the entire structure (the feasible domain for point x_1 in Figs. 8 and 9 could have been

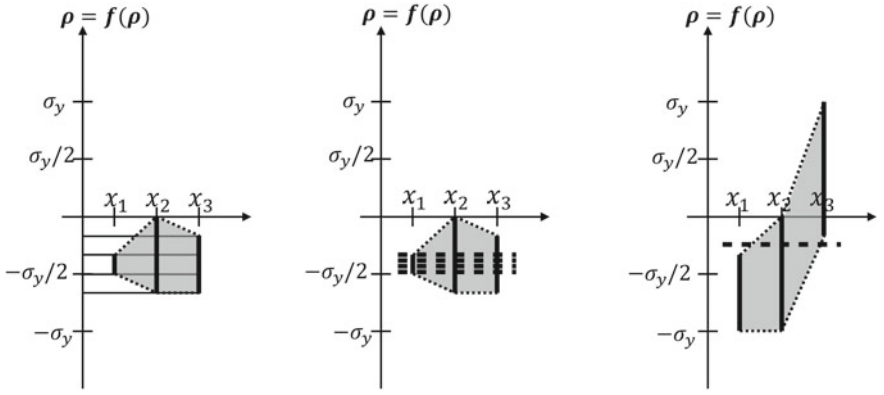

Fig. 11 *Left* feasible stress field domain from the combination of each point's feasible domain. *Middle* the same feasible stress field domain is shown with the self-equilibrating condition that indicates shakedown is possible. *Right* example of a possible feasible stress field domain where the intersection with the self-equilibrating fields is empty and shakedown is not possible

empty and then shakedown would not be possible for the structure). The feasible domain *for a point* may be empty due to the magnitude of stress levels associated with a single loading corner (i.e. greater than $2\sigma_Y$ in this example), or because the combination of feasible domains for each loading corner yields an empty set when combined for the final feasible domain determination at a point. Shakedown may also be prevented due to an empty feasible stress *field* domain. This failure relates to the "spatial" self-equilibrating shakedown condition: in these examples, the condition requires one to find a constant function that would remain in the feasible domain for every point in the solid (Fig. 11). As a lower bound for a structure, if it is found that shakedown is not possible for a loading corner within a given loading domain, L, then shakedown is also not possible for the entire loading domain.

For this kind of implementation of Melan's theorem, an example has been given to illustrate the set theory approach. It is a search for the intersection of stress fields that are admissible from pointwise and spatial-condition perspectives. It should be again emphasized that this kind of implementation does not require any elastoplastic analysis, it is based purely on elastic solutions. However, it will not provide information about the residual stress state, $\boldsymbol{\rho}$, that actually exists in the solid. Indeed, the uniqueness of the residual stress field is derived from the load history [19] which is not considered in direct methods.

5 Discussion

The graphical interpretations and approaches presented for some implementations of Melan's Lower Bound Shakedown Theorem offer tools for deeper understanding and for making design choices. The mathematical processes used in methods for shake-

down determination are often buried in computational codes. However, as is the case with many graphical representations in 2D and 3D, their practical utility is limited and the graphical tools presented are not intended to replace other tools nor are they recommended for complex geometries or loading domains. Nevertheless, the graphical tools offer complementary information to traditional Bree Interaction Diagrams. Bree diagrams give bounds for elastoplastic responses (including shakedown) under prescribed loading combinations but they do not indicate how shakedown conditions are met. By elucidating how pointwise and spatial shakedown conditions are met, directions for promoting and recovering shakedown behavior that are not indicated in the Bree Diagrams may be highlighted. These may include modifications of the material, geometry, and boundary conditions. Even for obvious changes such as increasing the material yield strength, interaction diagrams will give the revised shakedown domain, but the graphical approach and interpretations presented here allow one to see how and why this parameter influences the shakedown domain from a lower-bound perspective.

In the previous examples, several simplifying assumptions were made such as ignoring the dependence of material properties (yield strength σ_Y, Young's Modulus E), on parameters such as temperature [33]. Including these effects would fall under the pointwise conditions, modifying the shape of the feasible domain for each point. In addition, in the analysis presented, only simple tractions on the boundary, cycling between 0 and a maximum load have been considered. Including other loads, such as volumetric loads or temperature gradients is possible but adds significant visual complexity. The dimensions required to draw the feasible domains and especially the combination of feasible domains for many structures are often too high for visualization and defeat the purpose of these tools for understanding. Nevertheless, revisiting this well-established theorem from a graphical and pedagogical approach, provides a foundation for new interdisciplinary applications, including identifying pathways for incorporation of shakedown in modern structural topology optimization schemes.

6 Conclusion

Several graphical interpretations of direct methods that implement Melan's lower bound shakedown theorem have been developed. They serve as educational and simple design tools to complement existing Bree Interaction Diagrams. Where Bree Diagrams give the domains of expected elastoplastic responses for a structure under prescribed loading conditions, the graphical approaches developed here show how and why shakedown conditions are met. They provide a graphical representation of the mathematical processes at the foundation of computational shakedown codes. They also provide design insight by highlighting directions for promoting or recovering shakedown behavior in structures.

Acknowledgements Dr. Vermaak would like to acknowledge that, in part, this material is based upon work supported by the Air Force Office of Scientific Research under award number FA9550-16-1-0438. The authors would also like to thank Dr. Hany Fayek Abdalla for helpful discussions about the technique in Abdalla et al. [22].

References

1. Grüning M (1926) Die Tragfähigkeit statisch unbestimmter Tragwerke aus Stahl bei beliebig häufig wiederholter Belastung. Springer
2. Bleich H (1932) Über die Bemessung statisch unbestimmter Stahltragwerke unter Berücksichtigung des elastisch-plastischen Verhaltens des Baustoffes. Bauingenieur 19(20):261–266
3. Melan E (1938) Der Spannungszustand eines Mises-Henckyschen Kontinuums bei veraenderlicker Belastung. Sitzber Akad Wiss 147:73–78
4. Melan E (1938) Zur Plastizität des räumlicken Kontinuums. Ing Arch 8:116–126
5. Weichert D, Ponter A (2014) A historical view on shakedown theory. In: The History of theoretical, material and computational mechanics-mathematics meets mechanics and engineering. Springer, pp 169–193
6. Simoens B, Lefebvre M, Nickell R, Minami F (2012) Experimental demonstration of shakedown in a vessel submitted to impulsive loading. J Press Vessel Technol 134:1–6
7. Ponter A, Hearle A, Johnson K (1985) Application of the kinematical shakedown theorem to rolling and sliding point contacts. J Mech Phys Solids 33(4):339–362
8. Begley MR, Evans AG (2001) Progressive cracking of a multilayer system upon thermal cycling. J Appl Mech 68(4):513–520
9. Tao M, Mohammad LN, Nazzal MD, Zhang Z, Wu Z (2010) Application of shakedown theory in characterizing traditional and recycled pavement base materials. J Transp Eng 136(3):214–222
10. García-Rojo R, Herrmann HJ (2005) Shakedown of unbound granular material. Granular Matter 7(2–3):109–118
11. Sun H, Pathak A, Luntz J, Brei D, Alexander PW, Johnson NL (2008) Stabilizing shape memory alloy actuator performance through cyclic shakedown: An empirical study. In: The 15th international symposium on: smart structures and materials and nondestructive evaluation and health monitoring. International Society for Optics and Photonics, p 69300
12. Peigney M (2014) On shakedown of shape memory alloys structures. Ann Solid Struct Mech 6(1–2):17–28
13. Reedlunn B, Daly S, Shaw J (2013) Superelastic shape memory alloy cables: part II–subcomponent isothermal responses. Int J Solids Struct 50(20–21):3027–3044
14. Bree J (1967) Elastic-plastic behaviour of thin tubes subjected to internal pressure and intermittent high-heat fluxes with application to fast-nuclear-reactor fuel elements. J Strain Anal Eng Des 2(3):226–238
15. ASME Boiler and Pressure Vessel Code (2003) ASME, New York
16. BS 5500: British standard specification for fusion welded pressure vessels (1996) British Standards Institute, London
17. R5 Assessment procedure for the high temperature response of structures (1990) Nuclear Electric PLC
18. Abdel-Karim M, Ohno N (2000) Kinematic hardening model suitable for ratchetting with steady-state. Int J Plast 16(3–4):225–240
19. Koiter WT (1960) General theorems for elastic-plastic solids. North-Holland Amsterdam
20. König J (1987) Shakedown of elastic-plastic structures. Elsevier, The Netherlands
21. Bower A (2009) Applied mechanics of solids. CRC Press
22. Abdalla HF, Megahed MM, Younan MYA (2007) A simplified technique for shakedown limit load determination. Nucl Eng Des 237:1231–1240

23. Abdalla HF, Megahed MM, Younan MYA (2009) Comparison of pipe bend ratchetting/shakedown test results with the shakedown boundary determined via a simplified technique. In: Proceedings of the ASME 2009 pressure vessels and piping division conference PVP2009, pp 659–666
24. Abdalla HF, Younan MYA, Megahed MM (2011) Shakedown limit load determination for a kinematically hardening 90° pipe bend subjected to steady internal pressures and cyclic bending moments. J Press Vessel Technol 133:051212–1–10
25. Korba A, Megahed MM, Abdalla HF, Nassar MM (2013) Shakedown analysis of 90-degree mitred pipe bends. Eur J Mech-A/Solids 40:158–165
26. Elsaadany MS, Younan MY, Abdalla HF (2014) Determination of shakedown boundary and failure-assessment-diagrams of cracked pipe bends. J Press Vessel Technol 136(1):011209
27. Abdalla HF (2014) Elastic shakedown boundary determination of a cylindrical vessel-nozzle intersection subjected to steady internal pressures and cyclic out-of-plane bending moments. Nucl Eng Des 267:189–196
28. Oda AA, Megahed MM, Abdalla HF (2015) Effect of local wall thinning on shakedown regimes of pressurized elbows subjected to cyclic in-plane and out-of-plane bending. Int J Press Vessels Pip 134:11–24
29. Abdalla HF (2014) Shakedown limit load determination of a cylindrical vessel-nozzle intersection subjected to steady internal pressures and cyclic in-plane bending moments. J Press Vessel Technol 136(5):051602
30. Abdalla HF (2014) Shakedown boundary determination of a 90° back-to-back pipe bend subjected to steady internal pressures and cyclic in-plane bending moments. Int J Press Vessels Pip 116:1–9
31. Hafiz YA, Younan MY, Abdalla HF (2015) A proposal for a simplified assessment procedure to api-579 standard. J Press Vessel Technol 137(3):031007
32. Symonds PS (1951) Shakedown in continuous media. J Appl Mech-Trans ASME 18(1):85–89
33. Peigney M (2014) Shakedown of elastic-perfectly plastic materials with temperature-dependent elastic moduli. J Mech Phys Solids 71:112–131
34. Weichert D (1984) Shakedown at finite displacements; a note on Melan's theorem. Mech Res Commun 11(2):121–127
35. Spiliopoulos KV (1997) On the automation of the force method in the optimal plastic design of frames. Comput Methods Appl Mech Eng 141(1):141–156
36. Maier G (1969) Shakedown theory in perfect elastoplasticity with associated and nonassociated flow-laws: a finite element, linear programming approach. Meccanica 4(3):250–260
37. Bodovillé G, de Saxcé G (2001) Plasticity with non-linear kinematic hardening: modelling and shakedown analysis by the bipotential approach. Eur J Mech-A/Solids 20(1):99–112
38. Garcea G, Leonetti L (2013) Decomposition methods and strain driven algorithms for limit and shakedown analysis. In: Limit state of materials and structures. Springer, pp 19–43
39. Ponter AR, Engelhardt M (2000) Shakedown limits for a general yield condition: implementation and application for a von mises yield condition. Eur J Mech-A/Solids 19(3):423–445
40. Ponter A, Chen H (2001) A minimum theorem for cyclic load in excess of shakedown, with application to the evaluation of a ratchet limit. Eur J Mech-A/Solids 20:539–553
41. Stein E, Zhang G, König JA (1992) Shakedown with nonlinear strain-hardening including structural computation using finite element method. Int J Plast 8(1):1–31
42. Vu D, Staat M, Tran I (2007) Analysis of pressure equipment by application of the primal-dual theory of shakedown. Commun Numer Methods Eng 23:213–225
43. Simon JW, Weichert D (2013) Interior-point method for lower bound shakedown analysis of von Mises-type materials. In: Limit state of materials and structures. Springer, pp 103–128
44. Wiechmann K, Stein E (2006) Shape optimization for elasto-plastic deformation under shakedown conditions. Int J Solids Struct 43(22):7145–7165
45. Allaire G, Jouve F, Toader AM (2004) Structural optimization using sensitivity analysis and a level-set method. J Comput Phys 194(1):363–393
46. Wang M, Wang X, Guo D (2003) A level set method for structural topology optimization. Comput Methods Appl Mech Eng 192(1):227–246

47. Bendsoe M, Sigmund O (2004) Topology optimization: theory, methods and applications. Springer
48. Kammoun Z, Smaoui H (2015) A direct method formulation for topology plastic design of continua. In: Direct Methods for Limit and Shakedown Analysis of Structures. Springer, pp 47–63
49. Kammoun Z, Smaoui H (2014) A direct approach for continuous topology optimization subject to admissible loading. Comptes Rendus Mécanique 342(9):520–531

High Temperature Limit Analysis of Pressure Vessels and Piping with Local Wall-Thinning

X. Du, Y. Liu and J. Zhang

Abstract In order to evaluate the safety and integrity of pressure vessels containing volume defects and piping with local wall-thinning at elevated temperature, a numerical method for plastic limit load of modified 9Cr-1Mo steel pressure vessel and piping is proposed in the present paper. The limit load of pressure vessel and piping at high temperature is defined as the load-carrying capacity after the structure has served for a certain time period. The power law creep behavior with Liu-Murakami damage model is implemented into the commercial software ABAQUS via CREEP for simulation, and the Ramberg-Osgood model is modified to consider the material deterioration effect of modified 9Cr-1Mo steel by introducing the creep damage factor into the elasto-plastic constitutive equation. For covering the wide ranges of defect ratios and service time periods, various 3-D numerical examples for the pressure vessels with different sizes of volume defects, the piping with local wall-thinning defects, and creep time are calculated and analyzed. The limit loads of the defected structures under high temperature are obtained through classic zero curvature criterion with the modified Ramberg-Osgood model, and the typical failure modes of these pressure vessels and piping are also discussed. The results show that the plastic limit load of pressure vessel and piping containing defect at elevated temperature depends not only on the size of defect, but also on the creep time, which is different from the traditional plastic limit analysis at room temperature without material deterioration.

X. Du · Y. Liu (✉)
Department of Engineering Mechanics, Tsinghua University, Beijing 100084, China
e-mail: yhliu@mail.tsinghua.edu.cn

J. Zhang
Sino-French Institute of Nuclear Engineering and Technology,
Sun Yat-sen University, Zhuhai, China

O. Barrera et al. (eds.), *Advances in Direct Methods for Materials and Structures*, DOI 10.1007/978-3-319-59810-9_12

1 Introduction

With the rapid development of modern industry, it is estimated that the world demand for power supplies will increase by up to 50% in the next two decades [1]. Actually, it's inevitable for the appearance of defects with various dimensions for the pressure vessels and piping which are operated at elevated temperature. The defects of local wall-thinning can reduce the load-carrying capacity of pressure vessels and piping, even can lead to the leaking and explosion accident. Thus, the safety and integrity assessment of the pressure vessels and piping which should be serviced at elevated temperature for a long time becomes more significant.

The limit analysis is a method which is widely used for the pressure vessels with volume defect and the piping with local wall-thinning defect in the structure safety and integrity assessment at room temperature. The limit load of structure can be obtained by limit analyses, which is a theoretical foundation for rational design and safety assessment of pressure vessel and piping. In 1950s, the complete theory of upper and lower bound for limit analysis was presented by Drucker and Hill [2, 3]. Then, the plastic limit analysis for axial symmetry shell and plate structures was studied by Hodge and Belytschko [4–6]. Maier and Munro [7] reviewed the engineering application of plastic limit analysis. It can be found that the researches on the above are based on simple structures such as beam, axial symmetry shell and plane problems. However, it's difficult to obtain the analytical limit load solution for the complex structures in engineering. With the development of finite element method (FEM) and computer hardware, numerical method are widely used for the limit analysis of complex structures. Chen [8] proposed a numerical method for limit analysis of piping with local wall-thinning under multi-loading. Han et al. [9] studied the limit moment of local wall thinning in piping under bending using FEM. Kim et al. [10] calculated the collapse moment of pipe elbows with local wall thinning using the "twice the elastic slope" (TES) method. At the same year, by using the geometrically linear FE limit analyses, Kim et al. [11] proposed the effects of local wall thinning on plastic limit loads of elbows. Mackenzie et al. [12] proposed a simple method, named the elastic compensation method which is convenience for engineering application. By using the penalty-duality algorithm and direct iteration method, Liu et al. [13–17] calculated the limit load of 3-D structure with volume defect and local wall-thinning, which is indicated that the numerical method for limit analysis of complex structures is feasible and reasonable.

These researches of the limit analysis were conducted under room temperature situation. However, it's very different for the limit load analysis of pressure vessels and piping from room temperature to elevated temperature. On one hand, the creep regime of material must be considered when the components are subjected to elevated temperature compared with the room temperature. On the other hand, the material property is considered as virgin state without damage and deterioration during the operating service at room temperature. However, the creep damage due to the material property deterioration is inevitable, which leads to the cavity growth and nucleation in the microscale and the effective load-carrying area decreasing in the macroscale. Both

of the yield strength (YS) and the ultimate tensile strength (UTS) will be reduced when creep damage mechanism is considered [18]. Consequently, the limit load will correspondingly decrease when the components have served at elevated temperature for a long time. These two aspects are vital important to expand the method of limit load analysis for structures to elevated temperature field.

The material of interest in this study is modified 9Cr-1Mo steel, which is high-chromium ferritic steels containing 9–12% chromium and has higher creep strength and corrosion resistance than the traditional chromium-molybdenum steel used in pressure vessels and piping system. The creep behavior and creep damage model of modified 9Cr-1Mo steel have been studied by several researchers during the past decades. From the microcosmic point of view, Arzt and Wilkinson [19] proposed a dislocation based model for creep, which is valid for the local and general climb of dislocations regardless of the climb mechanisms. Fournier et al. [20] introduced a micromechanically based model for predicting the cyclic softening in the 9–12%Cr martensitic steels. For modeling the creep behavior of modified 9Cr-1Mo steel, Böck and Kager [21] performed an extensive research using the finite element method. Instead of using standard evolution law for predicting long term creep, the models based on microstructural variables are proposed. In order to take the dislocation density and subgrain coarsening into account, Sklenicka et al. [22] suggested that the role of the dislocation substructure is dominant for the creep behavior of 9Cr-1Mo steel. Based on phenomenological approach, numerous creep model have been presented by researchers, such as Graham [23], McVetty [24], Conway [25] and Norton [26], and corresponding creep constitutive functions include power law, logarithmic, exponential and hyperbolic sine law have been used for representing the creep behavior respectively. Nevertheless, these models cannot be used to describe the tertiary stage of creep. To characterize the full creep curve, the continuum damage mechanics (CDM) models coupling creep, plasticity and viscoplasticity have been developed to simulate material deterioration. The creep damage model in the pioneering work is Kachanov [27] and Rabotnov [28] (K-R) model which has been widely accepted and used for predicting the tertiary creep behavior [29]. Based on the concept of K-R model, dozens of creep damage models were presented according to the various definition of damage hereafter. Chaboche et al. [30], Lemaitre et al. [31], Hayhurst et al. [32, 33], Murakami et al. [34, 35], and Dyson et al. [36] presented creep models with different number of damage factors include single, double, triple or even quadruple variables, respectively. Hyde [37] et al. used different CDM models to approach the creep damage behavior of modified 9Cr-1Mo steel and to analyze simple pressurized pipe structures conjunction with the finite element method. Based on a micromechanical consideration of void growth and coalescence under creep damage conditions, a strain controlled creep damage model was presented by Cocks and Ashby [38]. Basirat et al. [39] proposed a CDM model based on dislocation and considered precipitate to simulate the creep behavior of modified 9Cr-1Mo steel.

It is worth noting that almost all the researches on creep damage models focused on the material deterioration in creep mechanism, but the material deterioration in plastic mechanism caused by creep damage, which is the key point to the limit load analysis, has not attracted sufficient attention. Researches showed that high creep

damage accumulation rate caused by high stress level and long time, which indicates that the material deterioration for plastic regime under creep condition is dependent on stress level, creep time and evaluated temperature. Xue et al. [40] and Wang et al. [41] presented creep damage model considering material deterioration in plastic mechanism for P91 and 2.25Cr-1Mo steels respectively. However, different stress levels in structures with defects have not been considered, which is a crucial factor to the limit load analysis at elevated temperature.

In the present paper, the limit load at elevated temperature is defined as the load-carrying capacity after the structure served for a certain period of time, and the limit analysis of pressure vessels and piping with local wall-thinning at 650 °C is numerically studied. The material is modified 9Cr-1Mo steel. The Liu-Murakami creep damage model and the modified Ramberg-Osgood model are implemented simultaneously in ABAQUS via CREEP and USDFLD subroutines. The creep damage due to the material deterioration at different stress levels is also considered. In addition, a series of numerical examples are completed to investigate the effects of defect dimensions on the limit load and the failure mode of pressure vessels and piping.

2 Continuum Damage Constitutive Equations

2.1 Creep Damage Constitutive Model

At high temperature, the creep deformation is dominated and the redistribution of stress is found to be dependent on the creep constitutive laws obeyed by the material [42]. Typical creep deformation includes three regimes: primary, secondary, and tertiary creep regimes. The continuum damage mechanics (CDM) models are adopted here to characterize the full creep curve. One of the most widely used CDM model is Kachanov [27] and Rabotnov [28] (K-R) model which has a single-state damage variable. However, the creep strain rate will approach infinity when the damage parameter approach to value 1.0. Though this effect can be reduced by setting the damage parameter to 0.99 when the material fails to complete the numerical calculation, the effect of damage localization of K-R constitutive equation cannot be avoid.

Attempting to address the issue of high damage rates as the damage parameter approaches value 1.0, Liu-Murakami (L-M) model has been presented in [34]. Multiaxial forms of the L-M model are given by

$$\dot{\varepsilon}_{ij}^{c} = \frac{3}{2} A \sigma_{eq}^{n-1} S_{ij} \exp\left[\frac{2(n+1)}{\pi\sqrt{1+3/n}} \left(\frac{\sigma_1}{\sigma_{eq}}\right)^2 \omega^{3/2}\right] \tag{1}$$

Table 1 Creep and damage constants for Mod. 9Cr-1Mo steel at 650 °C [43]

A	n	χ	q_2	B	α
1.09×10^{-20}	8.46	7.10	4.00	7.85×10^{-17}	0.19

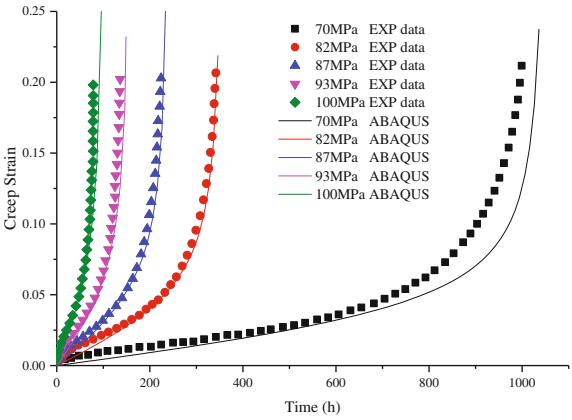

Fig. 1 Uniaxial creep validation of finite element analyses

$$\dot{\omega} = \frac{B[1-\exp(-q_2)]}{q_2}\sigma_{\mathrm{r}}^{\chi}\exp(q_2\omega) \tag{2}$$

$$\sigma_{\mathrm{r}} = \alpha\sigma_1 + (1-\alpha)\sigma_{\mathrm{eq}} \tag{3}$$

where $\dot{\varepsilon}_{ij}^{\mathrm{c}}$, σ_{eq} and S_{ij} are the multiaxial creep strain rate components, the von Mises equivalent stress, and the deviatoric stress components, respectively. The damage parameter ω represents the condition of the material deterioration in creep regime, which varies from 0 to 1 indicating virgin material and fully damaged material respectively. A, B, n, χ and q_2 are the material constants in Norton's law, which can be obtained in general by curve fitting. σ_{r} is the rupture stress.

The L-M model is implemented by the CREEP subroutine in ABAQUS, and the CREEP subroutine is verified by the uniaxial creep tests in [37]. All the constant parameters for the L-M model were listed in Table 1 [43]. Comparisons of the creep curves under different applied stresses obtained by creep tests and the present CREEP subroutine with ABAQUS are given in Fig. 1. It can be seen from Fig. 1 that the test data and the finite element analyses curves are correlated very well, which indicates that the L-M model can accurately represent the creep behavior of modified 9Cr-1Mo material and the subroutine codes are also validated.

2.2 General Hardening Elasto-plastic Constitutive Model with Damage

The calculation of structure limit load is dependent on the yield strength (YS) and ultimate tensile strength (UTS) of material. However, both of the YS and UTS of modified 9Cr-1Mo steel material are not constant under creep condition. It is revealed that YS and UTS would decrease with the increment of the temperature and creep damage increases due to material deterioration [44, 45]. Therefore, it is essential to induce creep damage into elasto-plastic constitutive model.

Ramberg-Osgood (R-O) equation [46] is an elasto-plastic constitutive model with an exponent law and widely used to describe stress-strain curve of ductile material with general hardening behavior. Hence, the R-O model has been employed in current paper for modified 9Cr-1Mo steel and the equation is given as

$$\varepsilon = \varepsilon_{\mathrm{e}} + \varepsilon_{\mathrm{p}} = \frac{\sigma}{E} + \left(\frac{\sigma}{H_{\mathrm{RO}}}\right)^{1/n_{\mathrm{RO}}} \tag{4}$$

where ε, ε_{e}, ε_{p} and E are total strain, elastic strain, plastic strain and Young's module, respectively. n_{RO} and H_{RO} are material constants and given by [47] (Table 2)

$$n_{\mathrm{RO}} = \frac{1 + 1.3495\left(\frac{\sigma_{\mathrm{ys}}}{\sigma_{\mathrm{uts}}}\right) - 5.3117\left(\frac{\sigma_{\mathrm{ys}}}{\sigma_{\mathrm{uts}}}\right)^2 + 2.9643\left(\frac{\sigma_{\mathrm{ys}}}{\sigma_{\mathrm{uts}}}\right)^3}{1.1249 + 11.0097\left(\frac{\sigma_{\mathrm{ys}}}{\sigma_{\mathrm{uts}}}\right) - 11.7464\left(\frac{\sigma_{\mathrm{ys}}}{\sigma_{\mathrm{uts}}}\right)^2} \tag{5}$$

$$H_{\mathrm{RO}} = \frac{\sigma_{\mathrm{uts}} \exp(n_{\mathrm{RO}})}{n_{\mathrm{RO}}^{n_{\mathrm{RO}}}} \tag{6}$$

The modified R-O constitutive model considering the material deterioration due to the creep damage is defined as below

$$\varepsilon = \frac{\sigma}{E} + \left(\frac{\sigma}{D_{\mathrm{ur}} H_{\mathrm{RO}}}\right)^{1/n_{\mathrm{RO}}} \tag{7}$$

where D_{ur} is the UTS damage ratio which is proposed by Du et al. [49,50]. Considering the creep damage, the limit analysis can be implemented via the modified R-O constitutive model and the L-M creep model at high temperature.

Table 2 Elasto-plastic properties for Mod. 9Cr-1Mo steel at 650 °C [44, 48]

E (GPa)	ν	σ_{ys} (MPa)	σ_{uts} (MPa)	n_{RO}	H_{RO} (MPa)
155	0.3	165	228	0.11	323.19

3 Finite Element Model

3.1 Cylindrical Pressure Vessel with Volume Defect

Only one eighth of the pressure vessel is modeled due to the symmetry of the structure. The geometry of the cylindrical pressure vessel with volume defect is shown schematically in Fig. 2.

In Fig. 2, R_o is the outer radius of the cylinder, R_i is the inner radius of the cylinder, T is the wall thickness of the cylinder, L is the length of cylinder, A' and B' are the half of axial and circumferential length of the volume defect, respectively, C' is the depth of the volume defect.

Define the dimensionless axial length ratio, circumferential ratio and depth ratio of the volume defect as $a = A'/B'$, $b = C'/B'$ and $c = C'/T$ respectively. The ratio of outer radius versus inner radius of cylinder is denoted by $K = R_o/R_i$. The basic geometry parameters are listed in Table 3. In order to calculate the limit load of cylindrical pressure vessel structure with different shape volume defect and creep time, the following non-dimension parameters are considered,

a assigns 1.0 or 3.0,
b assigns 1/1, 1/3 or 1/4,
c assigns 0.33, 0.5 or 0.6,
t creep time (hours), whose values are ranging from 0 to 10000.

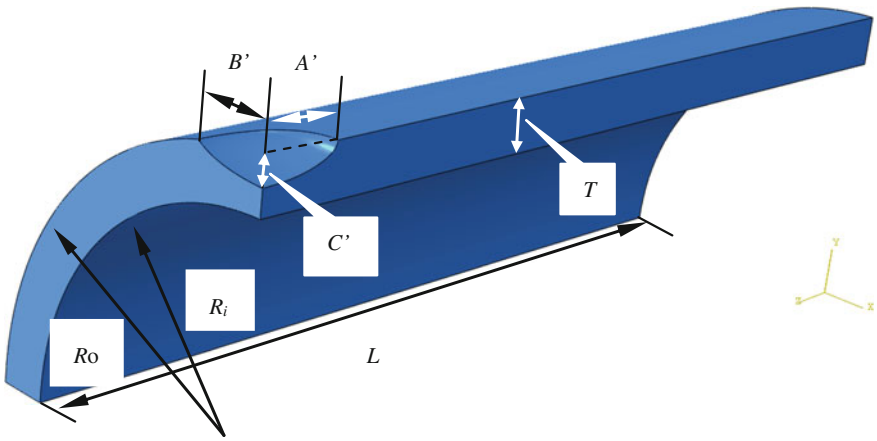

Fig. 2 Dimensions of the cylindrical pressure vessel with volume defect

Table 3 The basic geometry parameters of cylindrical pressure vessel structure

R_o (mm)	R_i (mm)	L (mm)	T (mm)	K
550	460	1500	90	1.20

3.2 Piping with Local Wall-Thinning

A quarter model of the piping with wall-thinning is modeled due to the symmetry of the structure. The geometry of the piping with local wall-thinning is shown schematically in Fig. 3.

Where R_o is the outer radius of piping, R_i is the inner radius of pipe, T is the wall thickness of pipe, L is the length of pipe, A' and B' are the half of axial and circumferential length of the local wall-thinning respectively, and C' is the depth of the local wall-thinning. The fillet is created along the corner of local wall-thinning in order to reduce the stress concentration.

The dimensionless axial length ratio, circumferential ratio and depth ratio of the local wall-thinning are defined as $a = A'/\sqrt{R_o T}$, $b = B'/\pi R_o$ and $c = C'/T$, respectively, and the ratio of outer radius versus inner radius of pipe is defined as $K = R_o/R_i$. The basic geometry parameters are listed in Table 3. In order to calculate the limit loads of piping with different life fraction and types of local wall-thinning which include small area pit, axial pit, circumferential pit and large area pit, the following non-dimensional parameters are considered,

a, dimensionless axial length ratio of the local wall-thinning, with values 0.61, 1.0 and 3.0, respectively.

b, dimensionless circumferential length ratio of the local wall-thinning, with values 0.08 and 0.25, respectively.

c, dimensionless depth ratio of the local wall-thinning, with values 0.1, 0.3 and 0.5, respectively.

$t_{lf} = t/t_r$, life fraction, with values 0, 0.2, 0.4, 0.6 and 0.8, respectively.

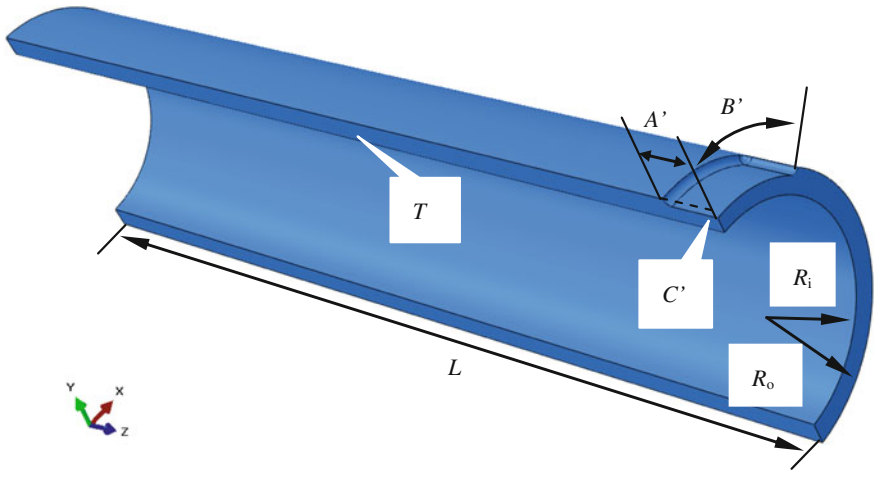

Fig. 3 Dimensions of the piping with local wall-thinning

3.3 Boundary Conditions and Applied Loading

The boundary conditions and applied loading of the cylindrical pressure vessel structure are shown in Fig. 4.

The symmetric boundary conditions (Sym-BC) are applied on the symmetry surface. P is the internal pressure which is 9.8 MPa at initial step. σ_t denotes the axial force.

The multi-loading systems in piping are more complex than that in cylindrical pressure vessel, which includes not only the internal pressure but also the bending moment M. In order to simulate the bending moment in the pipe FE model, the coupling technique is used to couple all the nodal freedoms of the end surface to a reference point (RP), and the ending moment has been applied to this RP in YOZ plane. The internal pressure is 4.81 MPa at initial step. σ_t denotes the axial force in order to simulate the closed-end condition. The symmetric boundary conditions (Sym-BC) are applied on the symmetry surface. And all the multi-loading systems and boundary conditions of the pipe structure are shown in Fig. 5.

In order to analyze effects of the combination of pressure and moment to the limit load, the limit pressure ratio, limit moment ratio and load combination ratio are defined as

$$\overline{P_L} = \frac{P_L}{P_{L0}} \tag{8}$$

$$\overline{M_L} = \frac{M_L}{M_{L0}} \tag{9}$$

$$m = \frac{\overline{M_L}}{\overline{P_L}} \tag{10}$$

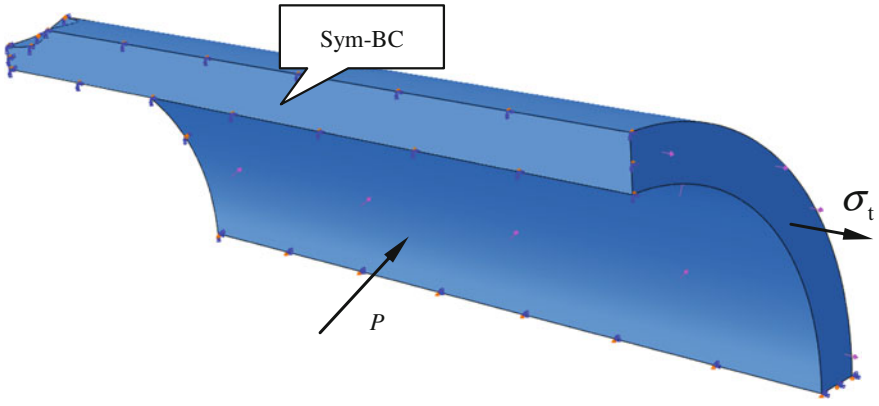

Fig. 4 Boundary conditions and applied loading of the pressure vessel structure

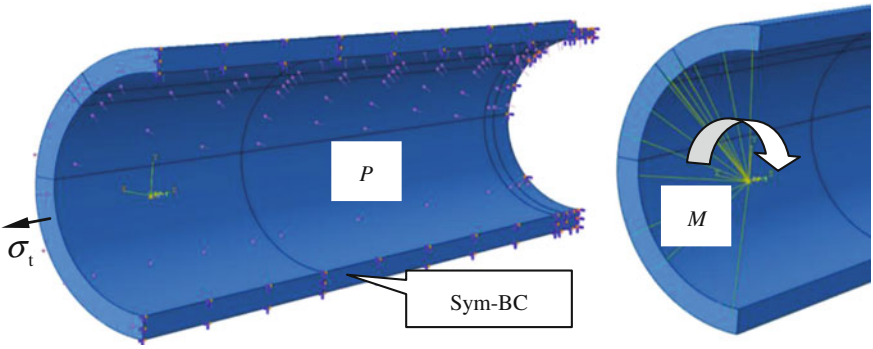

Fig. 5 Multi-loading systems and boundary condition of the pipe structure

where $\overline{P_L}$ and $\overline{M_L}$ are the limit pressure ratio and limit moment ratio, respectively. P_L and M_L are current limit pressure and current limit moment of structure with defect after service for a certain period, respectively. P_{L0} is the limit pressure of the perfect structure when the bending moment is zero and M_{L0} is the limit moment of the perfect structure when the pressure is zero. m denotes the load combination ratio, with 0, 0.5, 1.0, 2.0 and ∞, respectively. Specially, the single internal pressure condition or the single bending moment condition for piping has been accomplished when m is setting 0 or ∞.

The dimensionless defect factor considering multiple the defect dimensional parameters is defined as [51]

$$G_0 = \frac{C'}{T} \cdot \frac{A'}{B'} \cdot \frac{B'}{R_m} \cdot \sqrt{\frac{R_m}{T}} = \frac{C'A'}{T\sqrt{R_m T}} \tag{11}$$

where G_0 is dimensionless defect factor and R_m is middle radius of the cylindrical pressure vessel.

4 Numerical Results

4.1 Creep Damage and Material Deterioration

When the pressure vessels and piping with different defects have served for a long time, the field dependent R-O properties and creep damage factor fields for the pressure vessels and piping are shown in Figs. 6 and 7, where $t = t_{0.9}$ represents the service time when the creep damage is approaching to 0.9.

The results in Figs. 6 and 7 show that the von Mises stress around the local wall-thinning zone is lower than those in the other zones when the creep time is

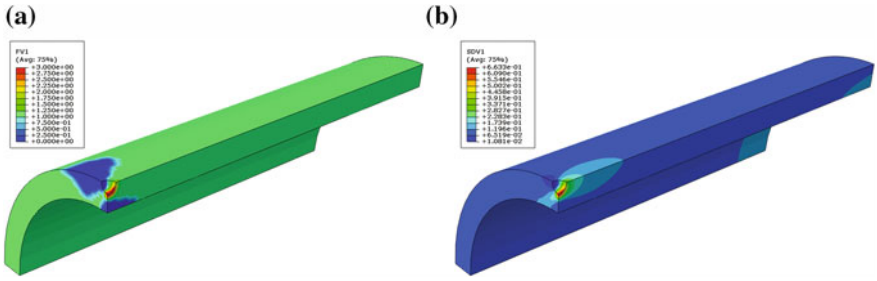

Fig. 6 Results for pressure vessel. **a** Field dependent R-O properties. **b** Current creep damage field

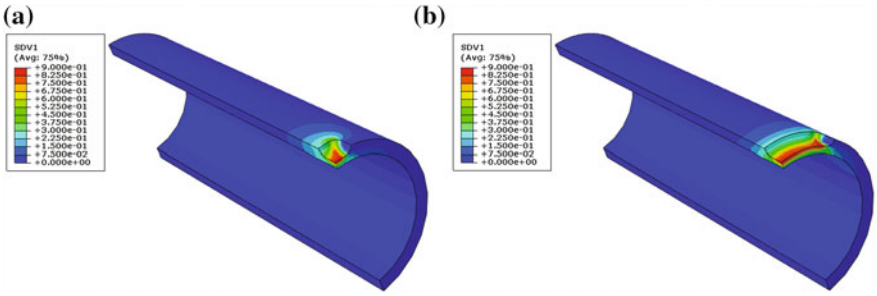

Fig. 7 The creep damage factor fields for piping with different local wall-thinning. **a** Small area pit. **b** Circumferential pit

approaching to $t_{0.9}$. It is also noted that the larger the damage factor becomes, the lower the von Mises stress is, which indicates that the effect of material deterioration can be successfully characterized by modified R-O model.

4.2 Limit State and Plastic Failure Modes for Pressure Vessel with Volume Defect

Considering the material deterioration at high temperature, the limit load and the plastic failure mode of the pressure vessel with volume defect under the creep damage condition depend on the defect ratio a, b, c and the creep time t. Assuming the radius ratio K is constant, the limit state of cylindrical pressure vessel with volume defect parameter ratios which are $a = 1.0$, $b = 1/1$ and $c = 0.33$ when creep time is ranging from 0 to 5000 h at 650 °C are shown in Figs. 8 and 9.

The results in Figs. 8 and 9 show that the modified field dependent R-O material properties are updated via USDFLD subroutine, corresponding to the current creep damage accumulated via CREEP subroutine. The maximum creep damage of cylindrical pressure vessel is increased from 0 to 0.663 and the limit load is

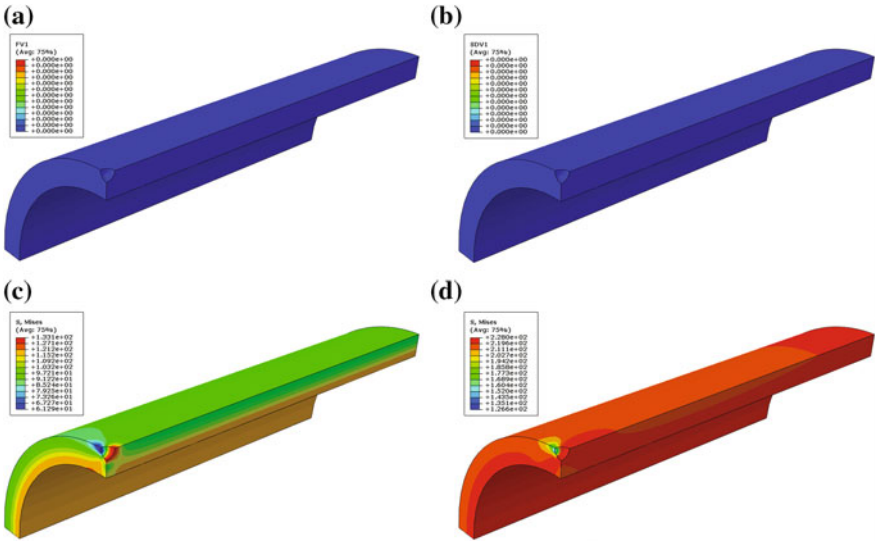

Fig. 8 The extension of plastic zone of cylindrical pressure vessel with outside volume defect ($K = 1.20$, $a = 1.0$, $b = 1/1$, $c = 0.33$, $t = 0$ h). **a** Field dependent R-O properties. **b** Current creep damage field. **c** von Mises stress field under $P = 22.12$ MPa. **d** Limit load state ($P = 42.64$ MPa)

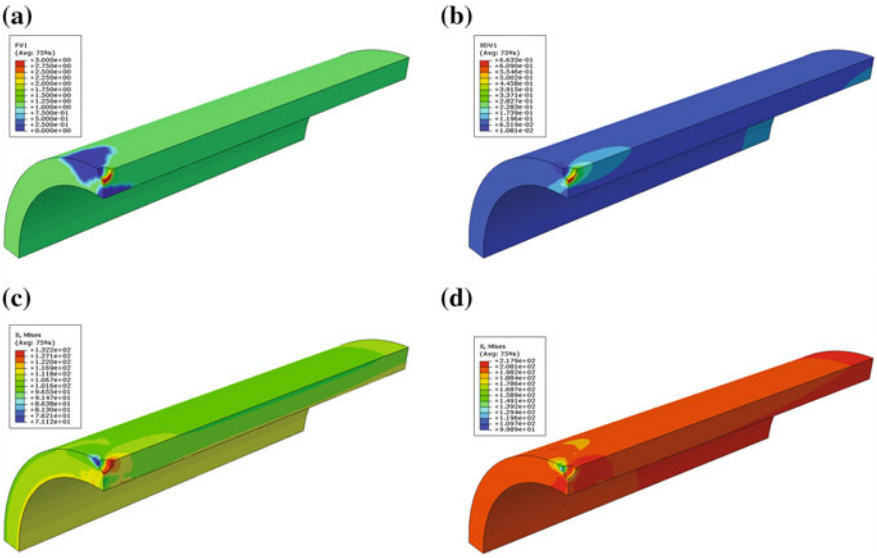

Fig. 9 The extension of plastic zone of cylindrical pressure vessel with outside volume defect ($K = 1.20$, $a = 1.0$, $b = 1/1$, $c = 0.33$, $t = 5000$ h). **a** Field dependent R-O properties. **b** Current creep damage field. **c** von Mises stress field under $P = 22.12$ MPa. **d** Limit load state ($P = 38.76$ MPa)

decreased from 42.64 to 38.76 MPa. Under the limit load state, the von Mises equivalent stresses around the high damage zone are less than those in the same places when creep time is 0, which means that the material strengths around the defect are reduced with accumulation of the damage. It can be indicated that the modified R-O damage model associated with the L-M creep damage model is implemented successfully though ABAQUS via subroutines. The initial plastic zone locates at the bottom of spherical pit when the defect ratios are small ($a = 1.0$, $b = 1/1$, $c = 0.33$). With the increment of internal pressure, the plastic zone is expended along the axial direction until almost the whole structure turns into plastic flow state, which means that the limit state is reached, and the failure mode of pressure vessel is the global structure plastic failure.

4.3 Limit Load Ratio with Defect Ratio for Pressure Vessel

By processing the results with zero curvature method, the curves of volume defect ratios to limit load ratio of cylindrical pressure vessel structure under high temperature are shown in Fig. 10.

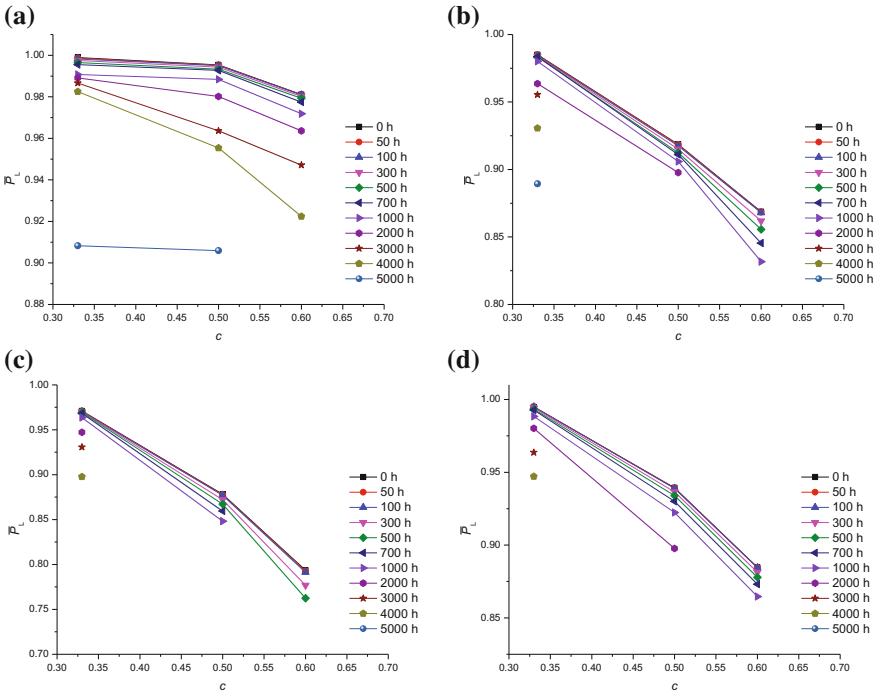

Fig. 10 Relationship of the limit load ratio with volume defect ratio. **a** $a = 1.0$, $b = 1/4$. **b** $a = 3.0$, $b = 1/1$. **c** $a = 3.0$, $b = 1/3$. **d** $a = 3.0$, $b = 1/4$

It can be seen from Fig. 10 that, with the increment of defect depth ratio c, the limit load ratio presents the descending tendency. The smaller the defect circumferential length ratio b is, the faster the limit load ratio decreases. In a similar way, the larger the defect axial length ratio a is, the faster the limit load ratio decreases. With the high creep damage rate, the secondary and tertiary creep stages are shorten substantially, and the limit load ratio decreases rapidly, even the limit load could not exist when the high creep damage zone appeared in a number of elements along the thickness of the cylindrical pressure vessel. Therefore, the defect ratio must be restricted carefully to ensure the safety of the pressure vessel structure at high temperature.

4.4 *Plastic Failure Modes at Limit States When Piping Under Multi-loading Condition*

The limit load and the von Mises stress results with different type of local wall-thinning (small area pit, circumferential pit, axial pit and large area pit) are given in Fig. 11.

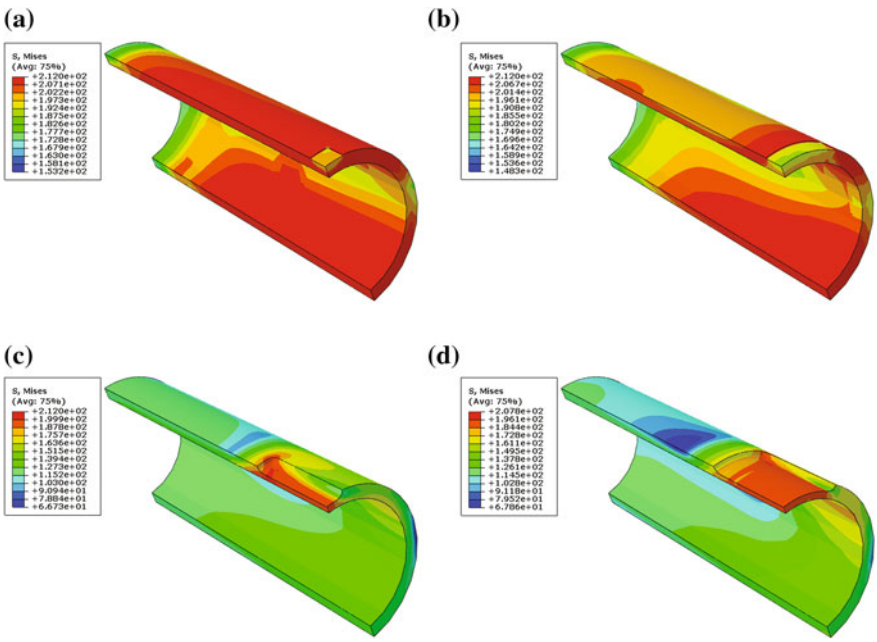

Fig. 11 The limit states of piping after serving for $t_{0.9}$ hours with different local wall-thinning and small defect depth under both internal pressure and bending moment loading condition. **a** Small area pit. **b** Circumferential pit. **c** Axial pit. **d** Large area pit

The failure modes of piping with local wall-thinning defect at limit states can be found from Fig. 11 when both the internal pressure and bending moment are applied. When both of the load combination ratio and the depth ratio are relatively small, which means the internal pressure is predominant compared with the bending moment, almost all the zones of the piping are getting into plastic flow state if the type of local wall-thinning is small area pit or circumferential pit. It means that the limit state of piping is reached, and the failure mode of piping is global plastic failure. Whereas, only the defect area of piping is getting into plastic flow state if the local wall-thinning type is axial pit or large area pit, and the plastic hinge is emerged in pit. It can be indicated that the failure modes of these types of piping are

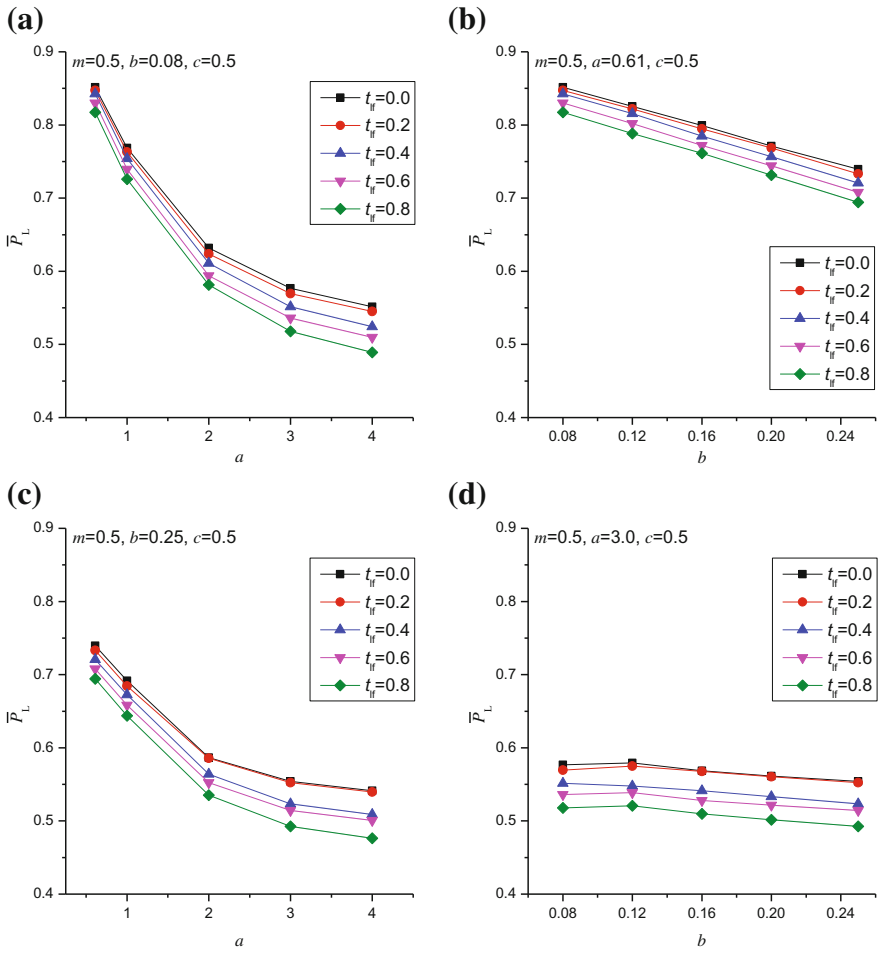

Fig. 12 Limit loads versus the ratios of local wall-thinning The limit states of piping after serving for $t_{0.9}$ hours with different local wall-thinning and small defect depth under both internal pressure and bending moment loading condition. **a** $m = 0.5, b = 0.08, c = 0.5$. **b** $m = 0.5, a = 0.61, c = 0.5$. **c** $m = 0.5, b = 0.25, c = 0.5$. **d** $m = 0.5, a = 3.0, c = 0.5$

local plastic failure. However, if the defect depth ratio is relative large, the failure modes of piping are changed to the local plastic failure if the local wall-thinning type is small area pit or circumferential pit. The failure modes of the other type of defect are the same as the small defect depth ratio.

4.5 Limit Load Ratio with Defect Ratio for Piping

Using the numerical method for the limit load of piping under elevated temperature proposed previously, the limit loads are calculated at each service timeline, then the limit pressure ratios $\overline{P_L}$ and the limit moment ratios $\overline{M_L}$ are obtained for the piping with one local wall-thinning defect type. By changing the defect ratios, all the limit loads for piping with local wall-thinning defect can be completed. Figure 12 shows the effect of defect ratios on the limit loads.

In order to analyze the effect of defect ratios a and b on the limit loads, the depth ratio c is set as a constant parameter ($c = 0.5$). It can be seen from Fig. 12 that, when the load combination ratio is relatively small, all the limit pressure ratios decrease with the increment of the service time due to the material deterioration, meanwhile, the limit pressure ratios also decrease sharply with the increment of axial length ratio a and circumferential ratio b. However, ratio b can be ignored when ratio a is large enough ($a = 3.0$), which indicates that the axial length ratio has main influence on the limit load when the internal pressure loading is dominant.

5 Conclusion

In this research, numerical limit analysis of modified 9Cr-1Mo steel pressure vessels with volume defect and piping with local wall-thinning at 650 °C has been studied. The creep behavior with L-M damage model and general hardening behavior with modified R-O model have been implemented in ABAQUS with the CREEP and USDFLD subroutine. The limit load under elevated temperature is defined as the load-carrying capacity after the structure serviced for a long time. The UTS damage ratio has been defined to consider the creep damage, and then, the R-O model has been modified by embedding the UTS damage ratio to take into account material deterioration. Thus, a numerical solution method for the limit load at elevated temperature considering creep damage due to material deterioration has been proposed.

Meanwhile, examples for pressure vessels and piping with different sizes of defects and multi-loading systems have been calculated and analyzed, and the following conclusions can be drawn:

1. The service life and limit load of pressure vessels and piping are very sensitive to the defect ratio at high temperature. The failure mode of pressure vessels and

piping is global structure plastic failure when the defect ratio is relative small, whereas the failure mode is local plastic failure in the limit state when defect ratio is relative large.

2. Large defect can speed up the accumulation of creep damage during creep deformation. With the high creep damage rate, the secondary and tertiary creep stages have been shorten substantially, and the limit load ratio is reduced rapidly, even the limit load is no longer exist when the creep damage zone is achieved in a number of elements along the thickness of the cylindrical pressure vessel. Therefore, the defect ratio must be restricted carefully to ensure the safety of pressure vessels and piping at high temperature.
3. For the piping with local wall-thinning at high temperature, the axial length ratio a has main influence on the limit load when the load combination ratio $m \leq 0.5$, which indicates that the internal pressure is dominant. In a similar way, the limit load is mainly effected by the circumferential ratio b when the load combination ratio $m \geq 2.0$, which indicates that the bending moment is dominant. If the load combination ratio $0.5 < m < 2.0$, the limit loads are not dependent on the single defect ratio.

Acknowledgements This work was supported by the National Science Foundation for Distinguished Young Scholars of China (Project No. 11325211) and National Natural Science Foundation of China (Project No. 11302023).

References

1. Perrin IJ, Hayhurst DR (1996) Creep constitutive equations for a 0.5Cr-0.5Mo-0.25V ferritic steel in the temperature range 600–675 °C. J Strain Anal Eng Des 31:299–314
2. Drucker DC (1951) A more fundamental approach to plastic stress-strain relations. J Appl Mech-T ASME 18(3):487–491
3. Hill R (1950) The mathematical theory of plasticity. The Oxford engineering science series. Clarendon Press, Oxford
4. Hodge PG (1963) Limit analysis of rotationally symmetric plates and shells. Prentice-Hall series in solid and structural mechanics, vol 147. Prentice-Hall, Englewood Cliffs, N. J.
5. Hodge PG Jr (1970) Limit analysis with multiple load parameters. Int J Solids Struct 6(5): 661–675
6. Belytschko T, Hodge PG (1970) Plane stress limit analysis by finite elements. J Eng Mech Div 96(6):931–944
7. Maier G, Munro J (1982) Mathematical programming applications to engineering plastic analysis. Appl Mech Rev 35(12):1631–1643
8. Chen HF (1998) Numerical methods for limit analysis and reference stress determination of structures under multi-loading systems and their engineering applications. Tsinghua University, Beijing (in Chinese)
9. Han LH, He SY, Wang YP, Liu CD (1999) Limit moment of local wall thinning in pipe under bending. Int J Press Vessels Pip 76(8):539–542
10. Kim JW, Na MG, Park CY (2008) Effect of local wall thinning on the collapse behavior of pipe elbows subjected to a combined internal pressure and in-plane bending load. Nucl Eng Des 238(6):1275–1285

11. Kim YJ, Kim J, Ahn J, Hong SP, Park CY (2008) Effects of local wall thinning on plastic limit loads of elbows using geometrically linear FE limit analyses. Eng Fract Mech 75(8): 2225–2245
12. Mackenzie D, Shi J, Boyle JT (1994) Finite-element modeling for limit analysis by the elastic compensation method. Comput Struct 51(4):403–410. doi:10.1016/0045-7949(94)90325-5
13. Liu YH, Cen ZZ, Xu BY (1995) Numerical limit analysis of cylindrical-shells with part-through slots. Int J Press Vessels Pip 64(1):73–82
14. Liu YH, Cen ZZ, Xu BY (1995) Numerical investigation of limit loads for the pressure vessels with part-through slots. Acta Mech Solida Sin 8(3):263–276
15. Liu YH, Cen ZZ, Xu BY (1995) A numerical-method for plastic limit analysis of 3-D structures. Int J Solids Struct 32(12):1645–1658
16. Liu YH, Zhang XF, Cen ZZ (2004) Numerical determination of limit loads for three-dimensional structures using boundary element method. Eur J Mech A-Solid 23(1): 127–138
17. Liu YH, Zhang XF, Cen ZZ (2005) Lower bound shakedown analysis by the symmetric Galerkin boundary element method. Int J Plast 21(1):21–42
18. Du XH, Liu DH, Liu YH (2015) Numerical limit load analysis of 3D pressure vessel with volume defect considering creep damage behavior. Math Probl Eng 1–13
19. Arzt E, Wilkinson DS (1986) Threshold stresses for dislocation climb over hard particles—the effect of an attractive interaction. Acta Metall Mater 34(10):1893–1898
20. Fournier B, Sauzay M, Pineau A (2011) Micromechanical model of the high temperature cyclic behavior of 9–12%Cr martensitic steels. Int J Plast 27(11):1803–1816
21. Böck N, Kager F (2005) Finite element simulation of the creep behaviour of 9% chromium steels based on micromechanical considerations. Paper presented at the materials science and technology 2005 conference and exhibition, Pittsburgh, PA, USA, 25–28 Sept 2005
22. Sklenička V, Kuchařová K, Dlouh SA, Krejci J (1994) Creep behaviour and microstructure of a 9%Cr steel. Paper presented at the proceedings of the conference on materials for advanced power engineering, Dordrecht, Netherlands
23. Graham A, Walles KFA (1955) Relations between long and short time properties of commercial alloys. J Iron Steel Inst 193:105
24. McVetty G (1933) Factors affecting the choice of working stresses for high temperature service. Trans ASME 55:99
25. Conway JB, Mullikin MJ (1962) An evaluation of various first stage creep equations. Paper presented at the proceedings of AIME conference, Detroit, Michigan
26. Norton FN (1929) The creep of steel at high temperature. McGraw-Hill, New York
27. Kachanov LM (1958) On destruction in creeping of materials. Izvestia Akademii Nauk SSSR, Otdelenie Tekhnicheskich Nauk 8:26–31
28. Rabotnov YN (1969) Creep problems in structural members. North-Holland series in applied mathematics and mechanics, vol 7. North-Holland Publishing Company, Amsterdam, London
29. Liu DH, Li HS, Liu YH (2015) Numerical simulation of creep damage and life prediction of superalloy turbine blade. Math Probl Eng 1–10
30. Saanouni K, Chaboche JL, Bathias C (1986) On the creep crack growth prediction by a local approach. Eng Fract Mech 25(5–6):677–691
31. Benallal A, Billardon R, Lemaitre J (1991) Continuum damage mechanics and local approach to fracture: numerical procedures. Comput Methods Appl Mech Eng 92(2):141–155
32. Hall FR, Hayhurst DR, Brown PR (1996) Prediction of plane-strain creep-crack growth using continuum damage mechanics. Int J Damage Mech 5(4):353–383
33. Hayhurst DR (2005) CDM mechanisms-based modelling of tertiary creep: ability to predict the life of engineering components. Arch Mech 57(2–3):103–132
34. Liu Y, Murakami S (1998) Damage localization of conventional creep damage models and proposition of a new model for creep damage analysis. JSME Int J Ser A: Solid Mech Mater Eng 41(1):57–65
35. Murakami S, Liu Y, Mizuno M (2000) Computational methods for creep fracture analysis by damage mechanics. Comput Methods Appl Mech Eng 183(1–2):15–33

36. McLean M, Dyson BF (2000) Modeling the effects of damage and microstructural evolution on the creep behavior of engineering alloys. J Eng Mater Technol Trans ASME 122(3): 273–278
37. Hyde TH, Becker AA, Sun W, Williams JA (2006) Finite-element creep damage analyses of P91 pipes. Int J Press Vessels Pip 83(11–12):853–863
38. Cocks ACF, Ashby MF (1980) Intergranular fracture during power-law creep under multiaxial stresses. Metal Sci 14(8–9):395–402
39. Basirat M, Shrestha T, Potirniche GP, Charit I, Rink K (2012) A study of the creep behavior of modified 9Cr-1Mo steel using continuum-damage modeling. Int J Plast 37(0):95–107
40. Xue JL, Zhou C, Wang B, Peng J (2013) Stress-strain constitutive relation of P91 steel based on creep damage. J Nanjing Univ Technol (Natural Science Edition) 35(4):33–37 (in Chinese)
41. Wang N, Liu H-Q, Tu S-T (2014) Elasto-plastic constitutive model of 2.25Cr1Mo steel considering initial creep damage. Press Vessel Technol 31(1):1–14 (in Chinese)
42. Goyal S, Laha K, Das CR, Panneerselvi S, Mathew MD (2013) Finite element analysis of effect of triaxial state of stress on creep cavitation and rupture behaviour of 2.25Cr–1Mo steel. Int J Mech Sci 75:233–243
43. Rouse JP, Sun W, Hyde TH, Morris A (2013) Comparative assessment of several creep damage models for use in life prediction. Int J Press Vessels Pip 108–109(0):81–87
44. ASME (2010) Boiler & Pressure Vessel Code Division 1. Subsection NH III. ASME, USA
45. Masuyama F (2006) Creep degradation in welds of Mod. 9Cr-1Mo steel. Int J Press Vessels Pip 83(11–12):819–825
46. Ramberg W, Osgood WR (1943) Description of stress-strain curves by three parameters. Technical Note No. 902. National Advisory Committee For Aeronautics, Washington DC
47. ASME (2010) Fitness-For-Service. API 579-1. ASME, USA
48. Takahashi Y (2008) Study on creep-fatigue evaluation procedures for high-chromium steels—part I: test results and life prediction based on measured stress relaxation. Int J Press Vessels Pip 85(6):406–422. doi:10.1016/j.ijpvp.2007.11.008
49. Du XH, Zhang J, Peng H, Liu YH (2017) Plastic limit analysis of modified 9Cr-1Mo steel pressure vessel containing volume defect with creep damage law. Int J Appl Mech 9(2): 1750025(1–29)
50 Du XH, Zhang J, Liu YH (2017) Plastic failure analysis of defective pipes with creep damage under multi-loading systems. Int J Mech Sci 128–129:428–444
51 Chen G, Liu YH (2006) Numerical theories and engineering methods for structural limit and shakedown analyses. Science Press, Beijing (in Chinese)